STUDY OF A HALL ACCELERATED PLASMA

by

JOSEPH DAVID KILKENNY

Thesis submitted to the University of London

for the degree of

Doctor of Philosophy

July 1972

Abstract

The polytron occupies an unusual position amongst plasma devices, resting between tokamaks, cusp containers and Hall accelerators. Hopefully such a hybrid system could combine the advantageous features of all three plasma devices.

In this thesis the acceleration phase of the polytron is studied. The first detailed measurements on the laboratory plasma are reported and in parallel a computational single particle model of the plasma both with and without a self consistent electrostatic field, is developed.

The simulation reveals the novel results that Hall acceleration occurs only at a thin sheath beneath the ring cusp and that an appreciable fraction of the plasma is lost after about 1 μs.

The experimental results are quantitatively explained by the single particle model. It is shown unequivocally that a single particle equation is experimentally applicable to the acceleration. A sheath width of 2mm is inferred. A momentum balance is demonstrated. An energy balance implies a large heat conduction loss. Consequently electron temperature, measured by laser scattering are only about 30eV, with electron number densities about $5\ 10^{20}\ m^{-3}$.

The predicted initial loss is experimentally identified. However, there is a later loss by radial drift of the plasma, thought to be due to the pressure difference of the poloidal magnetic field. Possible ways of suppressing this drift are discussed.

Subsidiary to this main theme the formation of the plasma for the polytron is described experimentally and computationally.

CONTENTS

Notation

Except where stated r.m.k.s. units are used. W is used to denote the temperature in electron volt units. The electron number density is usually referred to as n; occasionally and in chapter 3 n_e is used for emphasis, and in chapter 3 n is used to denote a principal quantum number.

CHAPTER ONE

AN INTRODUCTION TO THE POLYTRON CONCEPT AND PREVIOUS EXPERIMENTAL AND THEORETICAL WORK

The purpose of this chapter is firstly to provide a history of previous work on the polytron, but more importantly to unite the various authors' work and to state their results in terms of an experimental perspective.

1.1 The evolution of the polytron concept

(a) Cusps and losses from cusps

The evolution of the polytron idea can be presented very logically as an attractive way of overcoming the losses from a cusp, and at the same time providing an implicit means of heating a cusp plasma.

Cusp magnetic field geometries have been studied with great interest principally because of the almost total absence of experimentally observed instabilities, and the theoretical m.h. stability even for high β plasmas. The only experimentally observed macroscopic instability is a Rayleigh Taylor effect observed during compression of the plasma by a rapidly rising cusp field, (Allen & Bickerton, 1961). The work presented in this thesis does show instabilities (Chapter 10) but the magnetic field geometry is not that of a pure cusp.

However the cusp container has 3 non negligible holes in it, the line (ring) cusp, and the two point cusps, where the

lines of force leave the system. An absolute minimum hole width is 4 electron Larmor radii (Firsov, 1959). This is for the case where the magnetic field is excluded from the plasma. Loss occurs through a hole twice the width of the plasma field interface, which cannot be less than two electron Larmor radii. In this case ions are contained by space charge fields.

Usually (Allen & Bickerton, 1961) these space charge fields are shorted out by the solid wall that the field lines eventually contact. But even neglecting wall effects a plasma-field interface of 2 electron Larmor radii requires a large electron drift velocity/ion thermal velocity ratio, which is likely to be unstable to ion ac oustic modes. Thus Allen, Cox and Spalding (1965) consider the more realistic case of the hole being the size of the ion Larmor radius, and even supposing high temperatures can be attained, the losses through the holes alone requires 10^{23} particles in the plasma to satisfy the Lawson criterion $n\tau = 10^{14}$ s cm^{-3}, and a plasma energy of 10^{8} J. It is clear that attempts to plug the holes will be profitable as then the total number requirement is smaller.

(b) Ways of reducing cusp leakages

Several ways of reducing cusp leakage have been suggested. Some of the more important are listed.

(1) By the use of radio frequency fields at the ion cyclotron frequency, at the cusp holes. Energy is transferred to the ions, increasing their magnetic moment and thus the mirroring containment effect. Significantly improved containment

has been observed by Mijake (1971), but the method is only directly applicable for low desities such that the plasma frequency is below the ion cyclotron frequency.

(2) Electrostatic plugging by means of an electrostatic field parallel to the field lines (Ware and Faulkner, 1969). This has not yet been tested experimentally.

(3) Using a hybrid system such as a caulked and stuffed cusp (Burkhardt, Birkrew and Kan, 1968). Plasma lifetimes of 100μs have been observed in these systems but there are losses to the supports and the configuration is only m.h.d. stable on average.

(c) The polytron concept

The idea of the polytron is to avoid losses from the ring cusp by causing the plasma to move axially at a supersonic speed. This restricts the loss cone of particle to those, which in the c.m. frame are moving axially with the velocity of the c.m. frame, which is many times the thermal velocity. As also the transverse velocity must be large enough to overcome the mirror effect of the ring cusp, very few particles should be able to escape. The point cusps are eliminated by having many cusps arranged in a toroidal configuration.

The c.m. velocity is achieved by a Hall acceleration process. The magnetic field configuration is similar to linear Hall accelerators of the radial magnetic field variety (Cole

1970 , Morozov et. al. 1969). Centrifugal drift of the moving plasma is avoided by the focussing effect of the cusp fields as magnetic lenses. Two stream instability is avoided by restricting the c.m. velocity to being smaller than the electron thermal velocity, by the drag force of collisons with the stationary electrons. M.h.d. stability is ensured by restricting the number density so that the poloidal magnetic field caused by the toroidal plasma current is much less than the cusp field.

Inplicit in this scheme of cusp containment is a heating mechanism, the toroidal ion current.

The chronological development of the polytron was different. It evolved from a z pinch with one coil producing a radial magnetic field. Plasma acceleration was observed, (Etherington and Haines (1965)). From this Haines proposed the polytron concept as a kind of stabilised toroidal z pinch, the cusp fields being very stable and the cusp losses being avoided by the plasma motion.

Haines's work was presented in abstract form at the Salzburg conference of 1961, and again briefly in 1963(a). Unfortunately no complete paper is in the literature yet although an Imperial College internal report exists.(1963 b)

1.2 The Hall acceleration mechanism.

At the inception of the polytron little work had been done on Hall accelerators, and this was mainly on the propulsion

applications of such devices (Patrick, Schneiderman, Cann and Marlotte). Lately further effort has been devoted to Hall accelerators as a possible means of filling a fusion machine (Cole, Morozov).

Consider briefly the essential properties of an ideal Hall accelerator (taken from Haines, 1963). There is uniformity in the x and y direction, periodicity in the z direction, $\underline{B}\ (x,y,z) = (B_0 \sin kz,\ 0,0)$, $\underline{E} = (0,0,E_0)$. The z and y components of Ohm's law are:

$$\frac{j_z}{\sigma} = E_z' + \left(\frac{j_y B_0}{ne} - v_y B_0\right) \sin kz \qquad -(1.1)$$

$$\frac{j_y}{\sigma} = \left(v_z B_0 - \frac{j_z B_0}{ne}\right) \sin kz \qquad -(1.2)$$

E_z' takes into account a periodic electrostatic field necessary for $\mathrm{div}\, j = 0$. From 1.2 $j_y = j_{yo} \sin kz$ and $j_{yo} = \sigma v_z B_0 - j_z \omega\tau$ where $\omega\tau = \frac{\sigma B_0}{ne}$. Eq. 1.1 can be integrated from 0 to $2\pi/k$ giving giving

$$j_z = \sigma E_0 + j_{yo}\frac{\omega\tau}{2} - v_b \frac{\sigma B_0}{2} \qquad -(1.3)$$

where $v_y = - v_a \cos kz + v_b \sin kz$

Initially $v \ll j/ne$ and so

$$j_z = \frac{\sigma E_0}{1 + (\omega\tau)^2/2} \qquad -(1.4): \quad j_{yo} = -\frac{\omega\tau\, \sigma E_0}{1 + (\omega\tau)^2/2} \qquad -(1.5)$$

For $\omega\tau \gg 1$, j_z is greatly reduced from the field free value of σE_0 and $- j_{yo} = 2ne\, E_0/B_0$ is the current carried by the average electron E x B $/(B)^2$ drift, with n the electron number density. The plasma is also accelerated as

$$\frac{dv_z}{dt} = -\frac{1}{nm} j_y B_x = -\frac{2e}{m} E_0 \sin^2 kz \qquad -(1.6)$$

which gives $\frac{dv_z}{dt} = \frac{eE_o}{m}$ when integrated over τ. Thus in this limit the ions are being freely accelerated, and the electrons trapped, by virtue of their smaller (c.f 1/k) Larmor radius. As long as the Larmor radius of the ions is large c.f. 1/k, the ions are freely accelerated until $j_z \approx nev_i \approx \sigma E_o$ when $j_y = 0$, and there is no further plasma acceleration. If $k \to \infty$ then $v_y \to 0$; $j_z = \sigma E_z$, and $v_z = \frac{\sigma E}{ne}$ is the limiting drift velocity when the accelerating force, eE, on the ions is balanced by the electrons drag. The acceleration time to attain this velocity is

$$\tau_a = \frac{2\rho}{\sigma B_o^2} + \frac{\sigma \rho}{n^2 e^2} = \frac{2}{\omega_{ci}}\left(\frac{1}{\omega\tau} + \omega\tau\right)$$

where ω_{ci} is the ion Larmor frequency.

It should be clear from this simplified analysis the equivalence between particle and fluid approaches. However as there are large spatial variations in the polytron fields and partial differential equations such as the m.h.d. equations are difficult to solve, whereas the ordinary differential equations, describing particle trajectories are simpler, it is mainly a particle approach which has been used in this thesis.

1.3. Other Hall accelerators

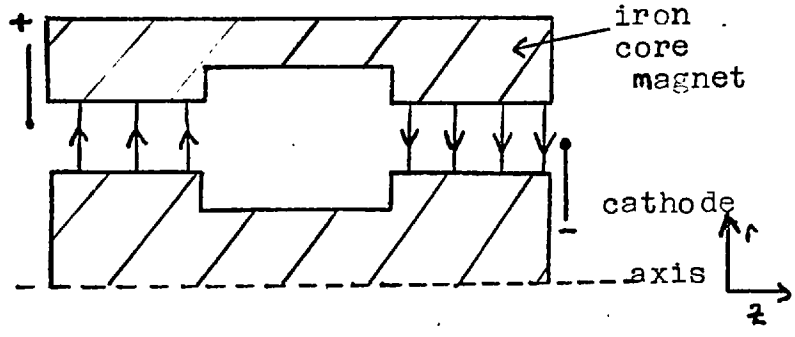

FIG. 1.1

r - z SCHEMATIC OF A LINEAR 2 STAGE HALL ACCELERATOR

Fig.1.1 illustrates a linear 2 stage Hall accelerator. The field is supplied by an iron cored magnet. A pair of electrodes supplies the accelerating field E_o. A neutral gas is injected by a fast action valve and is ionised near the anode . A neutral plasma is ejected from the end. With this type of device Cole has attained about 500A equivalent plasma current at 1.kV ion energy. Slightly better results have been attained by Morozov et al.

Common to both experiments is an absence of definitive measurement of basic physical processes and parameters, such as number density, temperature, force on the plasma, where the plasma starts from, time history, and loss of the plasma. On the polytron these have been measured. The periodicity, air core magnets, and preionisation make these intrinsically easier to study. As a result some aspects of the behaviour of a linear Hall accelerator can be understood by analogy with the polytron. The VI product for the ion current attained in the polytron is comparable with these linear Hall accelerators.

1.4 The objectives of the polytron project

The objectives of the polytron project, will now be explicitly stated.

(1) To examine the acceleration mechanism, that it is as predicted by a simple theory and that it will accelerate

plasma through cusps.

(2) Subsequently to examine the containment problem, both through the ring cusps and centrifugally.

This thesis broadly achieves the first objective. The second objective has been attained but only in a negative sense, studying the losses. Although the difference is only one of degree, it cannot be said that there is appreciable containment in the polytron yet.

1.5 Previous work on the polytron and the work presented in this thesis.

Etherington measured the axial Hall force on a z pinch with a superimposed radial field. As a result the polytron concept evolved. A polytron experiment was set up. Results were reported by Dangor et. al. (1968) and in more detail in Parkinson's thesis, showing that there was an acceleration of the plasma. Concurrently Dunnett (1968) extended the m.h.d. calculations of Haines (1963) to include the effect of the magnetic fields produced by the azimuthal plasma currents. Within the limitations of his assumptions he showed that the acceleration mechanism becomes ineffective if the fields of the plasma currents can destroy the applied cusp field.

The work in this thesis extends the understanding of the polytron by both experimental and computational work. The accelerator phase is quantified, i.e. a momentum balance is

demonstrated, and the variation of the acceleration with the initial parameters measured. This attains the first objective. Some of this work is already published.

There is however a rapid loss of plasma. This is measured experimentally and explained theoretically in terms of single particle models of the plasma both with and without self consistent electrostatic fields. Agreement with experiment is good. Some of these results are also published

The behaviour of the plasma after this loss is also examined. Because there are re-entrant impurities from the wall the results for this phase are not so definitive.

Subsidiary to this main theme, the thesis contains:-

(1) Calculations of the field of the polytron cusp coils and induction rods .

(2) An experimental and numerical study of the plasma formation , before the application of all the polytron fields. This is a study of a low voltage cusp compression experiment, with the advantage over earlier experiments of scattering diagnostics and numerical simulation.

(3) Calculations of the ionistation and heating rates for comparison with the ionisation burn through observed in the experiment.

(4) A detailed account of the laser scattering diagnostic, which even with a 10^8W laser is not a trivial experimental task for lower density plasmas.

1.6 A summary of the theoretical criteria necessary for polytron action

A list of the criteria for successful polytron action follows together with their origin .

(1) $\omega\tau \quad > 1$ (1.8)

otherwise no accelerating Hall currents flow (Haines 1963).

(2) $\frac{E}{B\omega_{ci}} \gtrsim \frac{L}{2}$ (1.9)

where L is the cusp separation $=\pi/k$. This is the condition that the ion Larmor radius is larger than the cusp separation[2], so that the ions are not trapped like the electrons (Haines,1963) For electrons the inequality 1.9 is reversed, but is easily satisfied.

(3) $\frac{E}{B^2}\mu_o ne < \frac{2}{L}$ (1.10)

This is the condition that the field produced by the azimuthal Hall current $\frac{L}{2}\mu_o neE$, is not large enough to destroy the cusp field, B, (Dunnett,1968 whose numerical values are $\frac{E}{B^2}\mu_o ne < \frac{3\pi}{8L}$)

From eq. 1.9 and 1.10 $\frac{2c}{L\omega_{Pi}} >> 1.$ (1.11)

where ω_{Pi} is the ion plasma frequency.

The above are all necessary before any polytron action can occur. The following are not so necessary as they assume polytron action is occuring.

(4) $v_z^2 >> \frac{2kT_i}{m_i}$ (1.12)

to reduce cusp losses (Haines, 1963)

(5) $v_z^2 << \frac{2kT_e}{m_e}$ (1.13) so that

a two stream instability does not occur. (Haines, 1963).

(6) $B_\theta << B$ (1.14)

for stability (similar to a Kruskal-Shafranov criterion, Haines, 1963) where B_θ is the poloidal field of the plasma and B the field of the cusp coils

(7) $\mu_o I_z^2 < 8\pi\ Nk(T_e + T_i)$ (1.15)

Where N is the line density, otherwise the discharge will pinch (the Bennett relation). Haines takes this further using his chosen steady state values of

$$v_z^2 = \frac{2kT}{(m_e m_i)^{\frac{1}{2}}}\ ,\ I_z = Nev_z$$

to get an upper limit to the line density.

$$N < \frac{8\pi\sqrt{m_e m_i}}{\mu_o e^2} = 4.3\ 10^{16}\ m^{-1} \qquad (1.16)$$

for hydrogen with $T_e = T_i$

It must be emphasised that this is only valid for the steady state of Haines. Otherwise eq. 1.15 is applicable.

I.7 Description of the apparatus

In its present form the apparatus consists of

(1) A toroidal quartz vacuum vessel, bore 72mm, major radius 25.4cm.

(2) 36 single turn cusp coils, of radius 5.2 cm, concentric with the minor axis and equally spaced toriodally with 10^o between them. Each is energised separately from 5kV,

216μF condenser banks, period 48μs.

(3) 6 (8 previously) 'induction' rods, current carriers in the toroidal direction, spaced poloidally around the vacuum vessel to give a locally small magnetic field but supplying a toroidal electric field by the flux change through the centre of the torus.

(4) A 'main bank' connected to the induction rods, of 60μF, 40 kV capacitance and small stray inductance, giving a period of 26μs.

(5) A 'preioniser' also connected to the induction rods, being a 2μF, 20kV capacitance, period 6μs. The triggering of the main bank is arranged so that the preioniser does not fire it (Parkinson, 1969).

The main bank voltage is a frequent variable in this thesis and is denoted by V_m. The relationship with the induced toroidal electric field is

$$E_\phi = .5\ V_m \quad V/m \qquad (1.17)$$ (where V_m is in volts).

The cusp bank voltage is denoted by V_c. Originally a two turn coil system was used, but for ease of assembly this was replaced by a one turn system which for a fixed charging voltage reduces the peak cusp field by 1.48. All values of V_c for this thesis are converted to the equivalent of a one turn coil system.

In the plane of the coils, $\phi = 0$, the average value of B_ϕ, the field in the toroidal direction is

$$\overline{B}_\phi = 1.8\ V_c \text{ gauss.} \qquad (1.18)$$

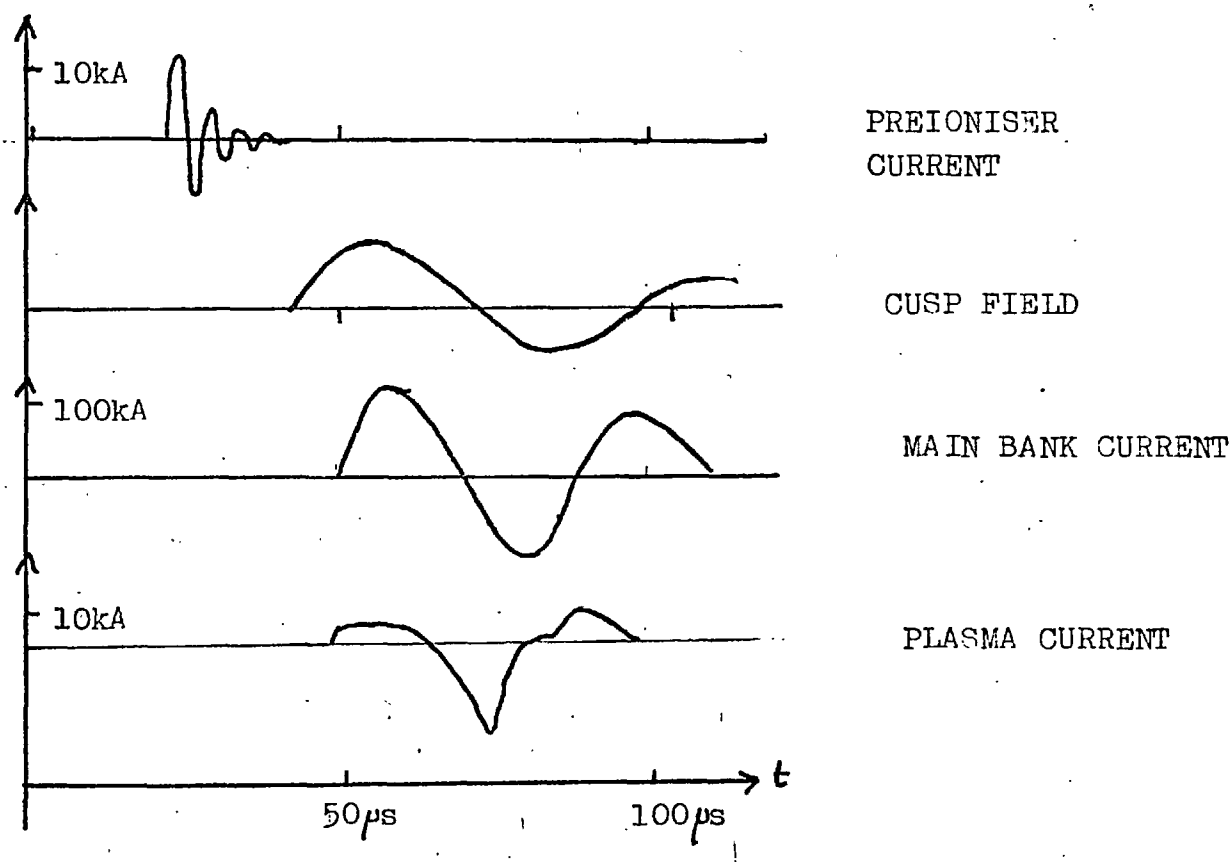

FIG. 1.2. TYPICAL TIMING SEQUENCE

In the plane of the ring cusp, $\phi = 5^{o}$, the average value of the radial magnetic field is $\overline{B}_r = 1.0\ V_c$ gauss. (1.19).

The preioniser is fired first. When the current of this ringing discharge has damped, the slowly rising cusp field is fired. When this is at its first peak the main bank is fired. This sequence is illustrated in fig. 1.2. Fig. 1.3 is a schematic diagram of the apparatus.

1.8 The role of the author in this work

Whilst acknowledging the great practical help of A.E. Dangor it must be mentioned, in accordance with London

University regulations that the work in this thesis essentially is solely the author's. Also for the sake of the regulations, of the three papers attached the experimental work of the first and third and the computational work of the second is due to the author.

FIG. 1.3: SCHEMATIC DRAWING OF THE POLYTRON APPARATUS

At present the induction rods are outside of the cusp coils, not inside as shown here.

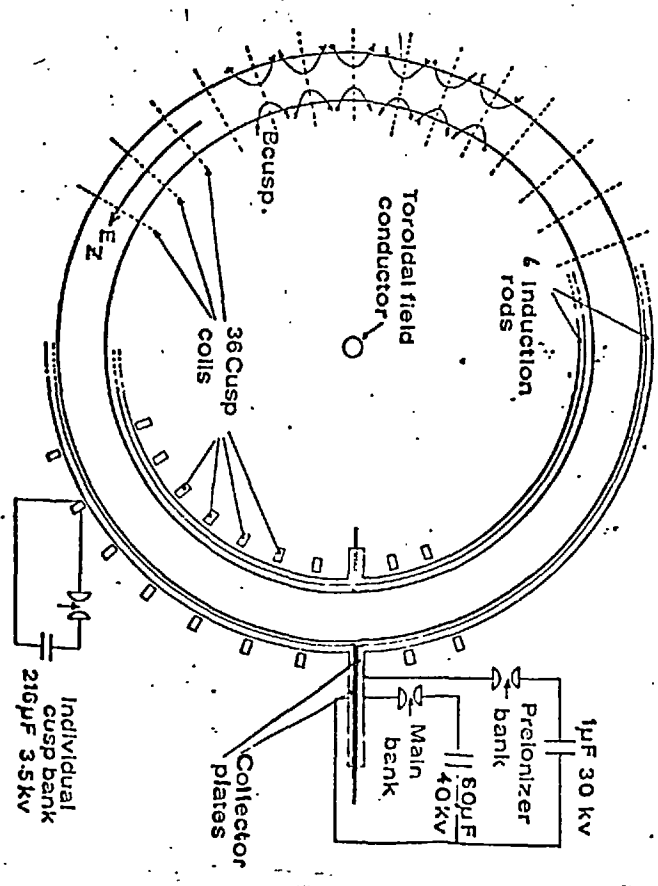

CHAPTER TWO

FIELD CALCULATIONS IN THE POLYTRON

The two sets of current elements in the polytron are the induction rods and the cusp coils. Calculations of the magnetic fields, the magnetic vector potential and the electric field are described. Comparison with the experiment is made. The calculations for the induction rods are used to redesign the system.

2.1. The field of a circular current element

Both the cusp coils and the induction rods are circular elements. Consider circular polar coordinates (r,e,z) coaxial with a coil of radius a. The magnetic vector potential

$$\underline{A} = \frac{\mu_0}{4\pi} \int I d\underline{l}/r' = A_e(r,z)$$

$$= \frac{\mu_0 I}{4\pi} \int_0^{2\pi} \frac{a \sin \phi \, d\phi}{(z^2+(a+r)^2+4ar \cos \phi)^{\frac{1}{2}}}$$

where r' is the distance from the field point to the current element, which carries a current I.

Therefore $A_e(r,z) = \frac{\mu_0 I}{k\pi} \left(\frac{a}{r}\right)^{\frac{1}{2}} \left((1-k^2/2)K - E\right)$ (2.1)

where $k^2 = \frac{4ar}{((a+r)^2 + z^2)}$

and $E(k^2) = \int_0^{\pi/2} (1-k^2 \sin^2 \alpha)^{\frac{1}{2}} d\alpha$

$$K(k^2) = \int_0^{\pi/2} \frac{d\alpha}{(1 - k^2 \sin^2\alpha)^{\frac{1}{2}}}$$

are the complete elliptic integrals of the first and second kinds respectively.

It is shown by Stratton (1941) that differentiating this expression for A_θ, gives the magnetic fields in the form

$$B_r = \frac{\mu_o I z}{2\pi r((a + r)^2+z^2)^{\frac{1}{2}}} \left(-K + \frac{a^2+r^2+z^2}{(a-r)^2+z^2} E\right) \quad (2.2)$$

$$B_z = \frac{\mu_o I}{2\pi((a + r)^2+z^2)^{\frac{1}{2}}} \left(K + \frac{a^2-r^2-z^2}{(a-r)^2+z^2} E\right) \quad (2.3)$$

It is important to evaluate $K(k^2)$ and $E(k^2)$ quickly. This is done using an algorithm from Lance(1960)

If $a_o = 1$: $b_o = (1 - k^2)^{\frac{1}{2}}$

The iteration $b^n = (a^{n-1}b^{n-1})^{\frac{1}{2}}$: $a^n = .5(a^{n-1} + b^{n-1})$

is used to evaluate the integrals by

$$K(k^2) = \frac{\pi}{(a^n + b^n)} \quad \text{as } n \rightarrow \infty$$

and

$$E(k^2) = K(k^2) \left(1 - \sum_{i=0}^{\infty} 2^i \frac{(a_i^2 - b_i^2)}{2}\right)$$

This is a rapidly converging iteration which gives an accuracy of 10^{-4} after about 4 iterations.

2.2 The field of the cusp system

In this section toroidal coordinates are used.

The calculation of the field of all the coils is a straight forward, if involved, exercise in coordinate

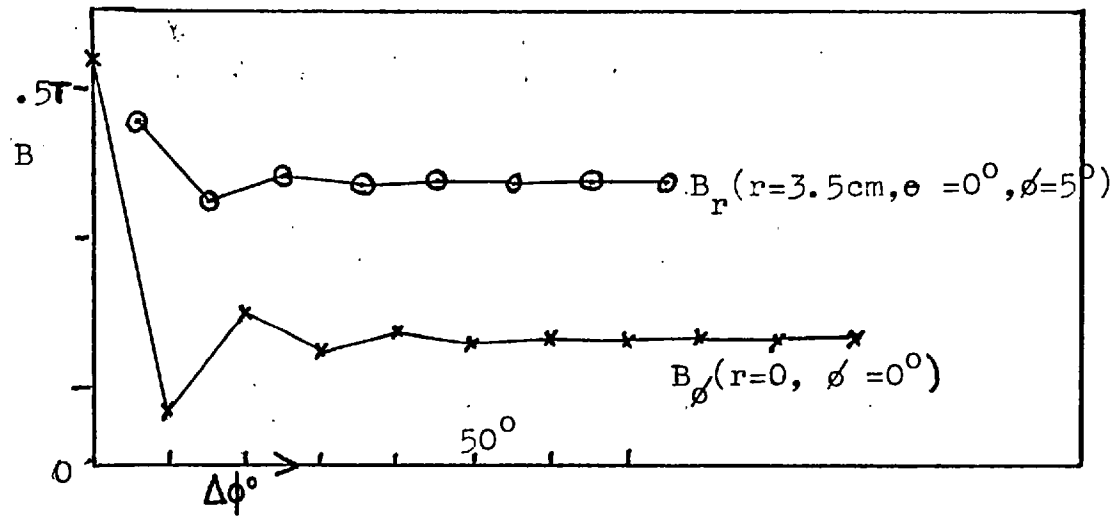

FIG. 2.1 THE FIELD FROM NEIGHBOURING COILS UP TO ± Δø AWAY

transformation. For a given field point each coil is considered in turn. The coordinates of the field point in the cylindrical coordinates of the coil under consideration are evaluated. The fields in this coordinate system are calculated using eqs. 2.1, 2.2 and 2.3.

These fields are then resolved into cylindrical coordinates based on the major axis, and added to the field of all the other coils.

The physical constants of the system resemble the experiment as closely as possible. They are:-

(1) 36 coils evenly spaced on a major radius of 25.4cm.

(2) The current through each coil alternatively ± 43.6 kA.

(3) The coils of radius 5.3 cm.

Only (3) is approximate in that the coils are not current elements but extend from radii 5.1 to 5.8 cm. The current corresponds to the peak current at a cusp bank charging voltage of 1.5kV.

The contribution of increasingly distant coils falls rapidly and is illustrated in fig. 2.1.

Previous to this work Dunnett had calculated the cusp field using the Legendre polynomial expansion of the magnetic scalar potential. However convergence of the polynomial is poor and so this is a very slow method. Additionally there was an error in his calculation. The error was only found by comparison with this calculation. As the experimental comparison was not made at the time the consistency of this calculation was checked by ensuring that $\nabla.\underline{B} = 0$.

Some of the results of the calculations are shown in figs. 2.2 and 2.3. The experimental values of the field and the first Fourier component of the Bessel function field

$$B_r = I_1(kr) \sin(18\phi) \quad : \quad B_\phi = I_0(kr) \cos(18\phi)$$

(see chapter 6) are also included. (here $k = \pi/L$).

The agreement between the calculation and the experiment is good and is within the experimental error. Also, with the neglect of toroidal effects, the Bessel function representation is reasonable (±10%).

The main effect of the torus is to shift the magnetic axis 6mm inwards from the geometric axis. This effect is because the field is larger outside of the minor

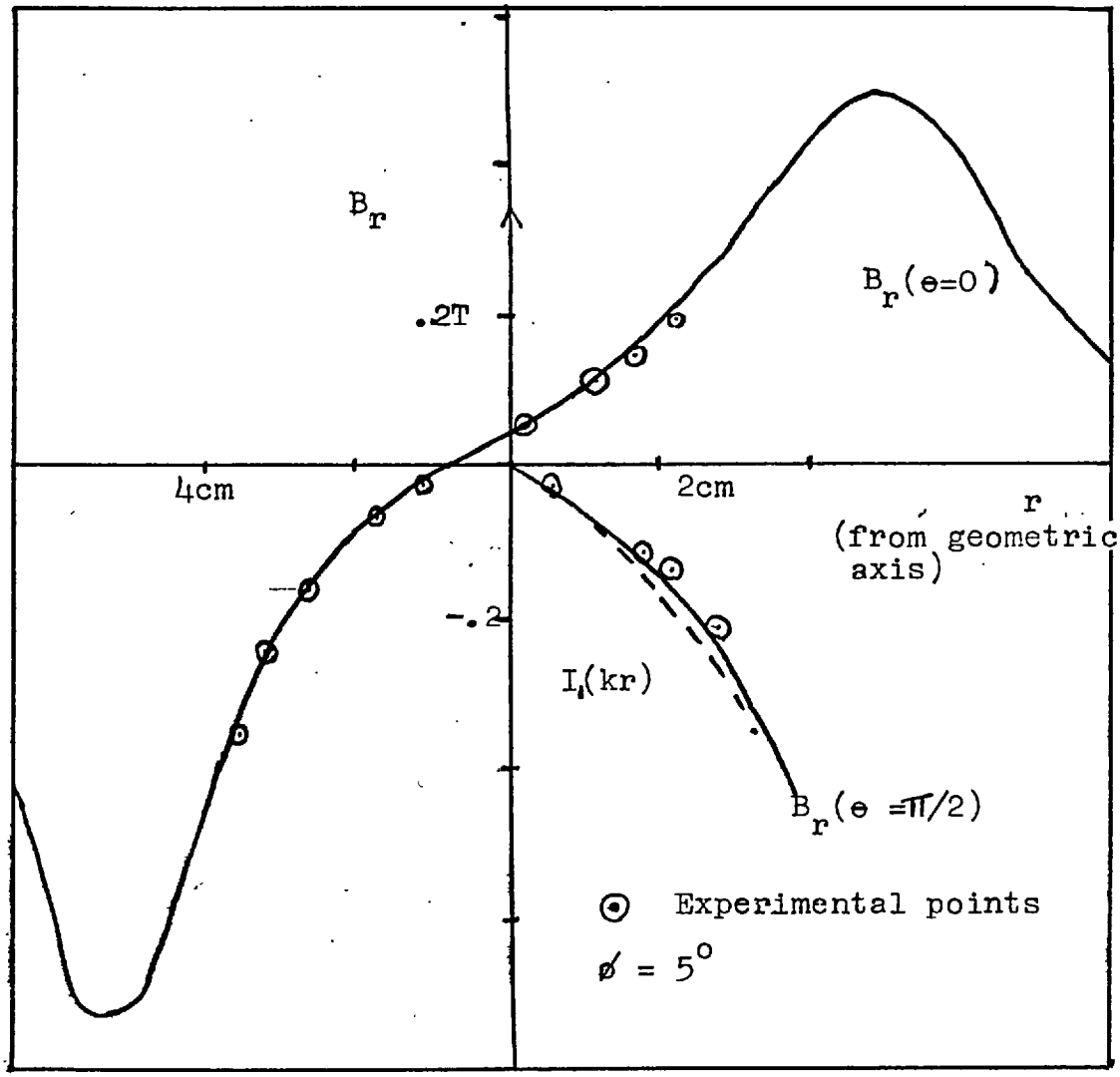

FIG. 2.2 B_r FOR THE CUSP COILS
(for V_c = 1.5kV)

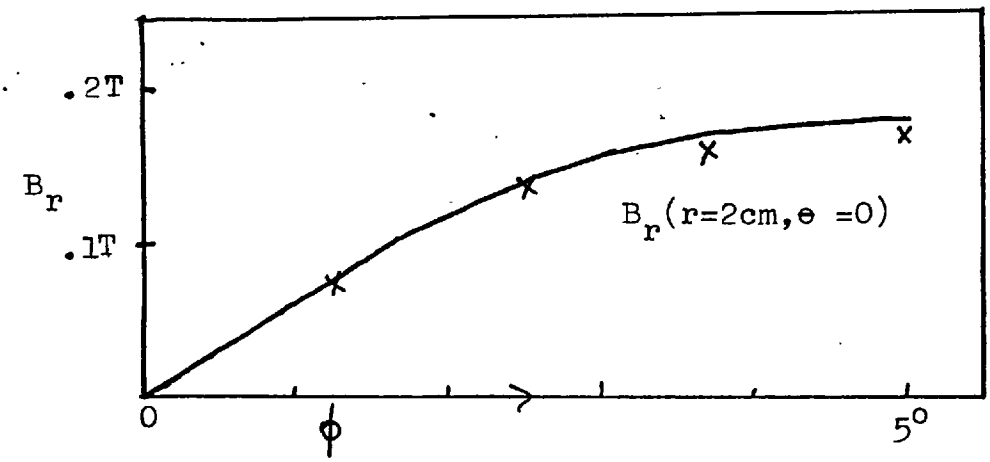

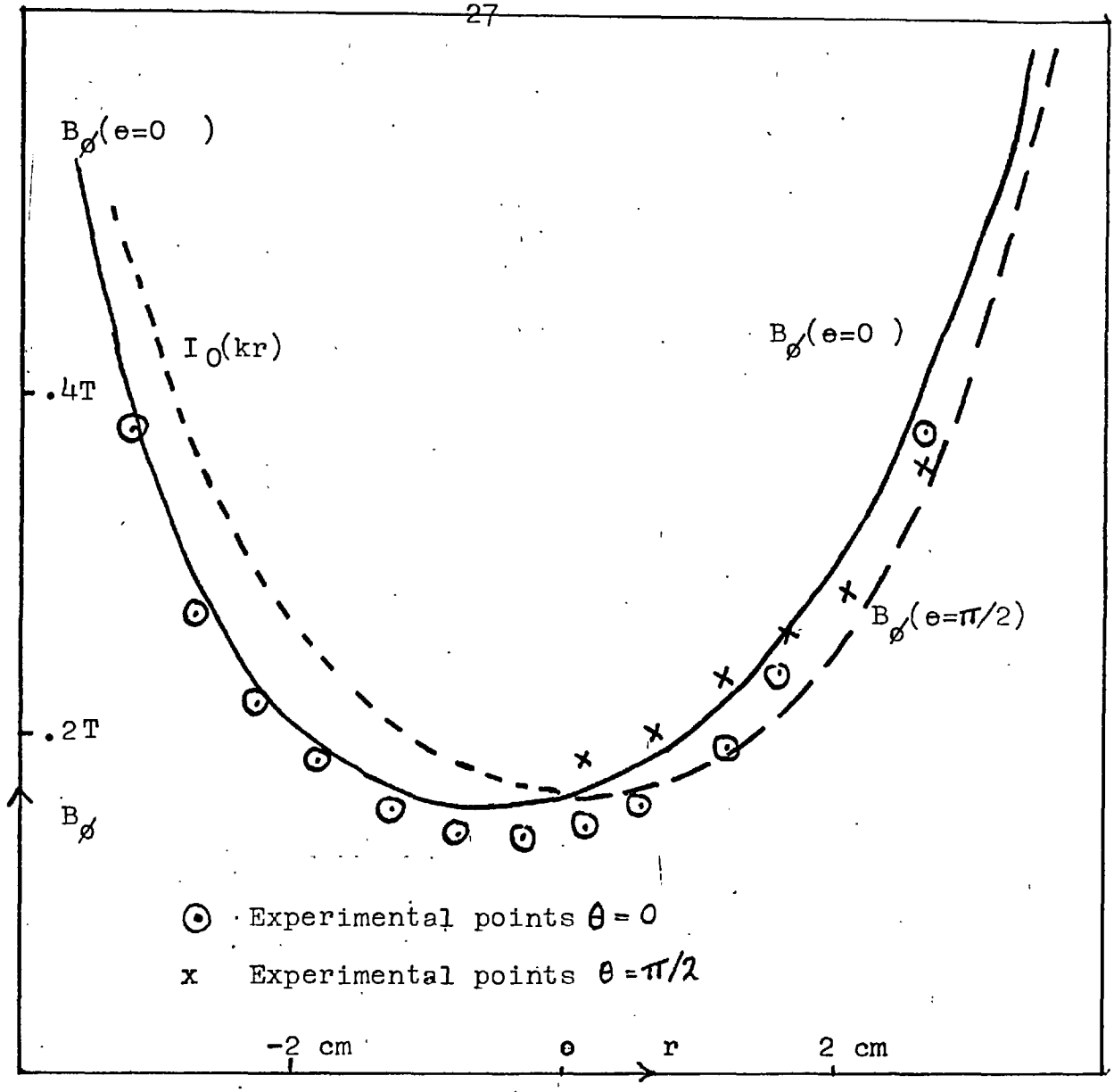

FIG. 2.3 B_ϕ FOR THE CUSP COILS AT $\phi = 0^o$ (V_c = 1.5kV)

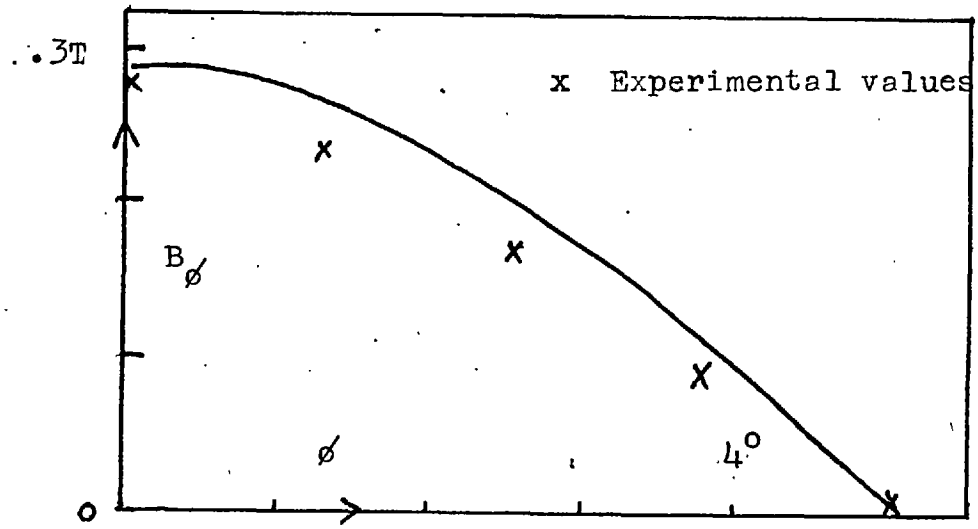

axis than an equal distance inside. The effect of the next pair of cusp coils, which decreases the field of the nearest coil (s), is smaller on the outside of the minor axis than it is on the inside of the axis, as the separation is larger, and thus causes the larger field outside of the axis.

The lines of force of the magnetic field are shown in fig. 2.4. They were obtained by integrating

$$\frac{d\underline{r}}{dt} = \underline{B}$$

Integration was by a first order scheme

$$R^{n+1} = R^n + \Delta t \; B_R^n \quad \text{etc.}.$$

The accuracy was checked by integrating backwards to get the original position. Δt was kept proportional to $1/B_R$. Each line was started from a position on the line ϕ = constant, z =0, the lines being separated by s where $\int_{R_0}^{R_0+s} B_\phi \, dR$ = constant.

2.3 The field of the induction rods

In this section cylindrical coordinates (R,ϕ,z) based on the major axis are used.

The original electrical design of the induction rods was based on the philosophy that the magnetic field inside a cage of parallel currents is small compared with that outside (Dunnett 1968b). For a conducting shell there is no field at all as no field line can penetrate the conductor. But as the field external to the rods in many kilogauss, it is worth investigating just how small the field inside the rods is.

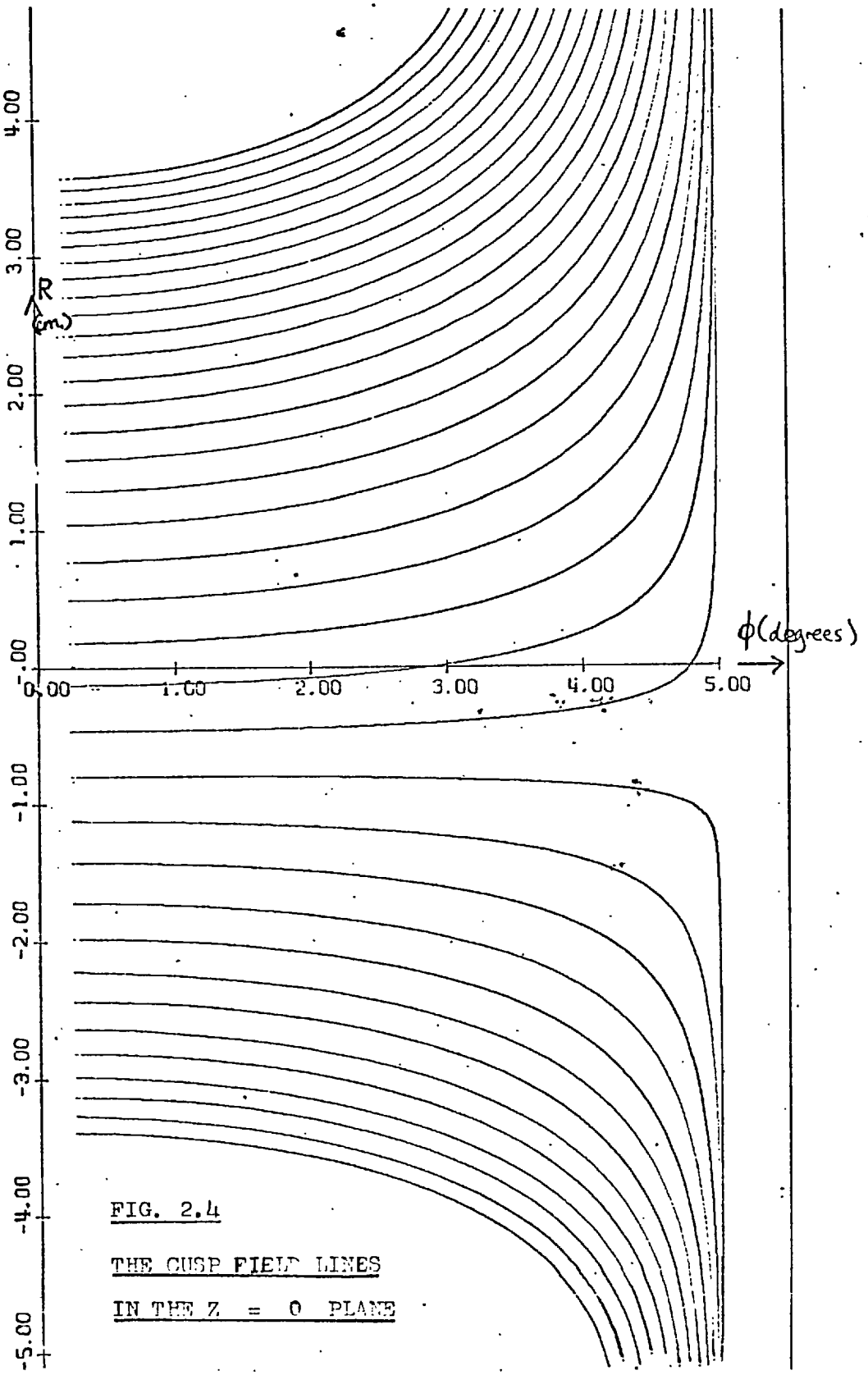

FIG. 2.4

THE CUSP FIELD LINES

IN THE Z = 0 PLANE

Using the prescription of section 2.1, calculation of the field of the rods is a simple matter once the currents have been determined. The current through the innermost rods is larger than the outer rods because of the smaller inductance. This allows the field to be small inside the cage of rods. Here the vertical field of the rods outside must cancel the field of the rods inside. As the vertical field of a loop is much smaller outside of the loop than an equal distance inside, cancellation can only occur if the current of the inside loops is much larger than the outside.

The electric field is insensitive to small flux through the centre of the cage and is approximately

$$E_{\phi}(R) = \frac{V_m}{2\pi R}$$

for R in the region of small magnetic field, where R is the major radius.

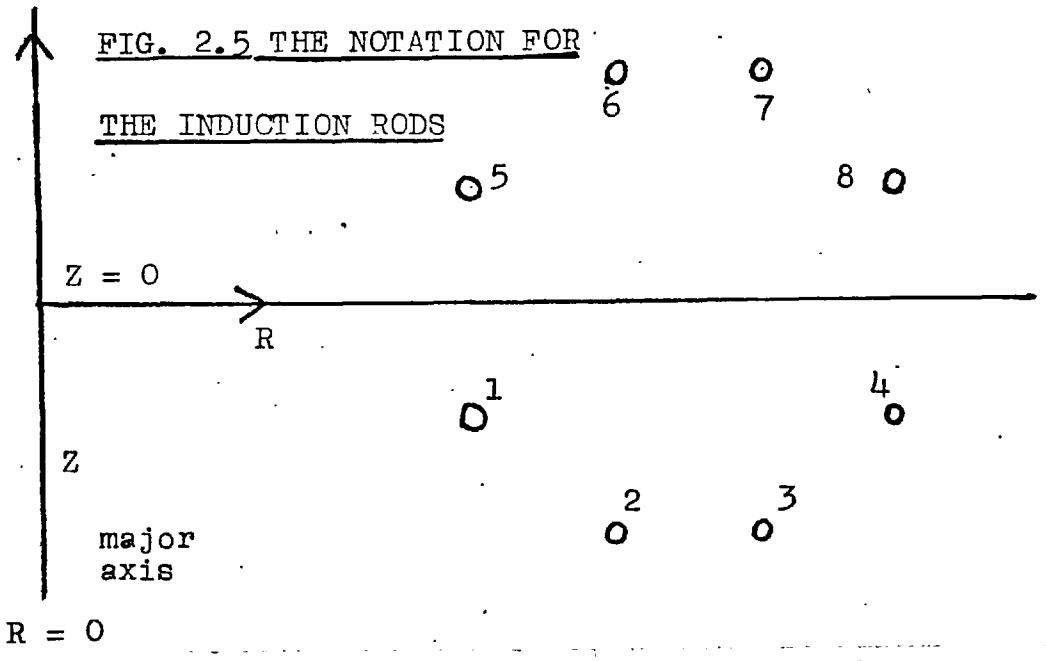

There is symmetry of position about the z = 0 plane, and hence symmetry of current. With the notation of fig. 2.5 the circuit equations for the currents in the rods are:

$$(L_1+M_{15})X_1+(M_{12}+M_{16})X_2+(M_{13}+M_{17})X_3+(M_{14}+M_{13})X_4 = 1 \qquad (2.4a)$$

$$(M_{21}+M_{25})X_1+(L_2+M_{26})X_2+(M_{27}+M_{23})X_3+(M_{24}+M_{28})X4 = 1 \qquad (2.4b)$$

$$(M_{31}+M_{35})X_1+(M_{32}+M_{36})X_2+(L_3+M_{37})X_3+(M_{34}+M_{38})X_4 = 1 \qquad (2.4c)$$

$$(M_{41}+M_{45})X_1+(M_{42}+M_{46})X_2+(M_{43}+M_{47})X_3+(L_4+M_{48})X_4 = 1 \qquad (2.4d)$$

where $X_i = \frac{\omega i_i}{V_m}$, i_i being the current through rod i, ω the angular frequency and V_m the main bank voltage. L_i and M_{ij} are the self inductance of rod i, and the mutual between rods i and j.

$$L_i = \mu_o R_i(\ln(8R_i/r) - 1.75)$$

where r is the minor radius of the rods. M_{ij} is taken from Grover (1962). This is the mutual inductance of coaxial current filaments, but as the separation of the rods is large compared with the rods' radius the filament approximation is good. Solution of eqs. 2.4 give X_i as a fraction of the total current in the rods, I_t. Substitution into say eq. 2.4a gives a simple harmonic equation for I_t. Thus ω can be evaluated and so the currents in the rods.

There have been 3 sets of induction rods in use on the polytron installation. The first two were built before these calculations of the field were made. The small rod assembly had 8 rods equally spaced poloidally on a radius of 3.8 cm from the minor axis . The assembly was built to fit in between the cusp coils and the small torus. The large, 8 rod assembly had

rods equally spaced poloidally on a minor radius of 7.4 cm, allowing the large torus to nearly fill the diameter of the cusp coils, the rods being a close fit outside of the cusp coils. The cusp coils had to be fitted after the induction rod cage and the close fit made this a complex manipulative procedure.

The fields and currents of the two 8 rod assemblies are shown in fig. 2.6. The field in the centre is larger for the small cage. The field lines of the large assembly are sketched in fig. 2.7. To check the calculation $\nabla.\underline{B}$ was evaluated with a difference of 1mm, and was found to be zero to 4% of $\frac{\partial B}{\partial z}_z$.

The line density of current on a shell has been calculated by Taylor (1960). Comparison with the currents in the rods is made in fig. 2.8 for the large assembly which was an aspect ratio of 25.4/7.4 = 3.4. From fig. 2.8 the cage is like a shell of aspect ratio 3.6. This would cause a larger inductance than a ratio of 3.4, as is necessary to account for the flux inside the cage.

2.4 The design of a new induction rod system

For the purpose of easier assembly and lower magnetic field in the cage, a new cage was designed. Near symmetry was retained about $z=0$ so that $B_R=0$ at $z=0$.

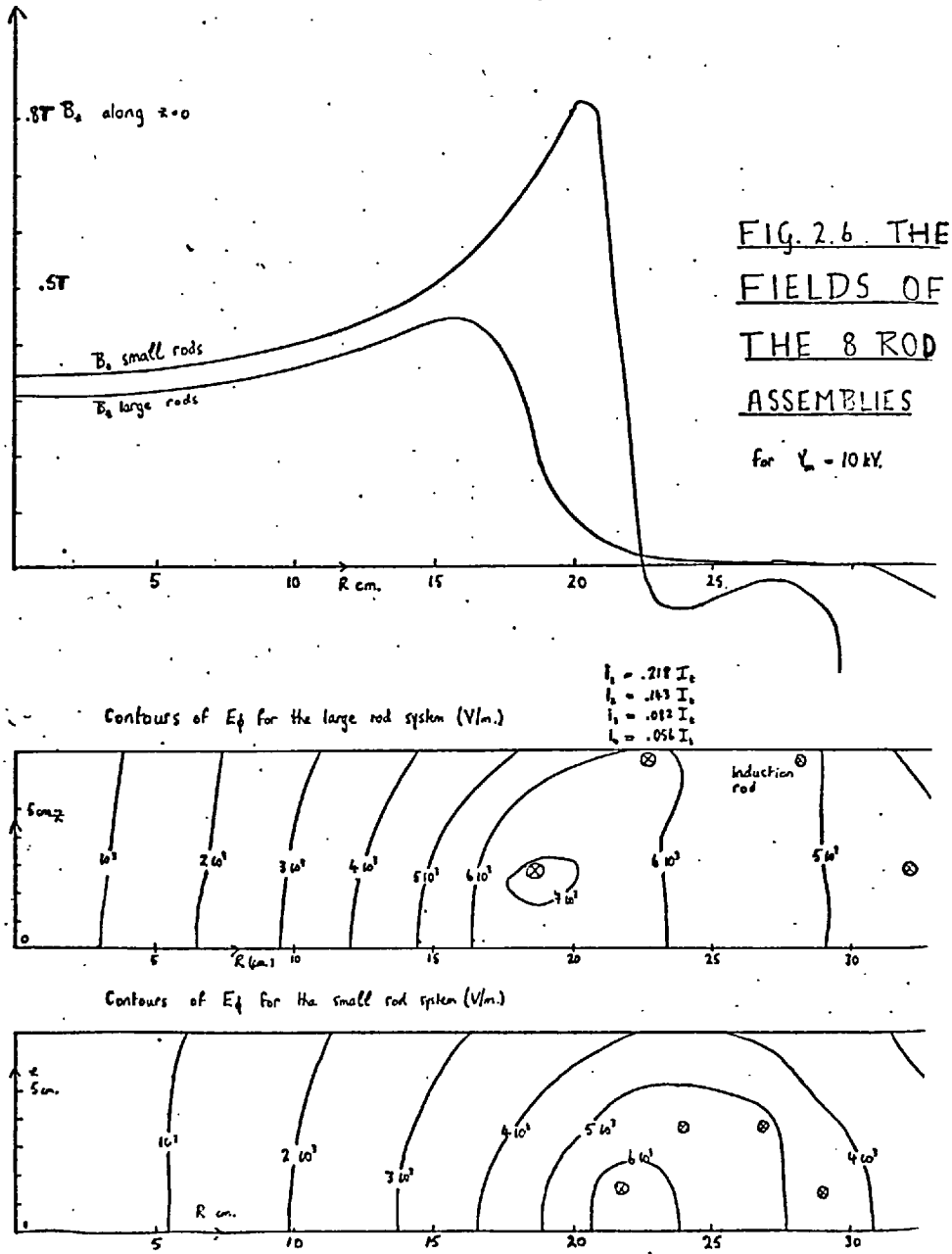

FIG. 2.6 THE FIELDS OF THE 8 ROD ASSEMBLIES

for V_m = 10 kV.

500 gauss cm^{-1}

100 gauss cm^{-1}

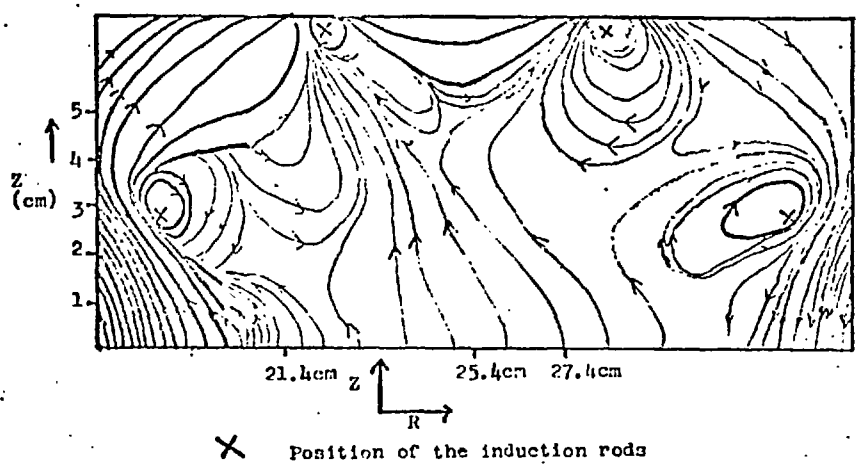

FIG. 2.7 THE FIELD LINES OF THE LARGE 8 ROD ASSEMBLY (SCHEMATIC)

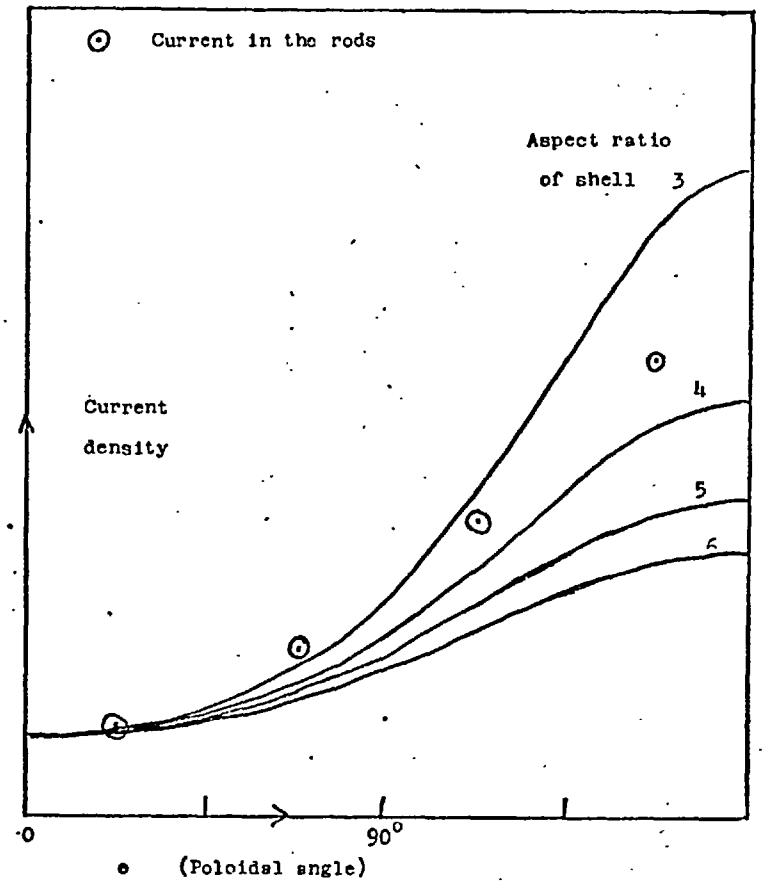

FIG.2.8 COMPARISON OF CURRENT IN THE INDUCTION RODS WITH THE SURFACE CURRENT ON A TOROIDAL CONDUCTING SHELL

A total of 30 different designs were tried and so the entire process was computerised. With an 8 rod system a very small field, a root mean square average of 20 gauss over the tube cross section was achieved. This was attained by moving the inner rods in, to radii 17 and 19 cm, and then moving the outermost rods further out, best cancellations being obtained when their radii were 44 cm.

However a 6 rod cage was designed. This is simpler to assemble and gives an unrestricted view radially inwards which is useful for the photographs in Ch.10. The inner rods were moved further inwards from the 8 rod assembly. As before the outer rods were then positioned for the minimum average field. This was 50 gauss. Contours of this field are shown in fig. 2.9 and the optimised position of the rods relative to the collector plate. Having the rods on a larger minor radius means that a larger hole can be made in the collector plate. This reduces the electrostatic and magnetic perturbation of the collector plate to the field of the cusp coils near to the plate. An assymmetry in the position of the induction rods is necessary to avoid the tufnol tables which support the cusp coils. The induction rods are supported by being clamped to the tables.

As in the case of 8 rods the electric field is smaller than $V_m/2\pi R$. This is because of lines of force closing around separate induction rods. At the minor axis

$$E_\phi = V_m \cdot .5 \quad V/m.$$

where V_m is the main bank charging voltage, and so there is a 20% loss of the main bank voltage. The field is inversely proportional to the R within the vacuum tube.

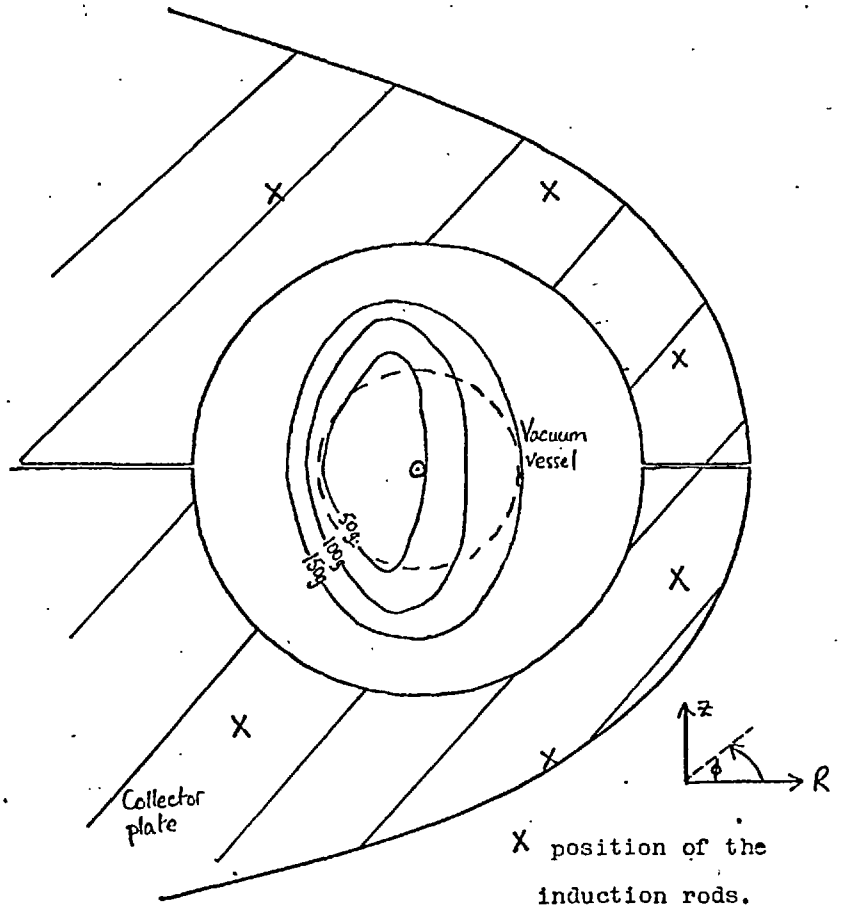

FIG. 2.9 OPTIMUM POSITION OF THE INDUCTION RODS ON THE COLLECTOR PLATE AND CONTOURS OF THE MAGNETIC FIELD.

scale 0 5cm

CHAPTER THREE

EXPERIMENTAL WORK ON PLASMA FORMATION: A CUSP COMPRESSION EXPERIMENT

The properties of the plasma formed by the preionisation system and the rising cusp magnetic field are described in this and the subsequent chapter. Here the use of a variety of diagnostics on the laboratory plasma is described. The spatial inhomogenity, lack of symmetry and access and low number density make the experiments difficult, most measurements being restricted to under the ring cusp. To enhance understanding of the plasma as a whole these measurements are compared with a m.h.d. simulation described in chapter 4.

This work is necessary to find the initial conditions of the polytron experiment. The variation of confinement and acceleration with the initial position makes these initial conditions important. Moreover it is an interesting experiment in its own right. It is similar to larger cusp compression experiments (Allen et al, 1962), without loss out of the spindle cusps, and with an order of magnitude lower size and temperature (about 4 eV).

Firstly in this chapter the formation and pinching of the plasma by the preioniser is measured. The parameters of the afterglow of this plasma are then measured by a variety of techniques. The evolution of the new plasma configuration caused by the rising cusp field is measured. Average and local electron number densities, $\bar{n}_e$ and n_e, electron and

atom temperatures T_e and T_a, are measured in the plane of the ring cusp. The axial variation of $\bar{n}_e$ is measured, the current which causes the plasma compression, and the regions of loss of plasma from the ring cusp during compression.

Parkinson made a few tentative measurements of the change in average density caused by the rising cusp. His conclusion, that the cusp field decreases diffusion is incorrect in the sense that the cusp field forms its own plasma configuration, and diffusion is a negligible process for change of the number density.

3.1. Breakdown of the gas by the preioniser

The low density limit at which breakdown of the filling gas occurs is of interest as:-

(1) the polytron mechanism will not work if $\omega\tau$ is too small.

(2) the current carried by the moving ions must not be large enough to cause self pinching of the discharge.

The brief investigation described in this section arose from a paper by Malesani (1970). In a toroidal quartz vessel with a toroidal induced electric field and a toroidal magnetic field the time delay between application of the electric field and breakdown of the gas, as measured by the toroidal current, was studied as a function of the

magnetic field . The toroidal field was limited to .4T and the electric field was quasi constant for only .5μs. The polytron apparatus is essentially similar. The currents in the cusp coils can be made to flow in the same direction producing a toroidal field of 3T, and the toroidal electric field is constant for about 2μs, the period being 24μs. Furthermore the stray electrostatic field at the collector plate is small. The separation of the two collector plates is 9mm, but the wall of the torus is 5 cm away from the edge of the collector plates. Thus the stray radial electrostatic field should be much less than the 10^5 V/m of Malesani's experiment.

The measured delay is shown in fig. 3.1. The error bars are representative of shot to shot variations in t_d.

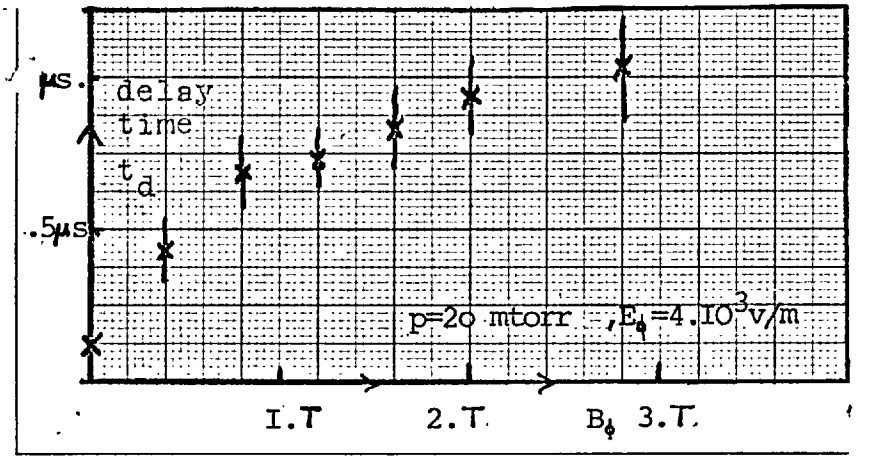

FIG.3.1 BREAKDOWN DELAY IN HYDROGEN

These results are similar to Malesani's results. The change of slope at 1 tesla indicates a change in the physical mechanism for the breakdown. The reported breakdown mechanism is by secondary emission from ion-wall collision, induced by

the stray radial electrostatic field. This is supposed to supply an initial number density of about $10^{13}m^{-3}$ in a time of 20 ns. Above this density collisional ionisation becomes effective, and this takes the rest of t_d before the electron number density is large enough to carry the toroidal current. It is difficult to explain how this ionisation could spread throughout the rest of the torus. Unimpeded electrons would take 70 ns to accelerate around the torus, but as the Debye length at $10^{13}m^{-3}$ is centimetres, the ions need to be accelerated. The secondary emission could be caused by centrifugal force along the whole length of the circumference. This causes a drift $\frac{2v_{11}^2}{R\omega_{ci}^2}$ (where ω_{ci} is the ion cyclotron frequency) of the ions radially from their initial position. This is of order 10^{-3}cm for ions freely accelerated for 100ns, and decreases as B_ϕ increases.

The change of slope shown in fig. 3.1 could indicate this ionisation by secondary emission becoming small, compared with a field independent ionisation mechanism such as photo-ionisation by light emitted from electron impact with the wall, or by secondary emission from ions following field lines which meet the wall because of field inhomogeneity.

3.2 The preioniser pinch

Compared with many linear pinches (Roberts, D.E., 1972)

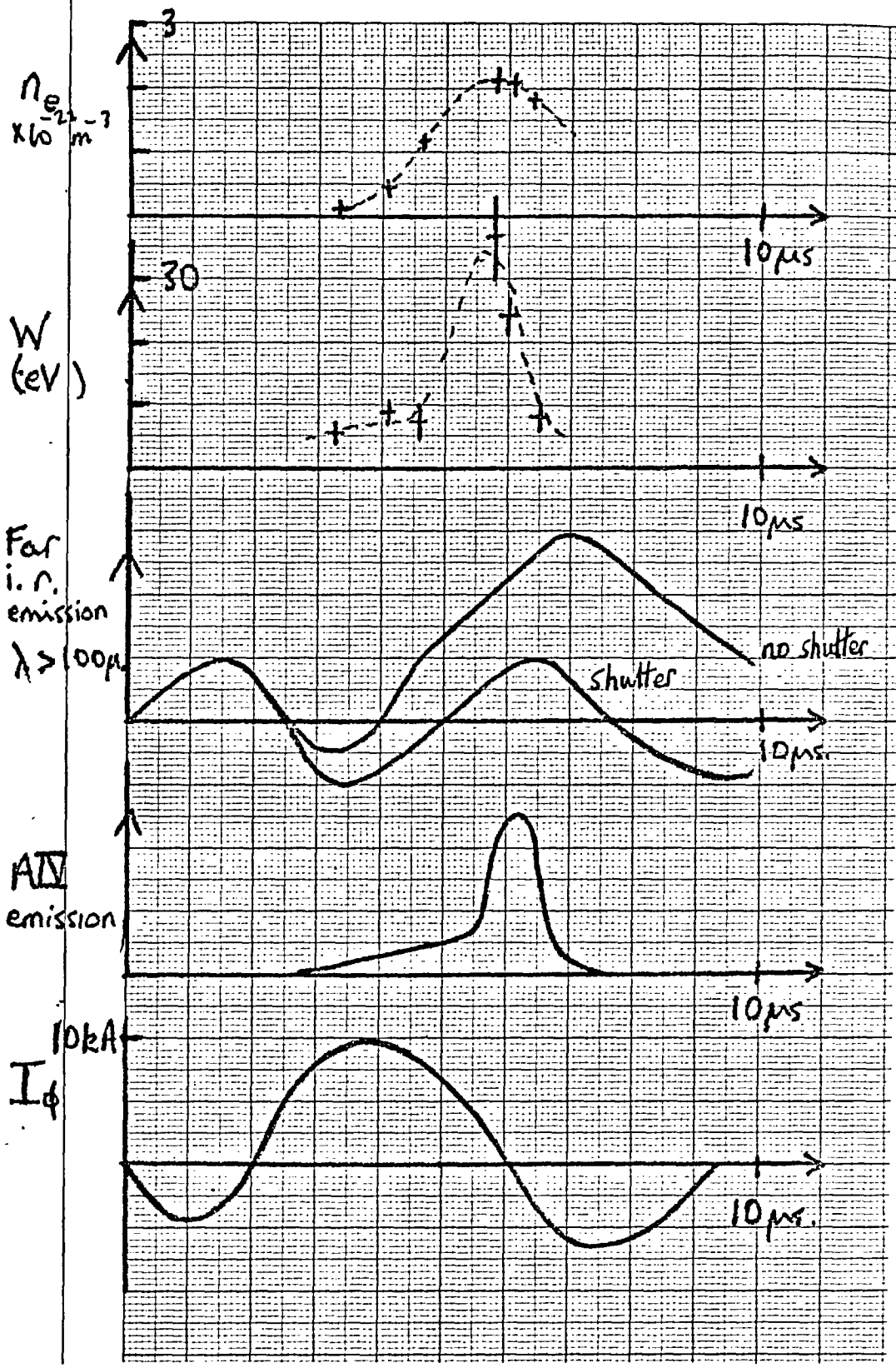

FIG. 3.2 CHARACTERISTICS OF THE PREIONISER PINCH

25mtorr argon, time measured from the start of the current.

the preioniser produces a high temperature plasma with reliable breakdown occuring at low filling pressures. It's characteristics are shown in fig. 3.2. The number density and temperature were measured by laser scattering, described in chapter 9. The values of n_e and W are consistent with $\alpha < .3$ (α is $1/k\lambda_d$, defined in chapter 9) as are the shapes of the scattered spectra. The values are averages over a length of 9mm transverse to the pinch, and so n_e and W could locally be higher. It is noticeable that the visible continuum emission peaks after the number density. The bremstrahlung emission/volume is proportional to $n_e^2/W^{\frac{1}{2}}$ and so if light is collected from a region larger than the pinch the light collected is proportional to $n_e/W^{\frac{1}{2}}$. The continuum emission peaks after the peak n_e because of the drop in temperature. Costely (1971) has also observed this phenomenon in a linear z pinch monitoring n_e with an axial Mach Zehnder interferometer.

The far infra red emission in fig. 3.2 was measured with a Putley detector. This observation was made whilst measuring the number density with a HCN laser and so the collecting optics were not maximised, and light was only collected over an f/12 aperture There was also a pick up problem. The detector was positioned directly beneath the torus. The pick up was due to B_z, a vertical field, penetrating the screening of 3mm brass. At this frequency the skin depth is 2mm.

If $n_e = 2\ 10^{22} m^{-3}$, the cut off wavelength is 70μm. The response of the Putley detector is low at this wavelength, rising monotonically up to a wavelength of 1mm. It is likely that the Putley signal is due to emission at a lower density than the pinch. As a direct result of this accidental observation a separate project to wavelength resolve the emission from the preioniser pinch using Fourier transform spectroscopy is being undertaken. Physically the interest is to see if enhanced emission such as seen by Griem (1970) is observed .

After the first pinch the preioniser probably repinches. No further observations have been made until later in the discharge, where the plasma parameters have been measured for the initial conditions of the cusp compression experiment. A major diagnostic is HCN interferometry so there will be a brief description of the interferometer.

3.3 The HCN laser interferometer

It is well known (e.g. Parkinson, 1968) that for $n < n_c$, the cut off number density, and ν_c the collision frequency $\ll \omega$ the frequency of the radiation, a plasma has a real refractive index

$$\mu_r = (1 - \frac{\omega_p^2}{\omega^2})^{\frac{1}{2}} = \left(1 - \frac{n_e}{n_c}\right)^{1/2} \qquad (3.1)$$

The attenuation of amplitude of an electromagnetic beam by electron ion collisions is given by an attenuation length d,

$$d = \frac{2c}{\nu_c} \frac{n_c}{n_e} (1 - \frac{ne}{n_c})^{\frac{1}{2}} \qquad (3.2)$$

M_1-M_7 MIRRORS; L_1-L_4 POLYTHENE LENSES; D_1-D_3 BEAM DIVIDERS; W_1-W_2 MELINEX WINDOWS.

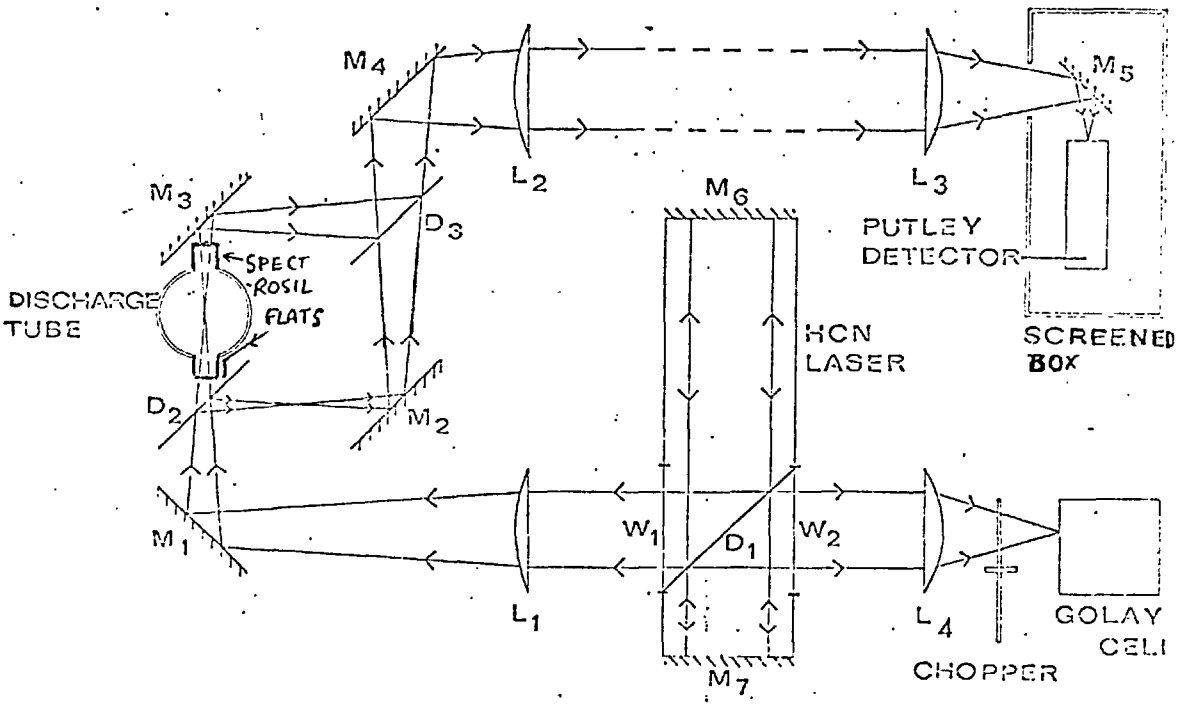

FIG.3.3 SCHEMATIC DRAWING OF THE HCN INTERFEROMETER

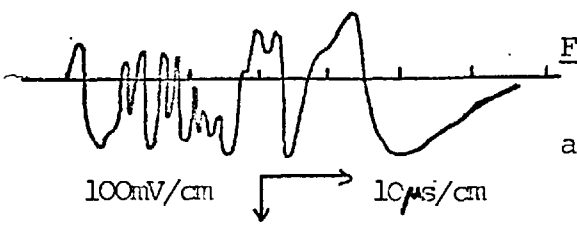

FIG.3.5 FRINGES FROM THE PUTLEY DETECTOR

a) 2 beam fringes: Mach Zehnder & Fabry Perot

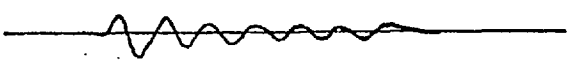

b) toroidal preioniser current

p=3.5mtorr, argon

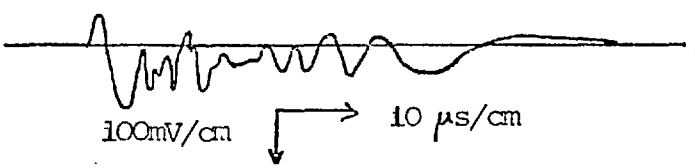

c) 1 beam fringes :Fabry Perot only

Ideally one should be able to measure the number density from the phase change

$$\phi = (1 - \mu)\frac{2\pi\ell}{\lambda} = \frac{\pi n_e \ell}{n_c \lambda} \qquad (3.3)$$

where ℓ is the length of plasma, and the temperature from the attenuation using eq. 3.2.

Parkinson (1968) used a Mach Zehnder interferometer shining through the wall of the torus. A similar interferometer was set up. To obtain less absorption the laser beam passed through ports with 2mm spectrosil flats as windows. Fortuitiously these flats acted as a reflection etalon reflecting 15% of 337 μm radiation . The interferometer used is shown in fig. 3.3.

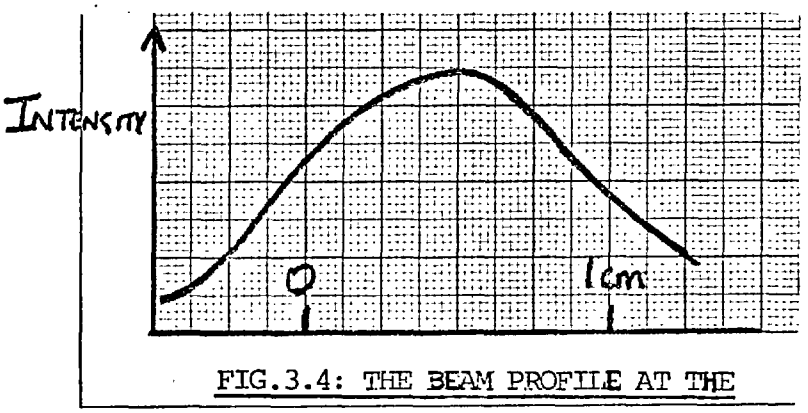

FIG.3.4: THE BEAM PROFILE AT THE 'FOCUS' OF A 60 CM. LENS

Lens L1 only 'focusses' the beam to a profile shown in fig. 3.4, marginally narrower than the beam profile without a lens. This is the diffraction limited spot. The limiting aperture in the system was the input to the light guide in the Putley detector.

The HCN laser was built at the National Physical

Laboratory. The cavity is 1m long with 5m mirrors; it is c.w., a mixture of ammonia and methane being optically pumped by an axial current of .5A , 1kV The cavity is tunable by a micrometer mount on one of the mirrors. The output is taken by a melinex beam splitter.

A Golay cell was used for setting up and a Putley detector for the experiment. The Putley detector needs to be worked at 1.7°K. The best bias current was 50μA for this particular detector, when the d.c. resistance was 5KΩ. The distance between the detector and the oscilloscope was about 5m and so a differential head amplifier, with a gain of 70 was used. The band width of the amplifier was restricted to 1MHz, matching the intrinsic frequency response of the detector and reducing the amplifier noise, which was then about 10mV on the output of the amplifier.

If A_1 is the wave amplitude of the interferometer reference beam and A_2 the wave amplitude of the measuring beam then the total output signal is

$$S = A_1^2 + A_2^2 + 2\,A_1\,A_2\,\cos(\phi-\phi_0).$$

ϕ_0 is the phase difference with no plasma. As ϕ the phase change caused by the plasma with respect to the phase with no plasma varies, the change in S must be less than

$$(S_{max} - S_{min}) = 4|A_1|\,|A_2|\,.$$

A_2, the beam passing through the torus was about .5 A_1 because of reflection and diffraction, but to retain maximum fringe size A_1 was not attenuated. This meant that the output could not be set to zero when $\phi = \phi_o$. The average number density corresponding to half a fringe, i.e. $\phi = \pi$ is $.5\ 10^{20} m^{-3}$.

Mach Zehnder fringes were obtained with the preioniser and are shown in fig. 3.5. It is evident that there are two sets of fringes, The higher frequency set were also seen when only A_2, the plasma leg, was going into the Putley detector as shown in fig. 3.5. These fringes are at twice the frequency of the Mach Zehnder fringes. That they are due to a Fabry Perot formed by the spectrosil flats was verified by moving the flats. There was a 30% modulation of the throughput, for movement of one flat with respect to the other. With this low finesse the fringes are nearly $\cos^2$. The average number density corresponding to half a fringe is $.25\ 10^{20} m^{-3}$. This added flexibility is very useful, halving the lower limit of measurable number density.

Plasma refraction. Beam attenuation is evident in fig. 3.5. However this is not due to collisional attenuation, but rather refraction by the plasma, so that not all of the beam is entering the detector. This can be easily shown now, as the temperature has been measured by laser scattering. The attenuation length is $d = \frac{5\ 10^{41}\ W^{3/2}}{n_e^2} m$.

After 40μs in fig. 3.5(a) the value of n_e is 7 $10^{20} m^{-3}$ and W is 2 eV from scattering. Therefore d = 3m. This is 50 times larger than would be apparent from the measured attenuation.

An exact criterion for the refraction loss would be difficult to derive in view of the beam profile in fig. 3.4, and so an approximate expression is obtained. The least effect that a cylindrical plasma column can have is to cause a beam divergence by acting as a lens of focal length f given by

$$\frac{1}{f} = \frac{2(\mu-1)}{r} = -\frac{n_e}{.035 n_c} \quad m^{-1}$$

The limiting aperture subtends a half angle of .05 at the plasma, and so assuming the beam to be a step function of width 1 cm, no loss requires

$$n < .14\ n_c \qquad (3.4)$$

But also negative dn_e/dr will cause refraction out of the plasma column; the radius of curvature R will be given by $\frac{1}{R} = \frac{1}{\mu}\frac{d\mu}{dr}$. If $n_e = n_o\left(1 - 1.5\left(\frac{r}{a}\right)^2\right)$ as given by Parkinson (1970) then for r = 6 mm

$$\frac{1}{R} = \frac{n_e}{16 n_c} \quad cm^{-1}.$$

Then $n_e < .1\ n_c$ (3.5) for no loss.

Effects (3.4) and (3.5) add and so $n_e < .05\ n_c$ for no refraction loss. This is an optimistic estimate. The beam is wider than assumed, and no account has been taken of the need to make the

beam interfere with a reference beam to see the fringes. A lens was tried, to see if the acceptance angle could be increased. It was unsuccessful because of the need to make the beams interfere. The limiting apertures in Parkinson's system were similar, and so the above criterion will apply. The higher criterion which he implies is wrong because he does not consider the spatial extent of the focussed laser beam.

That at least some of Parkinson's attenuation was due to refraction can be seen by the convergence of the envelope of his fringes. If $A_1 = A_2 = A, \phi_0 = 0, \phi = \pi/2$, then complete absorption will give a signal level of A^2. If however there is refraction causing loss of interference, but still collection of the beam the signal level will be $2A^2$. The envelopes of some of the low pressure cases, shown by Parkinson seem to converge to $2A^2$ showing that the attenuation is being caused by refraction, not out of the aperture of the Putley but away from the reference beam.

3.4 The expected temperature and density profiles in the preioniser afterglow

The electron density decay equation by three body recombination is

$$\frac{dn_e}{dt} + \frac{2\ 10^{-39}\ n_e^2}{W^{4.5}}\ n_i = 0 \qquad (3.6)$$

where the coefficient for 3 body collisional radiative recombination is from D'Angelo (1965). Early in the decaying

preioniser $n_e \sim 10^{20} m^{-3}$, $W \sim 1eV$ and so

$$\frac{1}{n_e}\frac{dn_e}{dt} = -40\ s.^{-1} \qquad (3.6a)$$

Thus the density decay is by diffusion. The diffusion equation is given by Chapman and Cowling (1939) as

$$\frac{\partial n_e}{\partial t} = D_a \nabla^2 n_e + \nabla n_e . \nabla D_a \qquad (3.7)$$

where D_a is the diffusion coefficient for ambipolar diffusion. It is approximated by

$$D_a = D_i (1 + W_e/W_i) \sim \frac{2\ kT_i}{m_i \nu_{ia}}$$

if W_e is close to W_i. ν_{ia} is the ion atom collision frequency. Hasted (1962) has shown that in the range $0 \rightarrow 5eV$ ν_{ia} is dominated by the charge exchange cross section σ_x, which is $50\ 10^{-20} m^2$, with little velocity dependence.

Therefore $\nu_{ia} = n_a \sigma_x \left(\frac{kT_i}{m_i}\right)^{\frac{1}{2}}$

where n_a is the atomic number density.

Therefore $D_a = 2\left(\frac{kT_i}{m_i}\right)^{\frac{1}{2}} \frac{1}{n_a \sigma_x}$

Assuming $\nabla . D_a = 0$, cylindrical symmetry and axial independence, the solution of eq. 3.7 is

$$n(r,t) = \sum_{k=0}^{\infty} A_k \exp(-t/\tau_k) J_o(\gamma_k\ r/a) \qquad (3.8)$$

where $\gamma_k = 2.405,\ 5.52,\ 8.56$ are the roots of $J_o(x) = 0$, a is the radius of the tube and

$$\tau_k = \frac{a^2}{D_a \gamma_k^2}$$

is the characteristic decay time of mode k. Thus the slowest decay time is

$$\tau_o = \frac{a^2 n_a \sigma_x}{2} \left(\frac{m_i}{kT_i}\right)^{\frac{1}{2}} \frac{1}{\gamma_o^2} \qquad (3.9)$$

T_i is measured to be about 1eV and $n_a = 10^{20} m^{-3}$ therefore $\tau_o = 3.6\mu s$, $\tau_1 = .8\mu s$ for argon. It is valid to neglect the second mode. Thus a profile with the shape of the zero order Bessel function is expected.

A similar diffusion equation will pertain for the electron temperature i.e.

$$C_v \frac{\partial T_e}{\partial t} = \eta \nabla^2 T_e \qquad (3.10)$$

where η is the thermal conductivity. Source terms which are omitted from equation (3.10) are equipartition, recombination, and a term due to $\frac{\partial n}{\partial t}$. The electron ion equipartition time is given by Spitzer (1956, p80) as $t_{eq} = 12\left(\frac{10^{20}}{n_e}\right) W^{3/2} \mu s$ for argon, which for $n_e = 10^{20} m^{-3}$, W = 1 eV, is $12\mu s$. Similarly the time for heating by recombination is larger than 1 ms, from eq. (3.6a).

The thermal diffusivity for equation (3.10) is

$$D = \frac{\eta}{C_v} = .4 \frac{10^{20} W^{5/2}}{(n_e + n_i)} \quad cm^2/\mu s.$$

Therefore $$\tau_o = \frac{a^2}{\gamma_o^2} \frac{(n_e + n_i)}{.4\ 10^{20} W^{5/2}} \qquad (3.11)$$

If $n_e = n_i = 10^{20} m^{-3}$, W = 1eV then $\tau_o = 10\mu s$.
However the decay time is liable to be longer than this.

Near the edges of the column W will be low producing low heat diffusion to the wall. In the centre of the tube W ~2 eV , and so rapid diffusion here will produce a flat top to the temperature profile.

A semi quantitative approach has shown that the number density profile is a Bessel profile, because of the low temperature dependence of the diffusion coefficient. In contrast a flat electron temperature profile is expected as $\eta \propto W^{5/2}$.

3.5. The afterglow temperature from its conductivity

A spatial average of the electron temperature was measured from the poloidal conductivity.

This is an unusual and accurate way of measuring an average temperature. A single turn coil of 5 cm radius was connected around the outside of the torus and pulsed by a .1 μF condenser giving a ringing period of 2μs. The phase and attenuation of the B_ϕ produced on axis with a plasma in the tube was measured. The phase was measured relative to the current and the attenuation measured by comparision with the signal with no plasma, giving an average conductivity. In this analysis toroidal effects are neglected; a cylindrical coordinate system based on the minor axis is used.

As long as $\omega_{ce}\tau_{ei} \ll 1$, $\underline{j} = \sigma \underline{E}$, and so the diffusion equation for the azimuthal magnetic vector potential A_θ is

$$\frac{\partial A_\theta}{\partial t} = \frac{1}{\mu_0 \sigma}\left(\frac{1}{r}\frac{\partial}{\partial r}\left(\frac{1}{r}\frac{\partial}{\partial r}(rA_\theta)\right) + \frac{\partial^2 A_\theta}{\partial z^2}\right) \qquad (3.12)$$

In the case of an infinitely long coil this can be solved analytically. For a single coil the problem needs a boundary condition at the wall which is the magnetic vector potential of a single turn coil,

$$A_\theta = \frac{\mu_0 I_0}{\pi} \frac{1}{k} \left(\frac{a}{r}\right)^{\frac{1}{2}} \left((1-\frac{k^2}{2}) K - E \right) \omega t \qquad (3.13)$$

where ω is the angular frequency of the B_ϕ field and $\omega t \ll 1$. Defining dimensionless variables.

$$t' = \frac{t}{t_c} = \frac{t}{a^2 \mu_0 \sigma} \qquad r' = \frac{r}{a} \quad : \quad z' = \frac{z}{a}$$

equation 3.13 becomes.

$$\frac{\partial A'_\theta}{\partial t'} = \frac{1}{r'} \frac{\partial}{\partial r'} \left(\frac{1}{r'} \frac{\partial}{\partial r'} (r' A_\theta) \right) + \frac{\partial^2 A_\theta}{\partial z'^2} \qquad (3.14)$$

This parabolic equation is solved as an initial value problem, using a two step Lax-Wendroff scheme, but with an unstaggered mesh(for an explanation of this nomenclature see chapter 4). $A_\theta = 0$, on axis, there is mirror symmetry underneath the coil, $A_\theta = 0$ at the far end of the domain, and A_θ is given by eq. 3.13 at the wall. By choosing a region 20 cells in radius and 80 in length the far end is sufficiently far away to simulate a real boundary condition of $A_\theta \rightarrow 0$ as $z' \rightarrow \infty$.

$$B_z = \frac{\partial A_\theta}{\partial r} + \frac{A_\theta}{r} \text{ and so } B_z(r=0) = \frac{2A_\theta(r=\delta a)}{\delta a}$$

where δa is the mesh size. The attenuation caused by the plasma in the simulation is, at $z = 0$

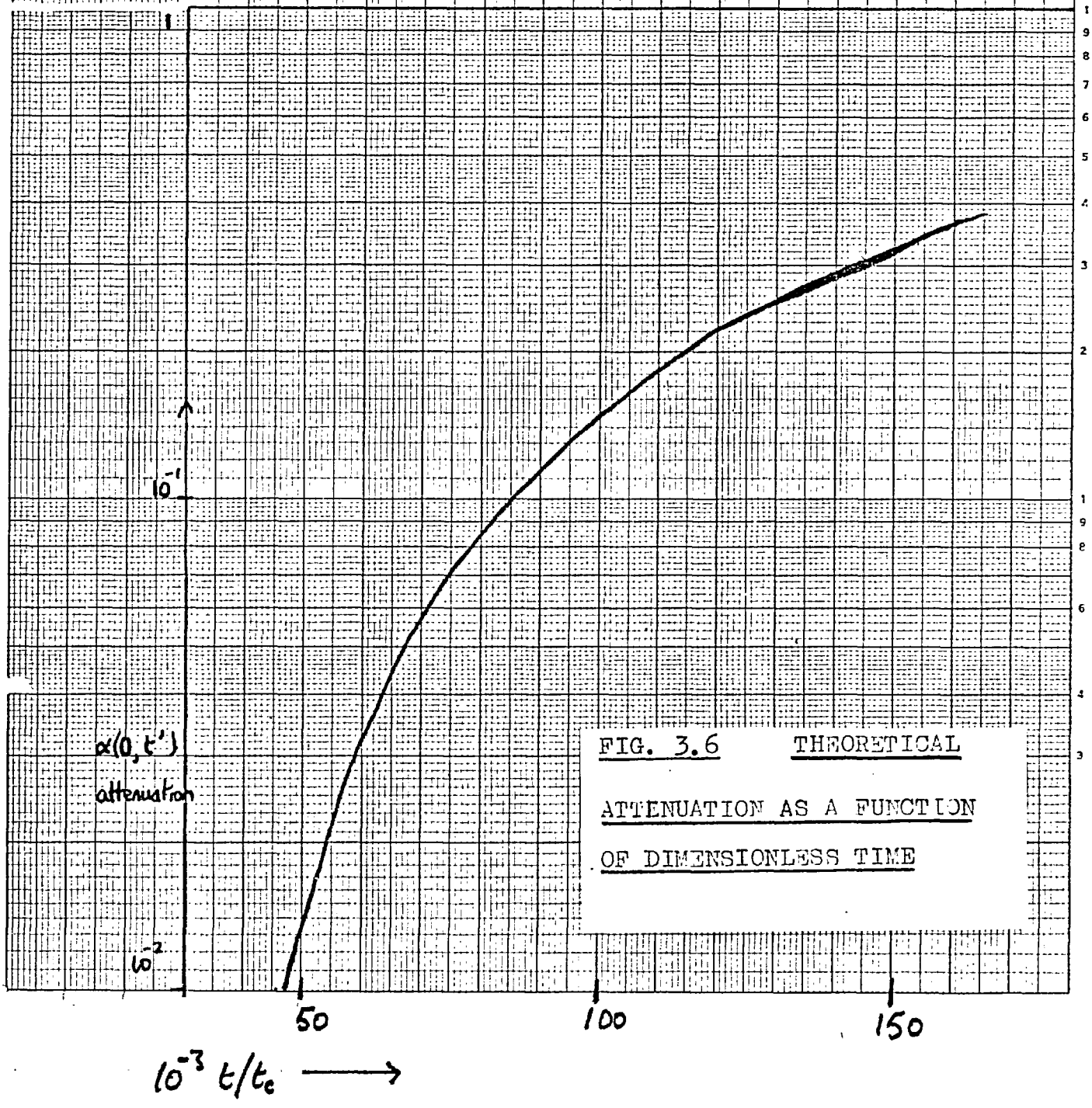

FIG. 3.6 THEORETICAL ATTENUATION AS A FUNCTION OF DIMENSIONLESS TIME

$$\alpha(r=0,t') = \frac{A_\theta(\delta a, t')}{A_\theta(a, t')} \quad \frac{A_\theta(a, \infty)}{A_\theta(\delta a, \infty)}$$

The computationally measured values are plotted in fig. 3.6. The attenuation from the probe at 200ns, for which $\omega t = .5$, is measured and the value of t' measured from fig. 3.6, ωt being .5 causes a 10% error. Taking $a = 3.5\ 10^{-2}$m, the bore of the torus, the value of $\ln\Lambda$ as 10, and using the value of σ given by Spitzer, the average temperatures are tabulated in fig. 3.7. This is a very accurate way of measuring δ as the attenuation is a very steep function of t'.

p mtorr.	α attenuation	$(t/t_c)10^{-3}$	W (eV)
80	.058	71	1.15 ± .1
40	.050	68	1.19 ± .1
20	.082	82	1.05 ± .1
5	.12	93	.96 ± .1

FIG. 3.7 POLOIDAL CONDUCTIVITY AT 40μs IN THE ARGON PREIONISER

The average values of W tabulated are unduly weighted to the larger radius as the diffusion takes longer the larger the radius. This is probably why the temperature appears to decrease with the pressure.

The temperature has also been measured from the toroidal resistance. In fig. 3.8 is shown the plasma and rod currents induced by the preioniser system. The currents

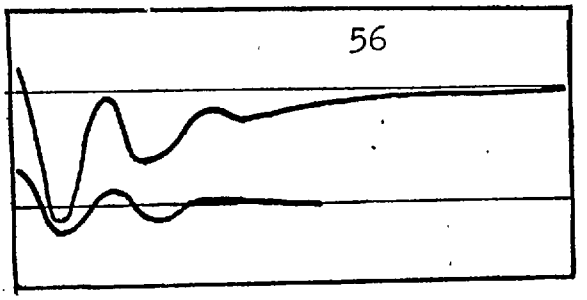

FIG. 3.8

UPPER PLASMA CURRENT

LOWER ROD RURRENT

5μs/cm

are in antiphase , but the rod current stops abruptly. The flux remaining in the torus drives the plasma current, there being a L/R decay time.

$$I = I_o \exp (-R_{pl} t/L)$$

where $R_{pl} = \frac{2R}{\sigma a 2}$, $L = \mu_o R(\ln(8R/a) - 1.75)$

assuming a uniform current distribution, R being the major radius.

Therefore $L/R_{pl} = 3.3\ W^{3/2} \mu s$.

The experimental results give at $t = 40\mu s$,

W = 1.8 eV for argon at 25 mtorr

W = 1.2 eV for argon at 3.5 mtorr.

Properly the resistance will depend on the current distribution and so this measurement will not be as accurate as the previous measurement.

Fig. 3.9 is a comparison of these average temperatures. The errors on the resistance temperatures are systematic. The errors on the scattering temperature are statistical and are large because the spectrometer was adjusted for a high temperature range. The Boltzmann temperature is explained in section 3.6.

p (mtorr)	W(eV) (Boltzmann)	W(eV) (θ res.)	W(eV) (φ res.)	W(eV) scattering
3.5			1.2±.2	1.9±.4
5.		.96±.2		
17.			1.8±.2	1.8±.3
25.	1.3±.2	1.05±.2		2.0±.4
40.		1.19±.2		

FIG. 3.9 TEMPERATURE AT 40μs IN THE ARGON PREIONISER

As expected the average values of temperature are only 30% ± 30% below the central values measured by the scattering. This indicates a reasonably flat top profile for the electron temperature.

3.6 The electron temperature by Boltzmann plot

Relative line intensity measurements, of lines whose upper states are in l.t.e. can be used to determine temperature. The line intensity from an optically thin plasma, whose upper state is an energy E above the ground state is:-

$$I \propto \frac{h\nu g_2}{B_z} A_{21} \exp(-E/kT_e) \qquad (3.15)$$

where B_z is the partition function

g_2 is the statistical weight of the upper line

A_{21} is the transition probability.

As the plasma temperature is low the often quoted reason for inaccuracy in this method, i.e. $E-E' \ll kT$ is inapplicable. (E' is the energy of another line used for comparison). The more fundamental reason is that l.t.e. does not exist. For hydrogen like ions Griem's (1964) criterion for l.t.e. to principal quantum number n is

$$n_e > 7.10^{24} \frac{Z}{n}^{8.5} \left(\frac{kT}{E_H Z^2}\right)^{\frac{1}{2}} m^{-3} \qquad (3.16)$$

Literal application to a 1eV argon plasma for n = 4 yields $n_e > 5\ 10^{19} m^{-3}$. For argon n in eq. 3.16 probably should be replaced by $n-n_g$ the difference between the level and the ground level, which yields $n_e > 3\ 10^{24} m^{-3}$; even so AII is not hydrogen like and the only test of l.t.e. is experimentally.

The grating spectrometer described in chapter 9 with an instrumental width of 3Å was used to obtain the Boltzmann plots shown in fig. 3.10. The error bars are due to intensity measurements being averages of several shots. The transition probabilities were taken from Olsen (1963). The relative positioning of AII 4609Å and AII 4589A in the plots is the same as Burgess obtained, suggesting a slight error in Olsen's transition probabilities here.

The plots enable an experimental criteria for l.t.e. of these AII lines to be derived, namely:-

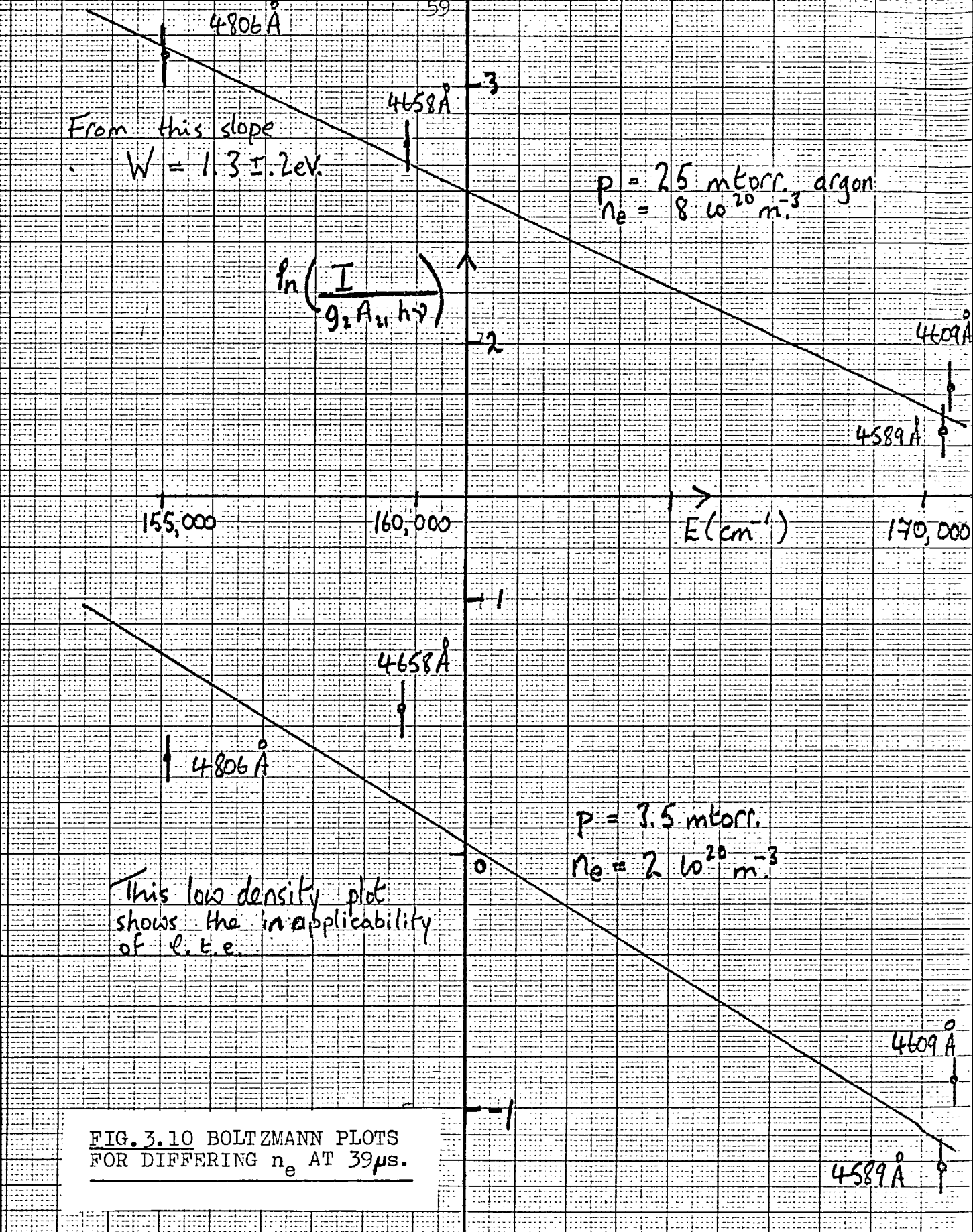

FIG. 3.10 BOLTZMANN PLOTS FOR DIFFERING n_e AT 39μs.

$$n_e > 4\ (W)^{\frac{1}{2}}\ 10^{20} m^{-3}\ (\pm\ 50\%) \qquad (3.17)$$

3.7 The afterglow number density using a double Langmuir probe

A double Langmuir probe was used to measure the number density profile in the decaying preioniser. The probe consisted of two aluminium wires set in a dual tube ceramic tube, with a 40V bias between them, held constant by a large ($36\mu F$) condenser. The current drawn by the probe was measured across a variable resistor of value 200Ω to $10k\Omega$. The probe was introduced into the torus through a sliding Wilson seal, it's position being adjusted by a micrometer table. A review of double probes has been given by Kagan and Perel (1963) from whom the saturation ion current is

$$i_p = b n_e e \left(\frac{2kT_e}{m_i}\right)^{\frac{1}{2}} S(V) \qquad (3.18)$$

where b is a geometric constant

S(V) is the sheath area (taken here as the tip area)

m_i is the ionic mass.

The profile of the current drawn by the probe is shown in fig.3.11. An absolute number density is evaluated using eq. 3.18 taking b = 1, W = 1eV, and so is somewhat arbitrary. It is noticeable that the number density is not zero at the tube wall; however the effect of the probe on the plasma is unknown. Zero number density is expected at the wall (sect.3.4) and the non zero value must be attributed to a systematic

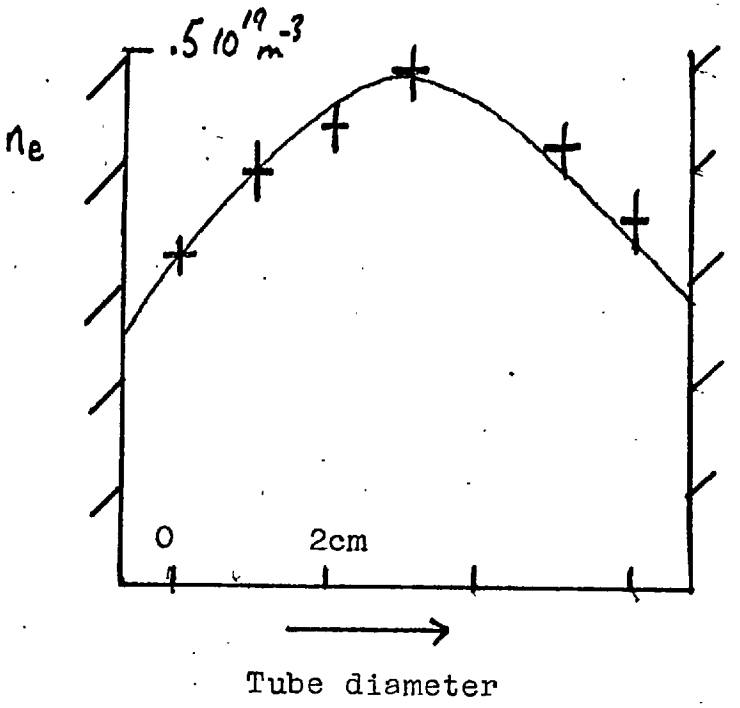

FIG. 3.11
LANGMUIR PROBE
NUMBER DENSITY
PROFILE AT 80μs
2 MTORR ARGON

experimental error.

3.8 Measurement of electron number density by Stark broadening of hydrogen lines.

Line broadening measurements were made for the dual purpose of obtaining an ion temperature and simply as a reliable number density diagnostic which can be used for the plasma under the coil. The dispersing instrument used was the grating spectrometer described in chapter 9; the wavelength scan was by a rotating glass block. The instrument line width was .2 to .3Å, limited by the collimating lens. The shape of the instrument line width was Voigt type.

Within this experimental constraint the only lines which are Stark broadened sufficiently at densities of

10^{20} to $10^{21} m^{-3}$ are hydrogen lines and in particular H_β. From Griem (1964) for H_β, the full half width $\Delta\lambda$(Å) is given by

$$n_e = 3.6\ 10^{20}\ \Delta\lambda^{3/2}\ \ m^{-3}$$

with only a small temperature variation.

An experimental line profile is shown in fig. 3.12. The error bars are the spread from 3 shots at a particular wavelength setting. The double peak shown in fig. 3.12 is similar to the split observed at higher number density (Wiese, 1962). This dip is probably for the same reason i.e. there is no unshifted energy level.

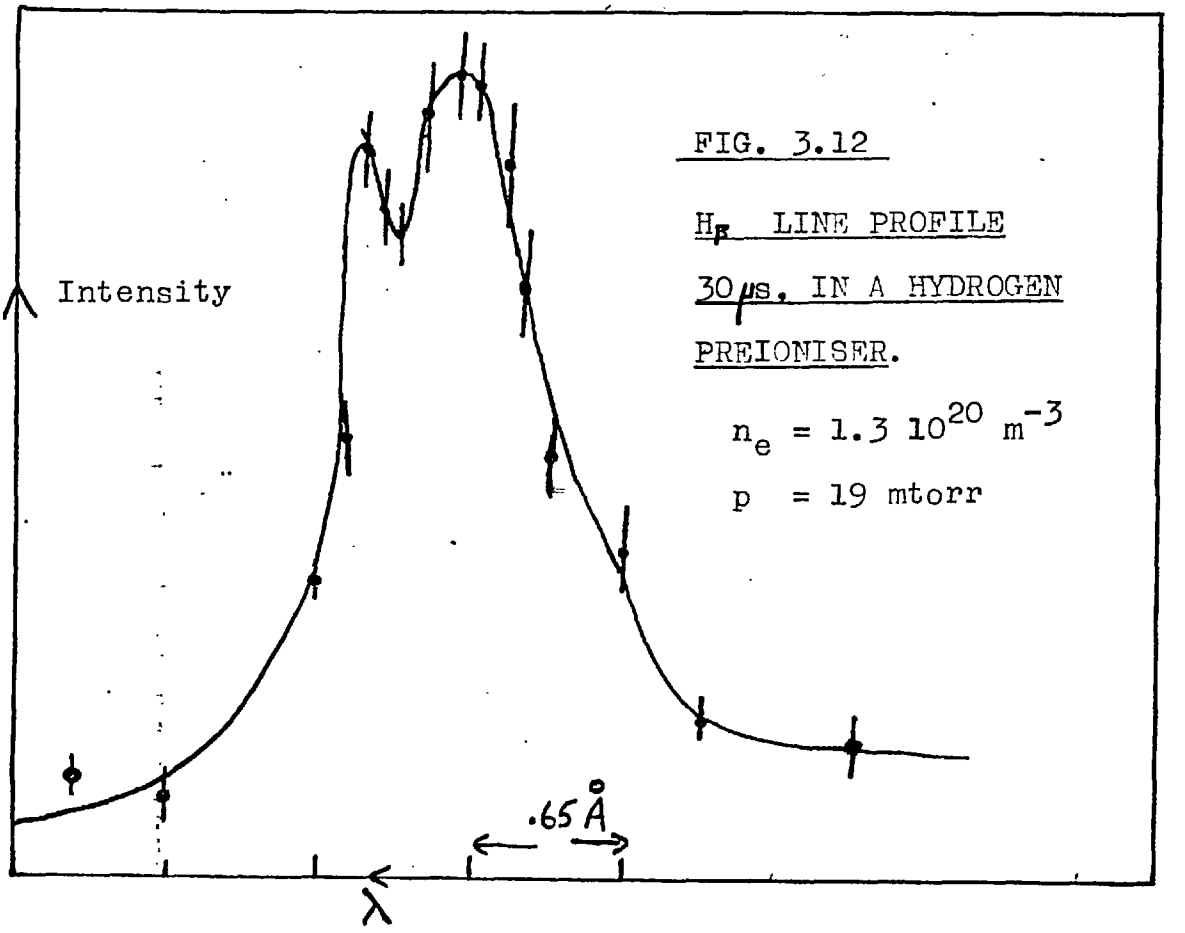

FIG. 3.12

H_β LINE PROFILE

30 μs. IN A HYDROGEN PREIONISER.

$n_e = 1.3\ 10^{20}\ m^{-3}$

p = 19 mtorr

An attempt was made to reduce the shot to shot variation by simultaneously monitoring the total line intensity. This gave a normalised signal

$$S_n(\lambda) = I(\lambda) \Big/ \left(\int_{line} I(\lambda)\, d\lambda \right)$$ which

was no more reproducible than $I(\lambda)$. The conclusion is that non reproducibility is due to number density fluctuations, (rather than fluctuations in the spatial profile) which alter the shape of the line.

The measured half width is unfolded simply from the instrument width by $\Delta\lambda_{m\beta} = \Delta\lambda_{i\beta} + \Delta\lambda_{p\beta}$

where $\Delta\lambda_{m\beta}$ is the measured full half width for H_β

$\Delta\lambda_i$ is the instrument full half width

$\Delta\lambda_{p\beta}$ is the plasma broadened full half width for H_β

the first order assumption being that the plasma broadening causes a Lorenztian profile, there being negligible Doppler broadening. The resultant number densities are higher than the values measured by the HC_N interferometer.

The Stark broadening of H_α is 20 times smaller than H_β and so the H_α will be mainly Doppler broadened. This Doppler broadening, scaled for the different wavelength, can be used to obtain a better value of the number density from H_β broadening.

For H_α $\Delta\lambda_{m\alpha} = \Delta\lambda_{i\alpha}$ (+) $\Delta\lambda_{s\alpha}$ (+) $\Delta\lambda_{d\alpha}$

where $\Delta\lambda_{s\alpha}$ is the Stark breadth

$\Delta\lambda_{d\alpha}$ is the Doppler breadth.

and (+) means convoluted .

As the Stark broadening is approximately Lorenztian,

$$\Delta\lambda_{s\alpha}(+)\Delta\lambda_{i\alpha} = \Delta\lambda_{s\alpha} + \Delta\lambda_{i\alpha}$$

The unfolding of $\Delta\lambda_{d\alpha}$ is then a simple matter of using the tables from Davies and Vaughan (1963). $\Delta\lambda_{s\alpha}$ is taken from Griem (1964) again, although the value of the constant has to be extrapolated for use at these low number densities. The value used satisfies

$$n_e = 10^{22}\Delta\lambda_{s\alpha}{}^{3/2}\ m^3.$$

Then the relation

$$\Delta\lambda_{d\beta} = .73\Delta\lambda_{d\alpha}$$

is used to revise $\Delta\lambda_{s\beta}$, using the Voigt profiles for evaluating

$$\Delta\lambda_{m\beta}(-)\Delta\lambda_{d\beta} = \Delta\lambda_{s\beta} + \Delta\lambda_{i\beta}$$

The process is outlined in fig. 3.13; there is good agreement between the value of n_e from Stark broadening and the HCN interferometer.

To apply this technique to argon plasmas the argon was doped with 10% hydrogen. The hydrogen lines could still be seen but there was an appreciable continuum, which had to be subtracted. The number densities and atom temperatures obtained are shown in fig. 3.14.

FIG. 3.13 · SCHEME FOR EVALUATING $\Delta\lambda_{s\beta}$

For the decaying preioniser, hydrogen p = 19 mtorr; instrument profile, $\Delta\lambda_{i\alpha} = .3$Å

Time (μs)	$\Delta\lambda_{m\beta}$ (Å)	$\therefore$ 1st order $n_e\ 10^{-20}m^{-3}$	$\therefore\Delta\lambda_{s\alpha}$ (Å)	$\Delta\lambda_{m\alpha}$ (Å)	$\Delta\lambda_{i\alpha}+\Delta\lambda_{s\alpha}$ (Å)	$\therefore\Delta\lambda_{d\alpha}$ (Å)	$\therefore W_d$ (eV)	$\Delta\lambda_{d\beta}$ (.73 $\Delta\lambda_{d\alpha}$) (Å)	$\therefore\Delta\lambda_{s\beta}+\Delta\lambda_{i\beta}$	$\therefore\Delta\lambda_{s\beta}$	$\therefore n_e$ $10^{-20}m^{-3}$	n_e $10^{-20}m^{-3}$ HCn.
20	1.46	4.7	.15	.92	.45	.64	1.1	.47	1.3	1.02	3.8±.1	
30	.98	2.1	.06	.76	.36	.54	1.	.39	.81	.52	1.3±.1	
40	.76	1.2	.04	.66	.34	.44	.9	.34	.60	.32	.6±.1	.66
50	.55	.55	.02	.56	.32	.34	.8	.25	.43	.15	.2±.1	.23

Pressure	Time μs	n_e m^{-3}	W_{atom}(eV)
25 mtorr argon	30	$4.8\ 10^{20}$	.9
+ 4mtorr H_2	40	$4.1\ 10^{20}$	.9
	45	$3.6\ 10^{20}$	.9
3.5 mtorr argon			
+ 2 mtorr H_2	45	$1.01\ 10^{20}$	.55

FIG. 3.14 NUMBER DENSITY IN ARGON PLASMAS FROM STARK BROADENING

Notice the low atom temperature at low pressure.

In fig. 3.13 a temperature is evaluated for the Doppler breadth. It is well known that this is a questionable operation because of the effect of mass motion. Hence a scan was made of the D_α line from an argon plasma doped with deuterium and compared with a hydrogen doped plasma.

FIG 3.15 DOPPLER HALF WIDTH FOR A DOPED ARGON PLASMA 25mtorr A.

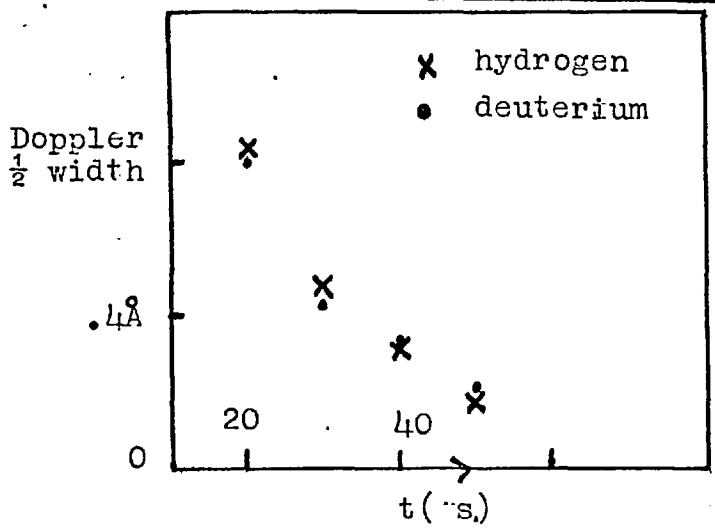

The lines widths due to Doppler broadening are shown in fig. 3.15. Accordingly deuterium is twice as hot as hydrogen. The inequality in temperature being this way around does show that the line width is not due to directed motion, as one would expect a higher velocity for hydrogen than deuterium. The equality of velocity of the two species suggests that the heating has come from the pinch, the impurity assuming the directed velocity of the imploding shell and then being randomised on axis.

The increase in the atom temperature with argon pressure can also be accounted for by this mechanism. The hydrogen atoms are accelerated by the frictional drag on the imploding shell. The mean free path is

$$\lambda = \frac{1}{n_e \sigma_x}$$

$$= 2.\text{cm} \quad \text{for } n_e = 10^{20} m^{-3}$$

$$\doteq 2.\text{mm} \quad \text{for } n_e = 10^{21} m^{-3}$$

In the first case the shell leaks and so there is a low atom temperature (this is at $\bar{p}$ = 3.5 mtorr) but at the higher pressure the ions are fully trapped.

3.9 The number density from the HCN laser and laser scattering

The electron densities in argon and hydrogen decaying plasmas are shown in fig. 3.16 and fig. 3.17. The scattering results are shown together with these results in fig. 3.18.

FIG. 3.16 ELECTRON NUMBER DENSITY FROM HCN LASER IN ARGON

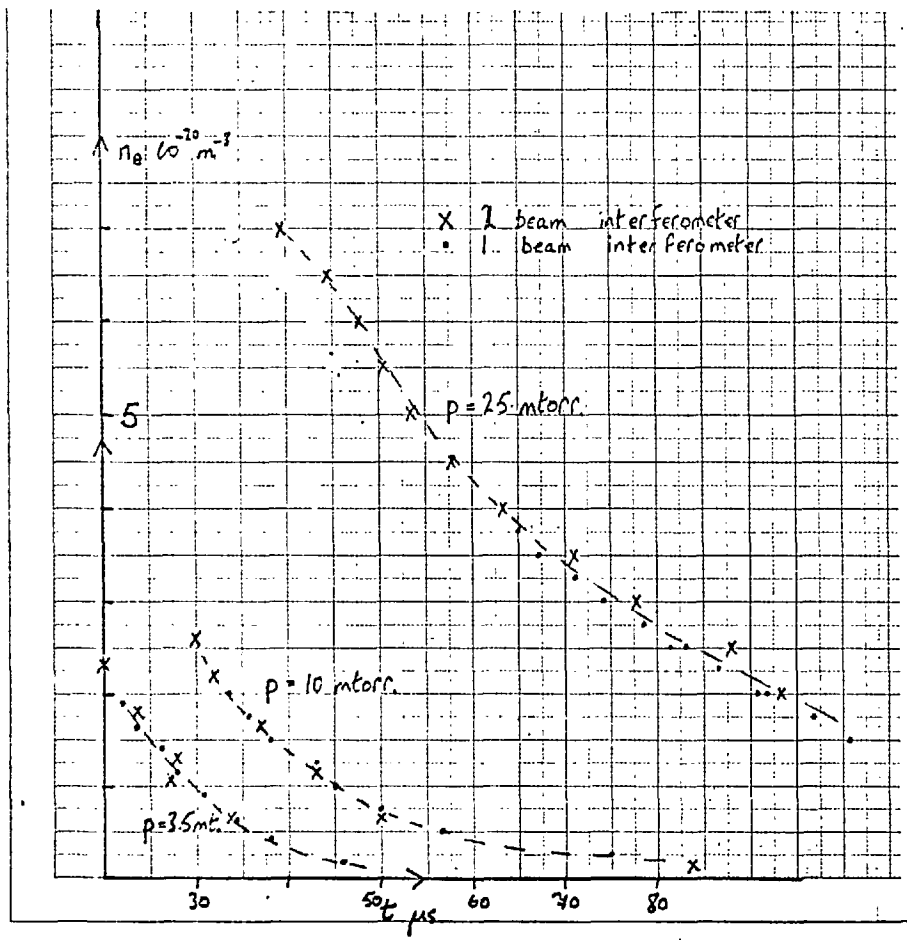

FIG. 3.17 ELECTRON NUMBER DENSITY FROM HCN LASER IN HYDROGEN

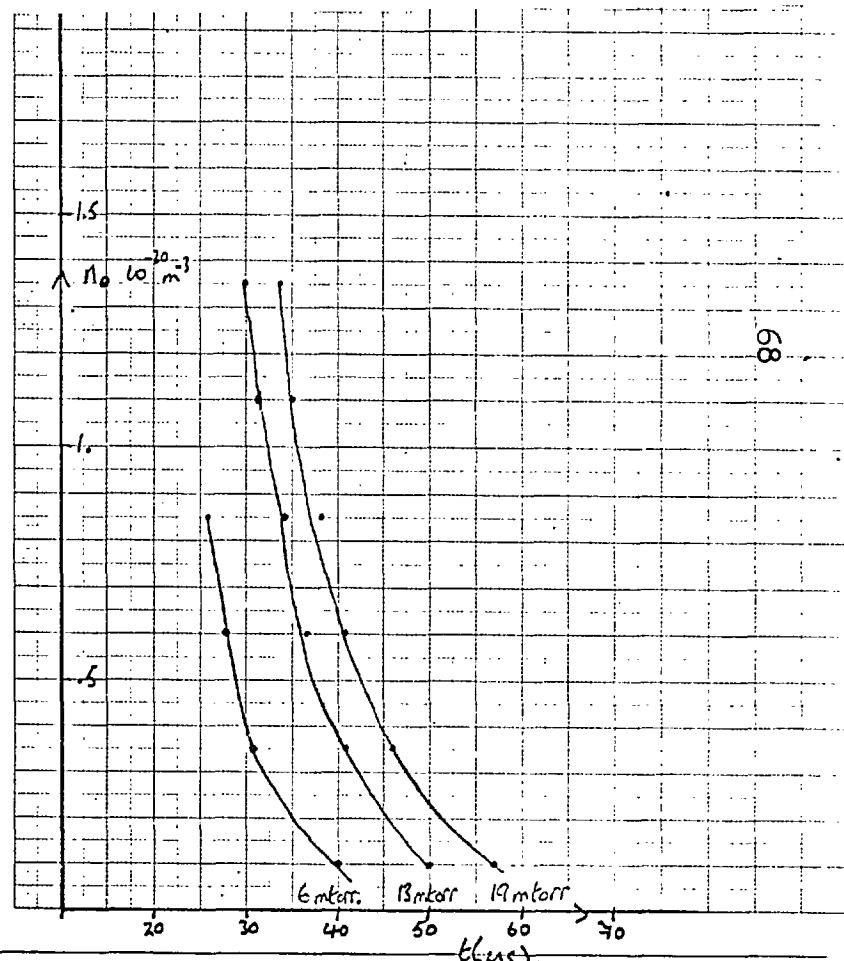

The scattering and interferometry diagnostics are unequivocal, except that there will be diffusion into the ports.
It is strange that the Stark broadening should give a value too low at 25 mtorr; the emission will be greater from regions of higher density and so a value equal to the higher density would be understandable. It is tentatively concluded that doping the plasma increased the diffusion. $D_a \propto \nu_i$, and so a

p mtorr	$\bar{n}_e$ 10^{-20} m.$^{-3}$ HCn	$\bar{n}_e$ 10^{-20} m.$^{-3}$ Stark broadening	$n_e 10^{-20}$ m.$^{-3}$ Scattering
3.5	.5 ±.1	1.	1.2 ± .2
10	1.3 ±.1		2.6 ± .4
25	7 + 1	4.1	

FIG. 3.18 ELECTRON DENSITIES BY DIFFERENT DIAGNOSTICS
t = 40μs., ARGON

small percentage of hydrogen could change D_a by virtue of the large velocity relative to argon at the same temperature.

The measured ratio $\frac{\bar{n}_e}{n_e(r=0)} = .42 \pm .1$

For $n_e = J_o(r/(2.4a))$, $\frac{\bar{n}_e}{n_e(r=0)} = .62$

so a profile as peaked as a Bessel function pertains.

The local decay time, as a function of time, $\tau_o(t)$ is measured from fig. 3.16 and fig. 3.17 and the quantity,

$$\frac{a^2 n_a \sigma_x}{(2.4)^2 \tau_o}\sqrt{\frac{m_i}{e}} = \sqrt{W_i}(1 + W_e/W_i) \qquad \text{(from eq. 3.7)}$$

evaluated below for filling pressures of 25 mtorr argon and 17 mtorr hydrogen.

time μs	40	45	50	60	80
$W_i^{\frac{1}{2}}(1 + W_e/W_i)eV^{\frac{1}{2}}$					
Argon	.2	.4	.87	.81	1.1
Hydrogen	.82				

The ion neutral momentum transfer cross section for hydrogen is 40 $10^{-20} m^2$ from Green (1966). Ambipolar diffusion can reasonably account for the diffusion time for all but $t = 40, 45\mu s$. However at this time the higher modes in equation 3.7 might still be appreciable.

The results of studies on the compression of the plasma by the rising cusp field are discussed in the rest of this chapter.

3.10 Heating by the cusp field

(a) The line to continuum ratio

An estimate of the temperature in a hydrogen plasma was obtained by the ratio of the line intensity of H_β and the neighbouring continuum. The theory has only been worked out for

hydrogen and helium, and so the method cannot be applied to an argon plasma.

As long as the upper state of H_β, n = 3, is in l.t.e. with the continuum, which requires $n_e \geq 2\ 10^{20} m^{-3}$, as well as sufficient time to populate the level from the continuum i.e. $t > 10^{-8}$s , then the line to continuum ratio is only a function of the electron temperature. Application to the hydrogen cusp compression with $n_e \sim 5\ 10^{20} m^{-3}$ is dubious because of the number density criterion. If the quantum level n = 3 is not in l.t.e. with the continuum it will be overpopulated (Bates and Kingston) relative to the l.t.e. values, increasing the line to continuum ratio, which will then give too low a value of electron temperature.

The apparent temperature of a hydrogen plasma is shown in fig. 3.19. The results in the ring cusp region are similar, being virtually constant at 4eV. The time is measured from the start of the cusp bank.

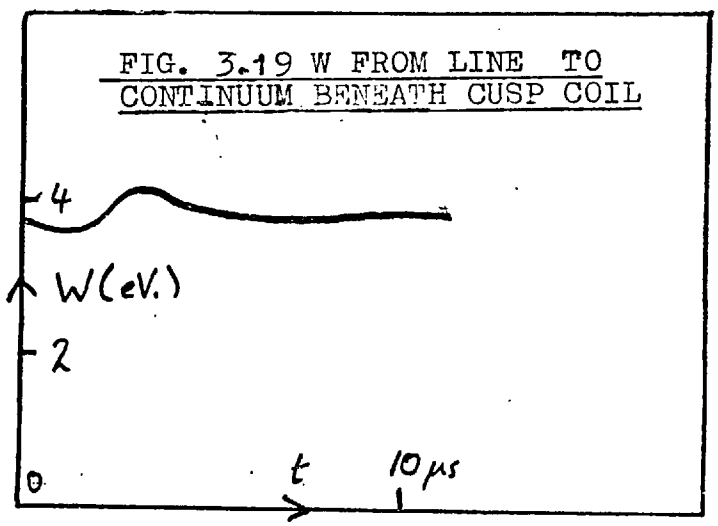

FIG. 3.19 W FROM LINE TO CONTINUUM BENEATH CUSP COIL

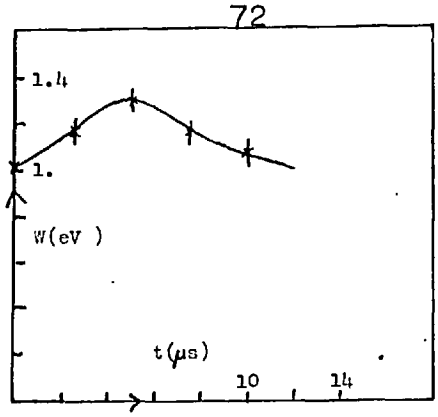

FIG. 3.20 ELECTRON TEMPERATURE BY A BOLTZMANNPLOT

25 mtorr argon, V_c 1.5kV, ring cusp

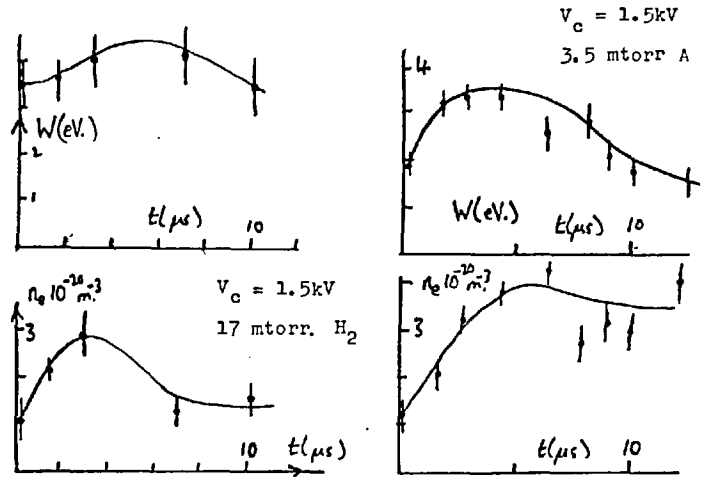

FIG. 3.21 LASER SCATTERING ON THE CUSP COMPRESSION

Values at the minor axis under the ring cusp

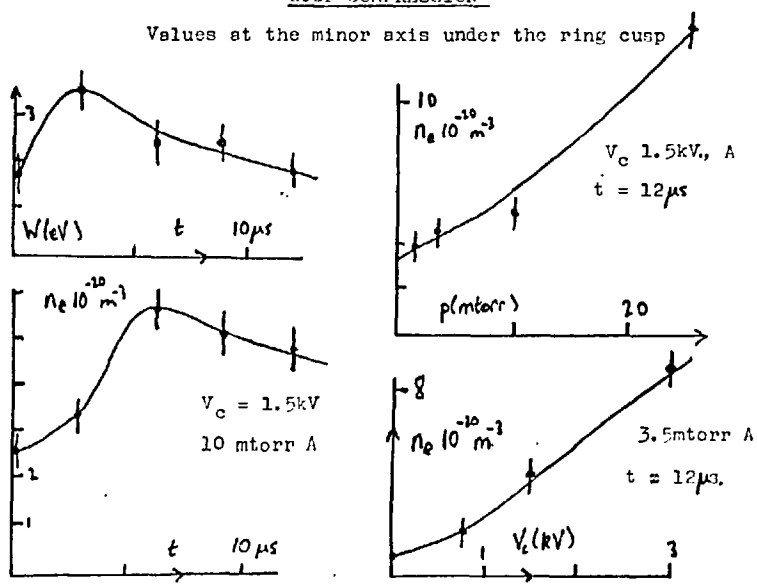

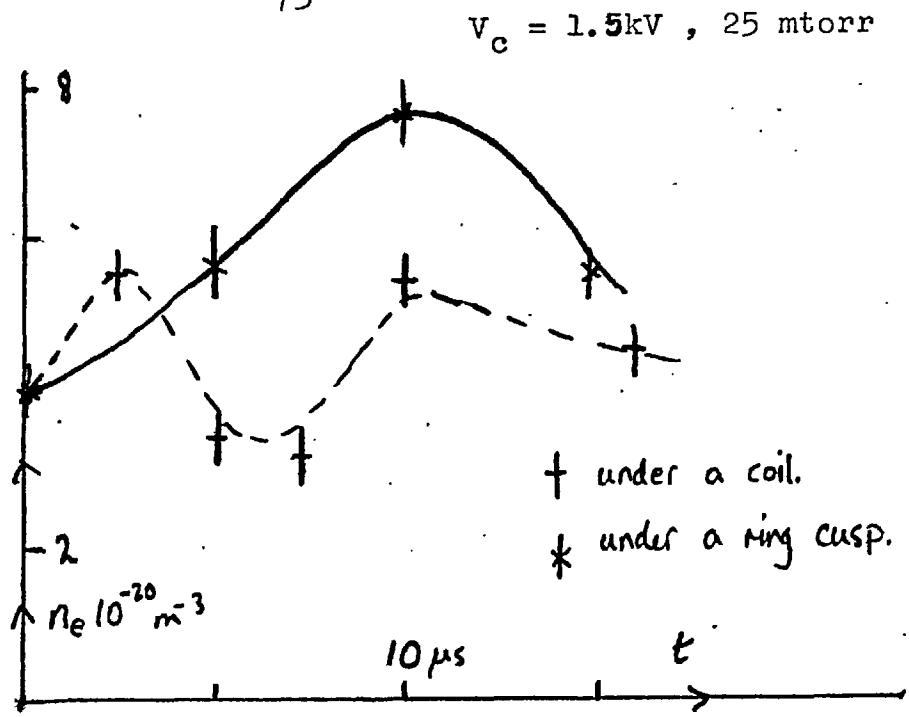

FIG. 3.22 NUMBER DENSITY FROM STARK BROADENING OF HYDROGEN DOPED ARGON PLASMAS

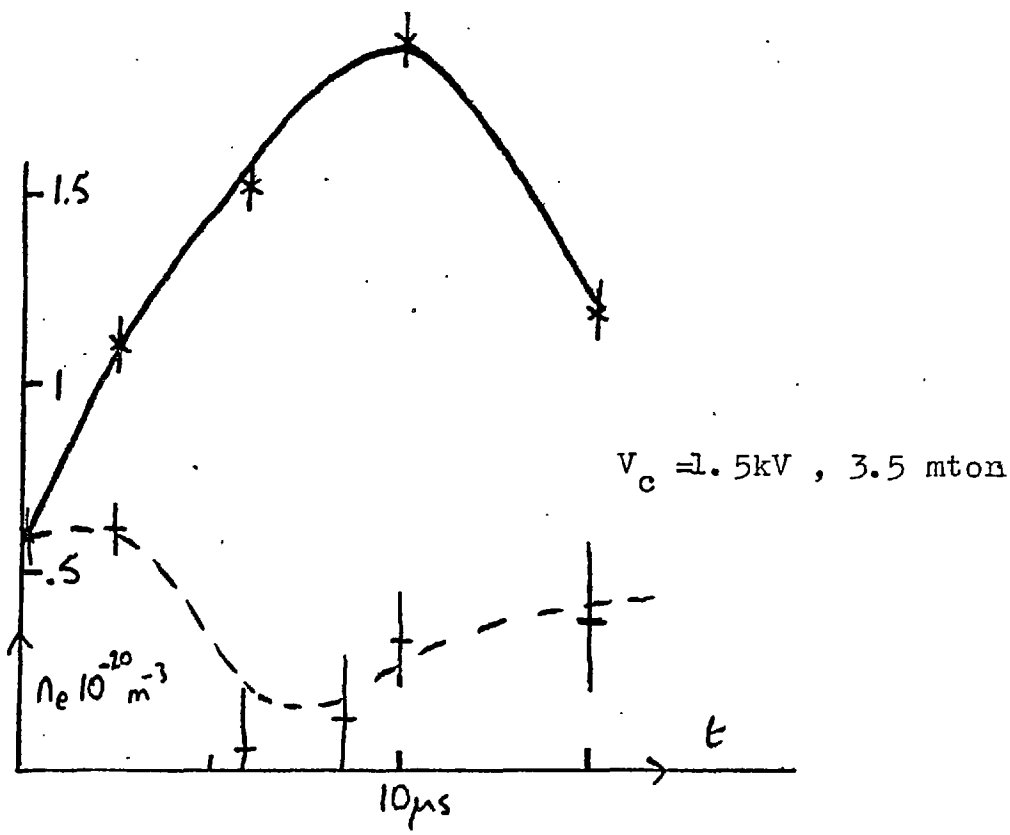

(b) Boltzmann plots

As before a Boltzmann plot was made for the higher pressure argon preioniser. The results are shown in fig. 3.20.

(c) Laser scattering

Some of the results for various parameters are shown in fig. 3.21. The results are for a volume of plasma 9mm x 1mm x 1mm at the centre of the ring cusp.

The variation of electron temperature against pressure and charging voltage, at 12 μs is not shown as it is constant.

By comparing the local scattering temperature and the line of sight Boltzmann plot at 25 mtorr the central temperature is less than double the average temperature. This is less evident in hydrogen, where there is a higher temperature, which agrees with the line to continuum measurements, a line of sight average.

3.11 The number density during the cusp compression

Stark broadening was used to measure the number density both under the ring cusp and under the coil. Results for a doped argon plasma are shown in fig. 3.22. The procedure for distinguishing Doppler and Stark broadening was as outlined previously . The atom temperature was constant at .9eV.

Consideration will now be given to the effect of spatial inhomogenity on the Stark broadening measurements.

The intensity of a line such as H_α is given by

$$I = A\, n(Z,p)$$

where $n(Z,p)$ is the number density of ions of charge Z, with principal quantum number p, and A is a constant of proportionality. One form of the Saha equation is

$$n(Z-1,p) = A' n_e n(Z,1) T_e^{-3/2} \exp((E_\infty - E_p)/kT) \qquad (3.19)$$

where E_p is the energy above the ground state of level p, and A' another constant. So for a pure hydrogen plasma, if n = 3 is in l.t.e., the intensity of H_β is

$$I_\beta \propto n(2,1)\ n_e \propto n_e^2.$$

As in the line to continuum measurement H_β is just in l.t.e. with the continuum for $n_e \sim 10^{20} m.^{-3}$ and so eq. 3.19 is valid. For a doped argon plasma

$$I_\beta \propto n_{\text{hydrogen}}\ (2,1)\ n_e$$

The dynamics of the hydrogen ions will be different from the argon ions, but there will be a collisional coupling, which will limit their relative drift velocity. An estimate shows this to be of the order of the radial velocity. In fact there is an additional coupling because of the magnetic field. As shown in the next chapter an approximation to the collapse velocity is given by

$$\underline{E} + \underline{v}_x \underline{B} = 0$$

Once this velocity is attained the hydrogen ions stay with the main body of the argon ions. Because of the ionising effect of the charge exchange process

$$A + H^+ \rightleftharpoons A^+ + H.$$

which occurs at a rate of 10^6 Hz, then

$$n(2,1) = f\, n_e$$

where f is the small fractional doping ratio and assuming the same percentage ionisation of hydrogen as argon. $E_\infty - E_3$ is less than 3.4 eV and so there is an appreciable temperature variation from the exponentional factor in eq. 3.19. The intensity of H_β will thus be an average, the n_e^2 factor weighting the intensity to the high number density, balancing the exponential weighting for the cool, low density region.

It was not practical to make Stark broadening measurements at many places and so the continuum level was used as a gauge of number density. The expression for the recombination and bremsstrahlung emission from a plasma is

$$P^{B+R}(\nu)d\nu = C\Big(C_1 \exp\left[E_\infty/W(q^*+1)^2\right] + C_2 Z^2 E_\infty/W \sum_{q_{min}}^{q^*} \exp(E_\infty/q^2W) + n_e n(z)(E_H/W)^{1/2} \exp(-h\nu/W)\Big)\, d\nu. \quad -(3.20)$$

q_{min} is the lowest quantum number which can contribute in recombination radiation, being 4 for $\lambda = 5000\text{Å}$ in hydrogen. In argon the value will be 7. q^* is given by the Inglis Teller limit being about 15 for $n_e \sim 10^{20} m^{-3}$. W is the electron temperature in eV , and C's are temperature independent constant For $W \sim 1$eV, $\lambda \sim 5000\text{Å}$ eq. 3.20 simplifies to

$$P^{B+R}(\nu)d\nu = C\, C_1\, 1.1\, n_e\, n(z)\left(\frac{13}{W}\right)^{\frac{1}{2}} \exp\,(-2.4/W)\, d\nu$$

That this is only a weak function of W as long as $W > 1.5$eV , is seen in fig. 3.23. Hence the continuum can be taken as

FIG. 3.23

$$y = \frac{\exp(2.4/W)}{W^{\frac{1}{2}}}$$

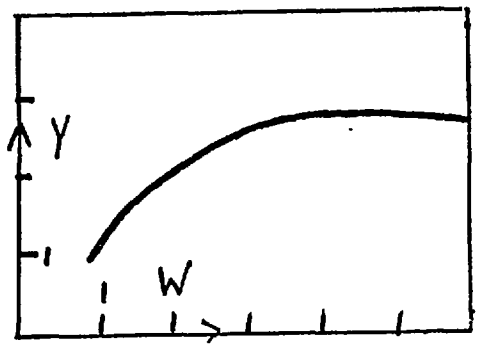

$\propto n_e^2$ in these experiments.

The continuum was measured at 5265Å, the nearest argon lines being at 5245 Å and 5286 Å. An instrumental width of 7Å was used. The slit height was 2mm. Absorption in the torus wall was allowed for in the toroidal direction by calibrating with the preioniser only.

Some spatial profiles obtained are shown in fig. 3.24. At 3.5 mtorr, 6μs the emission under the coil was half that under the ring cusp. The evacuation of the region under the coil is not as complete as suggested by the Stark broadening(3.22 The continuum measurement will give too high a value because of heating; the Stark broadening will give too low a value of number density because of species separation.

Although strictly, Abel inversion is necessary for the radial profiles, information can be obtained by inspection. The radial profile under the coil shows a shell of high number density imploding. The shell is about 1.5 times the central number density(at 3.5μs.) Under the ring cusp the shell gives way to a flat topped distribution. At 3.5 mtorr the shell

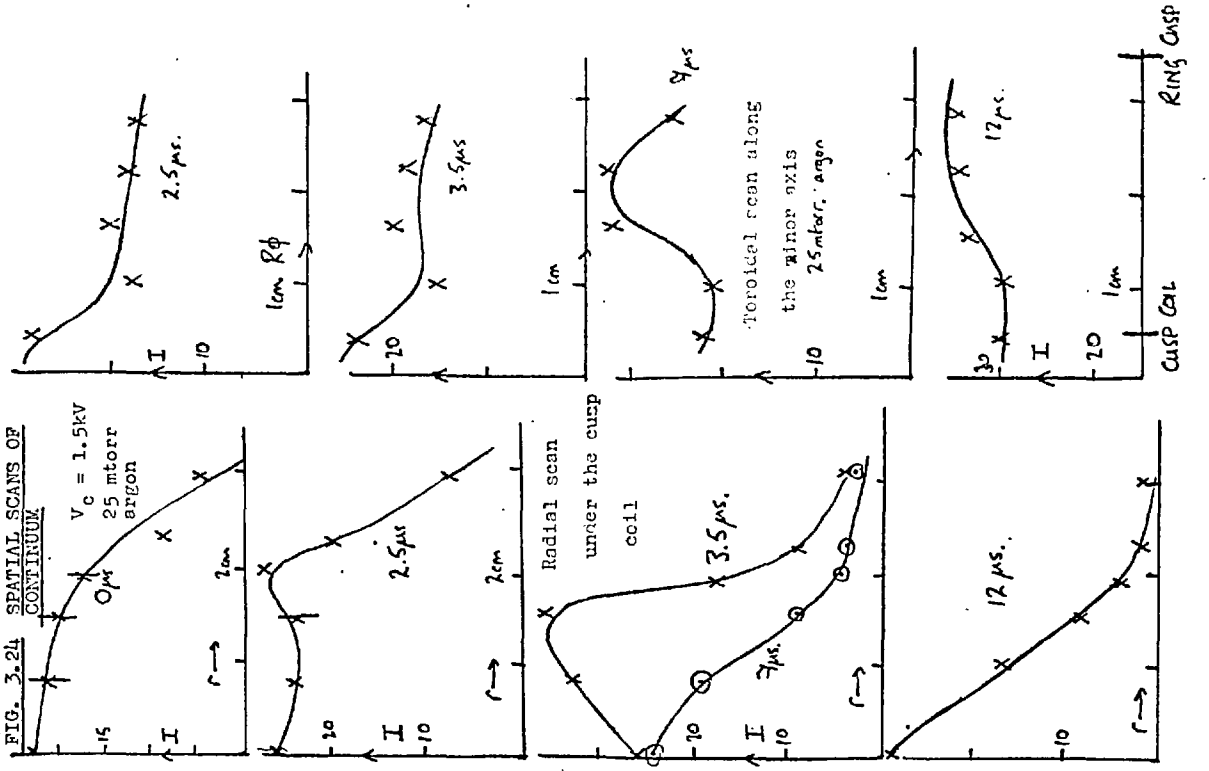

FIG. 3.24

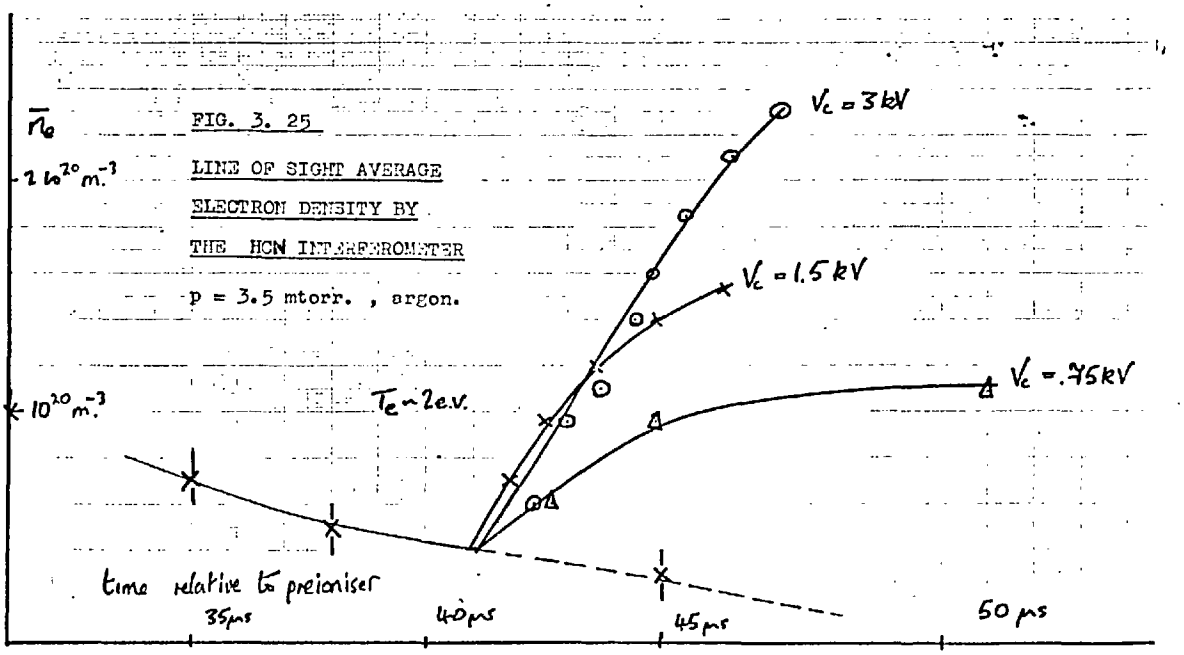

FIG. 3. 25

LINE OF SIGHT AVERAGE ELECTRON DENSITY BY THE HCN INTERFEROMETER

p = 3.5 mtorr. , argon.

underneath the coil is not as pronounced as at 25 mtorr.

The number density, measured by the HCN interferometer, giving a line of sight average of the electron number density in the plane of the ring cusp, is shown in fig. 3.25.

3.12 The number density profile from a Langmuir probe

The Langmuir probe described in sect. 3.7 was used. Simple probe theory says that when the bias voltage, $V_b = 0$, there should be no signal. However with no bias voltage there was a signal when the cusp fired. This signal changed polarity with the cusp current, and was not a common mode signal. The potential that the plasma assumes is defined with respect to the nearest conductor, the cusp coils. As all the condensers connected to the cusp coils are charged the same polarity the plasma potential will fluctuate by $\frac{1}{2} V_c$. The stray capacitance to earth from the probe wires to the cable outer must be charged to this voltage through the plasma which has a resistance

$$R_p \sim \frac{2r}{\delta \pi r^2} = \frac{2}{\delta \pi r} \sim 300\,\Omega$$

where r is the radius of the probe tip and the neighbouring plasma temperature is taken at $1000^{\circ}K$. $R_p C_s \sim 1\mu s$ and so can account for the signal observed. The difference between the signals with and without a bias voltage was taken proportional to $n_e W^{\frac{1}{2}}$.

The profile of this probe signal is shown in fig. 3.26. The profile could only be measured beneath the ring cusp

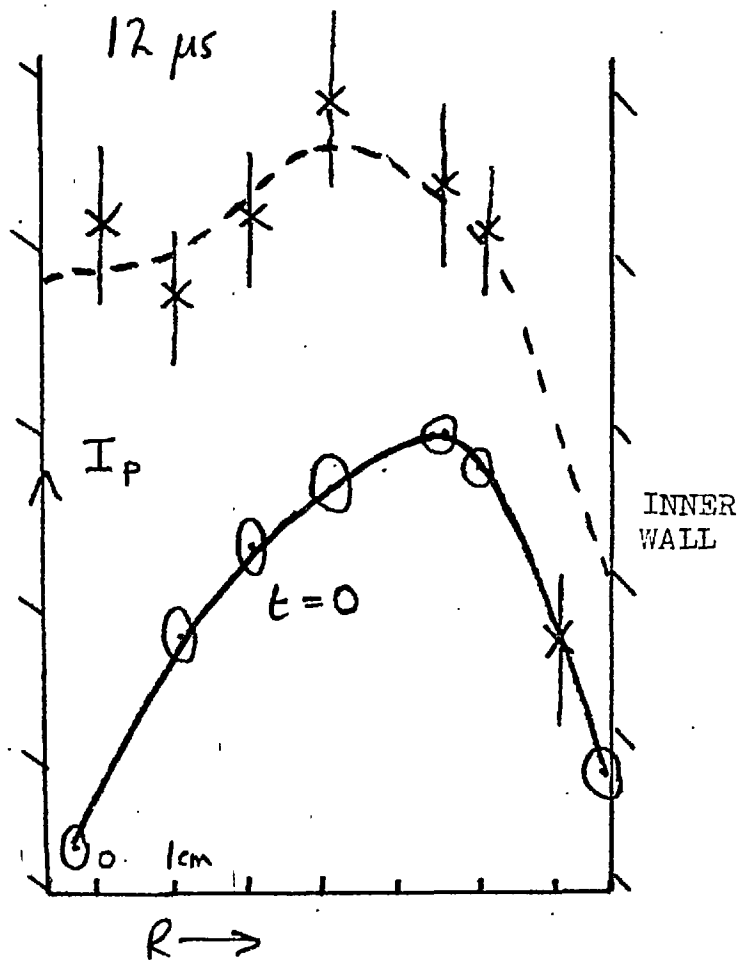

FIG. 3.26 RADIAL SCAN WITH A DOUBLE LANGMUIR PROBE

V_c=1.5kV , 3 mtorr under the ring cusp

and shows the characteristic flat top at peak magnetic field, rounding off when the field goes through zero.

3.13 The width of the ring cusp hole

An ion probe similar to the type developed by Ashby (1967) was used to measure the flux of the plasma to the wall in the region of the ring cusp. The probe essentially consisted of an outer plate with a .16mm radius hole in it, with a negatively biased collector inside. As long as the ion directed velocity v_i is larger than the thermal velocity.

$$I_p = An_i v_i q$$

where n_i = ion density

v_i = ion radial velocity

q = ionic charge

A = area of collecting hole normal to V_i

The probe was situated 10 mm from the wall and scanned in the toroidal direction, the excursions being limited to ± 10mm. The outer of the probe was inductively isolated from earth by a ferrite core, but there was still a large signal without a bias voltage, and so I_p was measured from the difference between the signal with and without V_b. The difference was only measurable 10μs after the cusp bank fired, as the signal without a bias voltage was largest when V_c was large. The ϕ scan of I_p is shown in fig. 3.27. The full half widths of the 'holes' are

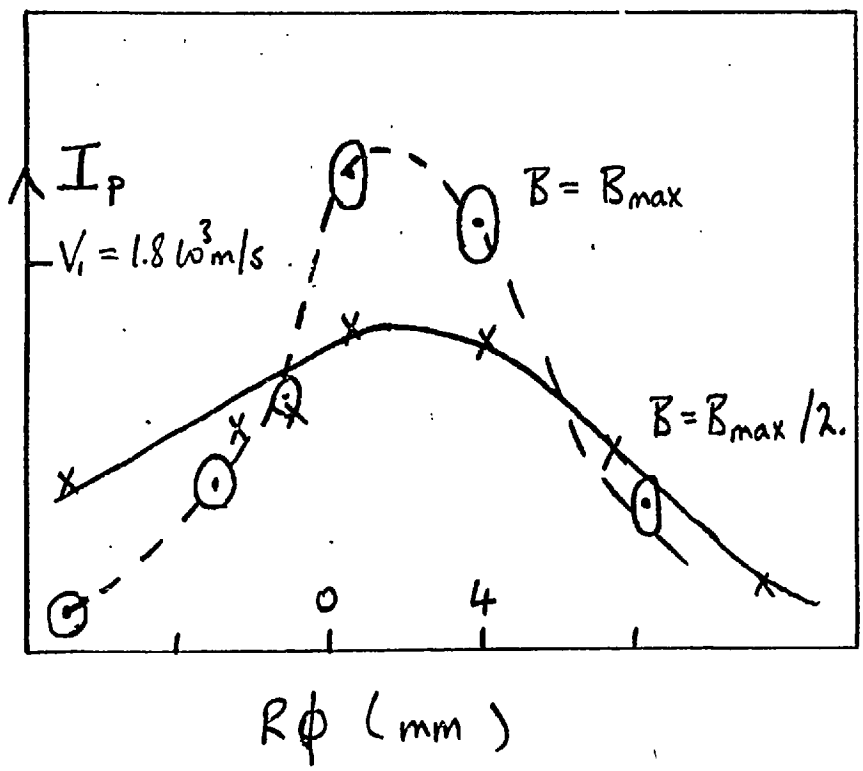

FIG. 3.27
TOROIDAL SCAN OF THE RADIAL FLUX THROUGH THE RING CUSP

V_c = 1.5kV ,
3.5 mtorr, argon

8mm and 13 mm when $B = B_{max}$ and $B = B_{max}/2$ respectively. When $B = B_{max}$, B_r, the radial magnetic field at this point is .33T. Hence the flux escapes through a ring of width 3 times the ion Larmor radius (taking leV as the temperature). A value of V_i is also evaluated. This is assuming a value for n_e of $4\ 10^{20} m^{-3}$. The value is shown on fig. 3.27.

3.14. The current which causes the compression

The magnetic field in the cusp was measured with the magnetic probes described in chapter 10. Initial measurement showed that the vacuum field was unaffected by the presence of the plasma, i.e. $<10\%$ pertubation.

An order of magnitude improvement was achieved by balancing the signal from inside the plasma, which did measure the field produced by the plasma b, against a magnetic probe of identical electrical characteristics picking up only the field produced by the cusp coil, B, outside and far away from the plasma. At the time the present more sophisticated electrical screening was not available for the oscilloscopes and so 2 large turns area coils had to be used. Hence the poor rise time of the probes of 400ns. Fig. 3.28 is the circuit used. The fine balance was obtained by varying the gain of the B input of the CA preamplifier. The best common mode rejection obtained was only 10:1. This was because the internal coil picks up the field from many cusp coils whereas the external coil only

FIG. 3.28 BALANCE CIRCUIT USED FOR MEASURING THE PLASMA FIELD

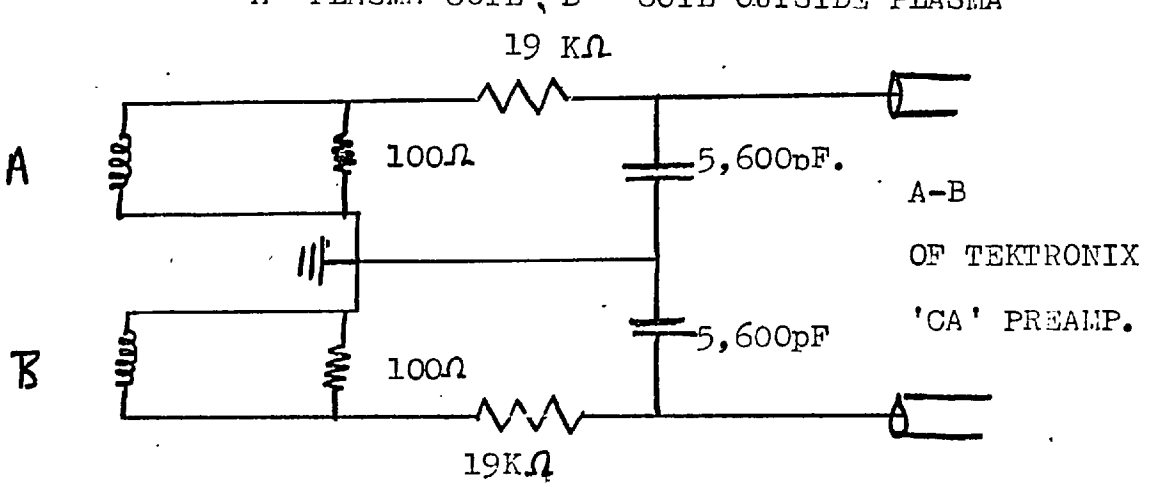

picks up the field from one cusp coil. Each cusp coil will have a slightly different period. The b_ϕ field produced by the plasma is then seen as the difference between the balance in the absence and presence of plasma. Three such traces are shown in fig. 3.29. These measurements were taken with the probe midway between the planes of the ring cusp and the coil.

Three pertinent features of these traces are:-

(1) a sharp rise and fall. The peak value of the plasma field b_x and the time taken for the field to return to zero, T_1 are shown in fig. 3.30 for a variety of plasma conditions

The rise time is a combination of the rise time of the coil and the time taken for the field to diffuse into the conducting plasma. A steady value is reached when

$$j_\theta = \sigma E_\theta$$

Then there is a fall in the field because the plasma starts to move in and

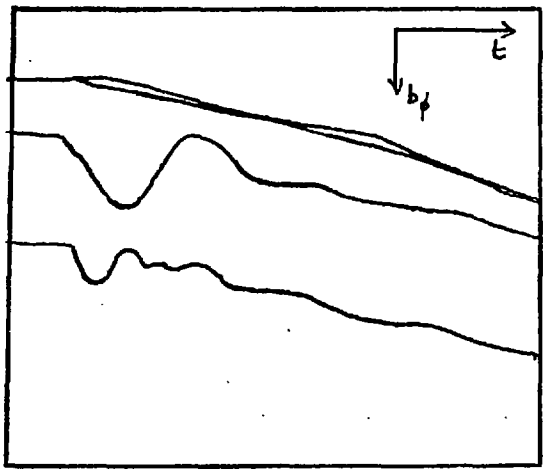

FIG. 3.29

FIELD PRODUCED BY THE PLASMA

2μs/cm, 167 gauss/cm

(a) balance, 2 shots with no plasma,

(b) 25 mtorr. argon, V_c 1.5 kV,

(c) 3.5 mtorr. argon, V_c 1.5 kV,

The vacuum field in the plasma is positive.

FIG. 3.30 VALUES OF b_ϕ FOR VARIOUS PLASMAS at r = 0, 1.2 cm from the coil

V_c (kV.)	1.5	1.5	1.5	1.5	3	1.5	1.5
p mtorr	2(A)	3.5(A)	10(A)	25(A)	25(A)	100(A)	20(H_2)
b_x (gauss)	82	116	150	200	370	250	82
T_1 (μs)	1.5	1.9	2.2	3.3	2.7	6.	1.6

$$E_\theta - v_r B_z = 0$$

(2) After the fall there are weak oscillations, similar to those in a theta pinch, being of a frequency $\sqrt{\frac{B^2}{\mu_0 \rho}}$ where ρ is the mass density of the plasma.

(3) When the cusp field next passes through 0 there is another slower rise of b_ϕ.

Now curl $\underline{b} = \mu_0 \underline{j}$

and so $$j_\theta = \frac{1}{\mu_0}\left(\frac{db_r}{Rd\phi} - \frac{db_\phi}{dr}\right)$$

assuming cylindrical geometry and $z = R\phi$. If the magnetic vector potential is A_θ and

$$A_\theta(r,z) = A_\theta(r) \cos kz$$

then $A_\theta(r)$ can be evaluated from $b_\phi(r)$ as

$$b_\phi = \frac{1}{r}\frac{d}{dr}(r A_\theta)$$

$\frac{db_r}{Rd\phi}$ can also be evaluated from this value of $A_\theta(r,z)$. $j_\theta = \frac{1}{\mu_0}\left(\frac{db_r}{Rd\phi} - \frac{db_\phi}{dr}\right)$ is evaluated in fig. 3.31. As can be seen j_θ is linearly proportional to r. For $r > 3$cm. the current starts to fall, as here the velocity is largest. No shell in the current forms. This is in contrast to the number density as shown by the continuum scans. Hence the shell of number density is due to a large mass flow from near the wall.

3.15 Photography

Image converter photographs were taken of the cusp compression with a filling pressure of 25 mtorr. These are shown

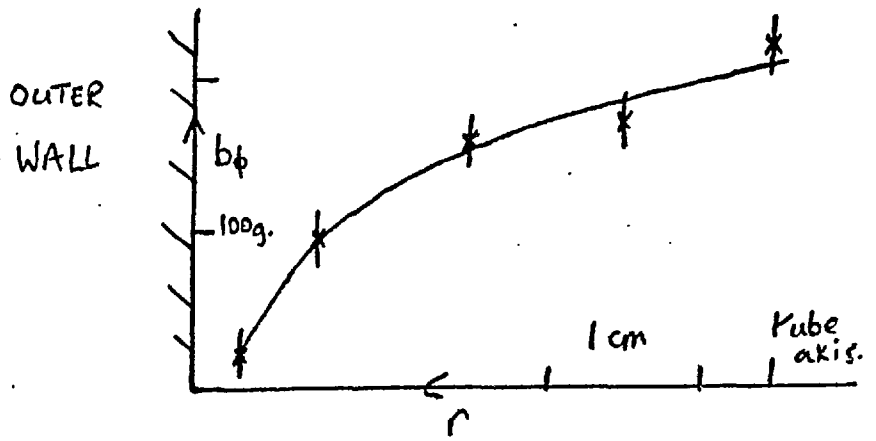

FIG. 3.31

THE SPATIAL VARIATION OF THE FIELD PRODUCED BY THE PLASMA

25 mtorr. argon

V_c = 1.5kV 3.3μs.

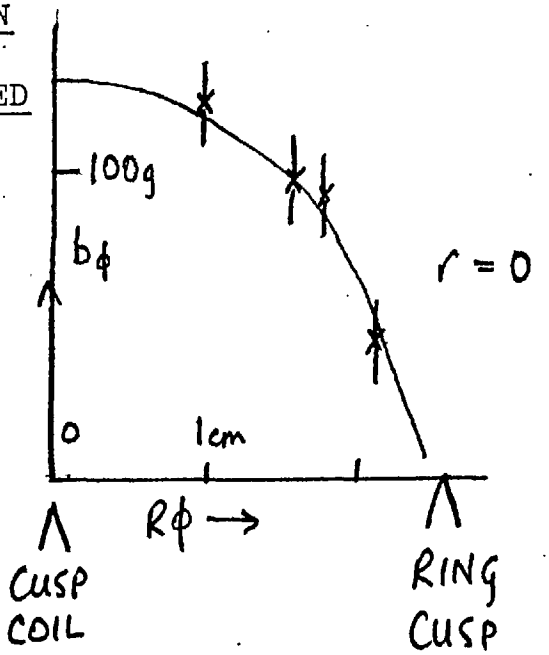

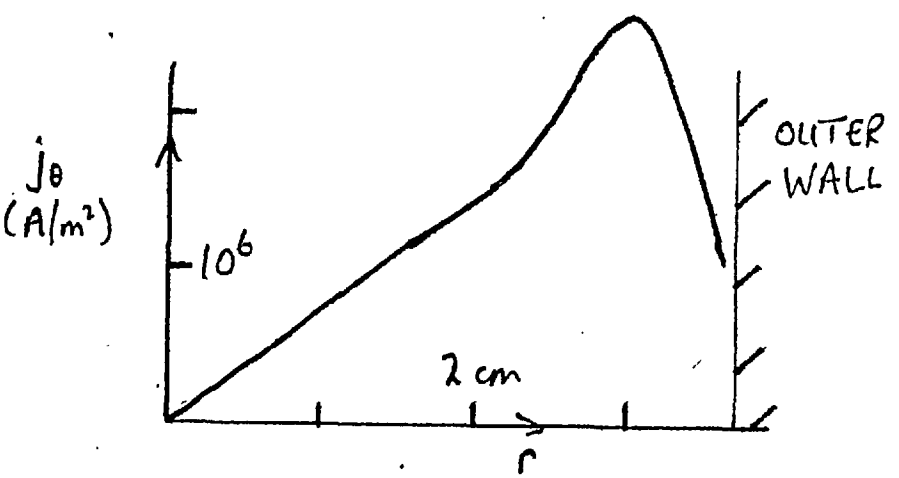

1 f/9

4 f/5

2 f/5

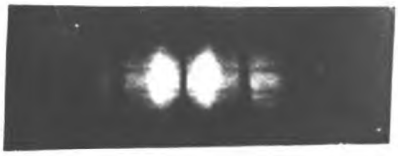

5 f/5

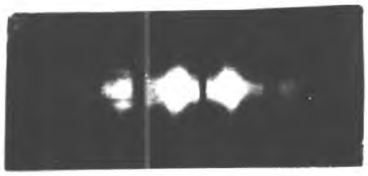

3 f/5

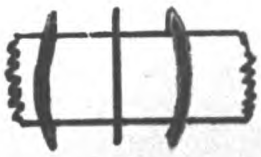

LINE DRAWING OF TUBE AND COILS

INTERACTION OF THE RISING CUSP FIELD WITH THE PREIONISER PLASMA
Filling pressure is 30 mtorr, cusp bank charging voltage is 1.5kv

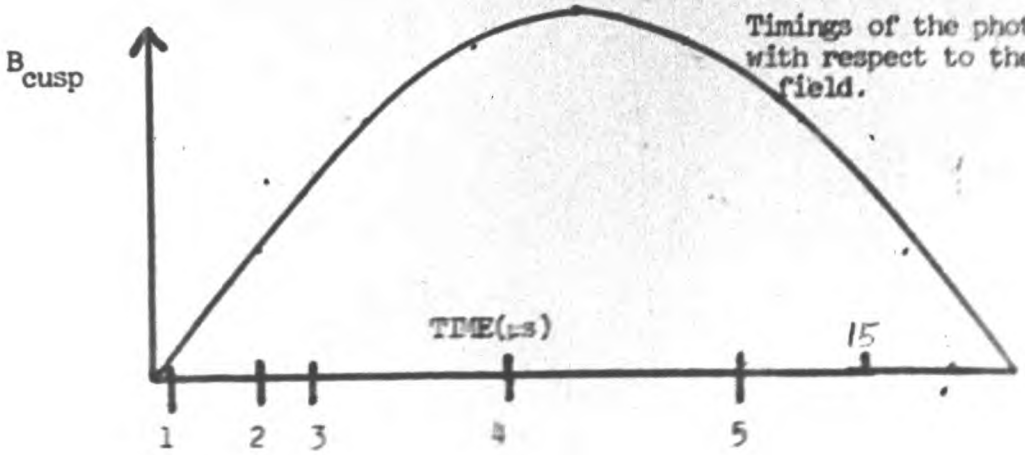

Timings of the photographs with respect to the cusp field.

FIG. 3.32

in fig. 3.32. Photography at 3.5 mtorr was impossible because of the low light level. The photographs show graphically the features found by the more quantitative methods described earlier.

3.16 Summary of results

(1) The plasma lights up quickly beneath the coil. A shell of number density forms. However, in hydrogen at least there is no appreciable heating.

(2) The current which drives this compression drops after 3μs. The number density under the coil also drops. The radial profile becomes centralised to about 1.5 cm.

(3) Simultaneously the number density under the ring cusp starts to rise as plasma flows into this region. The temperature of the plasma in this region rises to 4eV, and the number density trebles. The number density profile is flat topped.

(4) The number density under the coil drops to a minimum value of $\frac{1}{4}$ of the ring cusp number density. The plasma density under the coil then starts to rise again as the plasma flows back, driven by pressure gradients.

(5) The plasma flows out of the ring cusp region through a 8mm wide slit, with a velocity of $2\ 10^3$ m/s. This flux can account for loss of 1/10 of the total number of particles.

(6) At low pressure the number density in the ring cusp region starts to fall after 9μs. This is through the joint effect of loss of plasma through the ring cusp, and plasma flowing back into the region under the cusp coils.

The quantitative results of this chapter are summarised in fig. 3.33. At 3.5 mtorr there seems to be very full ionisation > 70%. The data is used to evaluate a line density under the ring cusp.

FIG. 3.33 SOME RESULTS OF CHAPTER 3

V_c 1.5 kV, 12μs after cusp

p mtorr	3.5	25
$\bar{n}_e$ r.c. 10^{-20} (Stark)	1.7 ±.2	7 ± 1
$\bar{n}_e$ coil 10^{-20} (Stark)	.4	5.5 ± 1
$\bar{n}_e$ r.c. 10^{-20} HCN (extrapolated)	1.7 ±.2	
$\frac{\bar{n}_e \text{ r.c. (continum)}}{\bar{n}_e \text{ coil}}$	2. ± .5	1.1
n_e peak 10^{-20} scattering	4 ± .5	11 ± 1
W (peak) eV. W (av) eV. T_a(eV)	1.8 ±.2	1.8 ± .1 1.0 .9

CHAPTER FOUR

THE CUSP COMPRESSION EXPERIMENT: THEORY

4.1 The neglect of the skin current and the resulting simplification

In the work of this chapter the effect of the skin current is neglected. It will be shown that this is consistent with the experimental observations.

In section 3.5 this neglect was shown to be valid for times longer than 500ns for the case when the skin currents are too small to cause appreciable heating. The case of the cusp coils was experimentally investigated in section 3.14 where it was shown that the cusp field diffuses into the plasma within 1μs of initiation.

This diffusion time is consistent with the measured temperature.

$$\tau_o = \frac{\mu \sigma a^2}{\gamma_o'} \sim 400\ W^{3/2}\ \text{ns}.$$

However the skin depth must remain large compared with the radius, that is the temperature must not rise. The temperature is kept low by the ionisation level in the bulk of the plasma and conduction near to the edge. The temperature can only rise above 1 to 2 eV if full ionisation of the neutrals occurs.

Therefore $$\int_0^{\tau_o} \frac{j_\theta^2}{\sigma}\, dt < n_n I$$

where n_n is the neutral number density and I the ionisation energy, to prevent a temperature rise and thus a skin. This is hardest to satisfy near the wall as E_θ is largest. At the wall this condition gives $n_n < 10^{20} m^{-3}$, using W = 1eV. This is approximately true for the experimental conditions.

To neglect the field produced by the plasma it is also necessary that the magnetic Reynolds' number, R_m, be small

$$R_m = \mu_o \sigma L V = \frac{\omega r^2 \sigma \mu_o}{4\omega t} = \frac{8\ 10^{-7}}{t} W^{3/2}$$

assuming $V = \frac{E_\theta}{B\omega t}$, where ω is the angular frequency of the cusp field. R_m is largest near to the wall and so W can be taken as 1eV. Therefore R_m is less than 1 for ωt greater than .1. In practice R_m is always<1 as it takes 2 μs to accelerate the plasma.

The simplification of the equations obtained by neglecting fields produced by the plasma has an important numerical implication. Alfven and whistler waves are eliminated and thus the stringent timestep criterion imposed by waves for an explicit numerical solution (Watkins et al, 1971) is eliminated.

4.2 Analogy with a low voltage theta pinch

The plasma acceleration is seen to occur in the first

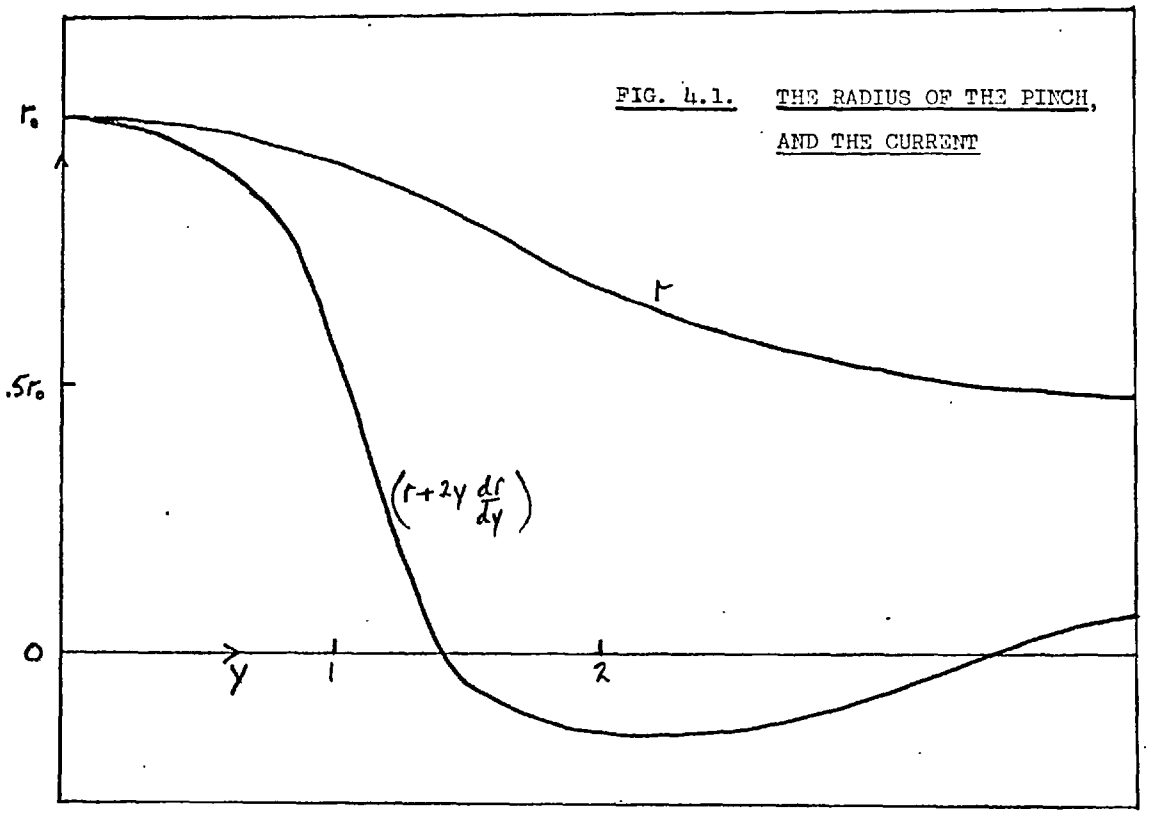

FIG. 4.1. THE RADIUS OF THE PINCH, AND THE CURRENT

Fig. 4.2. CALCULATED AND EXPERIMENTAL TIMES FOR $j_e = 0$

T_1 (fig. 3.30) μs	1.5	1.9	2.2	3.3	2.7	6.
$n_n\ 10^{-20}\ m^{-3}$	.6	1.	3.	10.	10.	5.4
$\frac{1.55}{W^{\frac{1}{3}}}\left(\frac{n_n}{10^{20}}\right)^{\frac{1}{3}}\left(\frac{1500}{V_c}\right)^{2/3}\mu s$	1.4	1.6	2.2	3.3	2.1	5.2

$\sim 3\mu s$. In this time the cusp nature of the field is unimportant as flow velocities are of the order 10^3m/s. The behaviour is like a low voltage theta pinch. An analytic solution for this special case where the skin depth is large is developed. Full ionisation is assumed, and constant temperature.

Let $B_z(t) = B_o \omega_b t$

Then $E_\theta = -\frac{r}{2} \omega_b B_o$ i.e. $\omega_b t \ll 1$.

The equation of motion of a region of plasma is $\frac{dv_r}{dt} = \frac{j_\theta B_z}{\rho}$

where $j_o = \sigma(E_\theta - v_r B_z)$

as $\frac{\partial}{\partial z} = 0$ which implies $j_r, j_z = 0$.

Therefore $\frac{dv}{dt}_r = -\frac{\sigma B}{\rho}_o \omega_b t \left(\frac{r\omega_b B_o}{2} + v_r B_o t \omega_b\right)$

$$= - B_o^2 \frac{\omega_b^2 \sigma t}{\rho}\left(\frac{r}{2} + v_r t\right)$$

Defining $\omega_1 = \frac{B_o^2 \sigma}{\rho} = \omega_{ci} \tau_{ei} \omega_{ce} = \alpha \omega_{ci}$

in terms of the cyclotron frequencies and the collision time, allows a suitable dimensionless time variable.

$$x = \omega_1 t = \frac{B_o^2}{\rho} \sigma t$$

to be introduced. α is the Hall parameter.

The equation of motion becomes

$$\frac{d^2 r}{dx^2} + \frac{\omega_b^2 x^2}{\omega_1^2} \frac{dr}{dx} + \frac{\omega_b^2}{2\omega_1^2} x r = 0$$

In terms of a new dependent variable $y = x\left(\frac{\omega_b}{\omega_1}\right)^{2/3}$ the equation becomes

$$\frac{d^2r}{dy^2} + y^2 \frac{dr}{dy} + \frac{1}{2} yr = 0.$$

To find a series solution a Frobenius method can be used. If $r = \sum_{n=0}^{\infty} a_n y^{s+n}$, then the usual method of equating powers of y gives $a_0\, s(s-1) = 0$

$$a_1\, s(s+1) = 0$$

$$a_2(s+2)(s+1) = 0$$

and so $s = 0$, $a_2 = 0$, $a_1 \neq 0 \neq a_0$, giving the two necessary independent solutions. The recurrence relations are

$$a_{3n+3} = \frac{-(3n + \frac{1}{2})}{(3n+3)(3n+2)} a_{3n};\quad a_{3n+4} = \frac{-(3n+1.5)}{(3n+4)(3n+3)} a_{3n+1}$$

When $y = 0$, $\frac{dr}{dy} = 0$ and so $a_1 = 0$.

The first few terms of the series are

$$r = r_o \left(1 - \frac{1}{12} y^3 + \frac{7}{720} y^6 - 0\,(10^{-3})\, y + \ldots\right)$$

The series was evaluated numerically and is shown in fig. 4.1.

$j_\theta = \sigma(E_\theta - v_r B_z) \propto (r + 2\frac{dr}{dy} y)$ is also plotted in fig. 4.1.

From this plot $j_\theta = 0$ when $y = 1.4$. The negative j_θ arises because $v > E_\theta/B_z$ and the plasma has to be decelerated.

$$y = \omega_b^{2/3} \quad B_o^{2/3} \quad t$$

and so the current reverses when

$$t = \frac{1.4\,\rho^{1/3}}{\gamma^{1/3} B_o^{2/3} \omega_b^{2/3}}$$

This is to be compared with the normal snow plough model where there is a $\rho^{\frac{1}{4}}$ dependence and $B^{-\frac{1}{2}}$. $\omega_b B_o$ depends only on the inductance of the circuit and the charging voltage.

For the plasma geometry used

$B = .4T$ (at $r = 3cm$), $\omega_b = 1.25\ 10^5 Hz$

then $$t = \frac{1.55}{W^{\frac{1}{3}}} \left(\frac{n}{10^{20}}\right)^{\frac{1}{3}} \left(\frac{1500}{V_c}\right)^{2/3} \mu s. \qquad (4.1.)$$

The agreement with the experimentally measured times of chapter 3 is shown in fig. 4.2. The value of n used is the filling pressure and then there is good agreement with experiment.

4.3 The symmetry of the experiment

It is obviously important to make full use of all available symmetries. There are advantages of simulating two adjacent symmetric regions. e.g. to check accuracy and to allow long wavelength instabilities to develop, but certainly in this experiment these are unimportant considerations.

The cusp compression experiment is assumed to be linear and so there is azimuthal symmetry. It is obviously

symmetric to axial displacements of $4z_0$, two coil separations. It is also symmetric to mirror displacements about both the ring cusp plane and the coil plane.

In the former case, mirror displacements about the ring cusp, the polarity of each component of the vector variables of the plasma is changed according to

$$\hat{\theta} \rightarrow -\hat{\theta} \ , \ \hat{r} \rightarrow \hat{r} \ , \ \hat{z} \rightarrow -\hat{z}$$

This is intuitively obvious, but can be justified rigorously by considering each term of each equation. This way every equation can be shown to be invariant. For example the $\hat{\theta}$ component of Ohm's law:-

$$j_\theta/\sigma = E_\theta + v_z B_r - v_r B_z + j_z B_r/ne - j_r B_z/ne$$
$$(-) \quad (+) \quad (-) \quad (+) \quad (+) \quad (-)$$

and the axial equation of motion:-

$$\rho \frac{\partial v_z}{\partial t} + v_z \frac{\partial}{\partial z} v_z + v_r \frac{\partial}{\partial r} v_z = -j_\theta B_r - \frac{\partial p}{\partial z}$$
$$(+) \quad (-) \quad (+) \quad (-) \quad (-)$$

For reflexions about the plane of coil, the polarities change according to

$$\hat{\theta} \rightarrow \hat{\theta} \ , \ \hat{r} \rightarrow \hat{r} \ , \ \hat{z} \rightarrow -\hat{z}$$

For example the radial equation of motion:

$$\frac{\partial v_r}{\partial t} + v_r \frac{\partial}{\partial r} v_r + v_z \frac{\partial}{\partial z} v_r = j_\theta B_z - \frac{\partial p}{\partial r}$$
$$(+) \quad (+) \quad (+) \quad (-) \quad (+) \quad (+)$$

Note here, that for mirror reflexion about the plane of the coil $B_z \rightarrow B_z$. B_z, B_r, E_θ are externally imposed quantities. Strangely $b_\theta \rightarrow -b_\theta$ for reflexions about the plane of the coil, but $v_\theta \rightarrow + v_\theta$ as above. This strange behaviour only affects the displacement term in Ampere's law.

Finally consider the azimuthal component of Ohm's law:-

$$j_\theta/\sigma = E_\theta + v_z B_r - v_r B_z + j_z B_r/ne - j_r B_z/ne$$

$$\downarrow\ + \quad \downarrow\ + \quad \downarrow\downarrow\ - - \quad \downarrow\downarrow\ + + \quad \downarrow\downarrow\ - - \quad \downarrow\downarrow\ + +$$

Hence it has been shown that the system is symmetric as these transformations do not change the equations.

Similarly in the polytron m.h.d. code developed by Watkins (1971) the author pointed out that there is a symmetry to axial displacements of $2z_0$ the polarities changing according to

$$\hat{r} \rightarrow \hat{r}\ ,\quad \hat{\theta} \rightarrow -\hat{\theta}\ ,\quad \hat{z} \rightarrow \hat{z}\ .$$

4.4 The plasma equations

The continuity equation is

$$\frac{\partial \rho}{\partial t} = -\nabla.(\rho \underline{v}) + m\,ION \qquad (4.2)$$

where ρ is the plasma density

m is the mass of the ions

and ION the number of neutrals ionised per unit volume per second.

The three momentum equations are

$$\frac{\partial}{\partial t}(\rho \underline{v}) = \underline{j} \times \underline{B} - \nabla.(\rho \underline{v}\underline{v}) - \nabla p$$
$$-\rho^n \rho_m (\underline{v} - \underline{v}^n) v_{rel}\, \delta_x + \underline{v}^n m\, ION \qquad (4.3)$$

The superscript n refers to the neutrals. $\underline{B}$ is the vacuum magnetic field . p is the scalar plasma pressure =

$n_e k T_e \cdot \sigma_x$ is the momentum transfer cross section between the ions and the neutrals. This is taken as 60 $10^{-20} m^2$ (Hasted, 1962). v_{rel} is the total ion–netural relative velocity.

$$v_{rel} = \left(\frac{8k}{\pi}\left(\frac{T^i}{m} + \frac{T^n}{m_n}\right) + (\underline{v} - \underline{v}^n)\right)^{\frac{1}{2}}$$

and is simplified to $v_{rel} = \underline{v} - \underline{v}^n$

The coupling time for the ion neutral velocity is 5μs for ion and neutral number densities of $10^{20} m^{-3}$. An order of magnitude either way and the neturals would be either completely coupled or decoupled, but unfortunately a detailed treatment is necessary.

The electron temperature is found by an energy equation

$$\frac{\partial U}{\partial t} = \underline{j}^2/\sigma - \nabla(U\underline{v}) - p\,\nabla.\underline{v} - \text{ION I} - \frac{3}{2} n_e k \frac{(T_e - T_i)}{\tau_{eq}} \qquad (4.4)$$

where U is the electron internal energy/volume = $\frac{3}{2} n_e k T_e$ and τ_{eq} is the electron ion equipartition time (Spitzer, 1956, p.80) .

An equation for the internal energy, rather than a total energy equation reduces the error in determining the internal energy as the kinetic energy can be many times the internal energy. In practice the heating and ionisation terms in equation 4.4. dominate. Electron thermal conduction is ignored.

The ion temperature is assumed to remain at a low temperature because of the close coupling to the neutrals and ion and atomic conduction.

4.5 The neutral equations

The continuity equation is

$$\frac{\partial \rho^n}{\partial t} = - \nabla (\rho^n \underline{v}^n) - m \text{ ION} \qquad (4.5)$$

The three momentum equations are

$$\frac{\partial}{\partial t} (\rho^n \underline{v}^n) = - \nabla . (\rho^n \underline{v}^n \underline{v}^n) + \frac{\rho^n \rho}{m} (\underline{v} - \underline{v}^n) \, v_{rel} \, \sigma_x - \underline{v}^n \, m \text{ ION} \qquad (4.6)$$

The azimuthal velocities of the plasma are small and so the azimuthal velocity of the neutrals is neglected as it affects the dynamics in the r - z plane only by the centrifugal force. Both plasma and neutral momentum equations are for ionising plasmas. For recombining plasmas the last terms should be $\pm \underline{v}$ m ION.

4.6 The ionisation rates

Without convection the rate equation for ionisation is

$$\frac{dn_e}{dt} = n_e \, n_n \, S(W) - \alpha(W) \, n_e^3$$

where S and α are the collisional radiative ionisation and recombination coefficients, and n_n the number density of neutrals.

$$\alpha(W) = \frac{2 \, 10^{-39}}{W^{4.5}} \; m^6 \, s^{-1} \quad \text{(D'Angelo (1965))}$$

and so for W > 1eV , which is the experimental regime, the recombination times are milliseconds .

The ionisation rate is taken from Griem as

$$S(W) = 4.2\ 10^{-12}\left(\frac{W}{E_I}\right)^{\frac{1}{2}} \exp(-E_I/W)\ m^{+3}\ s^{-1}$$

Here the coefficient for hydrogen, $7.\ 10^{-14}$, has been multiplied by 6 because of the optically active electrons, and 10 to account for ionisation from the upper state of the resonance line (estimated for $n_e = 10^{21}\ m^{-3}$ from Griem eq. 6.36). E_I is the energy of the level above which l.t.e. holds. As shown from the Boltzmann plot in chapter 3 the levels 6 eV below the continuum are just in l.t.e. for argon II. So for AI this could be expected to scale to 1.5 eV, which is also the value of E/n^2 given by Griem for a hydrogen atom. Hence $E_I = 13.6-1.5 = 12$eV. Hence $S(W) = 1.2\ 10^{-12}\ W^{\frac{1}{2}} \exp(-12/W)\ m^{+3}\ s^{-1}$. The ionisation and recombination times are given in fig. 4.3.

FIG. 4.3 IONISATION AND RECOMBINATION TIMES

W	τ_i (μs)	τ_r (μs)
1eV, $n_n\ 10^{20} m^{-3}$, $n_e 10^{21} m^{-3}$	140	350
1eV, $n_n\ 10^{20} m^{-3}$, $n_e 10^{20} m^{-3}$	1400	3500
2eV, $n_n\ 10^{20} m^{-3}$, $n_e 10^{20} m^{-3}$	3	10^6
3eV, $n_n\ 10^{20} m^{-3}$, $n_e 10^{20} m^{-3}$	.25	

These times show why low density plasmas with no source of energy have temperatures of 1eV → 2eV. Ionisation at high temperatures will cause a rapid drop in the temperature. But when $2eV > W > 1eV$, ionisations stops and recombination cannot occur. The only way of losing energy quickly in this region is by conduction.

In the cusp compression experiment temperaures will stay below 4 eV, unless full ionisation occurs, but will

stay above 1eV, because of the poor thermal conduction discussed in chapter 3.

4.7 The equation for j_θ

This is simply Ohm's law.

$$\frac{j_\theta}{\sigma} = E_\theta + v_z B_r - v_r B_z - \frac{1}{n_e}(j_z B_r - j_r B_z) \quad (4.7)$$

where E_θ, B_r and B_z are the vacuum values. As a check on the field produced by the plasma being small compared with the vacuum field the field produced by j_θ is evaluated. A s.o.r. method is used to solve

$$\nabla^2 A_\theta = -\mu_0 j_\theta$$

Null and periodic boundary conditions hold at the z boundaries. A_θ is zero on the axis and far from the plasma. This is simulated by a boundary condition at twice the radius of the vacuum vessel. The magnetic field is

then simply evaluated as

$$b_r = -\frac{\partial A_\theta}{\partial z} \qquad b_z = \frac{A_\theta}{r} + \frac{\partial A_\theta}{\partial r}$$

4.8 The equation for b_θ

b_θ is caused by j_r and j_z (or vice versa). There are no direct applied forces causing j_r and j_z but only the $j_\theta B_z$ and $j_\theta B_r$ Hall terms in the $\hat{r}$ and $\hat{z}$ components of Ohm's law. Additionally div. $j = 0$ and so to determine j_r and j_z it is simplest to solve for b_θ. As before, $\underline{b}$ is the field produced by the plasma and $\underline{B}$ the externally imposed field. $|\underline{b}| \ll |\underline{B}|$ and so Faraday's law and Ohm's law can be simplified to

$$-\frac{\partial b_\theta}{\partial t} = \nabla_\lambda \Big(\underbrace{\underline{j}/\sigma}_{A_\tau} - \underbrace{\underline{v} \times \underline{B}}_{B_\tau} + \underbrace{\frac{\underline{j} \times \underline{B}}{ne}}_{C_\tau} - \underbrace{\frac{\nabla p_e}{ne}}_{D_\tau} \Big)_\theta \qquad (4.8)$$

Solving eq. 4.8 as a parabolic equation explicitly would be time consuming as the time step would have to be shorter than the rapid characteristic diffusion time. Moreover the inductive term can be neglected as

$$b_\theta \approx \mu_0 \, \ell \, j_r$$

where ℓ is a characteric length $\leq r$.

The l.h.s. of eq. 4.8 can be neglected then if

$$\frac{\partial b_\theta}{\partial t} < \frac{j_c}{\ell \sigma}$$

i.e. $\mu_0 \ell \frac{\partial}{\partial t} < \frac{1}{\rho\sigma}$

which is just the criterion for the skin depth being greater than ℓ.

Eq. 4.8 is then solved as an elliptic equation, by setting

$$\frac{\partial b_\theta}{\partial t} = 0$$

Now examine the r.h.s. term by term:-

(1) $A_T = \nabla \wedge \underline{j}/\sigma)_\theta$

$$= \frac{1}{\sigma\mu_0}\left(-\frac{1}{\sigma}\frac{\partial\sigma}{\partial z}\frac{\partial b_\theta}{\partial z} + \frac{\partial\sigma}{\partial r}\frac{j}{r}\frac{\partial}{\partial r}(r b_\theta)\right) + \underline{\nabla}^2 b_\theta \Big)$$

(2) $B_T = -\nabla\wedge(\underline{v}\wedge\underline{B}))_\theta = -\frac{\partial}{\partial r}(v_\theta B_r) - \frac{\partial}{\partial z}(v_\theta B_z)$

which is computationally simpler than differentiating the products.

(3) $C_T = \nabla\wedge\left(\frac{\underline{j}\times\underline{B}}{ne}\right)\Big)_\theta = \frac{\partial}{\partial z}\left(\frac{\underline{j}\times\underline{B}}{ne}\right)_r - \frac{\partial}{\partial}\left(\frac{\underline{j}\times\underline{B}}{ne}\right)_z \equiv \frac{\partial}{\partial z}(D j_\theta) + \frac{\partial}{\partial r}(E j_\theta)$

$$j_\theta = \sigma(E_\theta + v_z B_r - v_r B_z - j_z B_r/ne + j_r B_z/ne)$$
$$\equiv F - G\mu_0 j_z + H\mu_0 j_r = F - G\frac{1}{r}\frac{\partial}{\partial r}(r b_\theta) + H\frac{\partial b_\theta}{\partial z}$$

$$\therefore\ C_T = \frac{\partial}{\partial z}\left(D(F - G\frac{1}{r}\frac{\partial}{\partial r}(r b_\theta) - H\frac{\partial b_\theta}{\partial z})\right) + \frac{\partial}{\partial r}\left(E(F - G\frac{1}{r}\frac{\partial}{\partial r}(r b_\theta) - H\frac{\partial b_\theta}{\partial z})\right)$$

Here there are 6 terms independent of b_θ and 12 with up to second derivatives of b_θ

(4) $D_T = -\nabla\left(\frac{1}{ne}\nabla P_e\right)\Big|_\theta = \frac{1}{w}\frac{\partial w}{\partial z}\frac{\partial W}{\partial r} - \frac{1}{w}\frac{\partial w}{\partial r}\frac{\partial W}{\partial z}$

where w is the electron density relative to the initial density at r = 0, and W is the electron temperature in eV.

The terms in eq. 4.8 are gathered into terms

dependent and independent of b_θ . The differentials are differenced in a space centered way, using two points for single differentials and three for second differentials. Compass notation is used, all coefficients of b_θ at each 9 compass points being collected. The symbolic form of the equation is

$$\text{Sourc} - \frac{b_\theta^c}{ST7} + b_\theta^n ST5 + b_\theta^s ST6 + b_\theta^e ST3 + b_\theta^w ST4 + ST8(b_\theta^{ne} + b_\theta^{sw} - b_\theta^{se} - b_\theta^{nw}) = 0$$

where Sourc and ST3 $\rightarrow$ ST8 are independent of b_θ

Solving for the centre point, and applying a relaxation factor ω_r, the equation becomes

$$b_\theta^{c,p} = b_\theta^{c,p-1} + \omega_r(ST7(Sourc + b_\theta^{n,p} ST5 + \ldots\ldots - b_\theta^{nw,p})) - \omega_r b_\theta^{c,p-1} \qquad (4.9)$$

the superscript p being an iteration counter.

The vacuum region must be treated differently as $\sigma = 0$ would allow singularities in b_θ. The iterative scan of eq. 4.9. is thus only done up to the plasma boundary and b_θ set to zero outside of the plasma.

The symmetry of the problem ensures that $j_z = 0$ across the plane of the coil and the ring cusp. So in the planes of the ring cusp and the coil $b_\theta = \frac{A}{r}$ and as $b_\theta = 0$ at r = a, then $b_\theta = 0$ for all r. The last boundary condition on b_θ is that $b_\theta = 0$ on the axis, from

$$\oint \underline{b} . d\underline{\ell} = \mu_0 \int \underline{j} . d\underline{A}$$

To check the coding and solving of this complex equation a value for

$$\nabla_\wedge \underline{E})_\theta = \frac{\partial E_r}{\partial z} - \frac{\partial E_z}{\partial r}$$

was calculated. The values of b_θ found from solving equation 4.9 were differenced to form j_r and j_z. Substitution into the $\underline{r}$ and $\underline{z}$ components of Ohm's law, together with the $\underline{\theta}$ Ohm's law, gave values of E_r and E_z. The derivatives of curl $\underline{E})_\theta$ were evaluated by differencing these values. The two terms in curl $\underline{E})_\theta$ cancelled to within 5% of the individual values, verifying the correctness of the solution.

4.9 The physical reason for b_θ

Contours of b_θ are shown in fig. 4.3. These results were taken at $t = 2\mu s$, and so there is some motion of the plasma. The arrows indicate the approximate direction of flow of current. b_θ contours are nearly the flow lines as

$$j_r = \frac{1}{\mu_0}\frac{\partial b_\theta}{\partial z} \qquad j_z = \frac{1}{\mu_0}\left(\frac{b_\theta}{r} + \frac{\partial b_\theta}{\partial r}\right)$$

At this time there is a simple explanation for the cause of b_θ. The $\hat{\underline{r}}$ and $\hat{\underline{z}}$ components of Ohm's law are

$$\frac{j_r}{\sigma} = E_r - \frac{j_\theta B_z}{ne} \qquad (4.10)$$

$$\frac{j_z}{\sigma} = E_z + \frac{j_\theta B_r}{ne} \qquad (4.11)$$

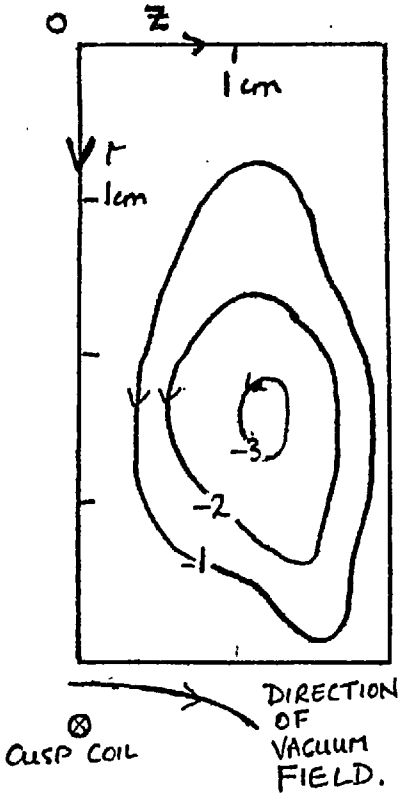

FIG. 4.3. CONTOURS OF b_θ IN GAUSS

j_θ is negative: the arrows indicate the direction of j_r, j_z.

FIG. 4.4. SCHEMATIC DRAWING OF THE ELECTROSTATIC FIELD THAT CAUSES j_r & j_z

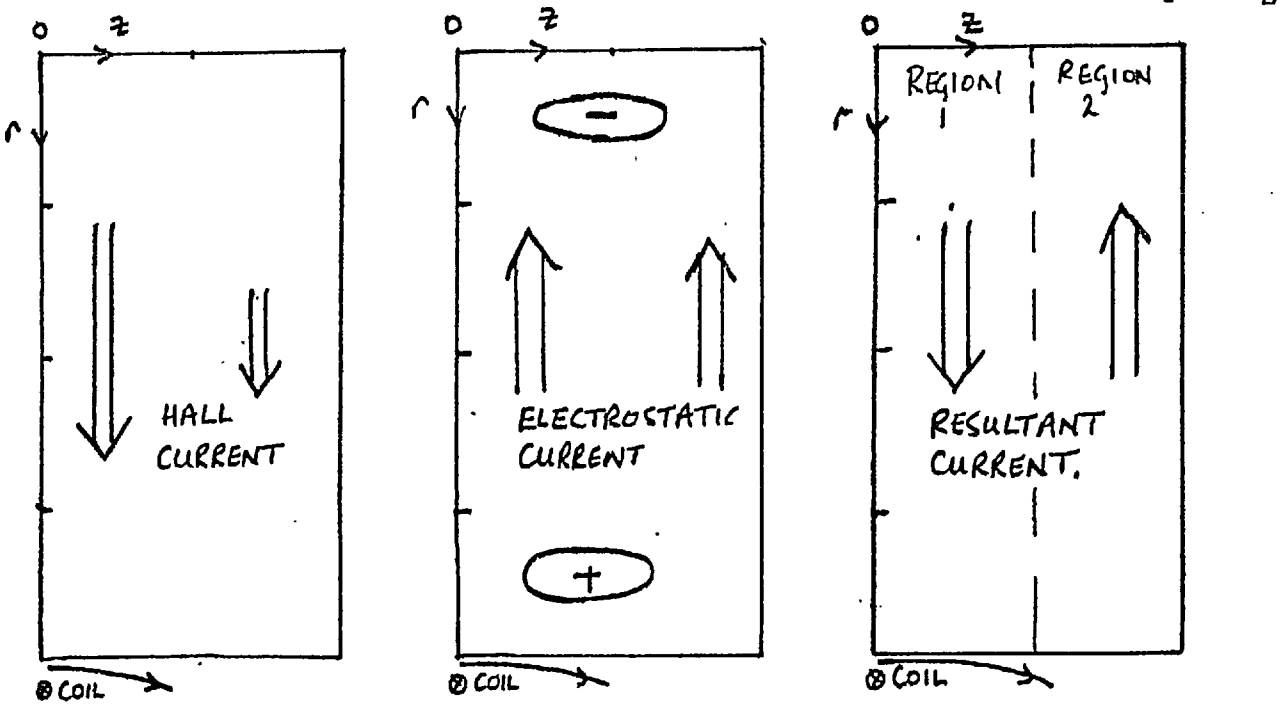

at a time when the pressure gradient and v_θ are both small. j_θ is negative and proportional to $j_{\theta 0} r \cos kz$. j_r and j_z must additionally satisfy

$$\nabla . j = 0$$

E_r and E_z are set up so that this condition is fulfilled. Suppose the two terms on the r.h. side of equations 4.10 and 4.11 are considered to cause separately a Hall current and an electrostatic current. The directions and magnitudes of these currents are shown schematically in fig. 4.4. The radial Hall current is largest near the coil, but is always outwards. This divergent current flow causes the outer region of the plasma to become positively charged; the resulting electrostatic current is inwards and approximately independent of z. The sum of these two currents is non divergent and is outwards under the coil, region 1, and inwards under the ring cusp, region 2.

That is

$$j_r(z)/\sigma = E_r - j_\theta B_z/ne \equiv \alpha - \beta \cos kz$$

$$\nabla . j = 0 \qquad \therefore \int_0^{z_0} j_r \, dz = 0 \qquad \therefore \alpha z_0 - \beta/k = 0$$

$$\therefore j_r(z) = \beta(2/\pi - \cos kz) = \beta(.64 - \cos kz)$$

$$\therefore \overline{j_r} = .2\sigma B_z/ne \; j_\theta = .2\omega\tau \, j_\theta$$

taking an average value. At early times $\omega\tau$ is small, and so

j_r, j_z are small c.f. j_θ

The applied E_θ is up to 1 kV/m and so the radial field caused by the Hall currents is much larger than kT/r, the electric field caused by the pressure gradient. When $\omega\tau$ approaches 1 the analysis is modified slightly, as

$$j_\theta = \sigma E_\theta + \omega\tau j_r.$$

Now Ohm's law is considered only on the line ℓ along which $j_z = 0$, and the neutrality condition becomes

$$\int j_r \, \underline{r}.\underline{n} \, d\ell = 0$$

then $$\frac{j_r}{\sigma}(1 + (\omega\tau)^2) = E_r - \omega\tau E_\theta$$

When $\omega\tau = (\omega\tau)_0 \cos kz \gg 1$ then

$$j_r = \frac{\sigma E_r}{(\omega\tau)_0^2 \cos^2 kz} - \frac{\sigma E_{\theta_0}}{(\omega\tau)_0}$$

The flow will still be in the same direction; the current will be reduced to $\sigma E_\theta / 2\omega\tau_0$ but the electrostatic fields will still be $\omega\tau E_\theta$. The characteristic size of the loop will decrease as flow will be restricted to regions of low $\omega\tau$.

It is unfortunate that in an exact solution for j_r and j_z the clarity of approach demonstrated above has to be lost. This is because one must use the fact that $\nabla \wedge \nabla U = 0$, and hence ∇U is not evaluated. (U is the e.s. potential)

4.10 The numerical solution of the equations

Schemes suitable for the solution of the m.h.d. equations are considered in Methods of Comp. Physics. Vol.9. (Roberts and Potter, 1969). Originally a leapfrog method of solution was used. However the weak coupling between the two sets of meshes caused a numerical instability.

To couple the meshes together the two step Lax Wendroff method was used (Lax and Wendroff, 1960). The equations to be solved are of the form

$$\frac{\partial u}{\partial t} = F + \nabla . \underline{G} + \frac{\partial P}{\partial r} \qquad (4.13)$$

The values of u on the subsidiary mesh at time level n + 1 are found from

$$\begin{aligned} u_c^{n+1} &= (u_{ne}^n + u_{se}^n + u_{sw}^n + u_{nw}^n)/4 + dt\, F_c^{n-1} \\ &+ dt/2a\,(((G_{se,r}^n + G_{sw,r}^n)(J-\tfrac{1}{2}) - (G_{nw,r}^n + G_{ne,r}^n)(J+\tfrac{1}{2}))/J \\ &+ (G_{nw,z}^n + G_{sw,z}^n - G_{se,z}^n - G_{ne,z}^n)\, dt/2a \\ &+ dt/2a\,(P_{nw}^n + P_{ne}^n - P_{sw}^n - P_{se}^n) \qquad (4.14) \end{aligned}$$

where the compass point relation to the r - z coordinate is shown in fig. 4.5. The radius of a mesh point is r = Ja where a is the length of the side of a cell, J the radial coordinate, and dt is the time-step. The conservative form of the second term on the r.h.s. of equation 4.13 has been used in the allogrithm. The

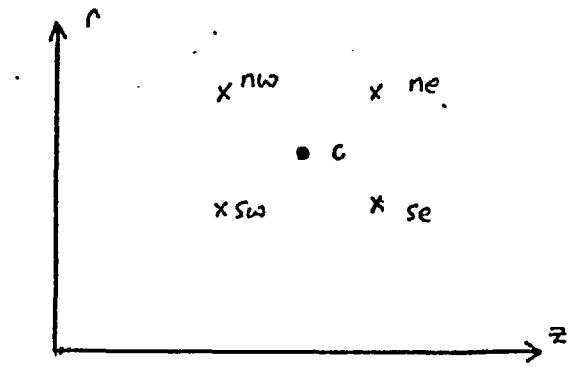

FIG. 4.5

flux of G through the surfaces of the cell are evaluated, taking the curvature into account. The first subscript on G is the compass notation: the second denotes the component (r or z) under consideration. For calculating the values of u on the main mesh, at time level n + 2 the algorithm is as eq. 4.14 except that:-

(1) $n \longrightarrow n+1$

(2) $u_c^{n+2} = u_c^n + \ldots\ldots$

that is, the new value is calculated from the old values on the main mesh.

The equation for b_θ (and so j_r and j_z) is only solved on the main mesh, the values on the subsidiary mesh being interpolated but at the wrong time level.

As the Lax Wendroff scheme is explicit the timestep must be smaller than all of the characteristic times of the physical processes represented by the equation, otherwise a numerical instability results. In practise the shortest time is the radial acceleration time of equation 4.3.

$$\tau_a = \frac{n\ m}{\sigma B_z^2} = \frac{1}{\omega_{ci}\ \omega_{ce}\tau_{ei}} \qquad (4.15)$$

When B_z has attained it's maximum value this can become as short as 10ns. During the calculation it is ensured that

$$.2 < \max(dt/\tau_a) < .5 \qquad (4.16)$$

by varying dt. Here max(x) is the largest value on the mesh.

To avoid too small a value of τ_a, once the electron density at a mesh point falls below .2 of the initial value, that mesh point is treated as a vacuum in which no current flows, and any residual neutrals are not ionised.

The plasma at the wall of the tube is kept at a low temperature. Whether more plasma reaches the wall or plasma comes off the wall depends on the radial velocity at the row next to the wall.

4.11 Results of the simulation

The results of some runs with a constant temperature of lev , no ionisation and no b_θ are shown in figs. 4.5, 4.6, and 4.7. This approximation is reasonable. The temperature is fixed by ionisation; $j_r \ll j_\theta$ if $\omega\tau \ll 1$, and when $\omega\tau \sim 1$. little current flows as then $v_r = E_\theta/B_z$.

Fig. 4.5 shows the field produced on axis under the coil. The comparison with the experiment (fig. 3.30) is within a factor of 2. (3mtorr $\equiv 10^{20} m^{-3}$, 25 mtorr $\equiv 5\,10^{20} m^{-3}$, fig. 3.18). The peak experimentally measured field should be doubled to take account of the position of the magnetic probe. From this comparison an average temperature of leV is deduced, again in agreement with the Boltzmann plots (fig. 3.10) and the conductivity measurements. The larger field at higher filling pressure in fig. 3.30 is in agreement with the higher temperature at higher pressure in fig. 3.9.

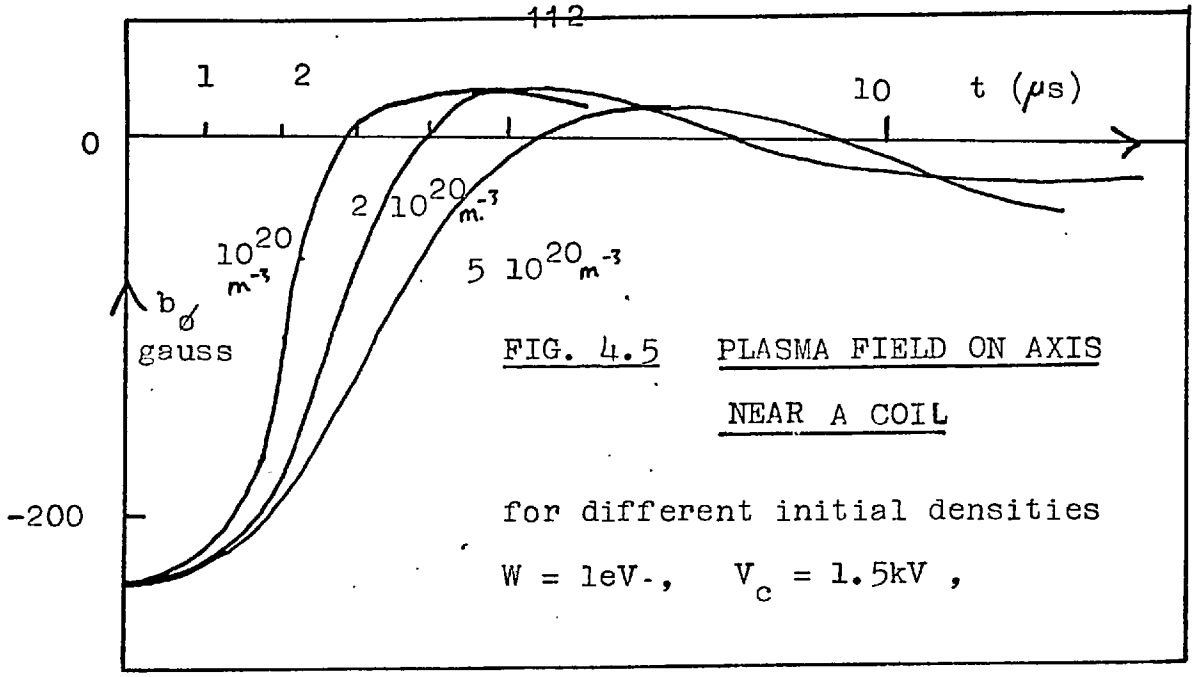

FIG. 4.5 PLASMA FIELD ON AXIS NEAR A COIL

for different initial densities

W = 1eV-, V_c = 1.5kV ,

The simulation starts with a uniform density and zero velocity and the magnetic field is equivalent to V_c = 1.5kV. Fig. 4.6 shows the plasma parameters at 3.6μs, for $n = 2\ 10^{20}\ m^{-3}$. The nett plasma current is small because $\underline{E} + \underline{v} \times \underline{B} = 0$

and as can be seen the plasma is moving perpendicular to the field lines. At a radius of 2cm at this time the value of

$$\omega\tau = \frac{\sigma B_z}{ne} \approx 5$$

and so for times later than this the effect of b_σ should be considered. However, experimentally j_θ is small and thus so is j_r and j_z. The dynamics of the plasma will be determined mainly by the pressure gradients set up rather than the currents at this time.

After 8μs the compression into the ring cusp

region and subsequent pressure gradient, causes the axial velocity to reverse. (For $n = 10^{20}$ and $5\ 10^{20}$ this reversal occurs 1μs earlier and later respectively). This is observed experimentally, occuring at about $7 \pm 2\mu s$ for 3.5 mtorr (fig. 3.22). The peak density at this time is 2.3 x the initial density, compared with 2x for the experiment (fig. 3.21, 10mtorr argon). Fig. 4.7 shows that loss of plasma is only occuring at the mesh point at the ring cusp. This is in slight disagreement with the experimental measurement where the full half width of 8mm seems wider than in the simulation. However poor agreement is to be expected because of the coarse mesh.

Results of the full simulation, including ionisation, heating and b_θ will now be discussed. A full set of runs has not been performed because of difficulty in solving the b_θ equation. Results of a run with $n = 5\ 10^{20} m^{-3}$, $n_n = 10\ 10^{20} m^{-3}$ and $\underline{v} = \underline{v}^r = 0$ initially, are shown in fig. 4.8. The temperature rapidly rises to 1.6 eV where j_θ is large, this temperature being fixed by the ionisation rate. Hence initially the line of sight density is larger under the coil than under the ring cusp. This is seen experimentally fig. 3.24 Consequently the field on axis is 400 gauss c.f. 200 gauss in fig. 4.5. However the effect of conduction is not included. Fig. 4.8. shows the plasma parameters at 3.5μs when the plasma field has nearly dropped to zero. The temperature has reached 2eV at the edge of the plasma as all of the

neutrals have either been ionised or moved. Later this causes trouble because of the very high local values of $\omega\tau$ when the temperature rises because of the absence of ionisation. Clearly conduction should be included but this is not simple because of the anisotropy and vacuum regions. The radial skin in the number density which is seen experimentally in fig. 3.24 is evident in fig. 4.8. It forms because of the ionisation and compression at large radii, As expected $v_\theta << v_r, v_z$. The simulation only continued to 5.3μs before the b_θ errors caused j_θ to become too large. The temperature on axis, under the ring cusp only reached 1.2 eV c.f. the experimental value of 3.5eV (fig. 3.21). The experimental value implies that there is a high degree of ionisation and the low temperature in the simulation probably arises because of the high initial neutral density and thus incomplete ionisation.

4.12 Summary

A simulation can account for most of the features of the cusp compression experiment of chapter 3 and indicates that the plasma behaviour is simply compression and then relaxation. The simulation is not successful in predicting the plasma currents when $\omega\tau \gg 1$ but fortunately in this experiment the plasma currents can be ignored when $\omega\tau \sim 1$.

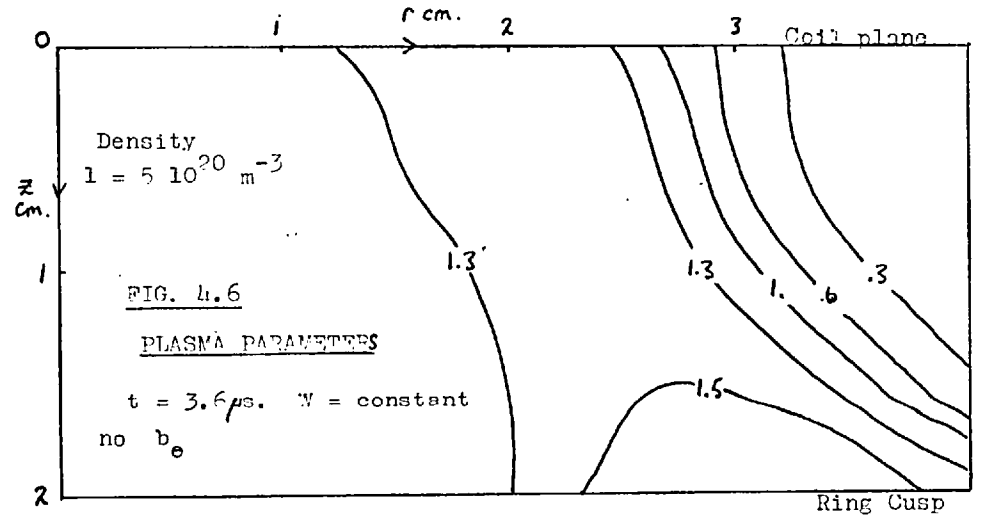

FIG. 4.6

PLASMA PARAMETERS

$t = 3.6\mu s$. W = constant

no b_θ

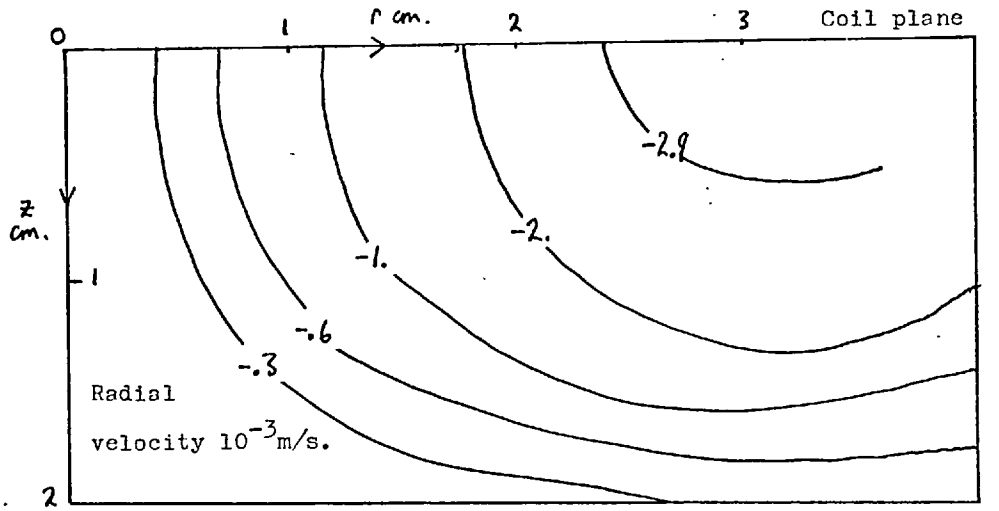

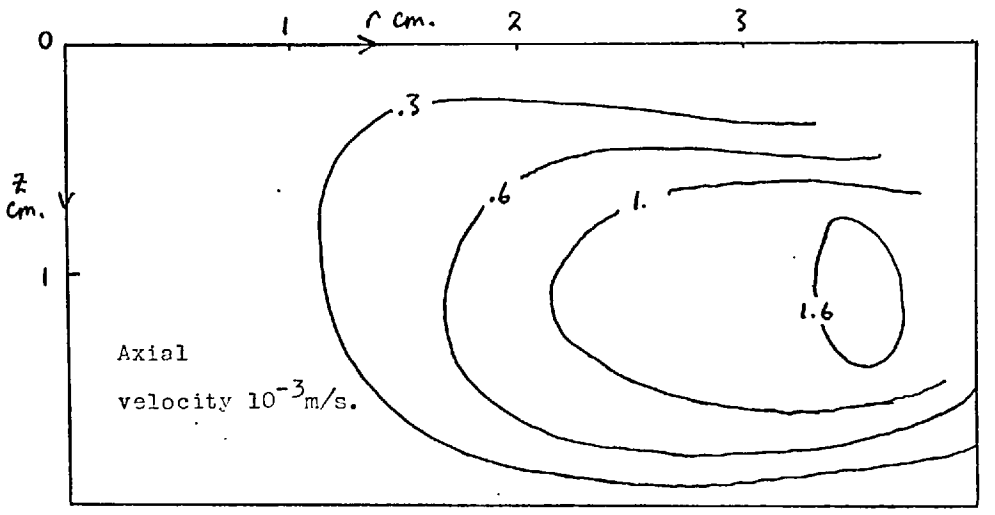

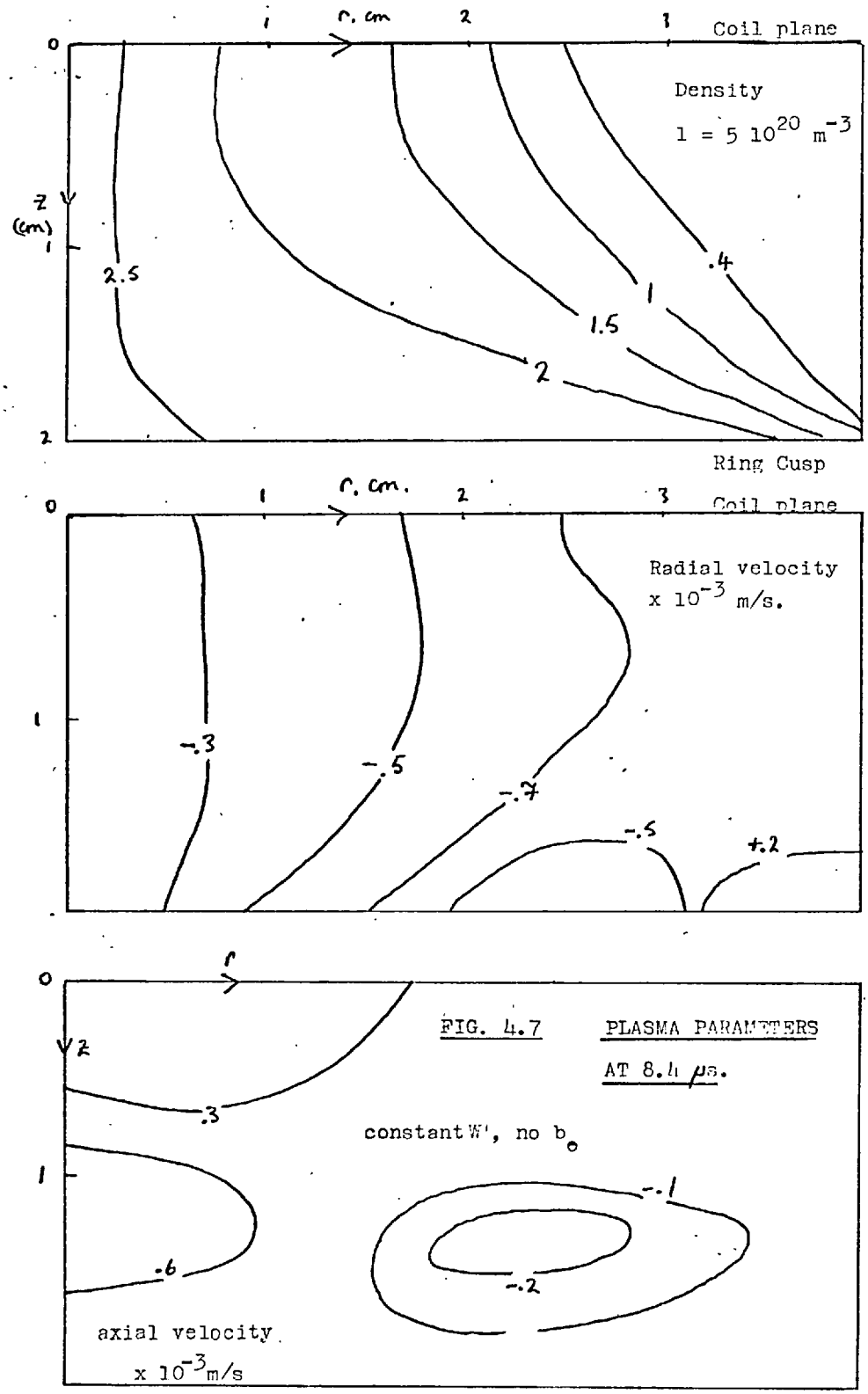

FIG. 4.7 PLASMA PARAMETERS AT 8.4 μs.

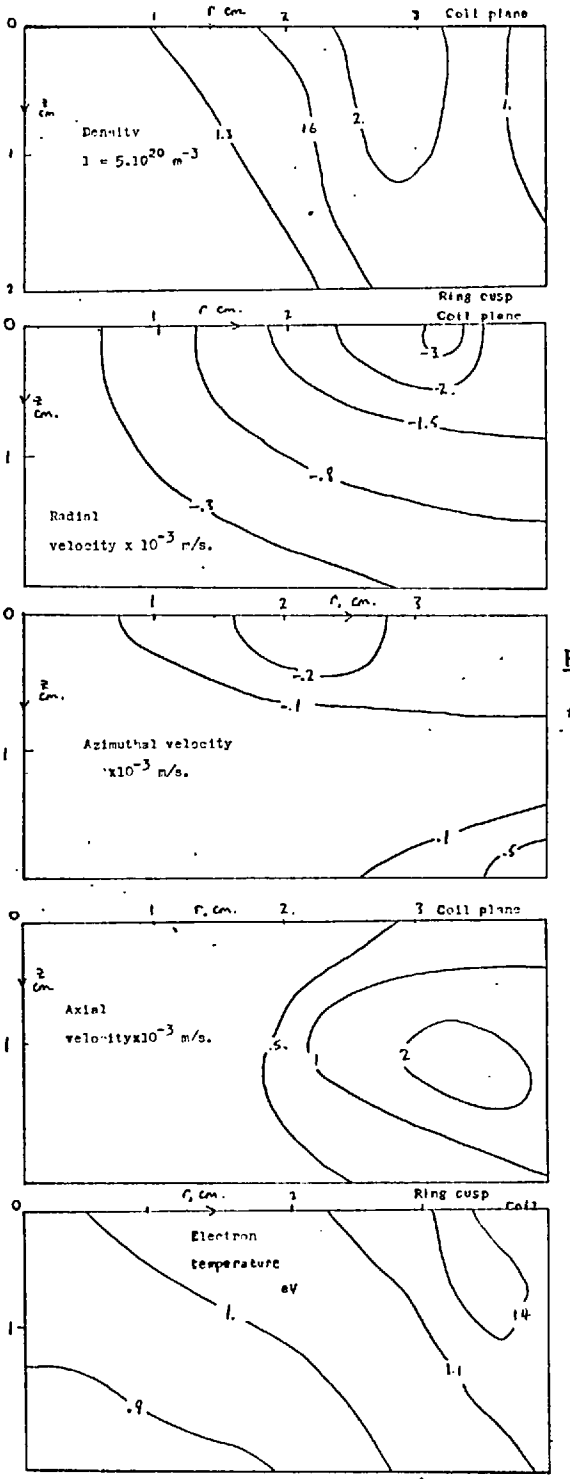

FIG. 4.8

PLASMA PARAMETERS FOR A FULL SIMULATION AT 3.6 μs.

CHAPTER FIVE

SINGLE PARTICLE MOTION IN THE TOROIDAL POLYTRON FIELDS

In this chapter the motion of particles, mainly ions, is calculated in the full three dimensional magnetic and electric fields of the polytron. The values of the fields used are the same as the experiment.

Some preliminary work was done by Dunnett (1969) on this problem. He considered a straight polytron with a limited choice of initial conditions. He chose only 3 points in configuration space and varied the initial positions in velocity space. A wiser policy, adopted in this work, is the converse. That is, initially all velocities are set to zero, and a wide variety of initial positions in configuration space examined.

There is some overlap between this chapter and chapter 6. The problems considered are similar but the emphasis is on different aspects of single particle motion. Here the accent is on the toroidal containment problem, whereas in chapter 6 the simpler linear geometry allows a more complete study of initial loss, plasma currents and coupling to the driving electric field.

Consideration was given to doing the single particle studies experimentally by radioactive particle formation. This has been done for a stellarator by Gibson(1969). But it was thought that a computation

could do this equally well, for a limited simulated time.

Furthermore it seems that the model successfully predicts some aspects of the experiment even though experimentally the Debye length is much less than the plasma dimensions. This is because the cusp magnetic field prevents the electrons from moving toroidally under the action of the applied electric field. Then the plasma motion can be approximated by the ion motion only. No consistent pertubation of the vacuum magnetic field is considered.

With regard to centrifugal containment of the ions it is shown computationally and analytically that the polytron field configuration can be sufficient to prevent loss, as long as the collisional frictional force limits the toroidal velocity to less than an upper critical value, and larger than a lower critical value.

5.1. The field representation

A fast solver for the field of a toroidal cusp configuration is described in chapter 2. Fast though this is, it is too slow to use every integration of the particle trajectory. For one particle it might have to be called

10,000 times and on every call the field of all 36 coils must be evaluated and then resolved into the local coordinates.

An attempt was made to use an analytic representation of the field. Various reasonable analytic functions which could include all of the essential features described in chapter 2, with up to 14 fitting parameters, b_j, were tried. The values of b_j were optimised by means of a least squares fit to the actual field. The least square fit was done using a programme due to Marquardt.

The mean square error for the best case was 5% which was thought to be unsatisfactory.

A smaller error was realised by storing the actual field values on a 3 dimensional mesh. Then for any field point interpolation between the nearest mesh points gives the field.

The coordinate system is cylindrical (R,ϕ,z) about the toroidal major axis but with R measured from the minor axis. $\phi = 0$ under a cusp coil. The symmetry of the field

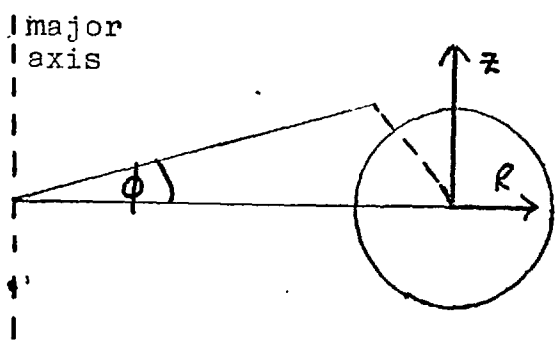

FIG. 5.1

COORDINATE SYSTEM

implies that any region can be reduced to:-

ϕ : 0 to 5°

z : 0 to r_{max}

R: $-r_{max}$ to r_{max},

where r_{max} is the radius of the plasma vessel. The field is only stored for this domain. If for example $\underline{r}$ is in the region, ϕ: 5° to 10°, z:$-r_{max}$ to 0 then the field is

$$B_R(\underline{r}) = + B_R(R, 10^o - \phi, -z)$$

$$B_\phi(\underline{r}) = - B_\phi(R, 10 - \phi, -z)$$

$$B_z(\underline{r}) = -B_z(R, 10 - \phi, -z)$$

and the fields at the coordinates $R, 10^o - \phi, -z$ are stored. The numbers of mesh points are 17 x 9 x 9 in the R, ϕ, z directions respectively. The r.m.s. error with this field representation was 1%. The magnitude of the field is scaled by a factor V_c, the charging voltage of the consenser bank. V_c = 1.5 kV gives B_ϕ = .168T at R = 0, ϕ = 0, z = 0.

The applied toroidal electric field is constant in time, ϕ and z. The R variation is

$$E_\phi = \frac{E_o}{(1 + R/R_o)}$$

R_o being the major radius. Thus E_ϕ is pseudo conservative. The flux through the induction rod region is designed to be small and so this is the correct variation of $E_\phi(R)$. The

assumption $\frac{d}{dt} = 0$ is experimentally valid for $t < 2\ \mu s$. The effect of electrostatic fields is included in chapter 7, but because of periodicity they can be considered to average out, to a first approximation. Provision was made for an r electrostatic field to simulate pressure gradients but this was generally set to 0.

5.2 The equations and their solution

This choice of coordinate system avoids difficulties due to singularities at the minor axis. Using $R_a = R_o + R$ the equations of motion become

$$\ddot{R} = \frac{Ze}{m}(E_R + v_\phi B_z - v_z B_\phi) + \frac{v_\phi^2}{R_a} \qquad (5.1)$$

$$\ddot{\phi} = \frac{Ze}{R_a m}(E_\phi + v_z B_R - v_R B_z) - \frac{2\dot{\phi}\dot{R}}{R_a} \qquad (5.2)$$

$$\ddot{z} = \frac{Ze}{m}(E_z + v_R B_\phi - v_\phi B_R) \qquad (5.3)$$

$$\dot{R} = v_R \qquad (5.4)$$

$$\dot{\phi} = \frac{v_\phi}{R_a} \qquad (5.5)$$

$$\dot{z} = v_z \qquad (5.6)$$

E_R and E_z are electrostatic fields which are generally set to zero. The equations are made dimensionless by the variables:-

$$k = \pi/\text{cusp separation}; \quad \omega = \frac{ZeV_c}{m};$$

$$E_R = E_2 k R \quad , \quad E_z = E_2 kz \; ;$$

and so the fields can be represented by the dimensionless variables

$$B(1) = \frac{k\ m}{Ze V_c^2} E_o \; : \; B(2) = \frac{k\ m}{Ze V_c^2} E_2 \qquad (5.7)$$

If $\underline{B} = V_c(FL(1), FL(2), FL(3))$

and dimensionless variables are denoted by asterisks, the dimensionless equations of motion are

$$\frac{dv_R^*}{dt^*} = B(2)\, R^* + R_a \dot{\phi}(FL(3) + \dot{\phi}) - v_z\, FL(2) \qquad (5.8)$$

$$\frac{d\dot{\phi}}{dt^*} = \frac{1}{R_a^*}\left(\frac{B(1)}{1 + R^*/R_o^*}\right) + v_z^* FL(1) - v_R^* FL(3)) - \frac{2\dot{\phi} v_R^*}{R^* + R_o^*} \qquad (5.9)$$

$$\frac{dv_z^*}{dt^*} = B(2)\, z^* + v_R^*\, FL(2) - R_a^*\, \dot{\phi}\, FL(1) \qquad (5.10)$$

$$\frac{dR^*}{dt^*} = v_R^* \qquad (5.11)$$

$$\frac{d\phi}{dt^*} = \dot{\phi} \qquad (5.12)$$

$$\frac{dz^*}{dt^*} = v_z^* \qquad (5.13)$$

The particles are started from rest, the philosophy being that their thermal velocity is much smaller than the directed motion which can be acquired in the applied field.

The position of each particle is integrated forward in time according to equations 5.8 to 5.13 . Merson's method is used for the integration (Lance, 1960). This is a fourth order Runge-Kutta type of integration scheme. If the equations to be solved are

$$\frac{dy_i}{dt} = f(t\ ,\ y_j)$$

the value of y_i at time level n + 1 is given by

$$y_i^{n+1} = y_i^n + .5(k_1 + 4k_4 + k_5) + O(h^5) \qquad (5.14)$$

An estimate of the error is

$$\epsilon_i = (k_{1,i} - 9k_{3,i}/2 + 4k_{4,i} - k_{5,i}/2)/5 \qquad (5.15)$$

where $k_{1,i} = h\ f(t_n, y_j^n)/3$

$$k_{2,i} = h\ f(t_n + h/3, y_j^n + k_{1,j})/3$$

$$k_{3,i} = h\ f(t_n + h/3, y_j^n + k_{2j}/2 + k_{1,j}/2)/3$$

$$k_{4,i} = h\ f(t_n + h/2, y_j^n + \tfrac{3}{8} k_{1,j} + \tfrac{9}{8} k_{3,j})/3$$

$$k_{5,i} = h\ f(t_n + h, y_j^n + 1.5\ k_{1,j} - 45\ k_{3,j} + 6k_{4,j})/3$$

The reason for choosing this method rather than the standard Runge Kutta is that the expression for the error, ϵ, allows the timestep to be constantly adjusted to keep ϵ below a given maximum.

The system of equations is antisymmetric to ϕ displacements of 10° (1 cusp separation). It will be shown that the equations stay the same for 10° displacements except that z changes sign.

The symmetry of the magnetic fields is:

$$B_R(\underline{r}) = B_R(R, \phi, z) = -B_R(R, \phi + 10, -z) = -B_R(\underline{r}^1)$$

$$B_\phi(\underline{r}) = -B_\phi(\underline{r}^1)$$

$$B_z(\underline{r}) = +B_z(\underline{r}^1)$$

where $\underline{r}^1 = (R, \phi + 10, -z)$

The equations of motion can be written as

$$\frac{d^2R}{dt^2} = R_a\dot{\phi}\,(B_z(\underline{r}) + \dot{\phi}) - \dot{z}\,B_\phi(\underline{r})$$
$$= R_a\dot{\phi}\,(B_z(\underline{r}^1) + \dot{\phi}) - \dot{z}\,B_\phi(\underline{r}^1)$$

$$\frac{d^2\phi}{dt^2} = (\dot{z}\,B_R(\underline{r}) - \dot{R}\,B_z(\underline{r}) + E_\phi - 2\dot{\phi}\dot{R})/R_a$$
$$= (\dot{z}\,B_R(\underline{r}^1) + E_\phi - \dot{R}\,B_z(\underline{r}^1) - 2\dot{\phi}\dot{R})/R_a$$

$$\frac{d^2z}{dt^2} = \dot{R}\,B_\phi(\underline{r}) - R_a\dot{\phi}\,B_R(\underline{r})$$
$$= -\dot{R}\,B_\phi(\underline{r}^1) + R_a\dot{\phi}\,B_R(r^1) = -\frac{d^2z}{dt^2}(\underline{r}^1)$$

where $z(\underline{r}^1) = -z(\underline{r})$

This shows that particles starting at R, ϕ, z, move along the same trajectory as those starting as R, ϕ + 10, - z, except that z is inverted.

5.3 Results of the calculations

Particle trajectories are integrated from their initial position until either the particle is lost, i.e. $r = (R^2 + z^2)^{\frac{1}{2}} > 4$ cm, or it's trajectory has reached an equilibrium, or computer time limitations intervene. Imposing a loss radius r_ℓ makes the dimensionless equations a function of two variables kr_ℓ and B(1). Alternatively the equations can be considered a function of 4 variables, the particle species (Ze/m), V_c, E_o and r_ℓ . This is a vast gain in practical clarity, the cost being a 50% loss of elegance.

(a) Electron motion

The motion of ions generally falls into a different category from the electrons because of the vastly different e/m ratio. Electrons which are very near to the axis behave like ions. The converse would be true if the tube radius were very large (see chapter 6). In chapter 6 a criterion for particle acceleration is found, and only electrons starting within a small radius are accelerated. For electrons which start further out a guiding centre approximation pertains. In chapter 7 it is shown that for cylindrical geometry the guiding centre motion stays, on average, on the initial flux surface. It is also shown that the $-\mu \frac{\partial |B|}{\partial s}$ term for the parallel motion of the guiding centre is negligible. For containment a radial electric field is necessary, strong enough to contain the particle despite the energy it acquires from E_ϕ.

Approximately $U(R_o, \phi_o, z_o) > eE_\phi R(\phi_w - \phi_o)$

where U is the potential and ϕ_w where the field line associated with the initial position R_o, ϕ_o, z_o meets the wall. Taking the maximum value at R = 0 gives a sufficient condition for containment.

$$U(0, \phi, z) > E_\phi R \frac{\pi}{18} \qquad (5.16)$$

This condition is modified in chapter 7 where the case $\lambda_D \ll r_\rho$ is considered.

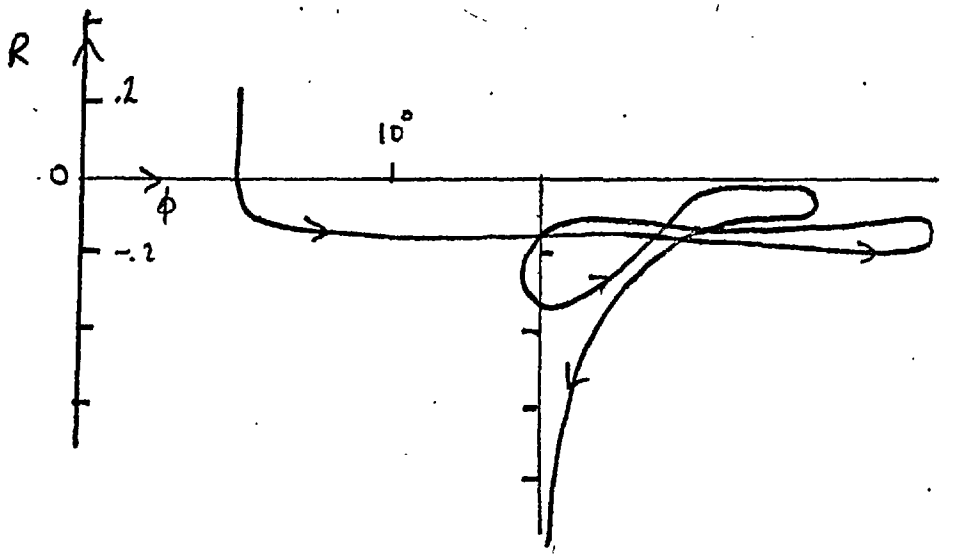

FIG. 5. 2 THE TRAJECTORY OF AN ELECTRON WHICH IS LOST

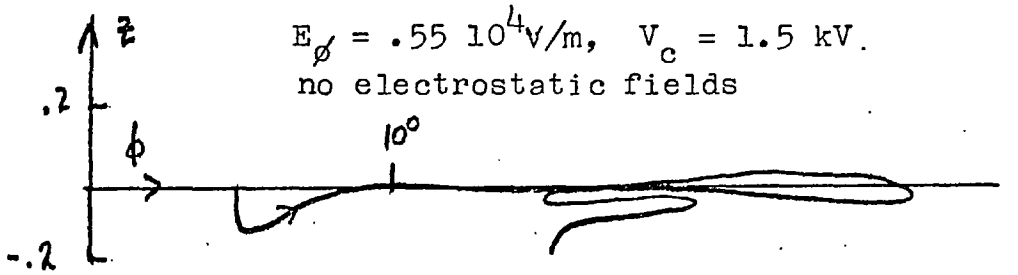

Even electrons which start from a position where they would be continuously accelerated in a linear system do not traverse many cusps because of toroidal effects. Fig. 5.2 shows the trajectory of an electron starting at $\phi = 5^\circ$. The particle spirals towards the magnetic axis under the action of $-\mu \frac{\partial |B|}{\partial s}$ in the parallel direction and $\underline{E} \times \underline{B}/B^2$ poloidally. When near enough to the magnetic axis the parallel direction turns and becomes parallel to the minor axis and so the particle is accelerated by E_ϕ. However the centrifugal drift eventually causes it to move to a region of larger B_R where it is reflected and eventually lost through a ring

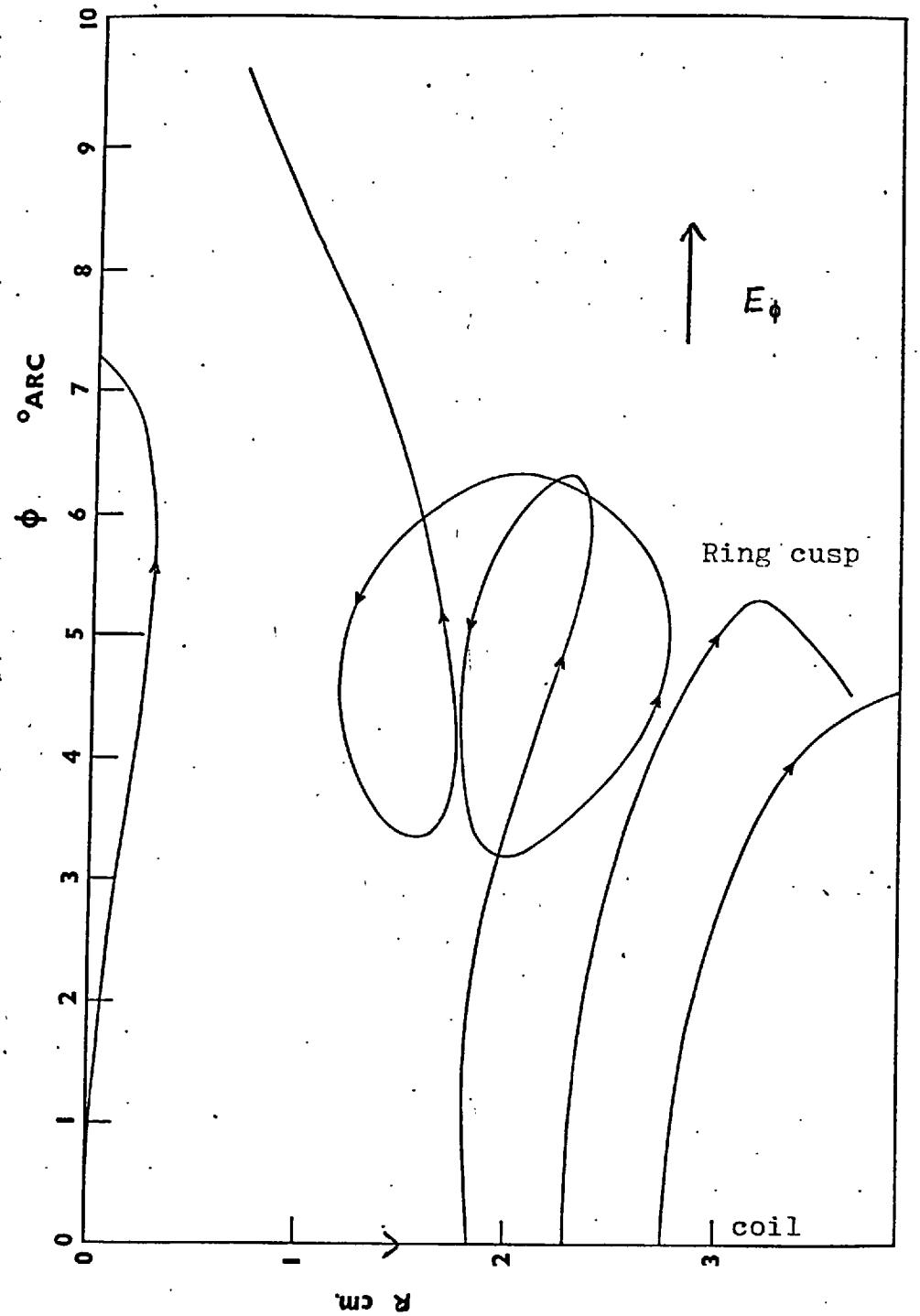

FIG. 5.3 THE R-ø TRAJECTORIES OF THE THREE CLASSES OF IONS

cusp. With reference to fig. 5.2 it must be remembered that the magnetic axis is not coincident with the minor axis.

To check the accuracy of the integration the sum of the kinetic and potential energies was found to be constant to 1 part in 10^4.

(b) Ion motion

As the ions have a lower Ze/m than electrons the different categories of particles can be seen. In contrast nearly all electrons have an initial Larmor radius much smaller than the tube. Examples of 3 categories of particles, lost, reflected and accelerated,and accelerated,are shown in fig. 5.3. This classification is examined in chapter 6. Here the centrifugal containment of the accelerations will be examined.

With the equations described,all accelerated ions are eventually lost centrifugally. Containment is by magnetic forces which are proportional to v_ϕ, whereas the centrifugal term is proportional to v_ϕ^2. As v_ϕ increases the centrifugal force eventually dominates the magnetic force. Roughly this is when

$$ev_\phi \bar{B}_z < \frac{m v_\phi^2}{R_o} \qquad (5.17)$$

The model can be moderated physically by collisions with the electrons which cannot move toroidally. If the effect

of the magnetic field on the ions is neglected, the ion fluid equation is

$$\frac{dv_\phi}{dt} = \frac{eE_\phi}{m_i} - \frac{m_e}{m_i}\frac{v_\phi}{\tau_{ie}}$$

Therefore $v_\phi = \tau_{ie}\frac{eE_\phi}{m}(1 - \exp(-m_e t/m_i \tau_{ie}))$

τ_{ei} is the electron ion binary collision frequency, the electron fluid being held stationary by the cusp field. The time taken to reach this limiting velocity, is similar to Haines's τ_a(1963) and is related to his acceleration time being $\frac{\sigma\rho}{n^2e^2}$, instead of his $\frac{\rho\delta}{n^2e^2} + \frac{2\rho}{\sigma B_x^2}$. Computationally this effect is accounted for by using a velocity dependent E_ϕ

$$\text{i.e.} \quad B(1)' = B(1)\ (1 - v_\phi/v_{\phi 1})$$

is used in equation 5.9. instead of B(1). The reaction force on the electron fluid causes an electron poloidal drift cancelling the $E_x B/B^2$ drift which on an m.h.d. model causes the acceleration. This is one of the limiting states considered by Haines (1963).

That is $\frac{F_x B}{B^2} = \frac{-E_\phi}{B^2} \times B$

Therefore $eE_\phi = \frac{m_e v_{i\phi}}{\tau_{ei}}$ or $v_{i\phi} = \frac{\sigma E_\phi}{n e}$ (5.18)

With this modification indefinite containment is observed, provided $1.4 10^4 \frac{V_c Z}{A}$ m/s $< v_{\phi 1} < 3.3\ 10^6 \frac{V_c Z}{A}$ m/s (5.19)

Where A is the atomic weight of the ion. This relation is empirically derived from the simulation. Fig. 5.4 is the trajectory of such a case. Ions have been followed for up to 20 times around the torus without loss occurring.

Paraxially one expects such a confinement because the cusp coils act as a series of lenses. The centrifugal force pushes the particles away from the magnetic axis. The focussing effect of the cusp field deflects them towards the axis, and so on average, the particles stay the same distance from the magnetic axis. The simple magnetic focussing was first discussed by Haines(1963b).

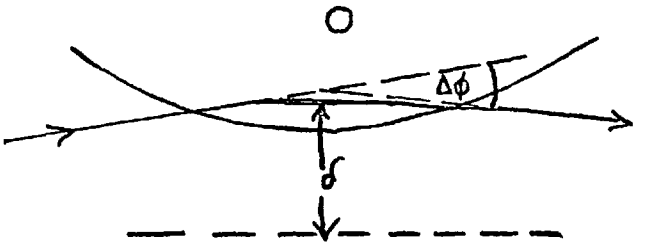

$$\text{i.e. } \Delta\phi = \frac{\delta}{f} = \frac{1}{4v_{\phi 1}^2}\left(\frac{eB_\phi}{m}\right)^2 L\delta$$

FIG. 5.5 FOCUSSING EFFECT OF A CUSP

using the Busch lens formula.

Here L is the cusp separation, δ the displacement from the magnetic axis as shown in fig. 5.5.

For containment

$$\Delta\phi = \frac{L}{R_o} = \frac{2\pi}{36}$$

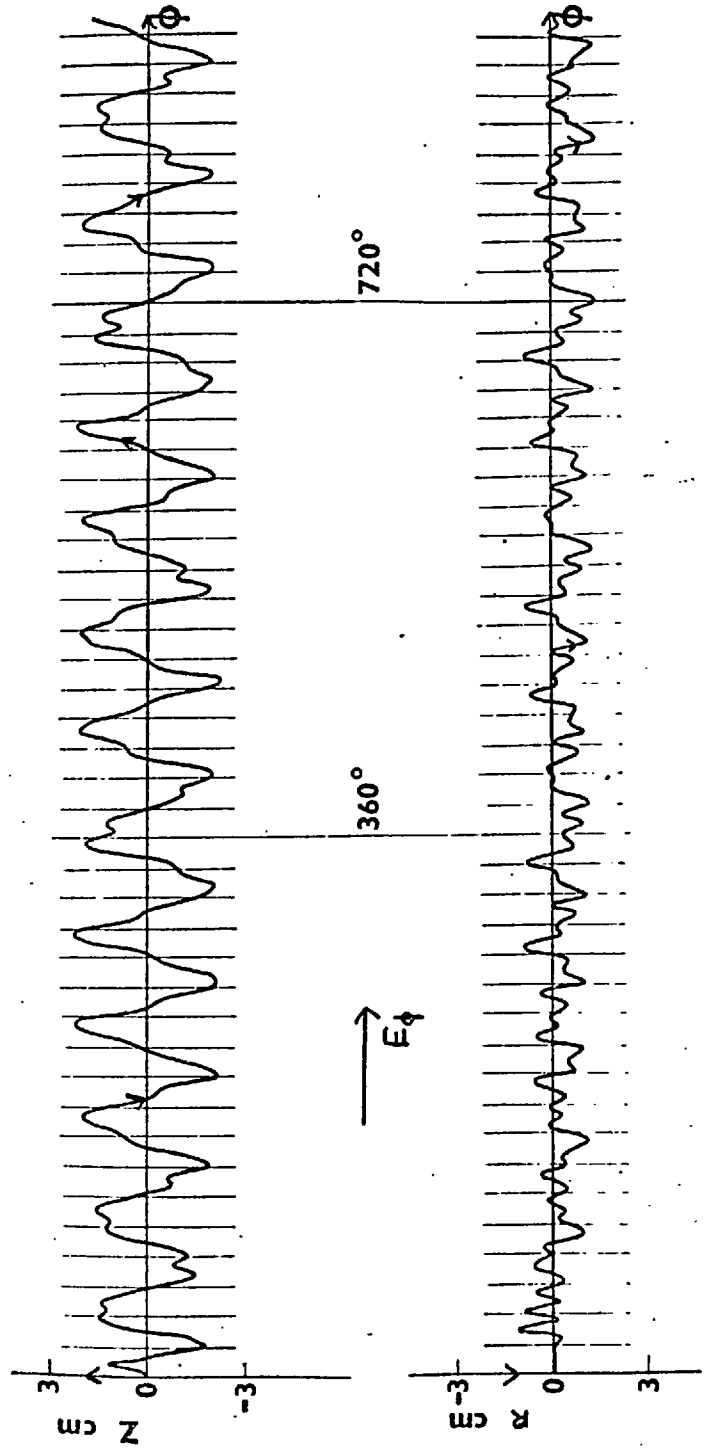

FIG. 5.4. THE TRAJECTORY OF A CONTAINED ION

satisfying eq. 5. 19.

Therefore $$\frac{\delta}{v_{\phi 1}}^2 > \frac{2\pi L}{9}\left(\frac{\overline{m_i}}{e\overline{B_\phi}}\right)^2$$

and as δ must be smaller than the tube radius there is an upper limit to $v_{\phi 1}$. Also too low a velocity leads to loss because (1) $\Delta\phi$ becomes too large

(2) the rotation about the minor axis

$$\Delta\theta = \frac{1}{2}\frac{(\overline{eB_\phi})}{m_i}\frac{L}{v_\phi}$$

becomes too large . If $\Delta\theta \ll 1$ then

$$\frac{L}{2}\frac{e\overline{B}_\phi}{m_i} \lesssim v_{\phi 1} \lesssim \frac{1}{2}\frac{(\overline{eB_\phi})}{m_i}\sqrt{r_\ell R_o} \qquad (5.20)$$

From this Busch result $v_{\phi 1} < 13.10^6 v_c Z/A$ m/s compared with $3.3\ 10^6 V_c Z/A$ computationally . In a way eq. 5.20 takes the non paraxial nature of the trajectories into account as $B_\phi(R)$, but does not consider the large oscillations shown in fig. 5.4. The effect of these oscillations is to make the tube radius r_ℓ in eq. 5.20, effectively smaller.

5.4 An analytic description of the numerically observed equilibrium and oscillations

The computer model shows that ions can be contained indefinitely in a volume radially displaced from the magnetic axis. Here an approximation to the equations is

investigated to show how this containment occurs and to account for the large oscillations of the trajectories. Here the case where

$$v_R/v_\phi \ll 1; \quad \frac{v_z}{v_\phi} \ll 1 \qquad \text{is examined}$$

It does not apply for the acceleration phase.

Oscillations about the equilibrium position are not large and so a representation of the field $B(R,\phi,z)$ is

$$\underline{B}(R,\phi,z) = (B_1 \sin \frac{n}{2}\phi,\ B_2 \cos \frac{n\phi}{2},\ B_3 hz \sin \frac{n\phi}{2}) \quad (5.21)$$

where n is the number of cusp coils, and h the scale length for changes in B_z.

As a first approximation v_ϕ = constant, and so with this approximation the equations become

$$\frac{dv}{dt}R = \frac{v_\phi^2}{R'} + \frac{q}{m}(v_\phi B_3 hz \sin \frac{n\phi}{2} - v_z B_2 \cos \frac{n}{2}\phi) \quad (5.22)$$

$$\frac{dv}{dt}z = \frac{q}{m}(v_R B_2 \cos \frac{n\phi}{2} - v_\phi B_1 \sin \frac{n}{2}\phi) \quad (5.23)$$

R', the denominator of the centrifugal term is assumed constant. The computer calculation shows that it varies by 1 part in 25.

As $v_R/v_\phi \ll 1$ a first approximation to eq. 5.23 is,

$$\frac{dv}{dt}z = -\omega_1 v_\phi \sin \frac{n}{2}\phi \quad (5.24)$$

where $\omega_i = \frac{q}{m} B_i$; $i = 1,3$

$$\frac{d\phi}{dt} = \frac{v_\phi}{R'} \qquad \therefore \quad \frac{d}{dt} = \frac{v_\phi}{R'}, \frac{d}{d\phi}$$

Therefore $v_z = + \frac{2 R'\omega_1}{n} \cos \frac{n\phi}{2} + \alpha$ (5.25)

and $z = \frac{4R'^2\omega_1}{n^2 v_\phi} \sin \frac{n\phi}{2} + \int \alpha dt + \beta$ (5.26)

α and β will be constants of integration but the approximate nature of eq. 5.24 can be allowed for by a slowly varying α and β. Consider first $\alpha = \beta = 0$. For this case it can immediately be seen how containment occurs as equation 5.22 becomes

$$\frac{dv_R}{dt} = \frac{v_\phi^2}{R'} + \omega_3 \omega_1 \frac{4R'^2}{n^2} h \sin^2 \frac{n\phi}{2} - \frac{2\omega_2\omega_1 R'}{n} \cos^2 \frac{n\phi}{2}$$

$$= \frac{v_\phi^2}{R} - \frac{2\omega_1 R'}{n} \left(\omega_2 \cos^2 \frac{n\phi}{2} - \frac{2R'}{n} \omega_3 h \sin^2 \frac{n\phi}{2}\right) \quad (5.27)$$

As long as $\omega_2 > 2\frac{\omega_3 hR'}{n}$ (5.28)

the last 2 terms of eq. 5.27 can balance the centrifugal term if the velocity is not too high. (i.e. on average)

Now let α be time varying but put $\beta = 0$. The time variation in α is necessary to describe the inaccuracy of replacing eq. 5.23 by eq. 5.24. These inaccuracies can be represented by α alone.

Equation 5.22 becomes, using 5.26 and 5.25.

$$\frac{dv_R}{dt} = \frac{v_\phi^2}{R'} - \frac{2\omega_1 R'}{n}\left(\omega_2 \cos^2\frac{n\phi}{2} - \omega_3 h \frac{2R'}{n}\sin^2\frac{n\phi}{2}\right)$$
$$+ \omega_3 v_\phi h \sin\frac{n\phi}{2}\int \alpha\, dt - \omega_2 \alpha \cos\frac{n\phi}{2} \qquad (5.29)$$

and equation 5.23 becomes

$$\frac{d\alpha}{dt} = \omega_2 v_R \cos\frac{n\phi}{2} \qquad (5.30)$$

describing the error in taking α as a constant.

It is implicit in the solution of eq. 5.24 that α represents a slowly varying term and so

$$\int \sin\frac{n\phi}{2} f(\alpha)\, dt = -\frac{2R'}{nv_\phi}\cos\frac{n\phi}{2} f(\alpha)$$

and the integral of eq. 5.29 becomes

$$V_R = \left(\frac{V_\phi^2}{R'} - \frac{\omega_1 R'(\omega_2 - 2\omega_3 h\frac{R'}{n})}{n}\right)t \quad -2\omega_3 R'\frac{h}{n}\cos\frac{n\phi}{2}\int\alpha\, dt$$

$$-\frac{2R'\omega_2\alpha}{nV_\phi}\sin\frac{n\phi}{2} + \frac{\omega_1 R'^2}{n^2 V_\phi}\left(2\omega_3 h\frac{R'}{n} - \omega_2\right)\sin n\phi \qquad -(5.31)$$

which gives the equilibrium condition that

$$V_\phi^2 = \frac{\omega_1 R'^2}{n}\left(\omega_2 - 2\omega_3 h\frac{R'}{n}\right) \qquad -(5.32)$$

When eq. 5. 32 is satisfied there remain only periodic terms in eq. 5.31, which becomes

$$V_R = -\frac{2\omega_3 R' h}{n}\cos\frac{n\phi}{2}\int\alpha\, dt - \frac{2\omega_2 R'\alpha}{nV_\phi}\sin\frac{n\phi}{2} + \left(\frac{2\omega_3 h R'}{n} - \omega_2\right)\frac{\omega_1 R'^2}{n^2 V_\phi}\sin n\phi$$
$$-(5.33)$$

Substituting into eq. 5.30, which describes the way α varies because of the neglect of the $v_R B_\phi$ term in eq. 5.23, gives

$$\frac{d\alpha}{dt} = -\frac{2\omega_2\omega_3 R' h}{n}\cos^2\frac{n\phi}{2}\int \alpha\, dt + \omega_3^2 R'\alpha \sin n\phi / n v_\phi$$
$$+ \sin n\phi \frac{\omega_2\omega_3 R'^2}{n^2 v_\phi}\cos\frac{n\phi}{2}\left(\frac{2\omega_3 h R'}{n} - \omega_2\right) \qquad -(5.34)$$

The last two terms here average to zero in a cusp period . They describe errors in eq. 5.24 at the frequency of the cusp separation, but they are negligible compared with the dominant term at this frequency in eq. 5.24. The first term does not average to zero and describes the low frequency variations in z.

Hence eq. 5.34 becomes

$$\frac{d\alpha}{dt} = -\omega_2\frac{\omega_3 R' h}{n}\int \alpha\, dt$$

Therefore $\alpha = \alpha_o \sin(\omega_z + \phi)$ (5.35a)

where $\omega_z^2 = \omega_2 \frac{\omega_3 R' h}{n}$ (5.35)

Low frequency oscillations in z have thus been accounted for.

The physical origin of these oscillations can easily be accounted for. As z increases so does $\dot{v}_R$ from eq. 5.22 and from the $v_R B_\phi$ terms in eq. 5.23 the acceleration back toward z = 0 increases. The smaller low frequency oscillations shown in fig. 5.4, in R cannot be accounted for by this model, because there is no field dependence on R. To take this into account consider a modification of the representation 5.21,

$$\underline{B}(R,\phi,z) = \left(B_1(1+ex)\sin\frac{n\phi}{2},\ B_2(1+fx)\cos\frac{n\phi}{2},\ B_3(1+gx)\sin\frac{n\phi}{2}\right)$$

This is a Taylor expansion about $R = R'$ i.e. $x = R - R'$ and $e = \frac{1}{B_R}\left(\frac{\partial B_R}{\partial R}\right)_{R=R'}$ etc. This makes equation 5.27

$$\frac{dv_R}{dt} = \frac{v_\phi^2}{R} - \frac{2\omega_1 R}{n}\left(\omega_2 \cos^2\frac{n\phi}{2} - \frac{2\omega_3 hR}{n}\sin^2\frac{n\phi}{2}\right) - \frac{2ex\omega_1 R}{n}\left(\omega_2\cos^2\frac{n\phi}{2} - \frac{2\omega_3 hR}{n}\sin^2\frac{n\phi}{2}\right)$$
$$- \frac{2\omega_1 Rx}{n}\left(\omega_2 f\cos^2\frac{n\phi}{2} - 2g\frac{\omega_3 hR}{n}\sin^2\frac{n\phi}{2}\right)$$

as long as $ex \ll 1$. The equilibrium condition 5.32 is unaffected as the sign of x varies slowly, and so averaging over a cusp separation and using 5.32 gives

$$\frac{d^2x}{dt^2} = -2x\frac{v_\phi^2}{R'^2} - ex\frac{v_\phi^2}{R'} - \frac{x\omega_1 R'}{n}\left(\omega_2 f - 2g\omega_3 h\frac{R'}{n}\right)$$

Hence the radial oscillations will be at a frequency ω_R given by

$$\omega_R^2 = \frac{v_\phi^2}{R'}\left(e + \frac{2}{R'}\right) + \frac{\omega_1 R'}{n}\left(\omega_2 f - 2g\omega_3 h\frac{R'}{n}\right) \quad -(5.36)$$

The amplitudes of both forms of oscillation are formally found by the boundary conditions. The preceeding analysis has only been concerned with $\dot{v}_\phi = 0$. At $t = 0$, $z = v_z = v_\phi = 0$ in the case of an accelerated ion. Suppose $v_\phi = \frac{t}{\tau_a} v_\phi^\ell$ initially, then

$$\frac{dv_z}{dt} = -\frac{\omega_1 t v_\phi^\ell}{\tau_a}\sin\frac{n\phi}{2} \qquad \text{again if} \quad v_R(t) \ll v_\phi(t)$$

$$\therefore v_z = 2\omega_1 \frac{R'}{n}\cos\left(nt^2 v_\phi^\ell/(4R'\tau_a)\right) \quad \text{if} \quad v_z(t=0) = 0$$

The integral is probably non analytic. The dominant contribution comes from the first period and so

$$z = 1.2\frac{\omega_1 R'}{n}\left(\frac{R'\tau_a}{n v_\phi^\ell}\right)^{1/2} + z_0$$

where the particle starts at $z = z_0$. This is how much the particle has been deflected by the passage through the first cusp, $\propto$ to the cusp separation x cusp transit

time/Larmor period.

The radial deflection is from eq. 5.22 similarly

$$\frac{dv_R}{dt} = \omega_3 h_z t \frac{v_\phi^\ell}{r_a} \sin\frac{n\phi}{2}$$

As $\omega_3 \sim \omega_1$ then the radial deflection will be smaller than the vertical deflection by h_z, as seen (fig.5.4)

5.5 Simulation of a plasma

In order to obtain plasma properties from this model a reasonable number (256) particles (ions) were considered, distributed uniformly throughout the region of the discharge vessel. As particles reach the wall in the calculation they are removed. The ϕ toroidal current and loss of particles are calculated as a function of time. The toroidal current is calculated assuming the ions are the only current carriers. These are shown in figs. 5.6 and 5.7. This illustrates the initial loss due to the particles originating near the wall. Later losses are due to violation of the $v_{\phi 1}$ criterion, which shows in this drawing because of the omission of collisions and hence $v_\phi > v_{\phi 1}$. There is an initial linear rise when all of the ions are being accelerated, and then a fall off in the current. This is due to particles being lost at this time as is shown in fig. 5.6, as well as a deceleration of the particles. The particle loss is confined to the region of the ring cusp and shifts downstream, i.e. in the direction of the applied electric field.

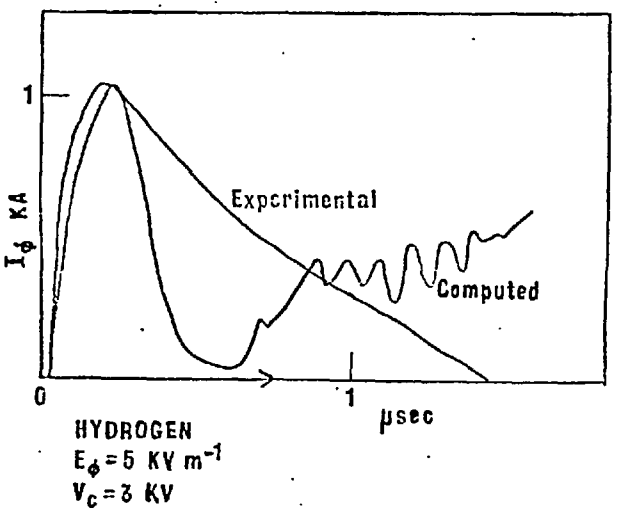

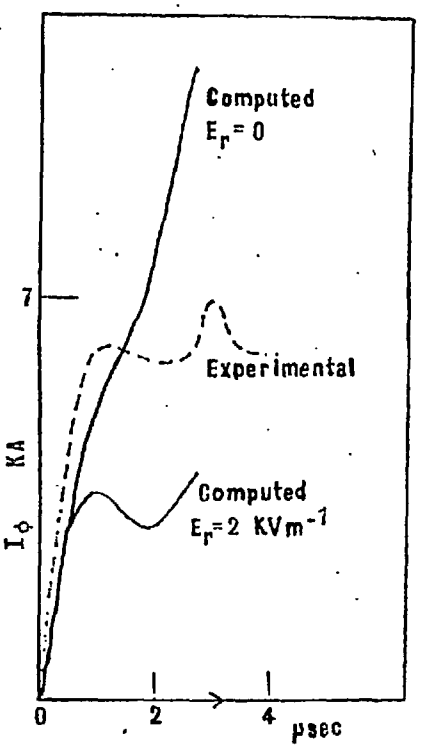

FIG. 5.7. COMPUTED AND EXPERIMENTAL TOROIDAL CURRENT WAVEFORMS

ARGON
$E_\phi = 5$ KV m^{-1}
$V_c = 1.5$KV
$Z = 3$

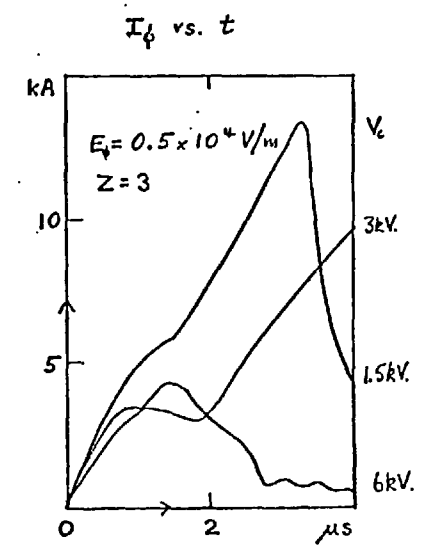

FIG. 5.6 TOROIDAL CURRENT AND LOST PARTICLES

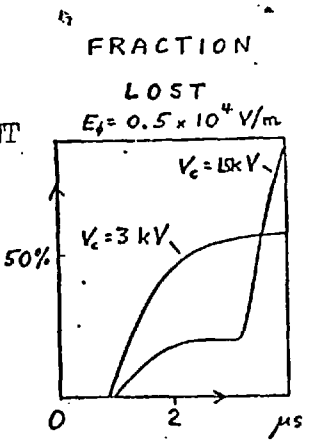

The effect of changing the magnetic field is also shown. With increasing magnetic field the volume of lost particles increases, so decreasing the current at the loss time.

For the case of hydrogen, also shown in fig. 5.7. the characteristic time is shorter and the characteristic loss larger. Fig 5.7 also shows the comparison with the experimental current waveforms. This is considered more fully in chapter 11 but is included here to offer some proof of the validity of the model. The value of Z for hydrogen is unequivocal but for argon an estimate of 2 is used (from spectroscopic work chapter 10) for comparison. Experimental agreement is certainly encouraging but it is improved by including the radial electric field due to charge separation. It is assumed to be given by a temperature gradient, the equivalent term in the m.h.d. equations being

$$\rho \frac{dv_R}{dt} = -nk \frac{\partial T_e}{\partial r} \equiv ne E_R$$

where the electron temperature is $T_e = T_{eo}\left(1 - \left(\frac{r}{r_e}\right)\right)$. By including this field with an equivalent temperature of 70 eV, all of the experimentally observed loss can be accounted for. It is shown in chapter 7 that an electrostatic field is set up even for a cold plasma, and so the above model is artificial.

Fig. 5.8 shows the R - ϕ projection of the volume from which the three categories of particle originate. The boundary is cusp shaped and shifted outwards from the

magnetic axis.

A graphic picture of the behaviour of the system is obtained by superimposing the trajectories of the particles on one plot. For a system where an appreciable fraction of the ions are contained, the R - ϕ and z - ϕ plots are shown in fig. 5.9 . These plots are in many ways like streak camera photographs of a plasma with a wide slit. The limiting velocity is reached in 10% of the total time plotted and thus even a smaller fraction of the ϕ values plotted in fig. 5.9 . After this, the abscissa is directly proportional to time. Because there is a spread in the initial value of ϕ there is a consequent blurring of the ϕ - time relation, corresponding to a wide slit. The density of lines also corresponds to the density of plasma.

The low frequency oscillations, due to the over-focussing effect described analytically in section 5.4. are clearly shown, together with the radial displacement of the equilibrium position. In contrast to tokamaks where a stabilising field is necessary to maintain a radial equilibrium the polytron cusp field theoretically maintains this equilibrium on its own. The oscillations in the z direction are larger than in the R direction.

There are two phases of the oscillation separated by π. These split the particles into two streams mirrored about z = 0. The phase of a particle is determined by it's

initial position. Those starting from R < magnetic axis, $0 \leq \phi < 5$, and R > magnetic axis, $10^{o} > \phi > 5^{o}$, move upwards first, the rest moving downwards first.

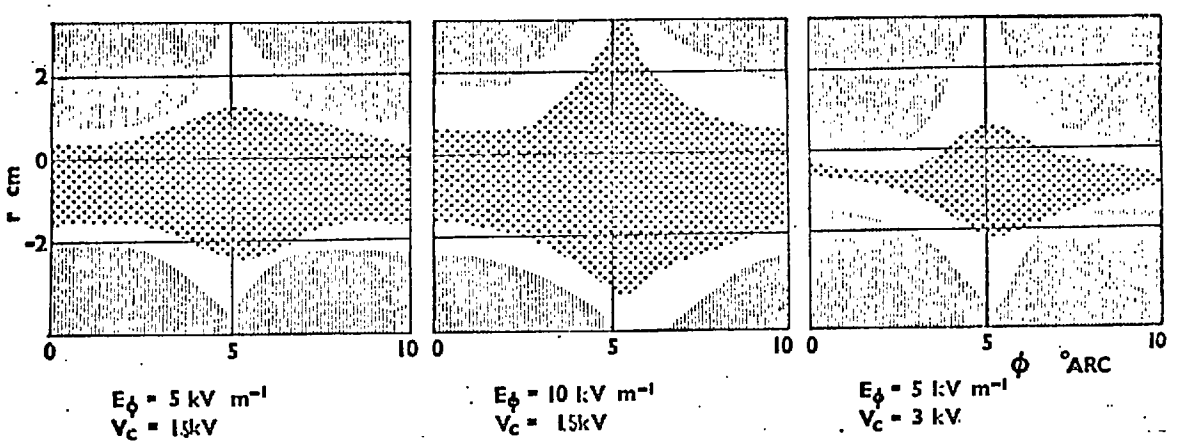

FIG. 5.8 CONTAINED AND LOST VOLUMES FOR A HYDROGEN PLASMA

contained particles

lost particles

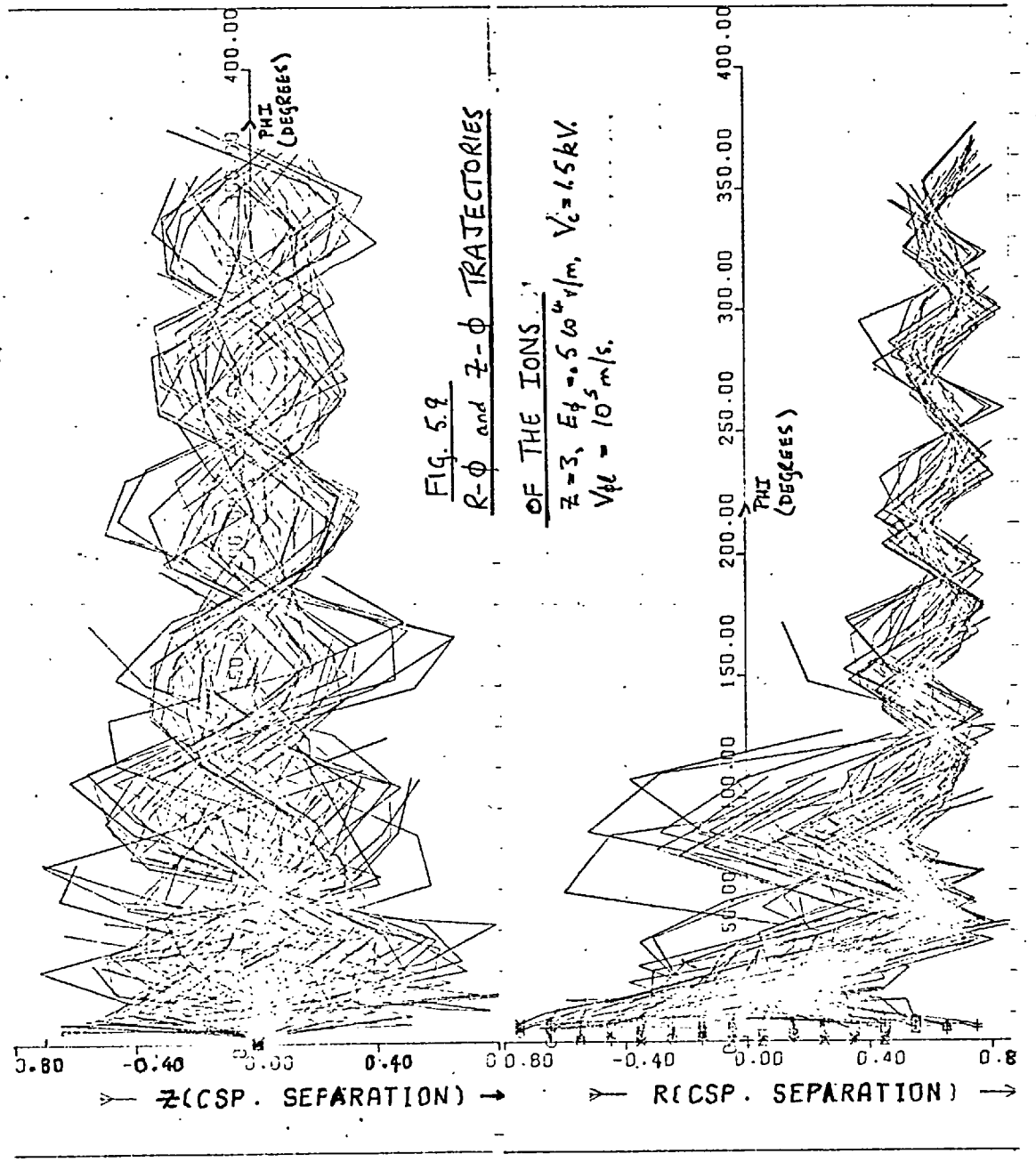

Fig. 5.9
R-φ and z-φ TRAJECTORIES OF THE IONS
z=3, $E_\phi = .5 \times 10^4$ v/m, $V_c = 1.5$ kV.
$V_{\phi l} = 10^5$ m/s.

CHAPTER SIX

SINGLE PARTICLE MOTION IN A LINEAR POLYTRON

In this chapter single particle motion in a linear polytron is investigated. In the preceeding chapter toroidal containment of the ions was considered. Little attention was paid to the initial loss.; the emphasis was on the containment against centrifugal loss. The work on the particle motion in the toroidal configuration was performed early in the project. The initial loss which is predicted was realised to be of importance in interpreting the experimental results. Hence the study of a linear system described in this chapter was initiated. A linear system is a good approximation to the experiment, which need be considered toroidal only when there is acceleration through more than 3 or 4 cusps.

By considering a linear system the description of the trajectories is simpler, a pseudo analytic approach is possible, the plasma can be realistically coupled to the driving circuits, and the magnetic fields produced by the plasma can be calculated for comparison with the experimental results.

The coordinate system used is cylindrical based on the imagined, straight minor axis of the torus.

6.1. Some properties of axisymmetric magnetic fields

An axisymmetric magnetic field can be described solely by an azimuthal vector potential A_θ. Div.$\underline{B}$ = 0 is then automatically satisfied. In a vacuum it is also required that curl $\underline{B}$ = 0

$$\therefore \nabla^2 A_\theta = 0 \qquad \text{using the Lorentzian gauge.}$$

$$\therefore A_\theta = \sum_{n=0}^{\infty} \frac{1}{k(2n+1)} B_{2n+1} I_1((2n+1)kr)\cos((2n+1)kz) \qquad (6.1)$$

with $A_\theta \to 0$ as $kr \to 0$ and imposing antisymmetry about $kz=\pi/2$, and symmetry about kz = 0 to obtain a cusp shaped field. Here B_{2n+1} are constants, k = 2π/cusp separation, and $I_1(x)$ the modified Bessel function. In the following work only the first harmonic is used. Furthermore a paraxial approximation is assumed, represented by

$$A_\theta = \frac{B_0}{k}\left(\frac{kr}{2} + \frac{1}{2}\left(\frac{kr}{2}\right)^3\right) \cdot \cos kz \qquad (6.2)$$

$$B_r = B_0\left(\frac{kr}{2} + \frac{1}{2}\left(\frac{kr}{2}\right)^3\right) \quad \sin kz \qquad (6.3)$$

$$B_z = B_0\left(1 + \left(\frac{kr}{2}\right)^2\right) \quad \cos kz \qquad (6.4)$$

$$\therefore \nabla.\underline{B} = 0 \quad \text{but} \quad \nabla_\wedge \underline{B} \leq O\left(\frac{kr}{2}\right)^3$$

In the analytic work only the first terms in eq. 6.2, 6.3, and 6.4 are used.

A useful quantity in this work is the canonical angular momentum. In a time independent magnetic field the azimuthal equation of motion is

$$\frac{1}{r}\frac{d}{dt}(rv_\theta) = \frac{Ze}{m}(+v_z B_r - v_r B_z)$$

$$= \frac{Ze}{m}\left(-v_z \frac{\partial A_\theta}{\partial z} - v_r \frac{1}{r}\frac{\partial}{\partial r}(rA_\theta)\right)$$

$$\therefore \quad rv_\theta = -\frac{Ze}{m} rA_\theta + K \qquad (6.5)$$

Ze is the charge on the particle, and K a constant of the motion. This equation allows the azimuthal velocity to be expressed as a function of the position of the particle only. K, is fixed by the initial position and velocity of a particle.

The acceleration of the particle can also be written as a function only of the coordinates, and in fact in terms of a potential. As long as $B_\theta = 0$

$$\frac{d^2r}{dt^2} = \left(r\dot{\theta}\frac{Ze}{m}B_z + r\dot{\theta}^2\right)$$

$$\frac{d^2z}{dt^2} = -\frac{Ze}{m} r\dot{\theta} B_r + \frac{Ze}{m} E_z$$

Using eq. 6.5

$$\frac{d^2r}{dt^2} = \left(\frac{K}{r} - \frac{Ze}{m} A_\theta\right)\left(\frac{Ze}{m}B_z + \dot{\theta}\right)$$

$$= \left(\frac{K}{r} - \frac{Ze}{m} A_\theta\right)\left(\frac{Ze}{m}\left(B_z - \frac{A_\theta}{r}\right) + \frac{K}{r^2}\right) \qquad (6.6)$$

and $$\frac{d^2z}{dt^2} = \frac{Ze}{m} E_z - \frac{Ze}{m} B_r\left(\frac{K}{r} - \frac{Ze}{m} A_\theta\right) \qquad (6.7)$$

If ψ is the Störmer potential defined as

$$\psi = \frac{1}{2}\left(\frac{K}{r} - \frac{Ze}{m} A_\theta\right)^2 \qquad (6.8)$$

then the equations of motion can be written in a conservative form as

$$\frac{d^2r}{dt^2} = -\frac{\partial\psi}{\partial r} \qquad (6.9)$$

and $$\frac{d^2z}{dt^2} = -\frac{\partial\psi}{\partial z} - \frac{e}{m}\frac{\partial U}{\partial z} \qquad (6.10)$$

U being the electrostatic potential, which can represent the applied electric field.

6.2 Particle motion in square field lines

The particle motion will first be examined in square field lines, represented by

$-\pi/4 < kz < \pi/4$ $\quad \underline{B}(r,\theta,z) = (0,0,B_o)$

$\pi/4 < kz < 3\pi/4$ $\quad \underline{B}(r,\theta,z) = (B_o kr/2,0,0)$

$3\pi/4 < kz < 5\pi/4$ $\quad \underline{B}(r,\theta,z) = (0,0,-B_o)$

L is the separation of the cusp coils , $L = \pi/k$, and E the applied axial field.

Suppose that $t = 0$, $r = r_o$ and $z = 0$, and the particle is at rest. The axial equation of motion is,

$$\frac{dv_z}{dt} = \frac{Ze}{m} E \qquad \text{for } 0 < kz < \pi/4$$

Therefore upon entry into the region where $B_r \neq 0$

$$r = r_o,\ v_z = \left(\frac{L}{2}\frac{ZeE}{m}\right)^{\frac{1}{2}},\ v_r = v_\theta = 0,\ z = L/4 \text{ at } t = 0$$

which defines a new time origin. The non zero equations of motion are

$$\frac{dv_\theta}{dt} = v_z \omega' \qquad \pi/4 < kz < 3\pi/4$$

$$\frac{dv_z}{dt} = -v_\theta \omega' + \frac{Ze}{m} E$$

where $\omega' = \frac{ZeB_o}{m} \cdot \frac{kr}{2}$

$$\therefore \quad v_z = \frac{ZeE}{m\omega'} \sin \omega' t + \left(\frac{L}{2}\frac{ZeE}{m}\right)^{\frac{1}{2}} \cos \omega' t$$

and $$v_\theta = \frac{ZeE}{m\omega'} (1 - \cos \omega' t) + \left(\frac{L}{2}\frac{ZeE}{m}\right)^{\frac{1}{2}} \sin \omega' t$$

To pass through this region into the region $z > 3L/4$ it is necessary that

$$\frac{ZeE}{m\omega'^2} + \frac{1}{\omega'}\left(\left(\frac{ZeE}{m\omega'}\right)^2 + \frac{LZeE}{2m}\right)^{\frac{1}{2}} > \frac{L}{2} \qquad (6.11)$$

(This is approximately the criterion that a Larmor radius is larger than L/2). Notice that in passing through the ring cusp region there is no radial motion. Radial motion only occurs if eq. 6.11 is satisfied and the particle reaches the region $z > 3L/4$. In this case the radial motion is inwards.

6.3 An approximate integration of particle motion in a cusp field

Here the single particle motion in a linear system is integrated analytically, making leading order expansions of the field about $z = 0$, and $z = L/2$, to make the equations tractable. A criterion for acceleration into the next cusp, and an expression for the maximum radial excursion, are derived.

The constancy of the canonical angular momentum is

$$rA_\theta + \frac{mv_\theta}{Ze}r = K = (rA_\theta)_o = \frac{B_o}{2} r_o^2 \cos kz_o = \frac{B_o}{2} r_o^2 \qquad (6.12)$$

if the particle starts, at rest, at $z = z_o = 0$, $r = r_o$. The vacuum field is the first order terms of the cylindrical Bessel function.

$$\therefore \quad v_\theta = \frac{ZeB_o}{2m\,r}\,(r_o^2 - r^2 \cos kz) \qquad (6.13)$$

Simplification occurs if k and $\omega = \frac{Ze}{m} B_o$ are used to make the equations dimensionless. The dimensionless variables are written with the same notation as the dimensional variables, and are simply the dimensional variables multiplied by the appropriate combination of k and ω. Adopting these variables the equations of motion become

$$v_\theta = \frac{1}{2r}\,(r_o^2 - r^2 \cos z) \qquad (6.14)$$

$$\frac{dv_r}{dt} = v_\theta \cos z \qquad (6.15)$$

$$\frac{dv_z}{dt} = \frac{kZeE}{m\omega^2} - \frac{rv_\theta}{2} \sin z$$

$$= \beta - \frac{rv_\theta}{2} \sin z \qquad (6.16)$$

where the small effect of the centrifugal term in eq. 6.15 has been neglected.

The trajectory in the neighbourhood of the starting point will be examined first. As $\sin z \approx z \ll 1$, an approximate solution to eq. 6.16 is

$$v_z = \beta t \;;\; z = \beta t^2/2 \qquad (6.17)$$

The radial motion near to z = 0 will be small and so $r = r_o + s$ where $s \ll r_o$. Together with the Taylor approximation for cos z, the expression for v_θ simplifies to

$$v_\theta = \frac{1}{2}\,\left(\frac{r_o z^2}{2} - 2s\right) \qquad (6.18)$$

$$\therefore \quad \frac{dv_r}{dt} = \ddot{s} = \frac{1}{2}\left(\frac{r_o z^2}{2} - 2s\right)\cos z \approx \frac{r_o \beta^2 t^4}{16} - s \qquad (6.19)$$

Suppose the second term of the r.h.s. of eq. 6.19 can be neglected

then $s = \frac{r_o \beta^2 t^6}{16 \times 30}$, and $\dot{s} = \frac{r_o \beta^2 t^5}{16 \times 5}$ (6.20)

showing that the second term on the r.h.s. of eq. 6.19 can be neglected provided $t^2 << 30$.

Suppose the approximate equations, 6.17, 6.18 and 6.20 are valid to $z = \frac{\pi}{4}$, $t^2 = \frac{\pi}{2\beta}$

Then $s = \frac{r_o \quad \pi^3}{16 \times 30 \times 8\beta}$, $\dot{s} = v_r = \frac{r_o \quad \pi^{2.5}}{16 \times 5 \times 4\sqrt{2\beta}}$

$v_z = \sqrt{\frac{\beta\pi}{2}}$ at $z = \frac{\pi}{4}$ (6.21)

This value of s is much less than 1 (and thus r_o) if β is approximately 1. A further check on the consistency of the approximation is that the second term of eq. 6.16, at $z = \pi/4$ has the value $r_o^2 \pi^3/256$ which is much less than β if $10\beta > r_o^2$.

Now consider the trajectory in the region of the ring cusp. The values of velocity at the new t = 0 are given by eq. 6.21, the time variable being shifted so that t = 0 when $z = \pi/4$. The axial variable is transformed to y, where $y = \pi/2 - z$. The magnetic fields are approximated in this region by

$$B_z = B_o\, y, \quad B_r = \frac{r}{2}\left(1 - \frac{y^2}{2}\right)$$

$$\therefore \quad v_\theta = \frac{1}{2r}\left(r_o^2 - r^2 y\right) \qquad (6.22)$$

The radial and axial equations of motion are

$$\frac{dv_r}{dt} = v_\theta y = \frac{(r_o^2 - r^2 y)}{2r} y \qquad (6.23)$$

$$\text{and } -\ddot{y} = +\frac{dv_z}{dt} = \beta - v_\theta \frac{r}{2}(1-\frac{y^2}{2}) = \beta - \frac{(r_o^2 - r^2 y)(1-y^2/2)}{4} \qquad (6.24)$$

As long as $r \approx r_o$ then $r_o^2 \gg r^2 y$ and eq. 6.24 becomes

$$\ddot{y} = -\beta + \frac{r_o^2}{4} = -\beta^1 \text{ where } \beta^1 = \beta - \frac{r_o^2}{4}$$

$$\therefore \quad y = -\beta^1 t^2/2 \sqrt{\frac{\pi\beta}{2}}\, t + \pi/4 \qquad (6.25)$$

If β^1 becomes too negative then eq. 6.25 will not have a solution at $y = -\pi/4$. For there to be a solution of eq. 6.25. at $y = -\frac{\pi}{4}$ and real t

$$\beta > \frac{r_o^2}{6} \qquad (6.26)$$

Furthermore if there is a solution at $y = -\frac{\pi}{4}$, $z = 3\frac{\pi}{4}$ then it is probable that a solution exists for z up to $\frac{3\pi}{2}$. This is because the acceleration in the region under the coil will change from a negative β^1 to a positive β. Eq. 6.25 can now be substituted into eq. 6.23. The radial acceleration changes from outwards to inwards as soon as the plane of the ring cusp is passed. Of more interest is the point at which the radial velocity changes sign. To find this time, integrate eq. 6.23 , using eq. 6.25. The approximation

$$r_o = \frac{(r_o^2 - r^2 y)}{r}$$

is made and the boundary condition, eq. 6.21 used. The time at which the largest excursion occurs is given when $v_r = 0$ as

$$0 = \frac{r_o}{2}\left(-\frac{\beta' t^3}{6} - \frac{t^2}{2}\sqrt{\frac{\pi\beta}{2}} + \frac{\pi t}{4}\right) + \frac{r_o \pi^{2.5}}{320\sqrt{2\beta}} \qquad (6.27)$$

The quadratic and linear terms are dominant. This first solution obtained by neglecting the cubic and constant term is

$$t = \frac{1}{2}\sqrt{\frac{2\pi}{\beta}} \qquad (6.28)$$

The values of the 4 terms, divided by r_o, at this value of t are:

$$-\frac{\beta' t^3}{12} = -\frac{\beta'}{\beta}\frac{\pi}{48}\sqrt{\frac{2\pi}{\beta}} \quad : \quad \frac{t^2}{4}\sqrt{\frac{\pi\beta}{4}} = -\frac{\pi}{16}\sqrt{\frac{2\pi}{\beta}}$$

$$\frac{\pi t}{8} = \frac{\pi}{16}\sqrt{\frac{2\pi}{\beta}} \quad : \quad \frac{\pi^2}{320}\sqrt{\frac{\pi}{2\beta}} = \frac{\pi}{204}\sqrt{\frac{2\pi}{\beta}}$$

From eq. 6.26 and eq. 6.25 $-\frac{1}{2} < \frac{\beta'}{\beta} < 1$. Hence, fortunately eq. 6.28 is a good solution to eq. 6.27 to next order. As well as being 6 times smaller than the linear and quadratic terms, the cubic and constant terms will normally cancel. The second integral of eq. 6.23 is

$$r = r_o\left(-\frac{\beta' t^4}{48} - \frac{t^3}{12}\sqrt{\frac{\pi\beta}{2}} + \frac{\pi t^2}{16} + \frac{\pi^2}{320}\sqrt{\frac{\pi}{2\beta}}\, t + 1\right)$$

Then the value of r at $t = \frac{1}{2}\sqrt{\frac{2\pi}{\beta}}$, when r is a maximum, is

$$r = r_o\left(1 + \frac{\pi^2}{16\beta}\left(\frac{\pi}{40} + \frac{1}{2} - \frac{1}{3} - \frac{\beta'}{12\beta}\right)\right)$$

$$\therefore \quad r_{max} = r_o\left(1 + \frac{1}{\beta}\left(.16 - .05\frac{\beta'}{\beta}\right)\right) \qquad (6.29)$$

The axial position at this time is given by eq. 6.25 as

$$y = -\frac{\pi}{4}\left(1 + \frac{\beta'}{\beta}^{-1}\right) \qquad (6.30)$$

Hence the value of r_{max} given by eq. 6.29 is only true when

$$\beta^1 < 0$$

However, the time to reach $r = r_{max}$ as given by eq. 6.28 is too long. As the particle moves into the region beneath the coil both v_θ and B_z increase , and so the force causing acceleration back towards the axis is larger than used in deriving eq. 6.28. Hence when $\beta^1 << \beta$ eq. 6.30 gives too small a value of y, i.e. the maximum value of r occurs before the plane of the coil is reached.

The consistency of the approximate solution can be checked, e.g. in this region it was assumed that $\frac{1}{r}(r_o^2 - r^2 y) = r_o$

When $y = -\frac{\pi}{4}$, $\beta = .2$ the value of $\frac{(r_o^2 - r^2 y)}{r}$ is 1.3 at $r = r_{max}$. This approximation in the axial equation of motion, eq. 6.24, is not so good. Here, $r_o^2 - r^2 y \approx 2r_o^2 \cdot \beta^1$ is modified to $\beta - \frac{r_o^2}{2}$ and so the condition for acceleration through the cusp is modified to

$$\beta > \frac{r_o^2}{4} \qquad (6.31)$$

Fortunately r_{max} does not depend strongly on β^1. Equation 6.30 is only valid for $\beta^1 < 0$ i.e. $2\beta < r_o^2$.

It is usual that β is fixed and the properties of the trajectories examined as r_o is varied. Thus:

(1) For $r_o > 2\sqrt{\beta}$ particles are trapped in the first cusp.

(2) For $\sqrt{2\beta} < r_o < \sqrt{4\beta}$, the particles are accelerated into the next cusp. The axial position of the maximum of

r varies from $z = \frac{\pi}{2}$ to $3\pi/4$ as r_o decreases from $\sqrt{4\beta}$ to $\sqrt{2\beta}$. The value of the maximum radius is approximately $r_o(1 + .2/\beta)$.

(3) For $r_o < \sqrt{2\beta}$ the axial position of maximum r goes past $3\pi/4$ and approaches the plane of the coil. The value of the maximum radius is given approximately by

$$r_{max} = r_o \left(1 + .\frac{15}{\beta}\right)$$

This modulation of the radial position is considerably more than that experienced by equilibrium particles. If eq. 7.44 is rewritten with $v_z^2 = \frac{2eEL}{m}$ then the modulation of the radial position is $.04/\beta$.

Typical values of β for the cusp separation used in the experiment are shown below.

β	E(V/m)	B(T)	Species
.7	10^4	.1	hydrogen
.17	10^4	.2	hydrogen
38.	10^4	.1	argon, z = 1
9.	10^4	.2	argon, z = 1
3.	10^4	.2	argon, z = 3
$3.5\ 10^{-4}$	10^4	.1	electron

6.4 Comment on the shape of field lines

In any cusp shaped field the motion of particles is complex. Suppose that a particle starts from rest at $r = r_o$, $z = z_o$ and does not move far radially.

Then $$A_\theta (r_o, z) = - \int_{z_o}^{z} B_r \, dz$$

$$\therefore \quad v_\theta (r_o, z) = \frac{Ze}{m} \int_{z_o}^{z} B_r \, dz$$

$$\therefore \quad \frac{d^2 r}{dt^2} = \frac{Z^2 e^2}{m^2} \, B_z \int_{z_o}^{z} B_r \, dz$$

and $$v_r(r_o, z) = \frac{Z^2 e^2}{m^2} \left(\frac{m}{2eZE}\right)^{\frac{1}{2}} \int_{z_o}^{z} \frac{B_z}{(z - z_o)^{\frac{1}{2}}} \int_{z_o}^{z} B_r \, dz \, dz$$

From this equation it can be seen that a square type of field line will not give rise to a large radial velocity because the product $B_r \, B_z$ is small. This is only evident from the above equation for particles which start in a region where B_r is small. The extreme case of square field lines was investigated in section 6.2. where it was shown that there is no radial motion in this case.

It is thought that the lower the value of $\int B_r \, B_z \, dz$ then the lower is the maximum excursion of a particle from the axis.

6.5 Application of energy principles to find accessible regions of the cusp field

The particle in the linear cusp system moves such that

$$rA_\theta + \frac{mrv_\theta}{Ze} = \text{constant} = K$$

where the magnetic vector potential $A_\theta = \frac{B_o}{k}\left(\frac{kr}{2}\right) \cos kz$.

Suppose the particle starts from rest at $r = r_o$, $z = z_o$ then

$$rA_\theta + \frac{mrv_\theta}{Ze} = \frac{B_o}{k}\frac{kr_o^2}{2} \cos kz_o = K$$

$$\therefore \quad \frac{2mr}{Ze} v_\theta = B_o (r_o^2 \cos kz_o - r^2 \cos kz) \qquad (6.32)$$

In a linear geometry, and even in a toroidal geometry, the accelerating field can be represented as conservative and so

$$v_r^2 + v_z^2 + v_\theta^2 = \frac{2ZeE}{m}(z - z_o) \qquad (6.33)$$

where E is the accelerating electric field which is constant in time and space. Substituting eq. 6.32 into eq. 6.33 gives

$$\left| r^2 \cos kz - r_o^2 \cos kz_o \right| \leq \left| \frac{r}{B_o} \left(\frac{8mE}{Ze}(z - z_o)\right)^{\frac{1}{2}} \right| \qquad (6.34)$$

where the positive square root is taken. This equation can be cast into a dimensionless form with

$$z^* = kz$$

$$r^* = kr$$

$$\alpha = \left(\frac{Ze}{8mEk}\right)^{\frac{1}{2}} B_o \quad \text{the equation becoming}$$

$$\left| r^{*2} \cos z^* - r_o^{*2} \cos z_o^* \right| \leq \left| \frac{r^* (z^* - z_o^*)^{\frac{1}{2}}}{\alpha} \right| \qquad (6.35)$$

The relation with β of section 6.3 is

$$\alpha = \frac{1}{2\sqrt{2\beta}}$$

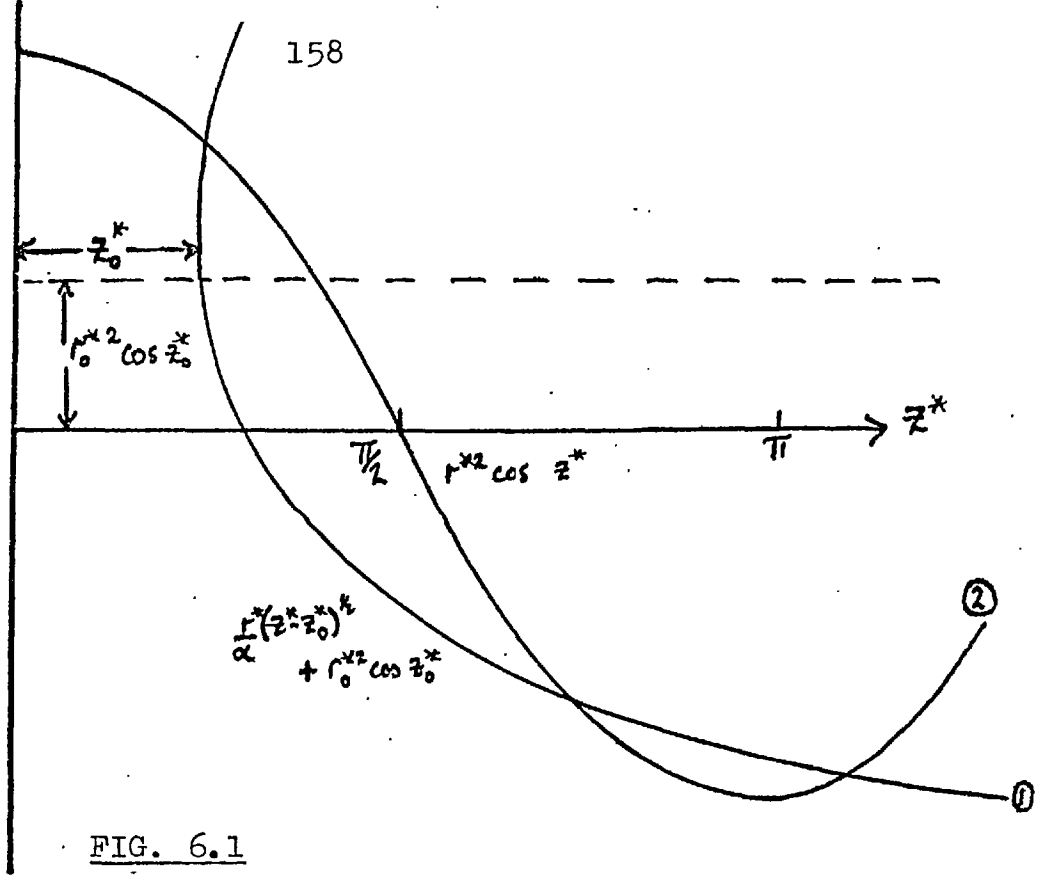

FIG. 6.1

GRAPHIC ILLUSTRATION OF INEQUALITY 6.35.

This inequality is graphically illustrated in fig. 6.1. Curve 2 must lie within curve 1. For example, for the value of r^* shown in fig. 6.1, particles cannot enter the region $\frac{3\pi}{4} \leq z \leq 1.1\pi$. When $\frac{\pi}{2} < z^* < \pi$ eq. 6.35 cannot be satisfied for $r^* << r_o^*$, nor can it be satisifed for $r^* >> r_o^*$, because then the r^{*2} cos kz term will be larger than $r^*(z^* - z_o^*)^{\frac{1}{2}}/\alpha$.

Eq. 6.35 defines a domain within which the particle must stay. There are certain noticeable features of this inequality:-

(1) It cannot be satisfied for $z^* < z_o^*$, as the r.h.s. then becomes imaginary.

(2) The limit of the region is given by the equality

$$r^{*2}\cos z^{*} - r_o^{*2}\cos z_o^{*2} = \frac{r^{*}}{\alpha}(z^{*} - z_o^{*})^{\frac{1}{2}} \qquad (6.36)$$

$$\therefore \quad \frac{dr^{*}}{dz^{*}}\left(2r^{*}\cos z^{*} - \frac{(z^{*} - z_o^{*})^{\frac{1}{2}}}{\alpha}\right) = r^{*2}\sin z^{*} + \frac{r^{*}}{2\alpha(z^{*} - z_o^{*})^{\frac{1}{2}}}$$

and so where $z_o^{*} = z^{*}$, $\frac{dr^{*}}{dz^{*}} = \infty$

(3) At $z^{*} = \pi/2$ eq. 6.35 gives

$$\frac{r^{*}}{\alpha}\left(\frac{\pi}{2} - z_o^{*}\right)^{\frac{1}{2}} \geq r_o^{*2}\cos z_o^{*}$$

$$\therefore \quad r^{*} \geq \frac{\alpha r_o^{*2}\cos z_o^{*}}{\left(\frac{\pi}{2} - z_o^{*}\right)} \qquad (6.37)$$

The outer radius of the allowed region when $z^{*} = \pi/2$ is at $r = \infty$. Inequality 6.37 can always be satisfied, but not necessarily within the tube radius.

(4) At $z^{*} = \pi$

$$r^{*2} < \frac{r^{*}}{\alpha}(\pi - z_o^{*})^{\frac{1}{2}} - r_o^{*2}\cos z_o^{*} \qquad (6.38a)$$

When the inequality is replaced by an equality the two roots of the equation define the inner and outer radii of the allowed region. For these roots to be real

$$\frac{(\pi - z_o^{*})}{\alpha^{2}} > 4\, r_o^{*2}\cos z_o^{*} \qquad (6.38)$$

If α is too large eq. 6.38 cannot be satisfied. In this case the allowed region does not extend to $z^{*} = \pi$. Even if eq. (6.38) is satisfied then it is not necessary that the allowed region should extend to $z^{*} = \pi$, as 6.35 may not be satisfied at some axial position $z < \pi$, such as illustrated in fig. 6.1.

(5) The allowed region is not always singly connected.

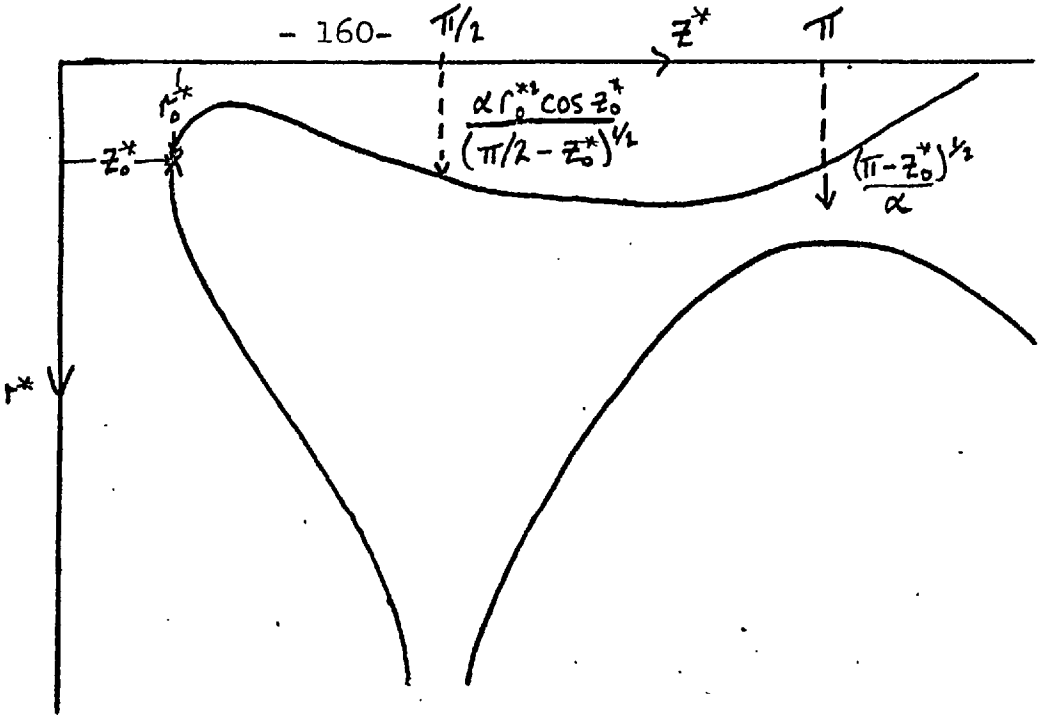

FIG. 6.2 SCHEMATIC OF THE ALLOWED REGION IN THE r^*- z^*PLANE

For $z^* = (2n+1)\frac{\pi}{2}$, 6.35 can always be satisfied, yet as shown there could be some values of z^* for which an allowed region does not exist.

These points are illustrated in fig. 6.2. The criterion for the allowed region to extend from cusp to cusp will now be examined. As can be seen from fig. 6.1, if the allowed region is cut off in one cusp only then, this will be near to $z^* = \pi$. So let $t = \pi - z$ and $t << \pi$.

Substitution into eq. 6.35 gives

$$r^{*2}(1-t^2/2) + r_o^{*2} \cos z_o^* \leq \frac{r^*}{\alpha} (\pi - t - z_o)^{\frac{1}{2}}$$

$$\approx \frac{r^*}{\alpha} (\pi - z_o^*)^{\frac{1}{2}} \left(1 - \frac{t}{(\pi - z_o)2}\right)$$

Taking the equality gives the equation of the edge of the region

$$r^{*2}(1 - t^2/2) - r^*\left(\frac{\pi - z_o^*}{\alpha}\right)^{\frac{1}{2}}\left(1 - \frac{t}{(\pi - z_o^*)2}\right) + r_o^{*2}\cos z_o^* = 0 \qquad (6.39)$$

This equation specifies the values of t at which the allowed region closes in the z^* direction. In general there are two values. The point of interest is when there is only one solution of eq. 6.39 for t. At this point the allowed region is just necking into two parts. For only one solution in r^* of eq. 6.39

$$2r_o^{*2}\cos z_o^*\ t^2 - \frac{t}{\alpha^2} + \frac{\pi - z_o^*}{\alpha^2} - 4r_o^{*2}\cos z_o^* = 0 \qquad (6.39a)$$

$$\therefore \quad 32\, r_o^{*4}\cos^2 z_o^*\ \alpha^4 - 8r_o^{*2}(\pi - z_o^*)\cos z_o^*\ \alpha^2 + 1 = 0$$

for only one solution in t, of eq. 6.39 a

$$\therefore \quad \alpha^2 = \frac{(\pi - z_o^*) \pm \sqrt{(\pi - z_o^*)^2 - 2}}{8r_o^{*2}\cos z_o^*} \qquad (6.40)$$

The solution is

$$t = \frac{1}{4\alpha^2 r_o^* \cos z_o^*}$$

There should only be one solution for α^2. This can be seen from inspection of fig. 6.1. Consider starting from a large value of α, when curve 1 is near to $r_o^{*2}\cos z_o^*$. As α is decreased, the distance from curve 1 to $r_o^{*2}\cos z_o^*$ monotonically increases, whereas curve 2 stays fixed. There will be only one value of α for which curves 1 and 2 make tangential contact near to $z^* = \pi$. This correspond to the positive sign of eq. 6.40. The value of α corresponding to the other sign is a result of the $\cos x = 1 - x^2/2$

approximation

$$\therefore \quad \alpha^2 < \frac{(\pi - z_o^*) + \sqrt{(\pi - z_o^*)^2 - 2}}{8 r_o^{*2} \cos z_o^*} \qquad (6.40a)$$

for the $r^* - z^*$ plane to be singly connected.

This equation is only a small modification to eq. 6.38. Typically $z_o^* = 0$ in which case eq. 6.38 and eq. 6.40a differ by only 5%.

As eq. 6.38 adequately describes the condition on α for the region to be singly connected, eq. 6.38 will be examined. The relation is plotted in fig. 6.3 as a curve of r_o, z_o for a fixed α, showing where accelerated particles originate. The characteristic cusp shape seen in the

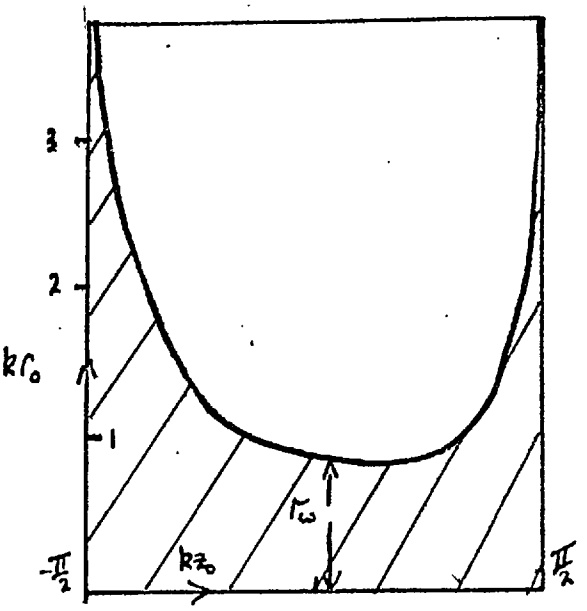

FIG. 6.3

THE ACCELERATED VOLUME

FOR $\alpha = 1$

TAKEN FROM EQ. 6.38

computations, e.g. fig. 5.8, is evident. The cut off at $z^* = \pm \frac{\pi}{2}$ is at the tube radius. The waist of this volume is approximately

$$r_w = \frac{\pi^{\frac{1}{2}}}{B_o} \left(\frac{2mE}{Zek}\right)^{\frac{1}{2}} \qquad (6.41)$$

Particles staring within this volume can be accelerated. In passing through to the next cusp the particles which start at the radius given by the equality 6.38 which for $z_o^* = 0$ is

$$r_w^* = \frac{\pi^{\frac{1}{2}}}{2\alpha}$$

must make excursions outwards to a radius.

$$r^* \leq \frac{\pi^{\frac{1}{2}}}{\alpha} = 2r_w^*$$

to pass through the neck of the allowable region. The value of z where the radial excursion of the particles is largest is $\frac{L}{4\pi\alpha^2}$ before the coil at $z^* = \pi$ (L is the cusp separation), provided α is not too small.

6.6 Comparison of integrated trajectories with the volume limited by the particle's potential

In section 6.5 it was shown that for the accessible particle volume to extend into the next cusp, that

$$4r_o^{*2} \cos z_o^* < \frac{(\pi - z_o^*)}{\alpha^2}$$

Transformed into the variable used in the analytic particle integration this becomes

$$r_o^* < \sqrt{2\pi\beta} \qquad (6.42)$$

for $z_o^* = 0$. This compares well with the comparable result

of section 6.3

$$r_o^* < \sqrt{4\beta} \,. \qquad (6.43)$$

The radius derived analytically(eq. 6.43)is expected to be smaller than by use of the potential. The result, from considering the potential gives the radius outside of which particles certainly cannot get into the next cusp. This is larger than the radius from which particle will move through into the next cusp; but as seen from eq. 6.42 and eq. 6.43 it is only 25% larger.

6.7 A computional model of the linear polytron

This section describes a linear model of the polytron. The reason for this model, in view of chapter 5, is to increase the realism of the simulation. The principle points are to couple the 'plasma' to the driving circuit, and to evaluate the plasma magnetic field , but not in a self consistent way. The effect of the space charge field is neglected, but is included in the subsequent chapter.

The particle integration. This is performed with the equations in the form of eqs. 6.6 and 6.7. This way integration of the $\underline{e}$ · equation is performed analytically. Far more important however, is that this scheme avoids a computational instability in the leapfrog integration process. If the motion in the magnetic field were solved according to

$$\frac{d\underline{v}}{dt} = \underline{v}_x \underline{B} \quad \text{by} \quad v_i^{n+1} - v_i^{n-1} = 2\,dt\,\epsilon_{ijk}\,v_j^n\,B_k$$

a computional instability arises as the odd time levels (the superscripts denote time levels, subscripts components) are effectively decoupled from the even time levels. Effectively two sets of equations

$$\frac{d\underline{v}^{n+1}}{dt} = \underline{v}_x^n \underline{B}, \quad \frac{d\underline{v}^n}{dt} = \underline{v}_x^{n-1} \underline{B}$$

are being solved and as well as the correct <u>in phase</u> solution of these equations an erroneous <u>out of phase</u> solution grows.

This is avoided by using eqs. 6.6 and 6.7, and then the r.h.s. is a function of coordinate only. A leapfrog scheme can successfully be used, velocities being defined at odd times and positions at even times. Integration errors are of order $(dt)^3$ and only 1 time level needs to be stored. Explicitly, the algorithm is

$$r^n = r^{n-2} + 2dt\,v_r^{n-1} \tag{6.44}$$

$$z^n = z^{n-2} + 2dt\,v_z^{n-1} \tag{6.45}$$

$$v_r^{n+1} = v_r^{n-1} + 2dt\left(\frac{K}{r^n} - \frac{Ze}{m} A_\theta^n\left(\frac{Ze}{m}(B_z^n - A_\theta^n) + \frac{K}{(r^n)^2}\right)\right) \tag{6.46}$$

$$v_z^{n+1} = v_z^{n-1} + 2dt\left(\frac{ZeE_z^{n-2}}{m} - \frac{Ze}{m} B_r^n\left(\frac{K}{r^n} - \frac{Ze}{m} A_\theta^n\right)\right) \tag{6.47}$$

where $B^n = B(r^n, z^n)$. A_θ, B_r and B_z are the vacuum values of the field, given by equations 6.2, 6.3 and 6.4. The retarded

value of E_z has to be used but fortunately E_z is not strongly time dependent. Care is taken in coding to reduce the number of multiplications necessary but the basic system of units is left as r.m.k.s. The philosophy here is that the ease of checking errors if the units are left in r.m.k.s. far outweighs the small gain in processing obtained by making the equations dimensionless.

If $E_z = 0$, any change of energy from equations 6.46 and 6.47 must be due to errors in differencing the differential equations. In terms of the Störmer potential of equation 6.8 the gain in energy given by eq. 6.46 and 6.47 is

$$(K.E.^{n+1} - K.E.^{n-1}) = -2 \frac{\partial \psi^n}{\partial t} dt - \frac{1}{2} dt^3 \left(\frac{d^2 v_r^n}{dt^2} \frac{\partial \psi^n}{\partial r} + \frac{d^2 v_z^n}{dt^2} \frac{\partial \psi^n}{\partial z}\right)$$

showing that the errors are of order dt^3.

Representing a plasma. The trajectories of 5000 ions are integrated as above. Each particle, really an annulus, has the correct Ze/m ratio for the species being considered, but is credited with a much larger charge. Initially the region $0 < kz < \pi$ is filled with these particles. As time progresses the particles move out of this region. To obtain macroscopic quantities in the original domain, the coordinates of any particle outside of $0 < kz < \pi$ are reduced to within this domain, by use of symmetry.

Suppose that at time t the position of a particle

is r, z , then for the purpose of evaluating macroscopic quantities only a reduced position is evaluated given by

$$z^* = z - nL, \quad r^* = r \tag{6.48}$$

where n is the integer so that $0 < z^* < L$. A particle which starts with $0 < z < L$ and reaches the region $nL < z < (n+1)L$ has a twin particle which starts with $-nL < z < -(n-1)L$ and reaches $0 < z < L$, the reduced coordinates being equal. However, the equations are antisymmetric to axial displacements of L and so the velocities have reduced values given by

$$v_r^* = v_r, \quad v_\theta^* = (-1)^n v_\theta, \quad v_z^* = v_z \tag{6.49}$$

Every particle carries the same charge Q. To represent a density which is independent of radius, the area density of particles in the r direction is proportional to the radius. Macroscopic quantities are represented on a mesh, the nearest grid point approximation being used. If a is the size of the mesh then the macroscopic quantities which are evaluated are:-

the number density

$$NDEN(I,J) = \frac{1}{(J-\frac{1}{2})} \sum \delta(INT(r^*/a)+1), J)\,\delta((INT(z^*/a)+1), I)$$

and the azimuthal ion current

$$ITHETA(I,J) = \frac{Q}{2\pi r} \sum v_\theta^* \,\delta(INT(r^*/a)+1, J)\,\delta(INT(z^*/a)+1, I)$$

The indices I and J label the axial and radial cells respectively and INT is the function which truncates

the argument to an integer. The summation is over all of the particles. When ions hit the wall of the tube they are lost to the calculation.

The motion of the electron fluid. In this approximation the motion of the electrons is given simply by their guiding centre drift. As shown in chapter 7 this is an azimuthal motion and as such the density in the r - z plane is unaffected. The electron number density is assumed equal to that of the ions and the azimuthal velocity of the electrons at a mesh point is given by

$$\underline{v}_{gc} = \underline{E} \times \underline{B} / |B|^2 + \frac{m v_{\parallel}^2}{e B^4} \underline{B}_{\wedge} (\underline{B}.\nabla)\underline{B} + \frac{m v_{\perp}^2}{2eB} \frac{\underline{B}_{\wedge} \nabla B}{B^2} \qquad (6.50)$$

where $\parallel$ and $\perp$ refer to the magnetic field. To help evaluate this vector expression the quantities

$$W1 = \frac{kB_o^2}{2}\left(\left(\frac{kr}{2} + \frac{1}{2}\left(\frac{kr}{2}\right)^3 \right)\left(1 + \frac{3}{2}\left(\frac{kr}{2}\right)^2\right) \sin^2 kz + kr\left(1 + \left(\frac{kr}{2}\right)^2\right)\cos^2 kz \right)$$

$$W2 = kB_o^2 \sin kz \cos kz \left(\left(\frac{kr}{2} + \frac{1}{2}\left(\frac{kr}{2}\right)^3\right) - \left(1 + \left(\frac{kr}{2}\right)^2\right)^2 \right)$$

are evaluated. The electrons' drift is then explicitly evaluated as

$$\underline{v}_{gc} = \hat{\underline{\theta}}\left(\frac{E_z B_r}{|B|^2} + \frac{m}{eB^4}\left((v_{\parallel}^2 + v_{\perp}^2/2)(B_z W1 - B_r W2) + v_{\parallel}^2 \frac{kB_o}{2}\left(\frac{kr}{2}\right)^2 \cos kz\, B^2 \right)\right) \qquad (6.51)$$

v_{11} and $v_{\perp}$ are evaluated from a scalar electron temperature. The curvature drift in the above expression is anti symmetric about the ring cusp, whereas E/B is symmetric. Only the sign of v_{gc} changes for axial displacement of $(2n+1)L$.

The azimuthal current density is then evaluated as

$$JTHETA(I,J) = ITHETA(I,J) - \frac{Qv_{gc}}{2\pi a} NDEN(I,J)$$

The magnetic fields produced by the currents. The primary quantity to be evaluated is the axial current. This is necessary for both the calculation of the axial electric field and for comparison with the experimental results. Only an ion current is allowed, and the value of this is

$$I_z = \frac{Q}{L} \sum v_z^* \qquad (6.52)$$

By evaluating a z average, difficulties which would arise from a z dependent I_z are avoided. In practice local axial electron currents(i.e. not crossing the ring cusp) will flow so that $\nabla.j = 0$.

The azimuthal current density is used to calculate the magnetic field produced by the Hall currents. As $\nabla.b = 0$ (where $\underline{b}$ is the field produced by the plasma currents) it is best to evaluate A_θ, the magnetic vector potential of the Hall currents.

The elliptic equation for A_θ is

$$\frac{\partial^2 A_\theta}{\partial r^2} + \frac{1}{r}\frac{\partial A_\theta}{\partial r} - \frac{A_\theta}{r^2} + \frac{\partial^2 A_\theta}{\partial z^2} = -\mu_0 j_\theta \qquad (6.53)$$

A five point difference scheme is used to solve this iteratively using an over relaxation method. The z boundary condition is antisymmetric, the boundary condition on the

axis is $A_\theta = 0$, (b_z allowed but not b_r), and on the outer radius $A_\theta \to 0$ as $r \to \infty$. As $A_\theta \propto 1/r$ when the plasma currents look like dipoles it was sufficient to solve for A_θ only in a region up to twice the radius of the tube, and to use $A_\theta = 0$ as the boundary condition at the edge of this region. A coarse mesh of side 4mm is used. By doing so the singularity of eq. 6.53 at the null point is avoided. Physically this is also correct as at about this radius the guiding centre approximation breaks down because of finite Larmor radius and small $\omega\tau$.

The magnetic fields produced by this A_θ is simply calculated by

$$b_r = -\frac{\partial A_\theta}{\partial z} \quad : \quad b_z = \frac{A_\theta}{r} + \frac{\partial A_\theta}{\partial r} \qquad (6.54)$$

Coupling the plasma to the primary circuit: In the experiment there is an intimate coupling between the plasma and the primary circuits. The ratios of current in the induction rods of the primary circuit as well as the total current flowing in the primary circuit is affected by the plasma. However the system can be represented as lumped inductances and mutuals, by the equations

$$E_z = -M \frac{di}{dt} - L_\ell \frac{dI}{dt} \qquad (6.55)$$

$$L_p \frac{d^2 i}{dt^2} + M \frac{d^2 I}{dt^2} + R_o \frac{di}{dt} + \frac{i}{C} = 0 \qquad (6.56)$$

where i is the current in the primary circuit

I is the current carried by the plasma

M is the mutual inductance between the plasma and primary circuits

L_p is the primary inductance

L_ℓ is the geometric inductance of the plasma

C is the main bank capacitance

and R_o is the resistance in the primary circuit

A straight-forward differencing of these equations using time derivatives at the last time level is unstable. The particle integration initially satisifes

$$L_H \frac{dI}{dt} = E_z \qquad (6.57)$$

where L_H is the Hall inductance (see chapter 11), and so using the time derivatives at the last time level the difference equation would be equivalent to

$$L_H \frac{dI}{dt} = -M\frac{di}{dt} - L_\ell \frac{dI}{dt} + dt\,(L_\ell \frac{d^2I}{dt^2} + M\frac{d^2i}{dt^2})$$

which is unstable to high frequency modes. For the magnitudes of L_H, L_ℓ, and M needed this is grossly unstable. To decrease the instability of the scheme an average value of E_z^n is used in eq. 6.47.

$$E_z^{n*} = (E_z^n + 2E_z^{n-1} + E_z^{n-4})/4 \qquad (6.58)$$

where $E_z^n = -\frac{M}{2dt}(i^{n+1} - i^{n-1}) - \frac{L_\ell}{2dt}(I^{n+1} - I^{n-1})$ (6.59)

and for the primary circuit

$$\frac{di}{dt}^{n+1} = \frac{di}{dt}^{n-1} + \frac{2dt}{L_p}\left(-M\,\frac{d^2I}{dt^2}^{n-3} - R\,\frac{di}{dt}^{n-1} - \frac{i}{c}^{n-1}\right) \quad (6.60)$$

$$i^{n+1} = i^{n-3} + dt\,\frac{di}{dt}^{n-1} \quad (6.61)$$

The initialisation has to be correct. If R is negligible then the initialisation is

$$i = I = 0; \quad \dot{I} = \frac{\dot{i}M}{(L_\ell + L_H)}$$

and $$\frac{di}{dt}\left(L_p - \frac{M^2}{(L_\ell + L_H)}\right) = -V$$

V is the charging voltage of the condenser and L_H is calculated from the initial number density. (chapter 11)

The values of the electrical constants used were approximately the experimental values:-

C 60μF

L_p (primary inductance) 400 nH

L (geometric plasma inductance) 400 nH

M 300 nH.

By including a realistically calculated electric field the usefulness of the dimensionless equations is lost. Runs are reported for hydrogen and argon with a varying ionic charge for the latter, and with varying magnetic and electric fields.

6.8 Results of the simulation

All of the cases taken had the same common features.

These are described quantitatively for one set of parameters . The values of the macroscopic quantities are shown in figures 6.4. and 6.5.

The case described is one in which there is a moderate amount of loss. As shown in fig. 6.4 this loss occurs mainly between 1μs & 2μs. This is the time taken to accelerate a stationary ion to the ring cusp plane. After 3μs there are no more ions lost.

The current shows a linear rise but starts to fall away from this line before many particles start being lost. This shows that there is a deceleration of the ions before and during loss. After the loss of particles has stopped, the rest continue being accelerated, and so the current continues to rise.

The Hall inductance of this plasma is 2μH, larger than the geometric inductance (.4μH). Hence most of the primary bank voltage is available to accelerate the plasma. At the time of loss the Hall inductance, $L_H = \frac{\ell m_i}{2e^2 n \pi r_0}$ increases further as well as there being an effective resistance due to the loss of particles, changing the inductance(similar to the $I \frac{dL}{dt}$ term in say z pinches). There is a consequent slight rise in the accelerating electric field, at the time of maximum loss. The field then starts to drop because of the limited amount of charge on the consenser (bank period 30μs).

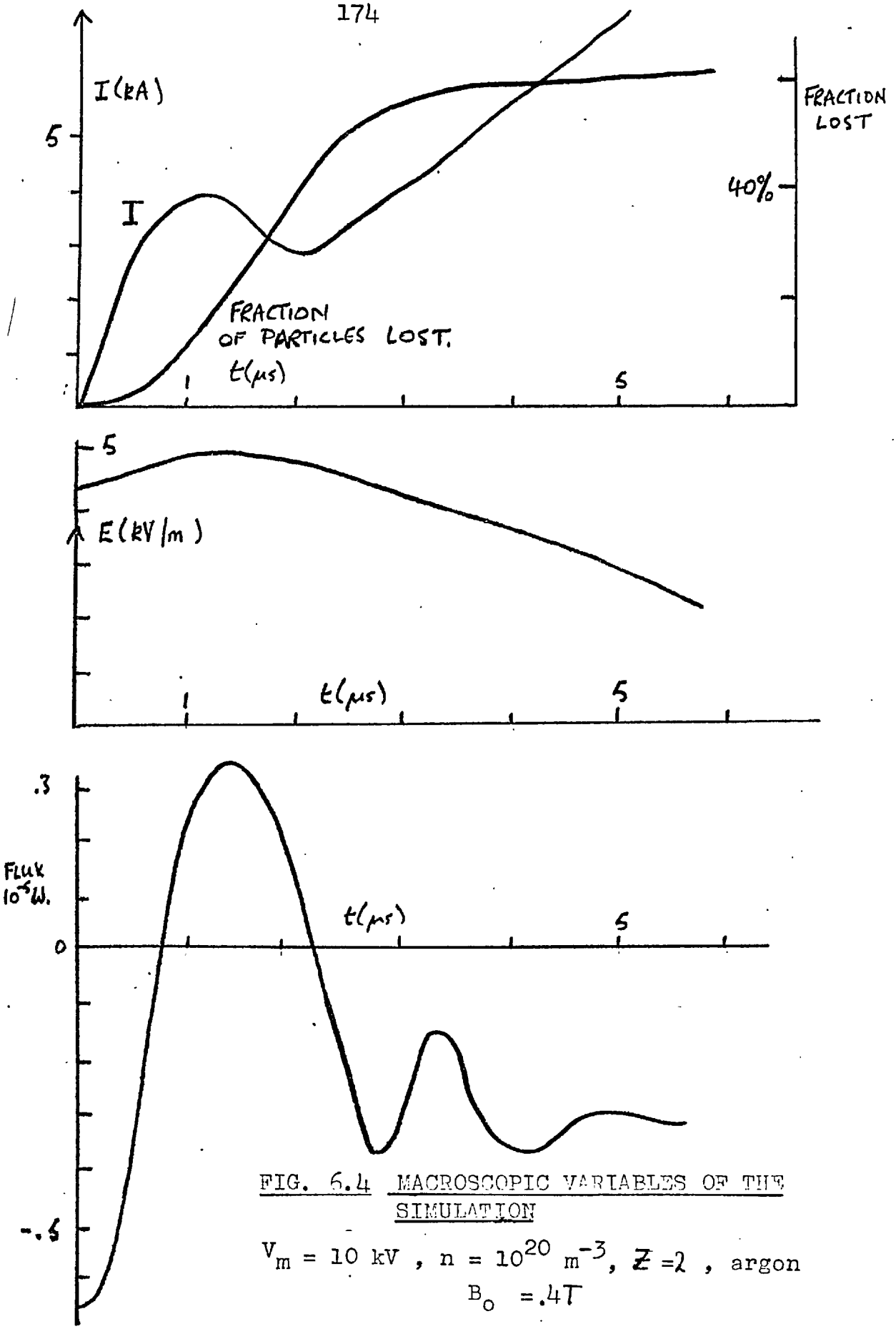

FIG. 6.4 MACROSCOPIC VARIABLES OF THE SIMULATION

V_m = 10 kV , n = 10^{20} m^{-3}, $\mathcal{Z}$ =2 , argon

B_o =.4T

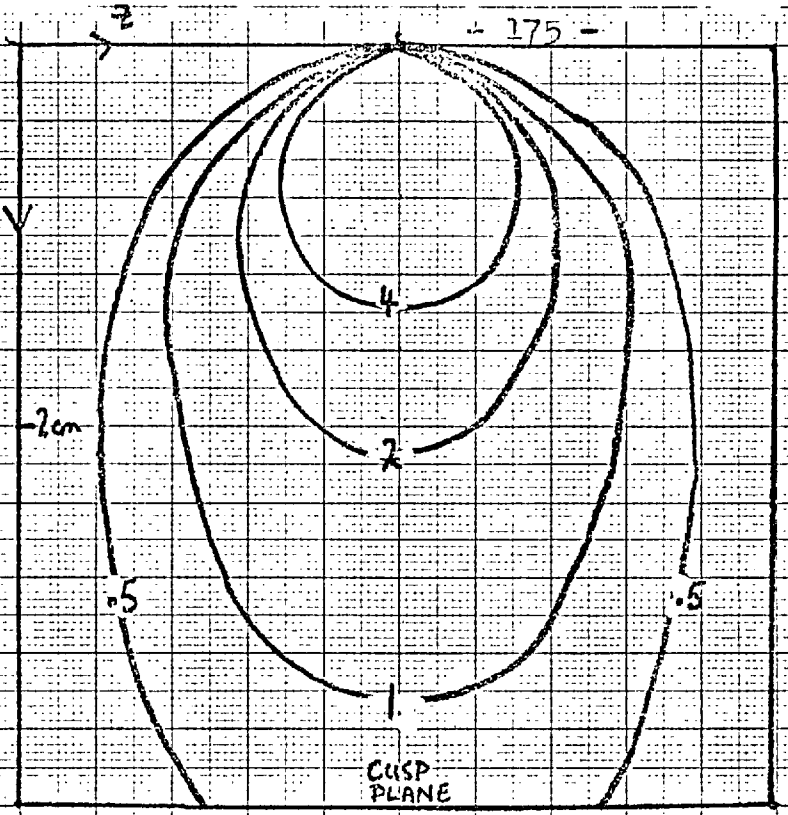

$\underline{E} \wedge \underline{B} / B^2$ DRIFTS

$B_0 = .2T$, $E = 5 \times 10^5 V/m$

FIG 6.5 THE ELECTRON AZIMUTHAL VELOCITY CONTOURS IN UNITS OF $10^4 m/s$

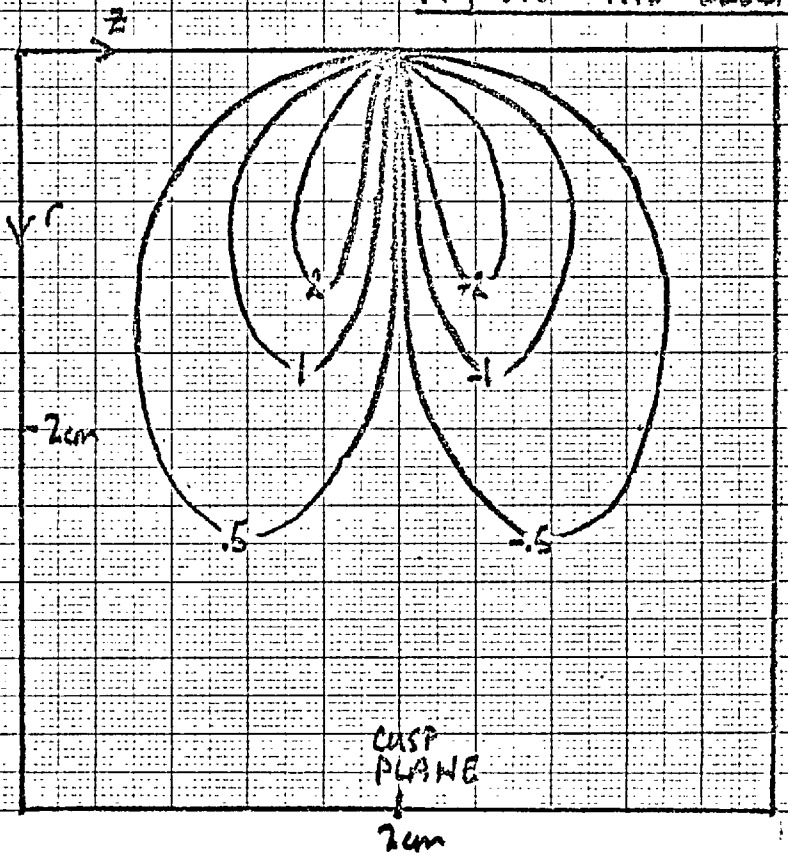

CURVATURE DRIFT

$B_0 = .2T$, $W = 20 eV$

The flux through a diamagnetic loop measuring the field of the plasma current, is also shown in fig. 6. As no inductance is included for the azimuthal currents the plasma field rises immediately to a high value due to the guiding centre drifts of the electrons.

The effect of the curvature drift is small compared with E/B drifts. This is generally because

$$mv_{\parallel}^2/r \ll eE \quad \text{i.e. } kT_e \ll 2\,reE$$

where r is a radius of curvature.
The contours of the two drift velocities are shown in fig. 6.5.

The shape of the field lines of the plasma current is initially as if the plasma current was all at a radius of 2 cm. The axial field can be seen to decrease from the centre outwards passing through zero at 2 cm in the plane of the ring cusp.

After the sudden rise, the field then decreases and is reversed at the time of maximum loss. The shape of this field is complex but shows the reversed azimuthal current of the ion motion at larger radius. There is still the same direction field at the centre of the coil due to the guiding centre drifts. With increasing radius this quickly reverses as the azimuthal current is dominated by the ions which are drifting azimuthally. In a steady state the ions can drift azimuthally at the same speed as the electrons i.e. E/B, but locally in time they can exceed this value by a factor of 2.

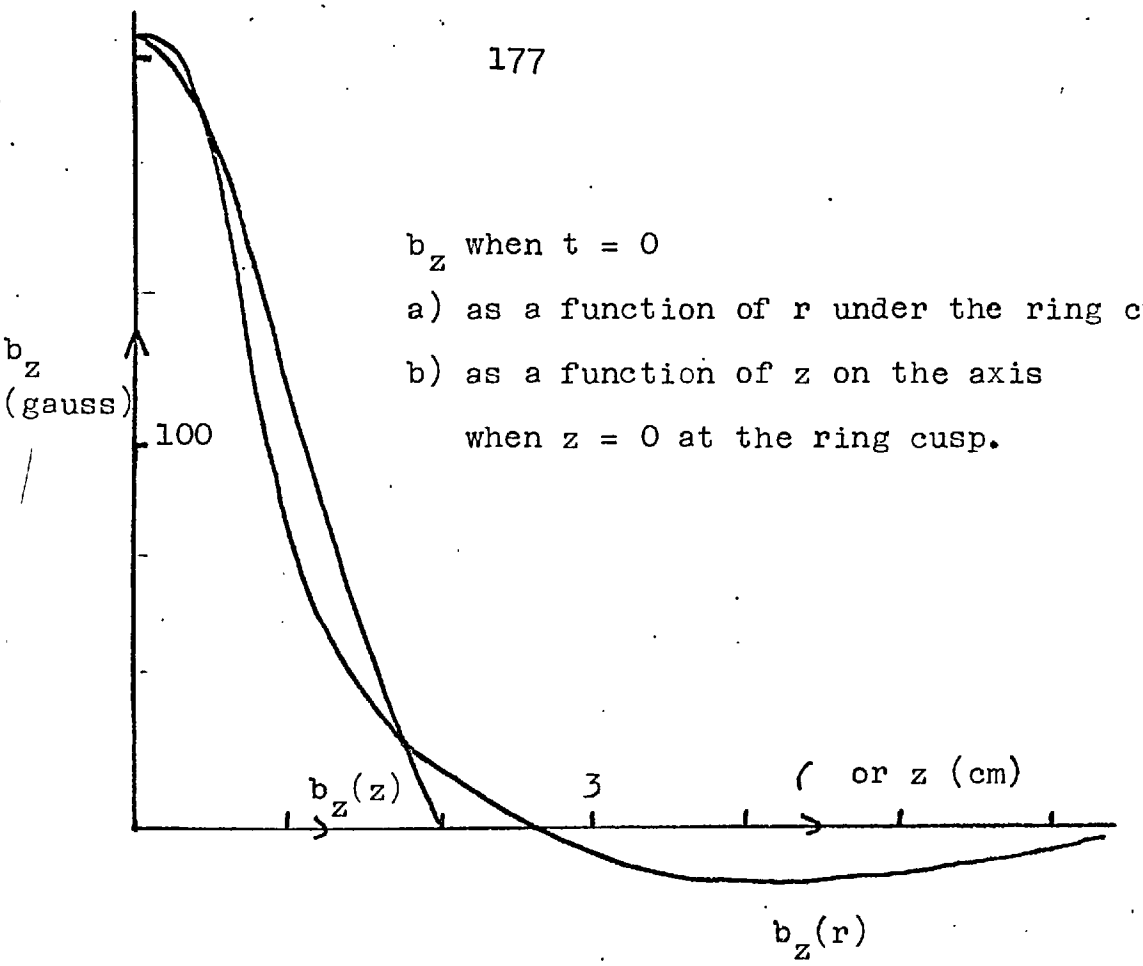

FIG. 6.6 THE FIELD PRODUCED BY THE PLASMA

$V_m = 20kV$, $B_o = .4T$, $Z = 2$, $n = 10^{20} m^{-3}$

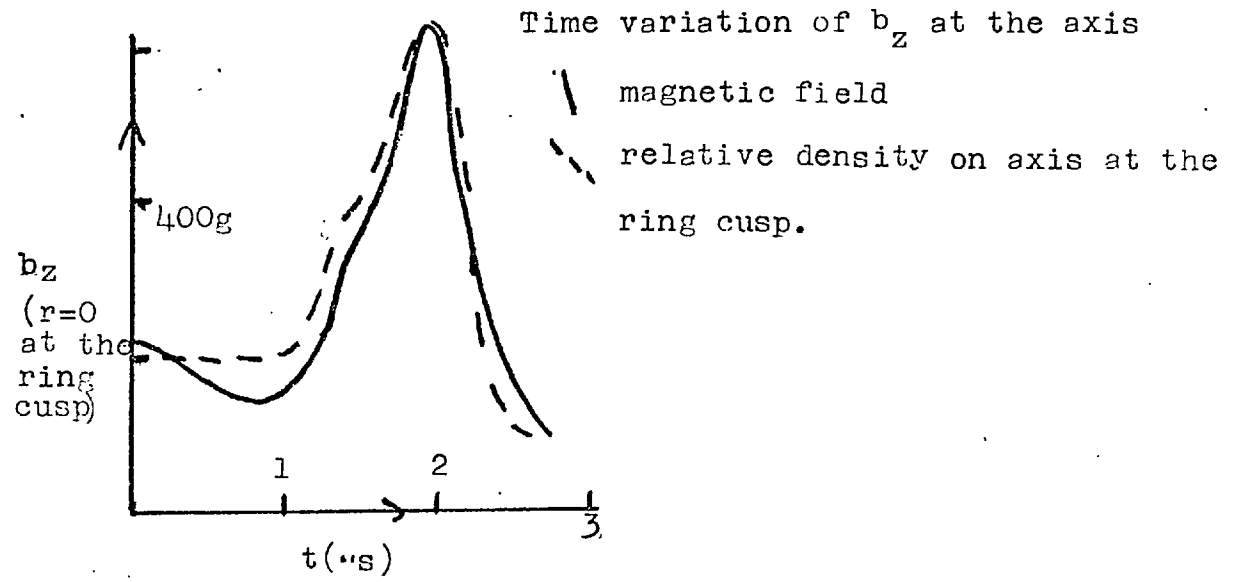

For a lower amount of loss the field at the centre of the tube is shown in fig. 6.6. There is not much decrease of the field at the loss time because of the low loss. The field generally follows the relative density at the centre of the tube which is also plotted on fig. 6.6.

After the time of maximum loss there are still oscillations on the flux signal. This is due to ions which have been trapped in the first ring cusp, and are causing a modulation of the electron azimuthal current.

Fig. 6.7 shows the density in the r - z plane at various times. A cusp shaped density profile is seen to arise. In isolation these diagrams are misleading. As shown analytically an ion which is accelerated and not lost moves so that it is radially displaced outwards when it is under a coil, and inwards when it is under a ring cusp. Fig. 6.8, a drawing of the trajectories of a representative class of particles, shows some which start within the accelerated region. The plotting step is large which is why some of the trajectories are so angular. For the accelerated particles note that they do in fact reach a maximum radius under a coil. The cusp shaped density distribution of fig.6.7 is not due to accelerated particles but rather particles which have been trapped and are probably being lost. Fig. 6.8 shows the large loss of particles initially through the ring cusp. It also shows, for the accelerated particles, the long

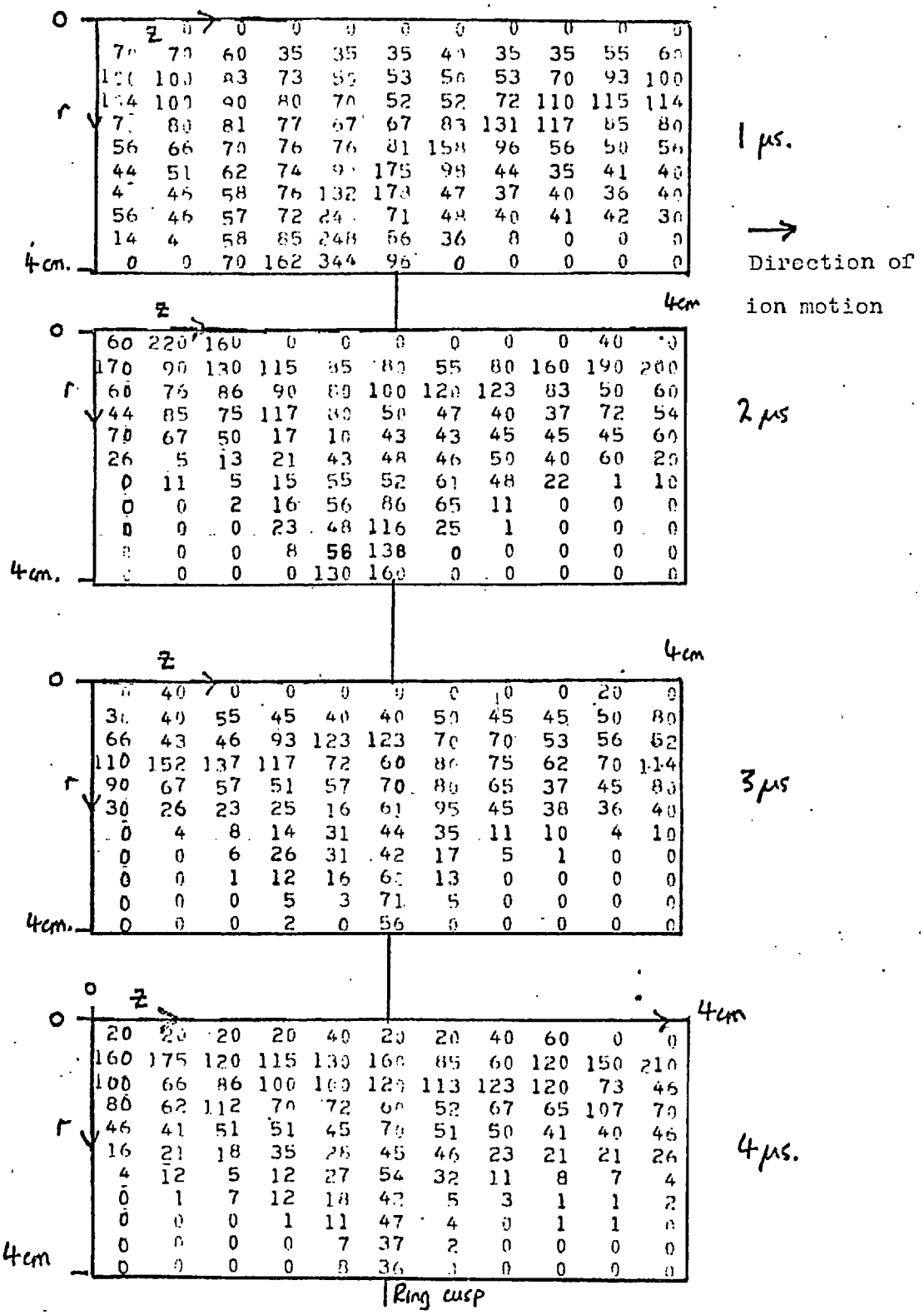

FIG. 6.7. TIME EVOLUTION OF PLASMA DENSITY

100 = 10^{20} m^{-3}, V_m = 10kV, Z = 3, B_o = .4T.

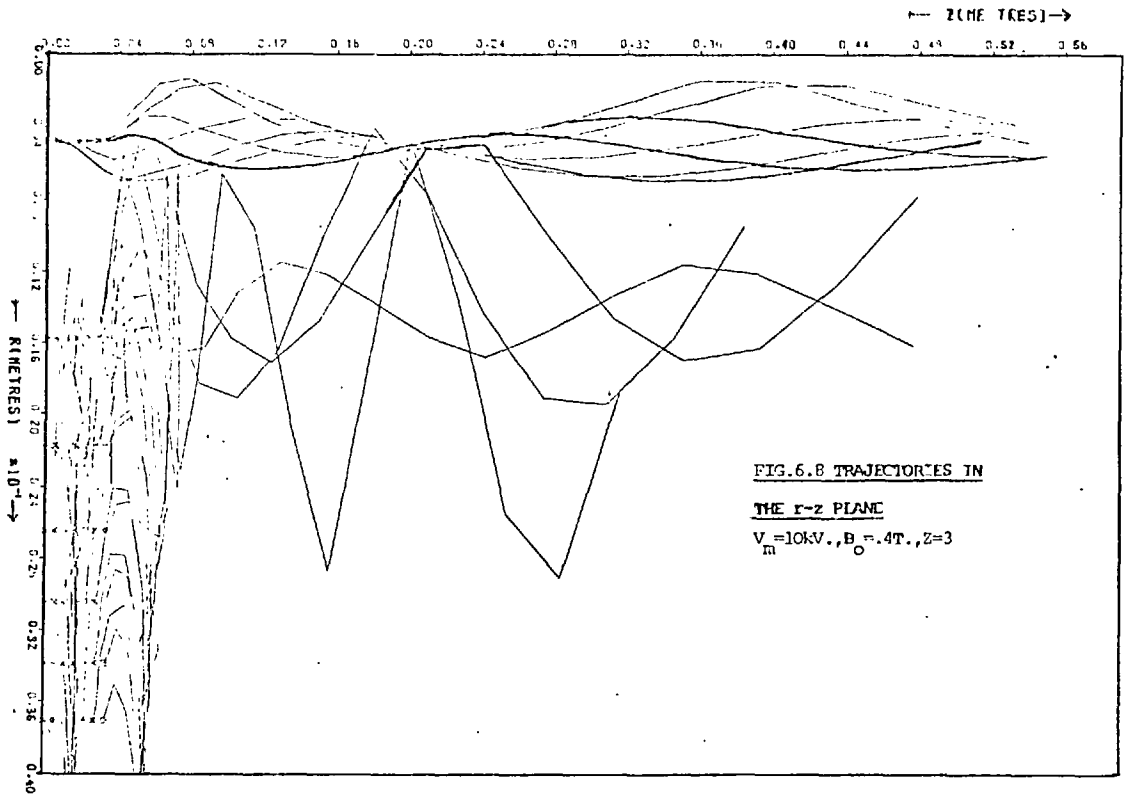

FIG.6.8 TRAJECTORIES IN THE r-z PLANE
V_m=10kV., B_o=.4T., Z=3

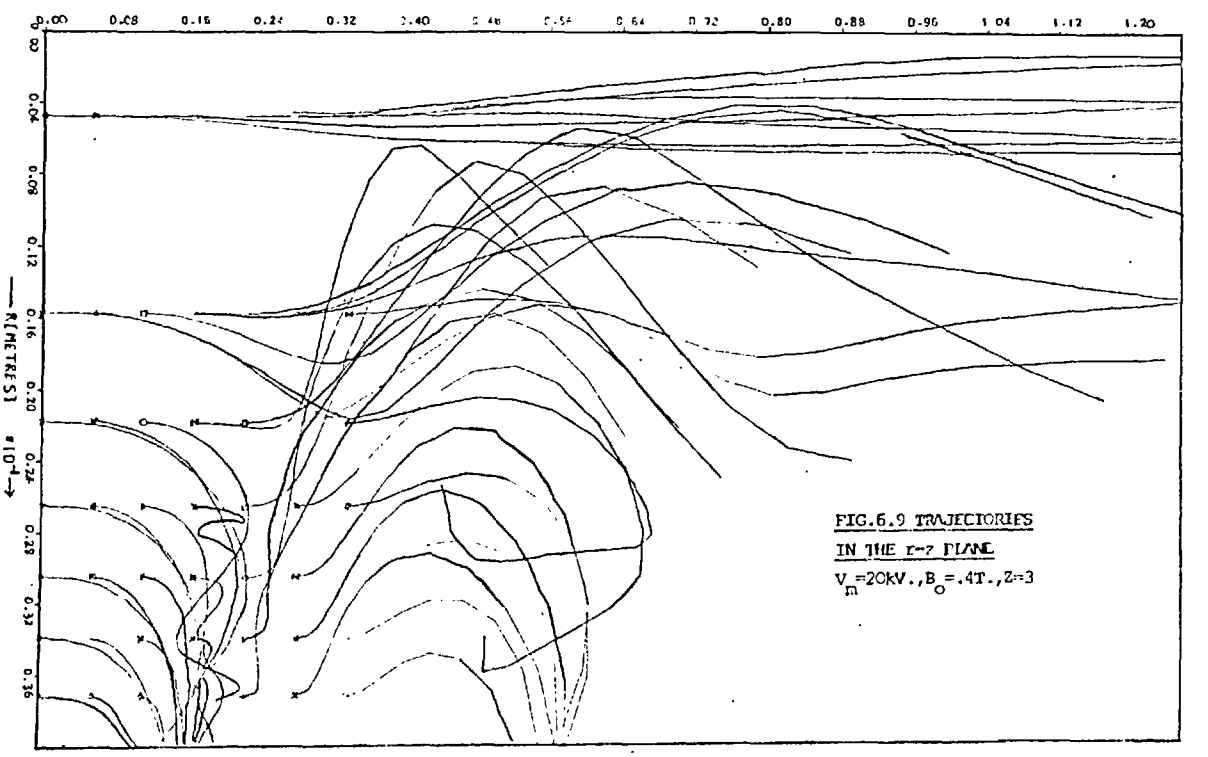

FIG.6.9 TRAJECTORIES IN THE r-z PLANE
V_m=20kV., B_o=.4T., Z=3

wavelength modulation of the radius due to the focussing of the cusp fields.

Unfortunately insufficient data was taken for an exact comparison of this frequency with the theoretical values of $\omega/2$. (section 7.17) An approximate comparison can however be made. The measured period is $3.6 \pm .8$ μs; the theoretical frequency should be ZeB/2m this being 4.3 μs. On the plot of fig. 6.8 there is insufficient data to see the fluctuations at the cusp frequency which cause this focussing.

Fig. 6.9 is another plot of the particle trajectories for a different set of conditions. The scales are expanded to see more detail than fig. 6.8. The trajectory starting at z = 0, r = .016m is a good example of outward motion in the first ring cusp, and a subsequent inward motion once the plane of the ring cusp is passed. For these field parameters.

$$\beta = \frac{k\, mE}{ZeB_o^2} = .77$$

From equation 6.29 a maximum excursion of $1.25\ r_o$ is expected. The maximum excursion measured from fig. 6.9 is $1.3\ r_o$.

The particles which start down stream of the ring cusp are initially accelerated radially inwards. However if they start near to the wall they are lost through the next ring cusp.

Fig. 6.10 is a plot of the initial positions of the particles showing which category they will fall in. These somewhat arbitrary categories are:-

particles which are monotomically accelerated denoted by 3

particles which are not lost but whose velocity reverses, denoted by 2

particles which are lost, but not through the first cusp, denoted by 1

particles which are lost through the first cusp denoted by 0.

The cusp shape predicted by eq. 6.38 is certainly evident. The ring cusp of the particles which are accelerated is downstream of the magnetic ring cusp. The interface of class 3 particles and class 0 particles is blurred by class 2 particles.

In fig. 6.11 the waist of the contained volume is plotted against an approximate value of β for that discharge. This is done for 15 discharge conditions with β varying by 100. Also plotted is the analytic result predicted by eq. 6.31.

Good agreement between the theory of section 6.3, and the computational results for the middle range of β is evident in fig. 6.11, where the computationally observed value of the waist of the contained region is

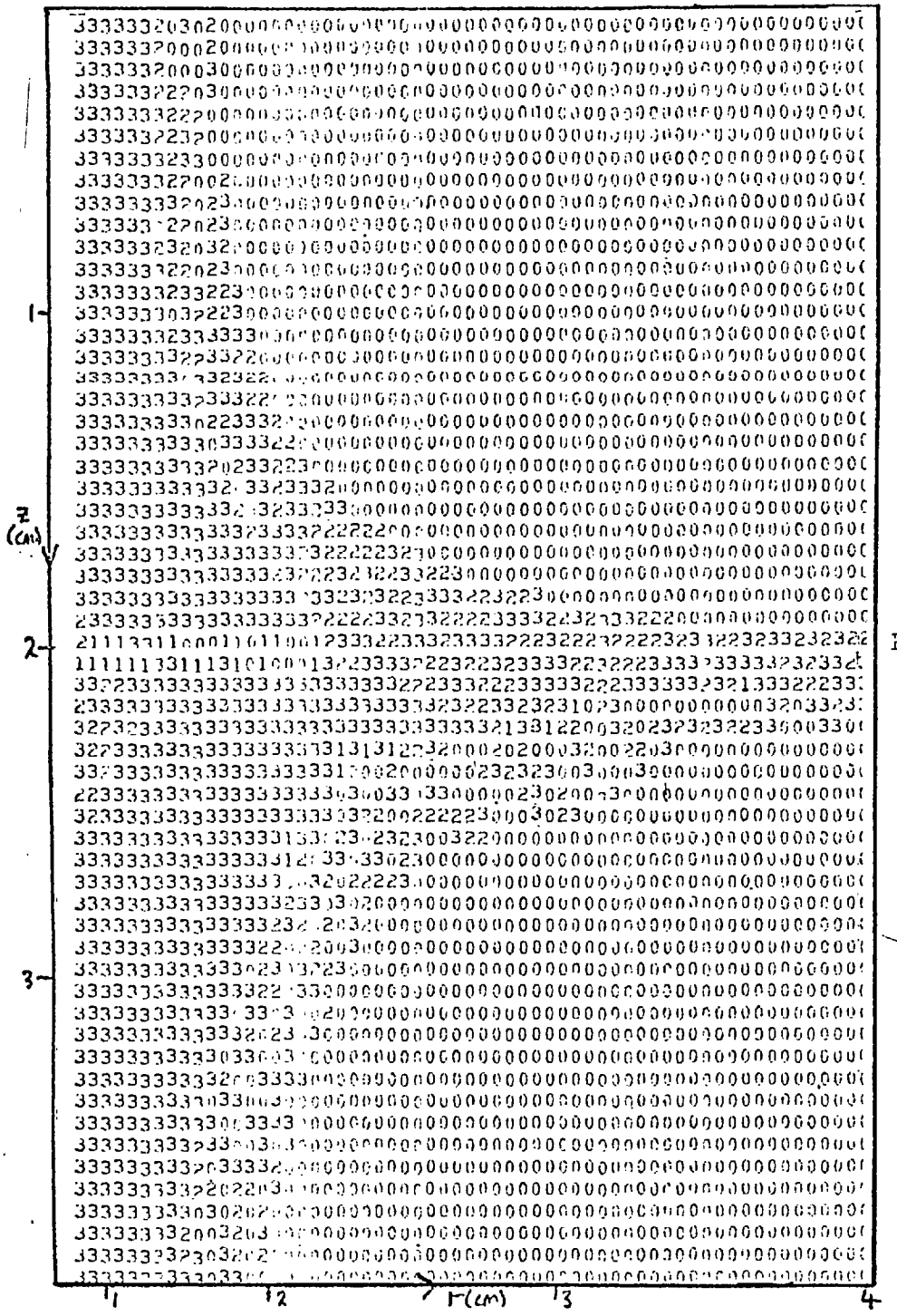

FIG.6.10 THE CATEGORIES OF PARTICLES AS A FUNCTION OF THEIR INITIAL POSITION IN THE r-z PLANE

V_m=10 kV , B_o=.4T , Z=3.

3 = monotonically accelerated: 2=v_ϕ reverses.

0 = lost through the first cusp: 1=lost through later cusp.

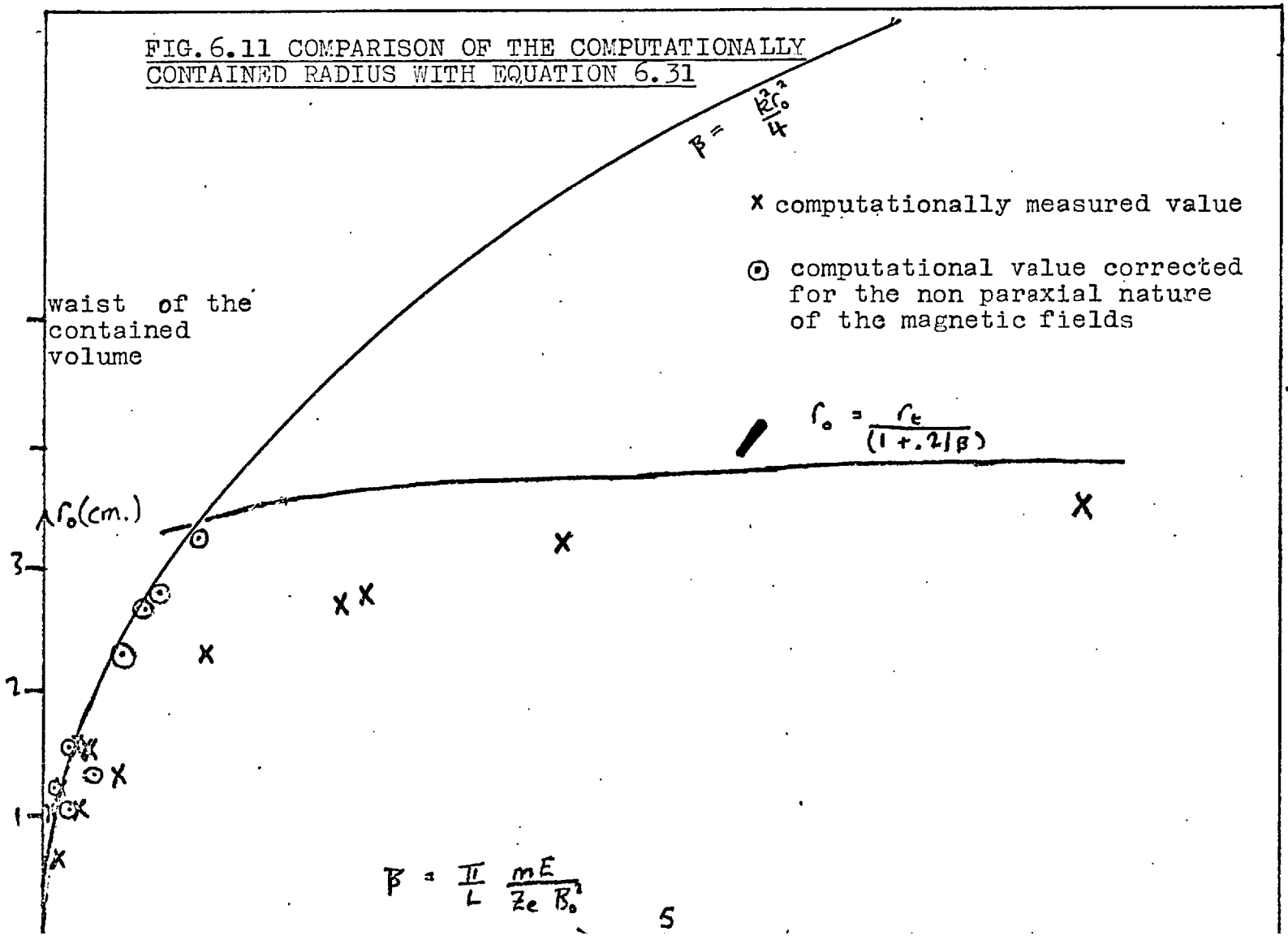
FIG. 6.11 COMPARISON OF THE COMPUTATIONALLY CONTAINED RADIUS WITH EQUATION 6.31
$\beta = \frac{R^2 r_0^2}{4}$
× computationally measured value
⊙ computational value corrected for the non paraxial nature of the magnetic fields
waist of the contained volume
$r_0 = \frac{r_c}{(1 + .2/\beta)}$
r_0(cm.)
3
2
1
$\beta = \frac{\pi}{L} \frac{mE}{Ze B_0^2}$
5

plotted as is the analytic result, (eq. 6.31). The difference between the analytic magnetic field and the computational field must be allowed for. This is achieved by correcting the value of β to $\beta/(1 + .75(kr_o/2)^2)^2$, for the computational results. The computational field is larger than the analytic field by $1 + \frac{1}{2}\left(\frac{kr}{2}\right)^2$ for B_r and $1 + \left(\frac{kr}{2}\right)^2$ for B_z. The different radial variation for the computational field would not affect the analytic result, which is independent of the variation.

For low β, particles are being contained as they are being mirrored by the cusp field. For high β, eq. 6.29 is probably more realistic. Using $r_{max} = r_t$ gives

$$r_o = \frac{r_t}{1 + .2/\beta}$$

This is also plotted on fig. 6.11.

The magnetic field produced at r = 0, z = L/2 is an important diagnostic aid. A fit of this to the parameter yields.

$$b_z(r=0, z=L/2, t=0) = -60\left(\frac{n}{10^{20}}\right)\left(\frac{V_m}{10kV}\right)\left(\frac{.4}{B_o}\right) \quad \text{gauss} \quad (6.63)$$

This is when:- (1) there is no azimuthal ion current,

(2) all of the applied field appears across the Hall inductance. In the experiment the L/R rise time of the azimuthal current is short so a meaningful comparison can be expected.

This field produces a shift of the null point of the cusp. This comes directly from eq. 6.63 and is

$$dz = -.02 \left(\frac{n}{10^{20}}\right) \left(\frac{V_m}{10kV}\right) \left(\frac{.4}{B_o}\right)^2 \text{ cm}$$

the magnitude of which is consistent with a small perturbation of the field line, one of the original assumptions of the model.

Fig. 6.12 shows the macroscopic quantities as the applied magnetic field is varied. The number of lost particles goes up as the magnetic field does. The maximum electric field is correspondingly larger as there is a larger effective resistance due to $I \frac{d}{dt} L_H$. The loss time, measured by the time of maximum current, is not affected much by the size of the cusp field. This is because the loss time is affected mainly by the outermost particles which are lost whatever the value of the cusp field. The loss time decreases slightly as the cusp field increases, by about 100 ns. for B_o varying from .2T to .8T. Over a wide range of variables this current loss time can be fitted to the expression.

$$t = \sqrt{\frac{mL}{eEZ}} = 280 \sqrt{\frac{(10{,}000)}{V_m} \frac{A}{Z}} \text{ ns.} \qquad (6.64)$$

where A is the atomic weight of the species. This can be fitted to both hydrogen and argon, but again depends on all the field appearing across the Hall inductance (as opposed to the plasma geometric inductance). It is the time taken

to accelerate a particle from the plane of the coil to the ring cusp. It is this distance, 2 cm, which is appropriate simply because it is an average time for any particle to reach a ring cusp.

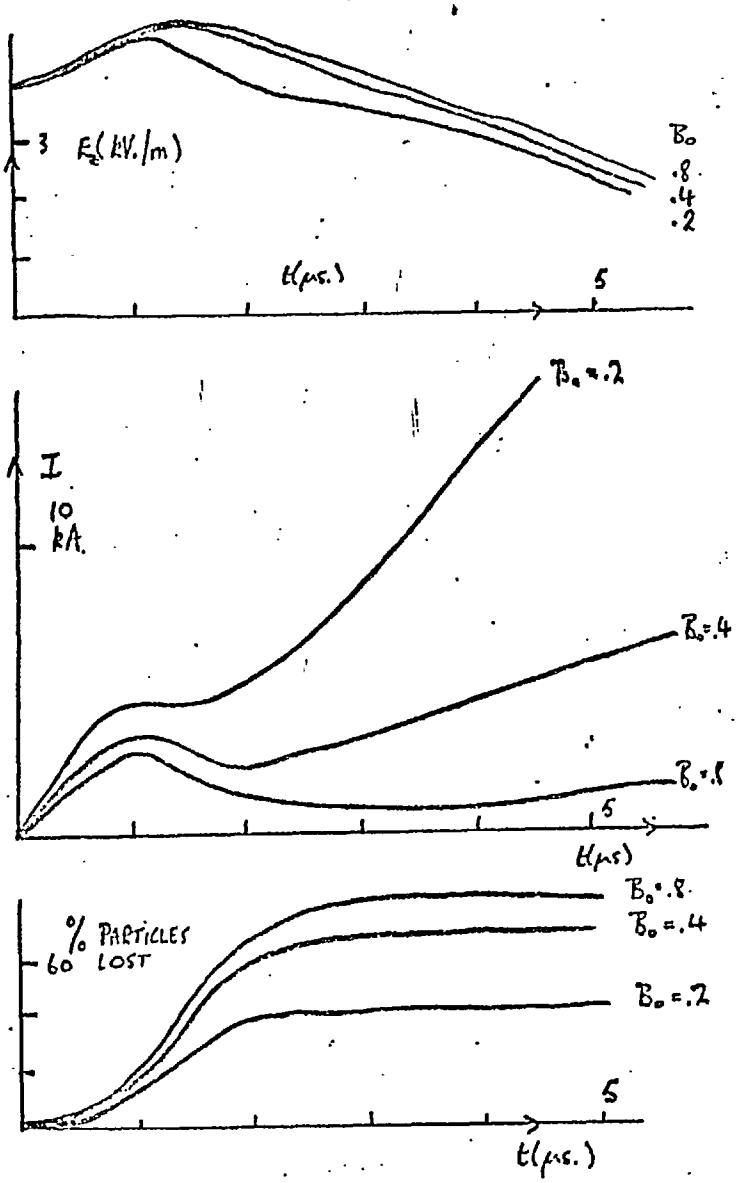

FIG. 6.12 LINEAR POLYTRON SIMULATION

Variation with B_o(T), argon, Z=3, n=$10^{20}m^{-3}$, V_m=10kV.

CHAPTER SEVEN

A COLLISIONLESS PARICLE SIMULATION OF THE POLYTRON WITH A SELF CONSISTENT ELECTRIC FIELD

This chapter describes an extension of the particle work in chapters 5 and 6. There it was seen that the ion trajectories in the vacuum field could account for the nature of the plasma losses. In this chapter inclusion of the electrostatic field due to charge separation , makes the problem more realistic; indeed within the computational constraints it simulates a zero β polytron exactly. The straight cylindrical coordinate system, r, e, z, is used.

7.1 Relation to earlier work

Particle simulations of plasmas were performed as early as 10 years ago (Dawson, 1962). However, the available computer power only allowed 1 dimensional plasmas to be studied. The plasmas consisted of sheets of charge. These models were used mainly to compare the properties of the model, such as collisions and equilibria, with analytic results.

Two dimensional simulations began about 1966 (Hockney, 1966). Typically the plasma is represented by a set of charged rods, in a Cartesian space. Because most experiments do not have plane symmetry, these simulations have been used to verify predictions of theory, such as

holes in phase space (Boris and Roberts, 1968) and anomalous diffusion (Hockney, 1966). There have been exceptions such as a simulation of the astron (Kileen, 1966) an unusual plasma, and a simulation of a stellarator (Smith and Bishop, 1968). It should be noted that most experimental plasmas do not adapt to this particle treatment because of the importance of the self consistent magnetic field. However the polytron does; at least a low density polytron does, and so a two species simulation has been performed.

Moreover a self consistent electric field is necessary to explain why confinement in the polytron is so poor. This is completely different from a stellarator where the electrostatic field improves confinement (Smith and Bishop). The electric field is found to be larger than the expected $\frac{kT}{er}$, and is shown to be proportional to the driving applied electric field.

Sophisticated programming techniques have to be used which are described elsewhere (Kilkenny, 1971). A comparison with the experiment is made in chapter 11. This ability to make a comparison is quite an unusual feature of particle simulations.

7.2 The physical model

The low density polytron does not distort the vacuum

fields. A criterion for low density, in this context is

$$\frac{\mu_0 j_0}{k} = \frac{\mu neE}{kB} = \text{plasma field} \ll B$$

where B is the order of magnitude of the vacuum field, and $k = \pi/$ cusp separation; therefore $n < 10^{21}\ m^{-3}$. The experiment shows that this limit is too high and that $n < 10^{19}\ m^{-3}$ is more appropriate. The number density which can be simulated is several orders of magnitude lower than this .

Both ions and electrons must be integrated. In other two species calculations a fictitious mass ratio has been used so that the ratio of the electron Larmor period (which restricts the integration timestep) to ion Larmor period is not too small. However, the naturally large ion to electron mass ratio, is essential for the polytron mechanism. Consequently a guiding centre approximation for the electrons has been used. Effectively a zero mass is used for electron motion perpendicular to the field lines, whilst the true electron mass is used for parallel motion. The equations of motion of an electron guiding centre are

$$\frac{dV_{\parallel}}{dt} = \frac{q}{m} E_{\parallel} - \frac{\mu}{m} \frac{\partial B}{\partial s} + \frac{m}{q} \underline{V}_e \cdot \left(\frac{\partial \underline{e}_1}{\partial t} + V_{\parallel} \frac{\partial \underline{e}_1}{\partial s} + \underline{V}_e \cdot \nabla \underline{e}_1 \right) \quad (7.1)$$

$$\underline{V}_{\perp} = \underline{V}_b + \underline{V}_r + \underline{V}_e \quad (7.2)$$

$$\underline{V}_b = \frac{m}{q} \frac{(V_{\perp}^2 + 2V_{\parallel}^2)(\underline{B} \times \nabla)\underline{B}}{|B|^3} \quad (7.3)$$

$$\underline{V}_e = \frac{\underline{E} \times \underline{B}}{|\underline{B}|^2} \quad (7.4)$$

$$V_r = -\frac{m}{q}\frac{Dv_e}{Dt} \times \frac{B}{|B|^2} \qquad (7.5)$$

$$\frac{\partial \mu}{\partial t} = 0 \qquad \text{(Northrop,1961)} \qquad (7.6)$$

to first order in m/q, as $\nabla_x \underline{B} = 0$, parallel and perpendicular referring to the local direction of $\underline{B}$. s is the coordinate along $\underline{e}_1$, the unit vector parallel to $\underline{B}$.

It would seem to be difficult to solve this complete set of equations for many particles, even with the obvious simplification of working in the r-z plane with azimuthal symmetry. However the set simplifies as both $\underline{v}_e$ and $\underline{v}_b$ are azimuthal and so do not change the system in the r-z plane. Also, $\underline{v}_r$, the only drift velocity in the r-z plane, can be neglected.

$$\text{If } \frac{\partial}{\partial t} = 0 \text{ then } \underline{v}_r = \frac{m}{q}\frac{v_{11}}{B^1}\ \underline{B} \times \frac{\partial}{\partial s}\left(\frac{E}{B}\sin\theta\right) \qquad (7.7)$$

with the notation of fig. 7.1, s being measured along a field line. Suppose that a guiding centre moves close to a field line from A to B then the drift along the radius of a curvature of a field line,

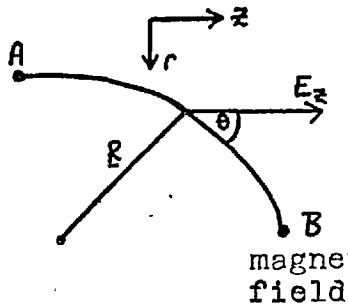

FIG. 7.1

$$d_r = \int_A v_r\, dt = \frac{E}{B}\frac{m}{qB} = \frac{v_e}{\omega_{ce}}$$

making the valid assumption that in this region, near to the cusp centre, $\frac{\partial}{\partial s}(|E|,|B|) = 0$, the field line turning through

90^{o} between A and B. Physically this displacement accounts for the energy of the $\frac{E}{B}$ drift. If the electron then moves back along the field line, v_r reverses and the particle moves back to A, the original position, even if $\frac{\partial}{\partial s}(|E|,|B|) \neq 0$.

For $d_r > 1mm$ it is necessary that $B < 10^{-2} T$. This is only a small region, where $\frac{d\mu}{dt} \neq 0$ anyway.

Furthermore, in equation 7.1 the term $-\mu \frac{\partial B}{\partial s}$ can be neglected c.f. $\frac{e}{m} E_{11}$. For the mirror effect will be largest near the ring cusp where $\underline{B} \approx B_r = B_o \frac{kr}{2}$ sin kz then

$$-\frac{\mu}{m}\frac{\partial B}{\partial s} \approx \frac{v_\perp^2}{2B(0)}\frac{\partial B_r}{\partial r} = \frac{q W_\perp}{m r} \approx \frac{2\omega'' W_\perp}{r} \quad m/s^2$$

where $W_\perp$ is the perpendicular temperature, in eV. This is taken as 1 eV, the original temperature, there being no heating. As shown later E_{11} at the edge of the cusp is several E applied and so $\frac{\mu}{m}\frac{\partial B}{\partial s}$ is about 10^2 times smaller than $\frac{q}{m} E_{11}$, which is $\sim 10^{16}$ m/s^2. In the programme provision is made for the inclusion of $-\mu \frac{\partial B}{\partial s}$, but it is not used.

As $\underline{v}_e \cdot \underline{e}_1 = 0$ the last three terms in equation 7.1 are zero.

There seems to be no precise criterion for the inaccuracy of a guiding centre treatment of particle motion (Grad, 1961). However a safe criterion seems to be

$$\frac{vm}{eB} \ll r \quad \text{or} \quad \frac{2vm}{eB_o k} \ll r^2$$

as the local radius, r, would be approximately equal to the scale length for changes in the magnetic field. This indicates that for electrons r > 1 mm.

Thus with very little loss of generality the equations for each particle simplify to

$$\frac{dv_{11}}{dt} = \frac{q}{m} E_{11} = \frac{q}{m} \left(\left(E_a - \frac{\partial U}{\partial z} \right) \cos e - \frac{\partial U}{\partial r} \sin e \right) \tag{7.8}$$

$$\frac{dr}{dt} = v_{11} \sin e \tag{7.9}$$

$$\frac{dz}{dt} = v_{11} \cos e \tag{7.10}$$

where E_a is the applied electric field, U the electrostatic potential, (obtained by solving Poisson's equation) and e defined in fig. 7.2. The position of each particle is specified by three coordinates r, z, v_{11}. e is a known, fixed function of r and z . As in chapter 6

$\underline{B} = (B_o \sin kz \, (kr/2 + (kr/2)^3/2), \, 0, \, B_o \cos kz \, (1 + (kr/2)^2)$.

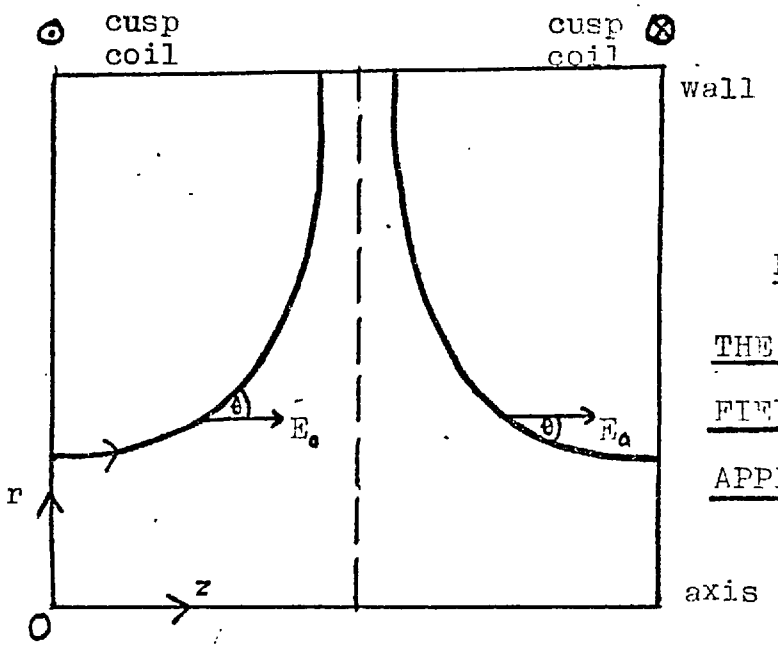

FIG. 7.2.

THE ANGLE BETWEEN THE FIELD LINES AND THE APPLIED FIELD

Each particle in this model is, in reality, a charged annulus. The charge on each annulus is the same, and so the initial constant number density is simulated by an area density of annulii, proportional to the radius.

To simulate the laboratory experiment the tube radius is 4cm , and the coil separation 4cm. Eqs. 7.8 - 7.10 are azimuthally independent and so the system is periodic from cusp to cusp. The potential is evaluated on 32 x 32 mesh points within this domain, the length of the cell side, a, being 1.25 mm. The density at the coordinate I,J (see fig. 7.3) is evaluated as

$$\rho^*(I,J) = \sum_{k=1,\text{all particles}} q\,\frac{\delta(I,\ \mathrm{Int}(r_k/a+1))\,\delta(J,\mathrm{Int}(z_k/a)+1)}{(J-\frac{1}{2})\,|q|} \qquad (7.11)$$

The function Int is the first integer whose value is less than the argument. For the purpose of equation 7.11 z_k is reduced to a value in the first coil.

This is the nearest grid point approximation, which is also used for the electric field which a particle experience Other weighting schemes such as cloud in cell (C.I.C.) are less noisy, so reducing false heating of the plasma, but have the same collision frequency as N.G.P. (Hockney, 1971). The

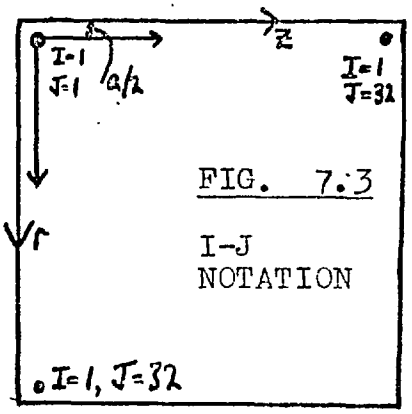

FIG. 7.3

I-J NOTATION

considerable extra programming necessary for C.I.C., especially compared with the simple shifts of N.G.P., makes N.G.P. preferable to C.I.C.

Poisson's equation which is in this geometry

$$\nabla^2 U = \frac{\partial^2 U}{\partial r^2} + \frac{1}{r}\frac{\partial U}{\partial r} + \frac{\partial^2 U}{\partial z^2} = -\frac{\rho}{\epsilon_0} \qquad (7.12)$$

is solved in the form

$$\frac{\partial^2 U^*}{\partial r^2} + \frac{1}{r}\frac{\partial U^*}{\partial r} + \frac{\partial^2 U^*}{\partial z^2} = -\frac{\rho^*}{a^2} \qquad (7.13)$$

where U^* is proportional to U, equation 7.13 being simply differenced to a form with no constants in it. Periodic boundary conditions are applied in the axial direction. $U = 0$ at the tube i.e. the tube is metal: the real condition of an insulating wall would require solving for U several radii outside of the tube. The row of mesh points next to the axis is solved by Gauss's law, so avoiding singularities in equation 7.13.

When ions hit the wall they are perfectly absorbed. In contrast when the electrons hit the wall they are brought to rest at zero potential. The first condition is realistic because of ion neutralisation; the electron boundary condition is necessary to allow flux to and from the wall at the plasma frequency.

U^* is differenced and stored to produce the r.h.s. of equation 7.8 by

$$E_r\ (I,J) = (U^*(I,J+1) - U^*(I,J-1))\ mC/2q \qquad (7.14)$$

$$E_z\ (I,J) = (U^*(I+1,J) - U^*(I-1,J))\ mC/2q \qquad (7.15)$$

where C is a constant allowing for the number of electrons on each annulus. The equations of each particle are reintegrated, the cycle being repreated. Fig. 7.4 is a block diagram of the process.

FIG.7.4 SCHEMATIC OF ELECTRON INTEGRATION

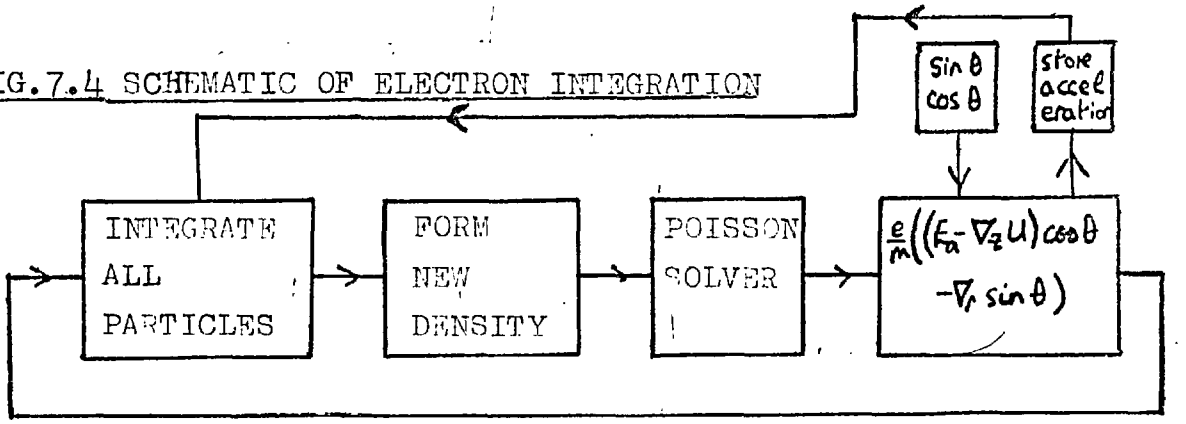

Once enough electron timesteps have occurred (Section 7.5) the ions are integrated according to

$$\frac{d^2r}{dt^2} = \left(\frac{K}{r} - \frac{Ze}{m}A_\theta\right)\left(\frac{Ze}{m}\left(B_z - \frac{A_\theta}{r}\right) + \frac{K}{r^2}\right) - \frac{Ze}{m}\nabla_r U \qquad (7.16)$$

$$\frac{d^2z}{dt} = -\frac{Ze}{m}B_r\left(\frac{K}{r} - \frac{Ze}{m}A_\theta\right) + \frac{Ze}{m}\left(E_z - \nabla_z U\right) \qquad (7.17)$$

This is as in chapter 6, apart from the inclusion of ∇U, the value of U being an average from all the electron timesteps.

7.3 The initial temperature

Initially the electron velocity distribution is approximated to the Maxwellian

$$f(v_{11}) = n \left(\frac{m}{2\pi kT}\right)^{\frac{1}{2}} \exp(-mv_{11}^2/2kT)$$

$$= n \left(\frac{m}{2\pi kT}\right)^{\frac{1}{2}} \exp(-v_{11}^2/v_{th}^2)$$

by a histogram of 60 fixed velocity intervals within the range $v_{11}^2 < 6v_{th}^2$. A Maxwellian is chosen as it is known to be stable. Computationally the probabilities for all of these intervals are assigned to an exclusive part of the range 0 to 1, the size of the part being proportional to the probability of the interval, and the sum of the probabilities being 1. For each particle a random number generator produces a number between 0 and 1, and the corresponding velocity interval within which the random number lies, is assigned to the particle.

7.4. Numerical details

High accuracy of equations 7.8, 7.9 and 7.10 can be achieved by using a leapfrog scheme.

$$v_{11}^{n+2}\, dt = v_{11}^{n}\, dt + \alpha^{n+1}\, dt^2 \quad (\text{error } O(dt^4)) \qquad (7.18)$$

where α is the acceleration along the field line,

$$z^{n+3} = z^{n+1} + v_{11}^{n+2}\, dt \cos\theta^{n+2} \quad (\text{error } O(dt^3)) \qquad (7.19)$$

$$r^{n+3} = r^{n+1} + v_{11}^{n+2}\, dt \sin\theta^{n+2} \quad (\text{error } O(dt^3)) \qquad (7.20)$$

The integer superscripts refer to time levels. Positions are not so far defined at time n + 2 and so $\cos\theta^{n+2}$ is found by $\cos\theta^{n+2} = .5\ (\cos(\theta(r^{n+1}, z^{n+1})) + \cos(\theta(r^{*n+3}, z^{*n+3}))$

Starred quantities are temporary values defined by

$$r^{*n+3} = r^{n+1} + v_{11}^{n+2}\ dt \sin\theta^{n+1}$$

$$z^{*n+3} = z^{n+1} + v_{11}^{n+2}\ dt \cos\theta^{n+1}$$

The accuracy of this scheme for equations 7.19 and 7.20 was checked for a 100 eV electron, $dt = 2\ 10^{-10}$s, giving an error of 19μm in integrating the position through 90° along a field line i.e. 4 cm.

Errors will occur in equation 7.18 but will be of order dt^4, as α is known at time n + 1. It is important to use such a scheme which requires storage of coordinates at only one time level, reducing memory requirements

7.5 Computational details

Programming the equations is a major effort, and is the subject of a separate report (Kilkenny,1971). A few details are included here. For most runs 32, 768 particles were used. The frequent electron integration has to be fast, and so is written in optimised machine language. The three electron coordinates are packed into 1 computer word; the position and velocity of each electron is integrated one timestep in 36μs computer time.

Only 60,000 words of central memory were available,

so when the ions are integrated the electron data is stored onto magnetic tape, and then the ions are integrated by using a rotating double buffer and another two tapes. Such slow information access (to magnetic tapes) is permissible because of the infrequency of ion integration.

Poisson's equation is solved iteratively by a S.O.R. process, on a 32 x 32 mesh (Hockney, 1970).

Hockney has shown that a Fourier transform method of Poisson solving, is faster than any iterative scheme. However he does not consider the improvement to an interative scheme caused by a good first guess. Also core store and programme development time for a Fourier transform programme are important considerations when the computer time taken for an iterative Poisson solver does not dominate the particle integrating time.

Thus Poisson's equation is solved iteratively using a S.O.R. method. A five point differencing scheme is used for the differentials. The algorithm for the row nearest to the axis, which is different from the main domain is

$$U^{*P+1}(I,1) = \omega/6\,(a^2\rho^*(I,1) + U^{*P}(I+1,1) + U^{*P+1}(I-1,1) + 4\,U^{*P}(I,2)) + (1-\omega)\,U^{*P}(I,1) \qquad -(7.21)$$

which is derived from Gauss's law. The superscript p is an iteration counter and ω is the same relaxation factor as in the main region.

The analytic expression, in a cartesian system,

for the best value of ω, the relaxation factor is

$$\omega = \frac{2}{1 + \pi\left(\frac{1}{2M^2} + \frac{1}{2N^2}\right)^{1/2}}$$

where the region is N mesh points by M. This gives $\omega = 1.84$ for a 32 x 32 mesh. For the mesh used here the best value is $\omega = 1.92$. This was found by trial and effor. As shown in fig. 7.5., using the exact value is critical.

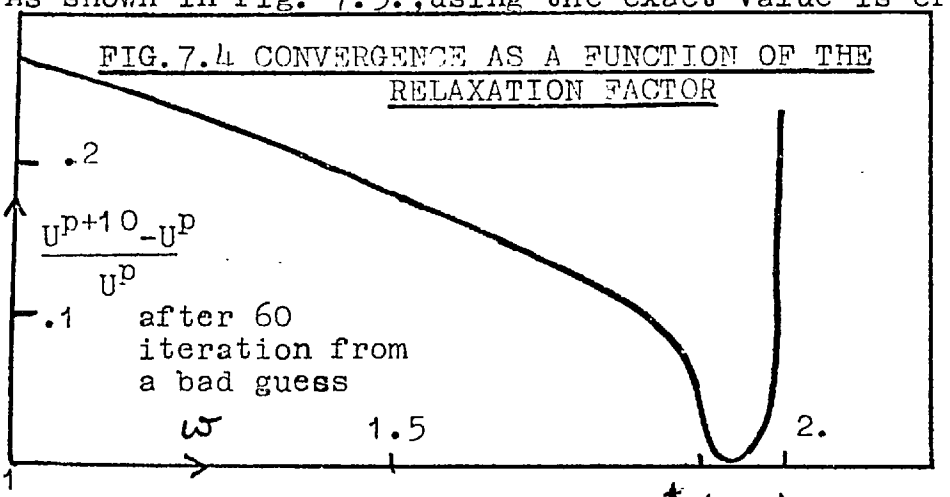

FIG. 7.4 CONVERGENCE AS A FUNCTION OF THE RELAXATION FACTOR

The value of the first guess to $U^*(I,J)$ is the extrapolated value from the last two timesteps i.e. $U^*_n = 2\,U^*_{n-1} - U^*_{n-2}$ where the subscript is a time level. This increases the convergence by approximately 10. Iteration continues until a fractional convergence of .001 is attained.

7.6 The scaling of the number density

The process outlined so far is a two stage simulation of the polytron plasma. The computer plasma has a real number density of 10^9 m^{-3} and is used to simulate a number density of 10^{15} m^{-3}, by increasing the mass and charge of each

particle by 10^6. Such a scaling allows important physical quantities to retain similar ratios as a real plasma of number density 10^{15} m^{-3} (e.g. the Debye length to the dimension of the plasma). This is the first stage of the simulation.

Then it is assumed that the properties of the polytron are independent of number density, apart from the toroidal and poloidal currents which are assumed to be proportional to the number density. This seems valid from the analytic work, at least in the lower density regime. If so the laboratory plasma will exhibit the same properties as the 10^{15} m^{-3} plasma. This is the second stage of the simulation.

The validity of the first stage of simulation can be verified in some detail, as the characteristics of the simulation can be measured. The second stage is not so easy to verify. An understanding of the process occuring in the 10^{15} m^{-3} plasma and proof that they are number density independent is required.

So far it has only been stated that the scaling of the number density is adjusted by the constant C (eq. 7.14 and 7.15). Also where mass and charge have been written it has only been as a ratio, which is independent of the scaling. Firstly, then it is necessary to be more specific about C. The notation of a superscript * signifies

a variable used for multiplicative simplicity in the programme. The subscripts c and s refer to the actual value of the quantity used on the computer and the value which the computer model simulates, respectively.

Charge and number density (n) defined by eq. 7.11 are related to computational quantities by

$$n_c^* = 2\pi a^3 n_c \tag{7.22}$$

$$\rho_c^* = 2\pi a^3 n_c = n_c^* = \frac{2\pi a^3 \rho_c}{q_c} \tag{7.23}$$

U_c^* is found from solving eq. 7.13 which is rewritten as

$$\nabla^2 U^* = -\frac{2\pi a \rho_c}{q_c} \tag{7.24}$$

Also $$\alpha^* = \alpha dt^2 = dt^2 \frac{q_c}{m_c} \nabla U = C\, dt^2 a\, \nabla U^* \tag{7.25}$$

Equation 7.25 gives the relation between U and U^*

$$U = \frac{Cam_c}{q_c} U^* \tag{7.26}$$

Therefore from equation 7.24 and 7.12 $\frac{Cam_c}{q_c} = \frac{q_c}{2\pi a \epsilon_o}$

$$\therefore \quad q_c = 2\pi a^2 \frac{m_c}{q_c} C\epsilon_o \tag{7.27}$$

This gives the charge on each computer particle, as $\frac{m_c}{q_c}$ is independent of the charge on a particle to preserve the correct particle dynamics. The number density being simulated (n_s) is then related to the number density being used on the computer (n_c) by

$$n_s q_s = n_c q_c \tag{7.28}$$

where $q_s = -1.6\ 10^{-19}$c and $m_s = .91\ 10^{-30}$ kg.
The necessary conditions on the characteristic lengths and times are now considered.

7.7 Characteristic lengths

For lengths, one set of conditions is

$$a \ll \lambda_s \ll 2R \text{ and } L \qquad (7.29)$$

where λ_s is a plasma screening length, R the radius of curvature of $\underline{B}$, and L the dimension of the tube. $\lambda_s \ll L$ is necessary for the particles to constitute a plasma. That $\lambda_s \ll 2R$ is necessary for the second stage of simulation. It can be seen from fig. 7.6, in which the screening of a field charge in a circular magnetic field is illustrated. The screened potential produced by the field point is

$$U \approx \frac{q}{4\pi\epsilon_o} \frac{\exp(-2R \sin(\psi/2)/\lambda_s)}{2R \sin(\psi/2)}$$

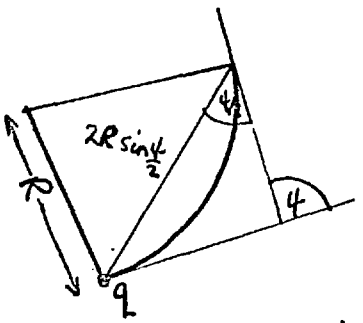

FIG. 7.6 PLASMA SCREEN IN A CURVED MAGNETIC FIELD

A plasma of density 10^{20} m^{-3} will always have $\lambda_s \ll R$. For the simulated plasma of 10^{15} m^{-3} it is necessary that $\sin(\psi/2) \approx \psi/2 \leq \frac{\lambda_s}{2R} \ll 1$

That $a < \lambda_s$ is necessary for an accurate solution to Poisson's equation.

The Debye length of the simulation

Condition 7.29 is very stringent. a, the length of

the side of a cell cannot be too small because of the need to solve Poisson's equation. The screening length is thus fixed at about the geometric mean of the cell side and the plasma dimensions, and this determines the number density of the simulation.

The Debye length for a plasma is

$$\lambda_d = \sqrt{\frac{kT\epsilon_0}{nq^2}}$$

At first sight this appear to be dependent on n_s/n_c. However, the velocity of a super particle is the same as the corresponding electrons, as they have the same charge to mass ratio, and so their temperature is scaled up by the number of electrons,

$$\text{i.e. } \frac{kT}{2}c = \frac{1}{2} m_c v^2 = \frac{m}{m_s}c \quad \frac{kT}{2}s$$

$$\therefore \quad \lambda_d = \left(\frac{\epsilon_o m_c}{n_c q_c^2}\right)^{\frac{1}{2}} \left(\frac{kT_e}{m_s}\right)^{\frac{1}{2}} = \frac{4.2\ 10^5\sqrt{W}}{\omega_p} \quad m. \qquad (7.30)$$

The Debye length for the simulation will be different from equation 7.30; for distances short compared with the local radius, the simulation plasma is pseudo two dimensional. However, the potential of an annular charge depends on the direction from the annulus and does not fall off as fast as $\frac{1}{r^2}$. An anisotropic screening length, λ_s longer than λ_d, is to be expected.

To ascertain the value of λ_s, the real screening length in this particular problem, a set of straight field

lines parallel to the axis, with the charge density at four mesh points held at a negative value of 5 times the local number density, was used. The values of n_s and W were 6.2 10^{14} m^{-3} and 40 eV, and so λ_d = .18 cm. The screening legnth λ_s, from fig. 7.7 is .35cm, 3 mesh sides. As this is small compared with the local radius, 17a, there is no anisotropy in λ_s. It is approximately true that $\lambda_s = 2\lambda_d$. (This was also checked when the Debye length was twice as long, in case grid effects were important.)

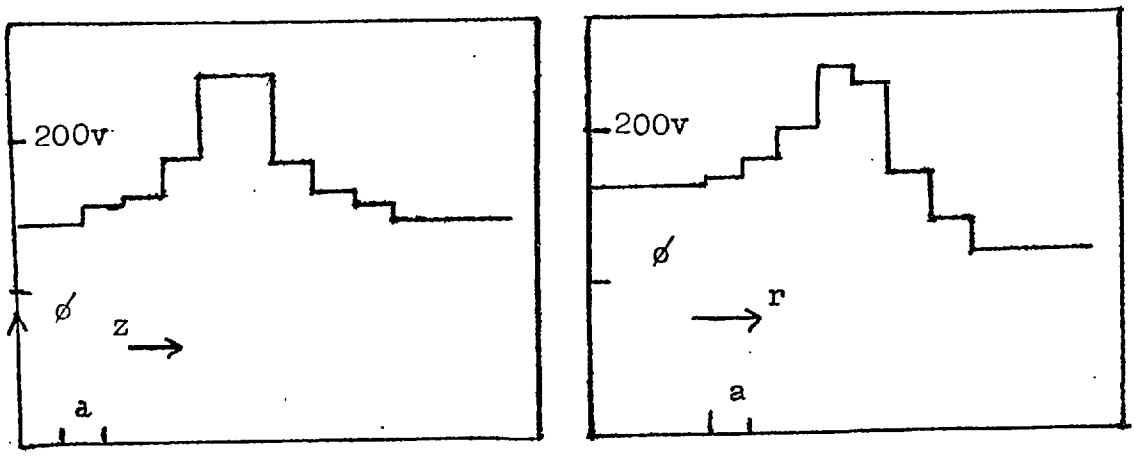

FIG. 7.7 THE SCREENING OF A CHARGE BY THE SIMULATION PLASMA

7.8 Characteristic times

The characteristic times are tabulated and defined in fig. 7.8. There are computational restraints on these times for accurate integration, and physical restraints for meaningful simulation.

FIG. 7.8 CHARACTERISTIC TIMES

Notation	Description	Value (s)	Side conditions
t_{min}	smallest time set by fixed format of storage	$2\ 10^{-12}$	$E_z = 10^4$ V/m
t_e^c	electron cyclotron time	$10^{-11} \rightarrow 10^{-9}$	$B_o = 1 \rightarrow .01$T
dt_e	electron time step	10^{-10}	$dt_e < t_e^t$
t_e^t	electron transit time of cell	$3\ 10^{-10}$	100eV electron
t_e^{tr}	electron transit time around B curvature	$\geq t_e^t$	
$1/\omega_p$	inverse plasma frequency	$2\ 10^{-9}$	$n_s = 6\ 10^{14} m^{-3}$
dt_i	ion timestep	$8\ 10^{-9}$	$dt_i < t_i^t$
t_i^t	ion transit time	$10^{-8} \rightarrow 6\ 10^{-8}$	100eV H→A
t_i^c	ion cyclotron time	$10^{-8} \rightarrow 10^{-6}$	$B = 1 \rightarrow .01$T H
t_i^ℓ	ion loss time	$2\ 10^{-7}$	H
t_c	electron - ion collision time	$> 10^{-6}$	$n_s = 6\ 10^{14} m^{-3}$

Computationally the ion and electron timesteps must be chosen to minimise the errors of the integration. This is ensured if

$$t_{min} \ll dt_e \ll t_e^t \qquad (7.31)$$

which also means that

$$dt_e \ll 1/\omega_p \qquad (7.32)$$

In the plasma there will be an oscillating field at the plasma frequency i.e. $\underline{E}(t) = \underline{E}_o(t) \sin \omega_p t$ with $\frac{d}{dt} E_o(t) \ll \omega_p \underline{E}_o$. The criterion for a particle on the mesh to be affected by the plasma frequency is found from

$$\frac{dv}{dt} = \frac{e}{m} \underline{E}_o \sin \omega_p t \text{ giving}$$

$$\frac{e}{m} \frac{E_2}{\omega_p} > a \qquad (7.33)$$

For hydrogen ions the l.h.s. is about 10^{-5}m, and so the ions in the simulation are unaffected by the plasma oscillations. Consequently the criteria for accurate integration of the ions are

$$1/\omega_p \ll dt_i \ll t_i^t \qquad (7.34)$$

with the field that acts on the ions being an average over the plasma period.

As v_{11} dt is stored in a fixed format, using only 19 bits, small values of v_{11} dt cannot be represented. This is the reason for t_{min}.

The ordering of the plasma parameters in the 10^{15} m^{-3} plasma which is being simulated is

$$t_e^c << 1/\omega_p < t_e^t \ll t_i^\ell \ll t_c \qquad (7.35)$$

The guiding centre approximation makes $t_e^c = 0$. The values of ω_p and t_c are not obvious and so are investigated further, but it is found that the scaling, which is fixed by the Debye length, still allows equation 7.35 to hold. Thus the first stage of the simulation is valid.

7.9 The plasma frequency

This is given by $\omega_p^2 = \frac{n_c\, q_c^2}{\epsilon_o\, m_c}$ which stays constant as q and m are decreased and n increased to represent a large number of single electrons. As with the Debye length this formula will not be exactly true for the simulation. The exact value is unimportant, but an approximate value is necessary for the timestep criterion.

This is obtained from fig. 7.9 which is a plot of the average z velocity of the electrons for a stationary and homogenous background of ions. For the case shown

$$n_s = 6.28\ 10^{14}\ m^{-3}$$

$$\therefore \omega_p = \left(\frac{n_s\, e^2}{\epsilon_o\, m_e}\right)^{\frac{1}{2}} = 1.4\ 10^9\ Hz$$

From fig. 7.9 $\omega_s = .4\ \ 10^9 Hz$. This is consistent

with the screening length being larger than the Debye length, screening being less effective than a three dimensional plasma. As an approximation the screening frequency is given by $\omega_s = .3\omega_p$.

The degradation of the oscillations in fig. 7.9 is due to differing frequencies in different parts of the plasma. The depth of the first minimum (90% of the first maximum)shows how conservative the system is; few electrons remove energy from the system by hitting the walls.

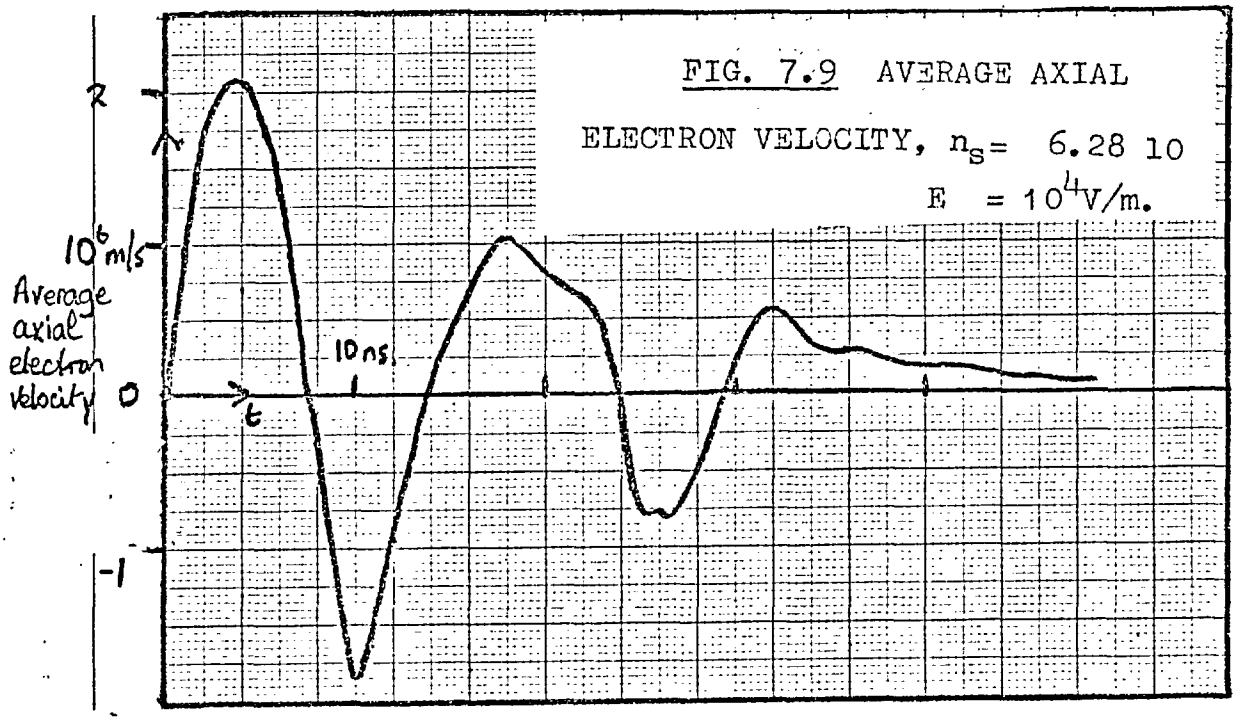

FIG. 7.9 AVERAGE AXIAL ELECTRON VELOCITY, $n_s = 6.28\ 10$ $E = 10^4$V/m.

7.10 The collison frequency

The collision frequency $\omega_c \propto q_c^4$. Hence the collision frequency of the computer plasma will be much

higher than that of the plasma which is being simulated (in the first stage of the simulation). The simulation will be meaningless for times, t, greater than $1/\omega_c$, but valid as long as $t < 1/\omega_c$. As before this quantity has been measured on the computer and compared with the value in a three dimensional plasma.

The particles are constrained to move in one direction and so it is the diffusion coefficient of the parallel velocity which is relevant. This has been calculated by Chandrasekhar (1943) as

$$\langle (\Delta w_{\parallel})^2 \rangle = \frac{q^4 n \ln \Lambda}{2\pi \epsilon_0^2 m^2 w} G(\ell, w)$$

where $\ell^2 = \frac{m}{2kT}$ and $G(x) = (\phi(x) - x\phi'(x))/2x^2$

ϕ being the error function, and $\langle (\Delta w_{\parallel})^2 \rangle$ the rate of change of parallel velocity as an ensemble average.

$$\therefore \quad \omega_c^{\parallel} = \langle (\Delta w_{\parallel})^2 \rangle / w_{\parallel}^2$$

More usefully $\omega_p/\omega_c^{\parallel} = \frac{3\sqrt{2}\ N_d (w\ell)^3}{\ln \Lambda\ G(\ell w)}$ (7.36)

where $N_d = \frac{4}{3}\pi n \lambda_d^3$, the number of particles in the Debye sphere.

To check the validity of eq. 7.36, $\Delta w_{\parallel}$, the rate of change of parallel velocity was measured in the simulation: so that this change is primarily due to interactions with particles within the Debye sphere, a field free, Maxwellian and homogenous plasma was set up, with no applied electric

field and straight field lines parallel to the axis. ($\Delta W_{\parallel}$) was only measured for one particle, being the change of velocity in one timestep/dt_e. But measurements were made over 100 timesteps giving $\langle (\Delta W_{\parallel})^2 \rangle$ and an experimental value of $\omega_c^{11} = 2\ 10^5\ s^{-1}$, for $\ell w = 1.8$.

For comparison with equation 7.36 the correct value of $\Lambda = \frac{\lambda_d}{b_{min}}$ must be used. b_{min}, the smallest value of the impact parameter is effectively given by the cell size, closer particles not interacting. From eq. 7.36. $\omega_p/\omega_c'' = 10^5$ Therefore $\omega_c^{11} = 1.4\ 10^4 s^{-1}$, using the measured ω_p. Both of these values give collision times which are an order of magnitude above the longest time of a run and so the plasma will remain collisionless.

The collision time measured could be due to collective fluctuations, as well as interactions within the Debye sphere. However the measurement does provide a lower limit to the collision time.

The collision frequency of the simulation will be different from equation 7.36 in several ways One basic difference is that the particle forces are calculated as if all the particles were at the centres of the cells. As well as the effect described in equation 7.36 there is also a collision time with the mesh. The precise effect is not clear. The situation appears to be completely different when there is much less than one particle/cell from when

there are many particles/cell. However, as long as the collision time is sufficiently long compared with the time of interest its precise value does not matter.

Unrelated to the collision time is the heating time. This is due to errors in integration. The total thermal energy has been measured. The electric field is a small fraction of the total thermal energy (Hockney, 1971). The heating time is the time for the total average energy of the electrons to rise, and is long (300ns), comparable with the time for which electrons are integrated.

7.11 Programme tests

Routine checks on the Poisson solving and number density scaling were carried out by evaluating the potential from the ions only and checking with the analytic result. Checks on the electron dynamics have already been mentioned (i.e. Debye length, plasma frequency and collision frequency). With the straight lines of force, parallel to the axis, and a uniform background of ions, fluctuations of potential are to be expected at about the thermal levels. These were observed with the simulation. A positive region near the axis was observed, due to the positive fractional background charge, there only being electrons from the third row outwards.

7.12 Results with fixed, uniform background of ions

(a) No applied electric field. The electrons were started with a temperature of 40 eV , and the motion followed for 30 ns, with a uniform background of ions, and no applied electric field. In the absence of an applied E the plasma should be symmetric about the ring cusp. Fig. 7.11 shows the potential field at 13.8 ns. Symmetry is evident. Also shown is the average potential that is seen, needed to contain the electrons; fluctuations at the plasma frequency result from initiating with zero charge density, there being no collisions to damp out the oscillations of individual electrons.

The shape of the potential field does not stay as in fig. 7.11. The region A rises to+100 V at 17.8 ns as opposed to 30V near to the axis,(region B.) Moreover the two regions do not oscillate at the same frequency, A oscillating faster than B, although the potentials in the two regions are correlated.Quasineutrality is obtained overall, .3% of the electrons being at the wall although there are regions where there is only 50% neutrality.

The average plasma potential is 80v , twice the electron temperature. Ben Daniel (1961) has investigated the plasma potential in a mirror machine and finds that it is 5 times the electron temperature, this high a potential

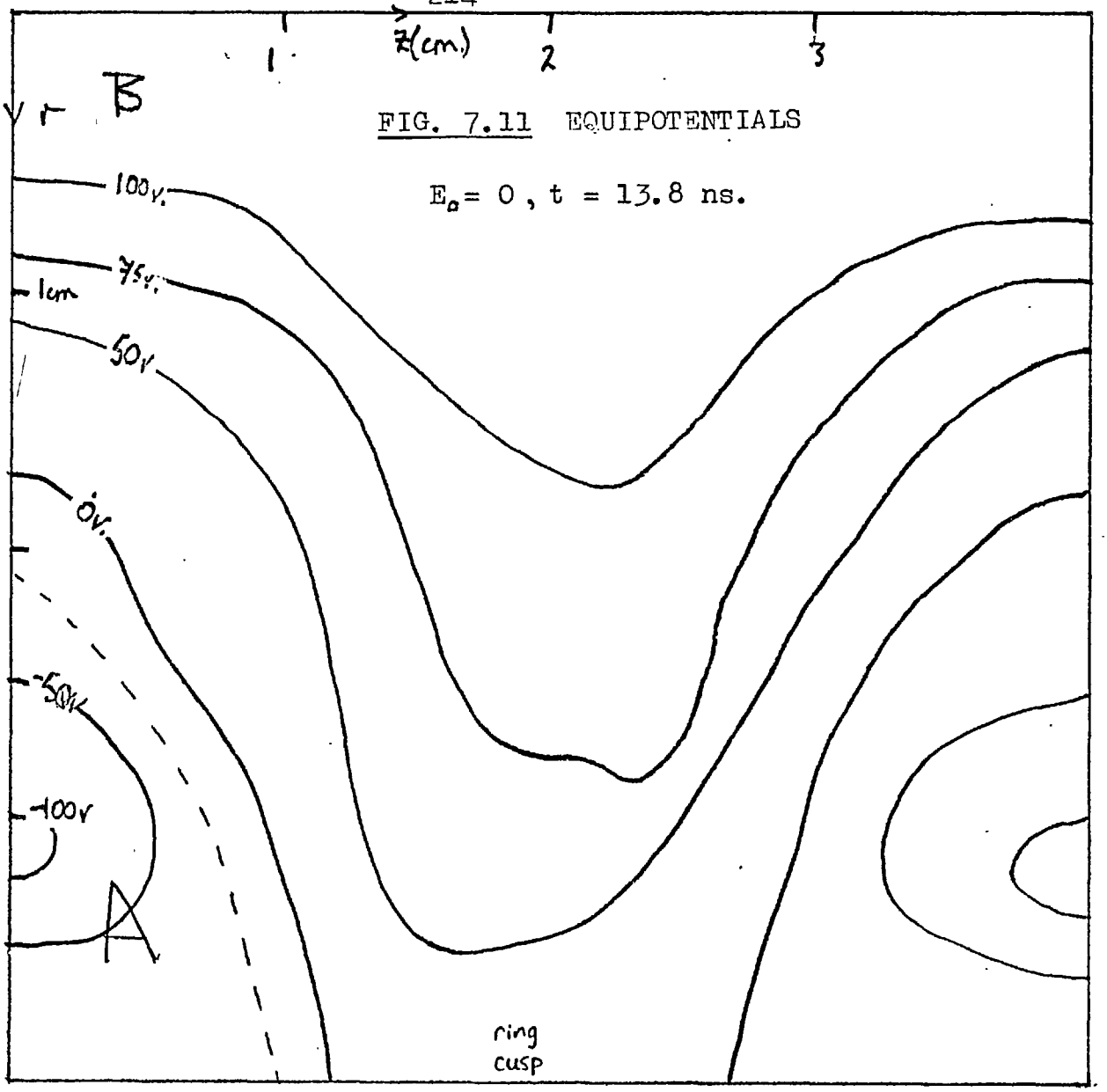

FIG. 7.11 EQUIPOTENTIALS

$E_a = 0$, t = 13.8 ns.

7.11a AVERAGE POTENTIAL ON AXIS AS A FUNCTION OF TIME

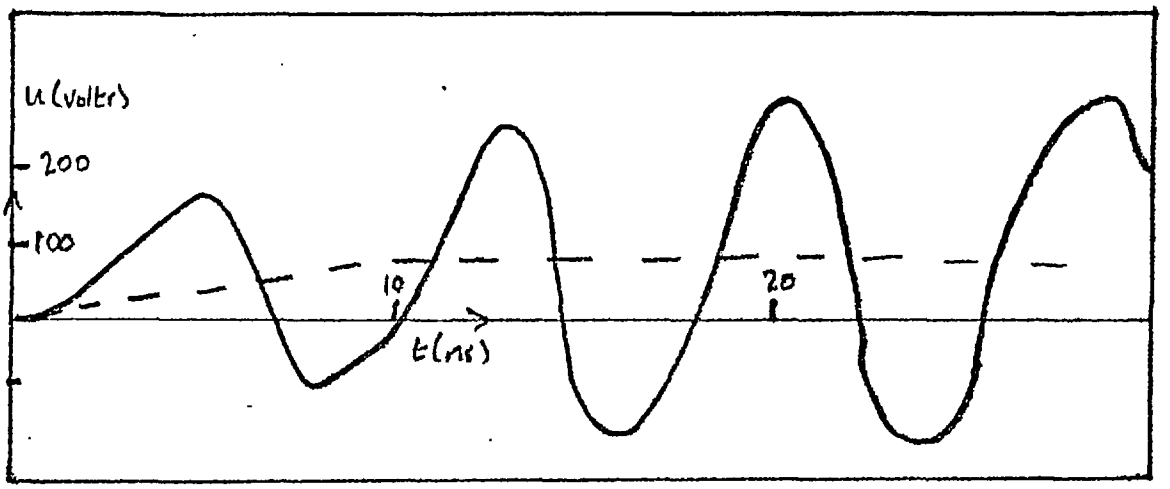

being necessary to restrain the high energy tail of the velocity distributuion. He only considers a stationary solution to the Vlasov equation, whereas this particle model describes a time dependent solution. Thus electrons in the tail of the velocity distribution are allowed to escape on a time scale of $1/\omega_p$ but can only go as far as the wall. A very high average potential is not needed to contain the electrons.

(b) An applied electric field. The electron motion with an applied E_z was studied. Results are reported varying the number of particles, the number density and E_z. The numerical results are explained by means of a qualitative theory.

Initially both 32,400 and 16,328 electrons, but constant n_s, were tried, and as expected the results were very similar. Henceforth 16,328 electrons were used because of the smaller core store needed and thus better job turnaround. The results of a run with $E = -10^4$ V/m, $n_s = 6.28\ 10^{14} m^{-3}$, $T_e = 40$ eV, are shown in figs. 7.12, 7.13, 7.14, and 7.15. I_z in fig. 7.12, is the average of $v_{11} \cos\theta$ over all of the electrons. Fluctuations occur at the plasma frequency and the zeroes of the current are related to the maximum in the average potential near to the axis, as at this time the number of electrons at the wall is at a turning point.

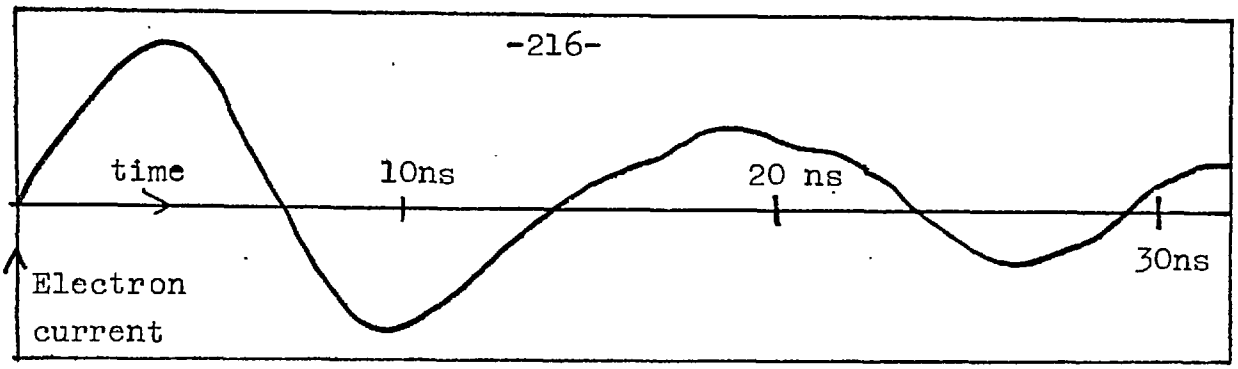

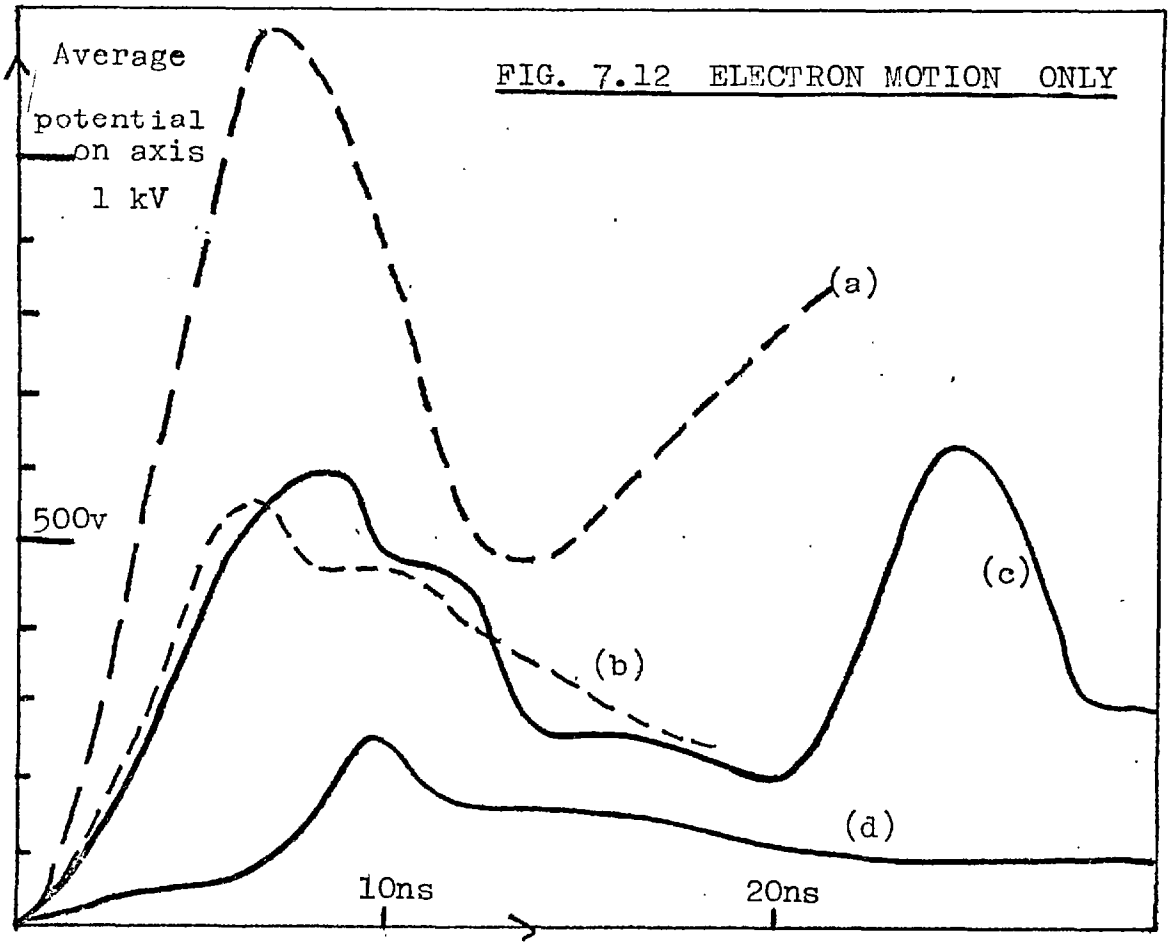

FIG. 7.12 ELECTRON MOTION ONLY

(a) $E=2\ 10^4 v/m, n_s=6.3\ 10^{14} m^{-3}$: (b) $E=10^4 v/m,\ n_s=1.2\ 10^{15} m^{-3}$

(c) $E=10^4 v/m, n_s=6.3\ 10^{14} m^{-3}$: (d) $E=10^4 v/m,\ n_s=6.2\ 10^{14} m^{-3}$

square field

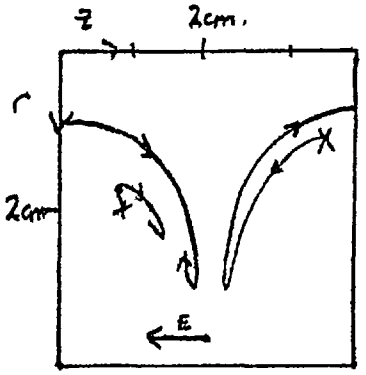

TYPICAL TRAJECTORIES

A fast and slow electron are shown: the displacement perpendicular to the field lines is for display.

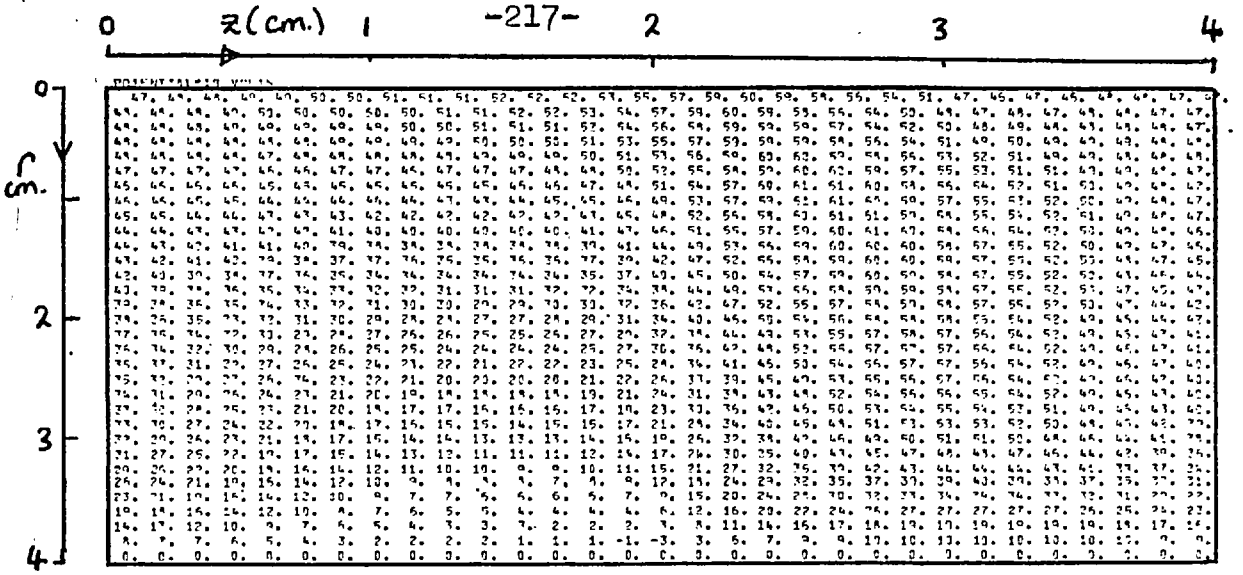

FIG. 7.13 THE POTENTIAL AT 5.8ns. 1 ≡ 10 volts

E_a

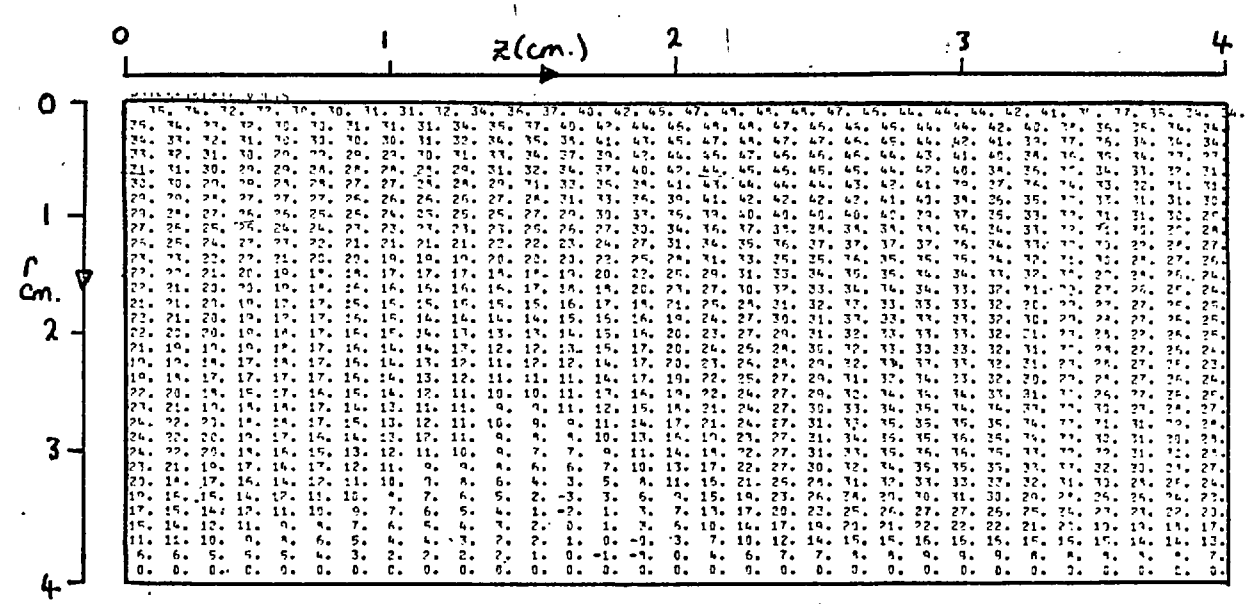

ring
cusp

E_a

FIG. 7.14 THE POTENTIAL AT 34ns. 1 ≡ 10 volts

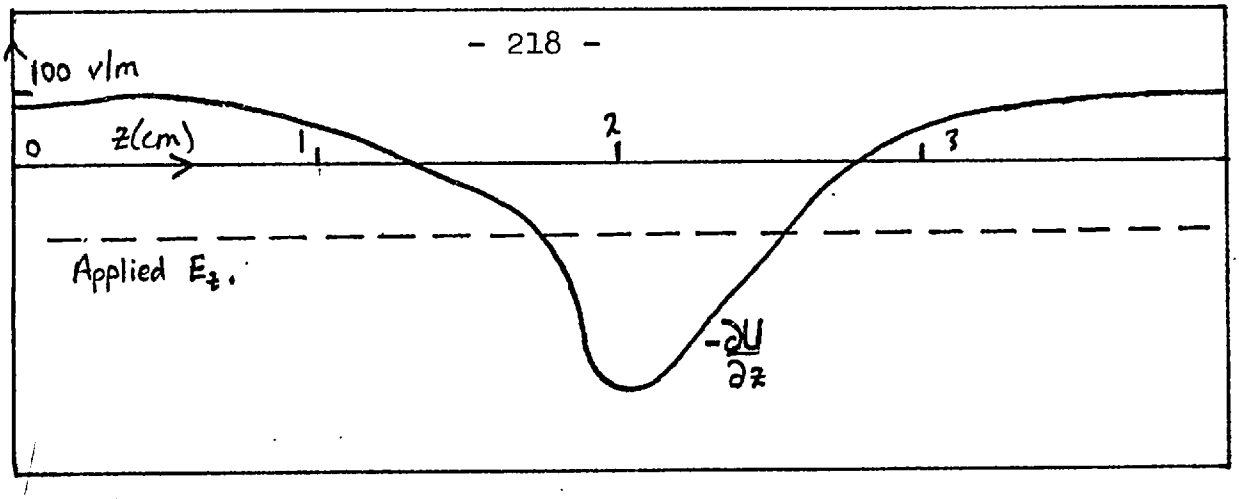

FIG. 7.15 AVERAGE $-\frac{\partial U}{\partial z}(z)$

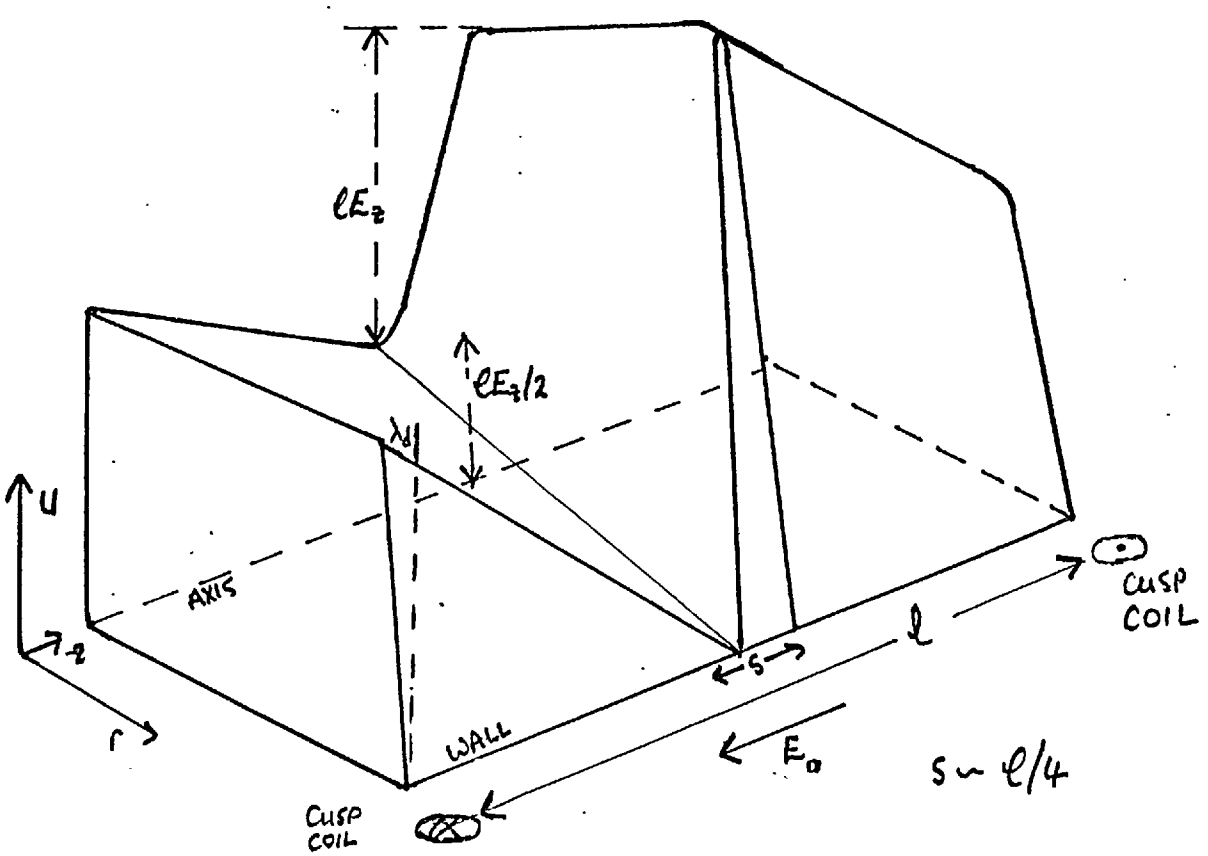

FIG 7.16 THE ELECTROSTATIC POTENTIAL (Schematic)

Individual electrons oscillate along their field lines. Their maximum excursion is approximately $\lambda_s \frac{v}{v_{th}}$. The two electrons shown in fig. 7.12 are low and high velocity. The high energy one moves the length of the cusp against the applied E_a but eventually is reflected by the radial electrostatic field. The low energy electron does not move far against E_a, and then moves 1 cm before being reflected by $-\frac{\partial U}{\partial r}$. After reflection it hovers, there being no E_{11} at this point. Cases of $T_e = 0$ were also run. All electrons in this case are accelerated by E_a and are displaced by about .5 cm. The overall potential is similar to the case of hot electrons, being about 20v lower.

Fig. 7.13 shows the electrostatic potential on each cell at the time of greatest general excursion along the field lines(note that the number/cell equals the radial cell number for constant density). Departures from neutrality occur in sheaths at both the edge of the tube and the ring cusp. The screening length is larger than the 3 cells of section 7.6 because the velocity of the electrons is larger than the 40eV thermal velocity, being between 100 to 200 eV. Even at this time of least neutrality only 30% of the electrons are at the wall. At later times, e.g. fig. 7.14 greater neutrality is achieved, with a lower average potential.

As before, the simulation is producing oscillations at the plasma frequency about d.c. values of potential, number density, current, etc., It is the d.c. values which are of interest, and which must be averaged. The average current is zero; the average potential is 300V; the average $-\frac{\partial U}{\partial z}$ under a coil, near to the axis is 85V/cm, which nearly cancels the applied field of - 100v/cm. Fig. 7.15 shows the value of $-\frac{\partial U}{\partial z}$ as a function of z. The applied field is partially annulled over 3 cm under the coil, and enhanced by up to 3 across the ring cusp.

The unexpected results on the potential field can be qualitatively explained. In the m.h.d. approximation an electrostatic potential is set up so that div $\underline{j}$ = 0. Similarly in this model the charge separation causes a field which opposes any further motion of electrons along the field lines. Electron motion along the field lines causes charge separation despite div $\underline{B}$ = 0, because the region is bounded and $v_{11} \propto E \cos\theta$.

An approximation to the condition of annulment of the applied field

$$E_a \cos\theta = \frac{\partial U}{\partial z} \cos\theta + \frac{\partial U}{\partial r} \sin\theta \qquad (7.37)$$

This omits terms equivalent to $\propto \nabla T$, $-\frac{1}{ne} \nabla nkT$ and $\frac{m_e c^2}{ne^2} \frac{dj}{dt}$ in the Ohm's law. Eq. 7.37 can however be qualitatively satisfied, and implies that the field lines are equipotentials of the sum of the electrostatic and the applied potentials.

Under a cusp coil $\frac{\partial U}{\partial z} = E_a$, from eq. 7.37. This is seen in fig. 7.15. Downstream (parallel to E) of the ring cusp the diverging field lines have to be opposed by $\frac{\partial U}{\partial r}$.

$$\frac{\partial U}{\partial r} = (E_a - \frac{\partial U}{\partial z}) \cot \theta$$

Upstream this effect is reversed, and so the potential should increase towards the outside. In the case shown in fig. 7.14 the potential increases with r upstream of the ring cusp. The potential jump between the wall and plasma upstream of the ring cusp occurs over a screening distance. This is in contrast to downstream where the radial field occurs over the whole radius. The potential, in the simulation is poor on axis as here there are no electrons.

The essential features of the potential predicted by this model and verified by the simulation are sketched in fig. 7.16. It must be emphasised that the potential arises from a slight displacement of the electrons, of the order of the Debye length. It is not caused by the electrons being accelerated to this energy in E_a. They do not move far enough.

As a further check of this model runs were performed with a larger n_s and E_a. These are also drawn on fig. 7.12, and show, as expected, that the potential is proportional to E_a and independent of n_s.

Striations in the number density were observed. The modulations were in the direction normal to the field lines, and are thought to be similar to the normal modes of oscillations of beads on a string, the beads being the electrons oscillating along the field lines.

These large electric fields will have an adverse effect on the containment of the ions. The quantitative effect can be seen by integrating the ions.

7.13 Integrating both species of particles

A hydrogen plasma was chosen for the simulation as Z is known. As the simulation will exhibit losses greater than those in chapter 6 ,the case of most successful confinement i.e. $E_z = 10^4$ V/m, $B_o = .2$T and a homogenous initial density was considered. With an ion timestep of 8 ns , integrating the electrons for 2 ns every ion integration, 1 hour of CDC6600 time is needed to simulate 600 ns.

The average value of v_z(for the ions) , and the number of ions lost, which are shown in fig. 7.17, are similar to chapter 6, but the losses are greater. The number density and velocity in the r - z plane are shown in figs. 7.18 and 7.19.

After 60 ns (fig.7.18), the large axial acceleration under the cusp has cleared the plasma from this region and

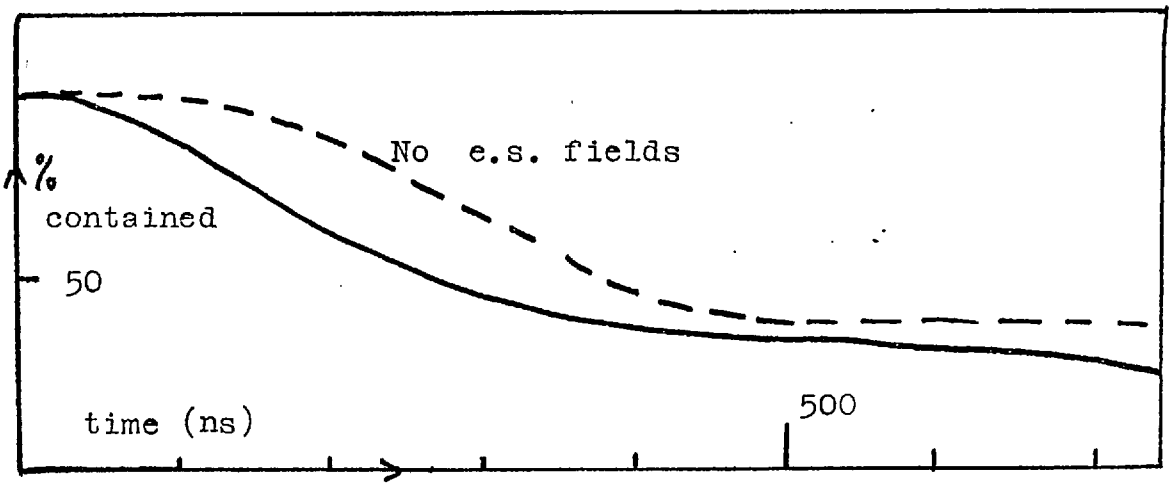

FIG. 7.17 ION MOTION WITH ELECTROSTATIC FIELDS

Hydrogen , E = 10^4 v/m, B_o = .2 tesla.

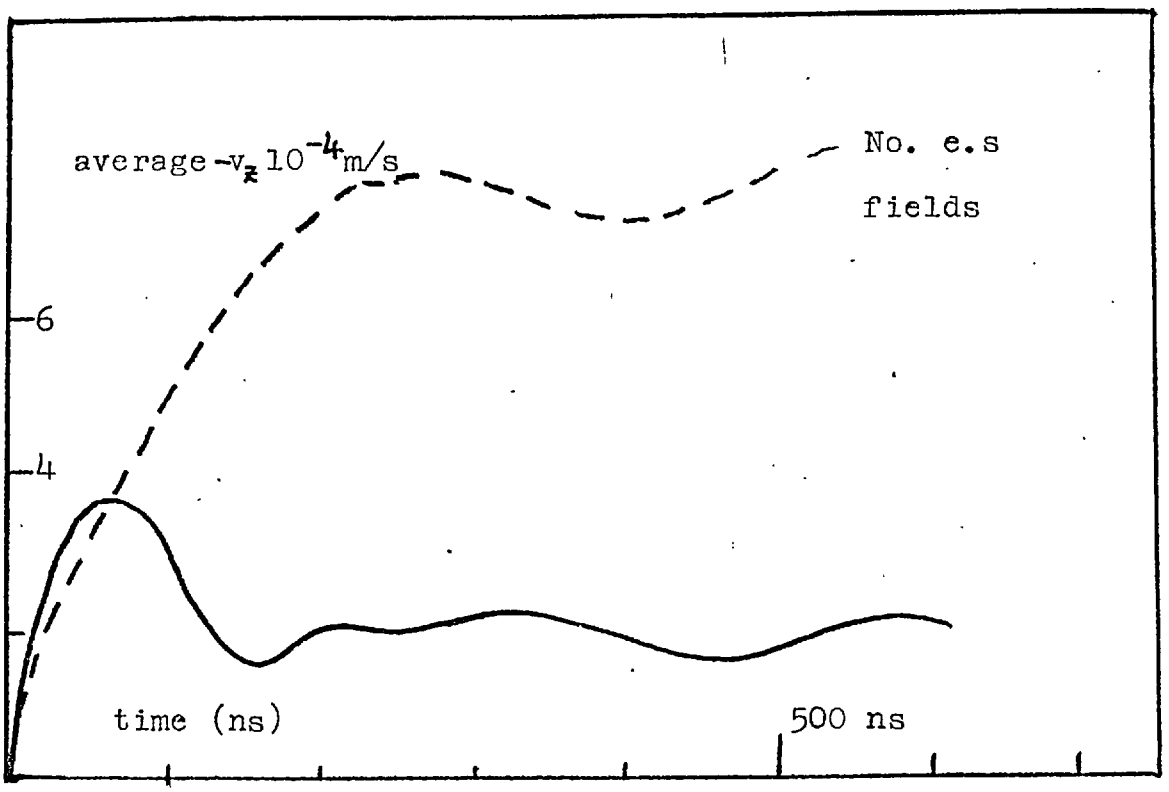

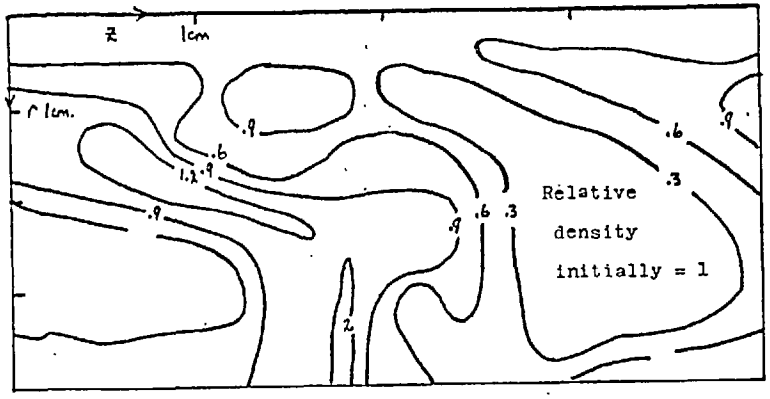

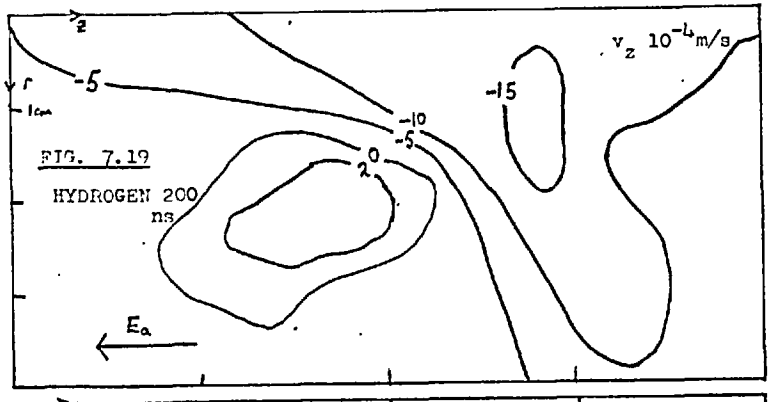

FIG. 7.19

HYDROGEN 200 ns

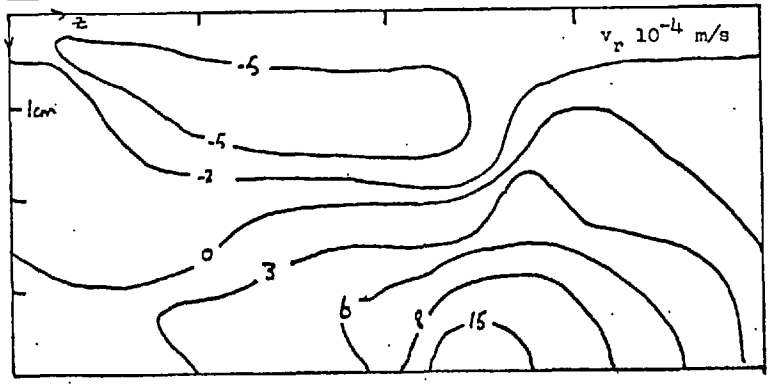

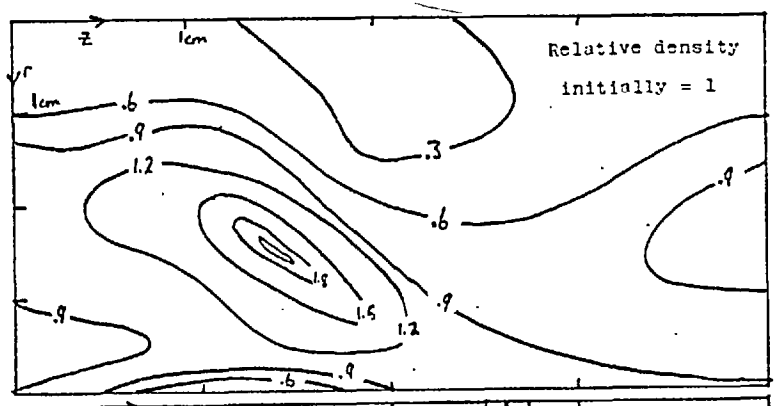

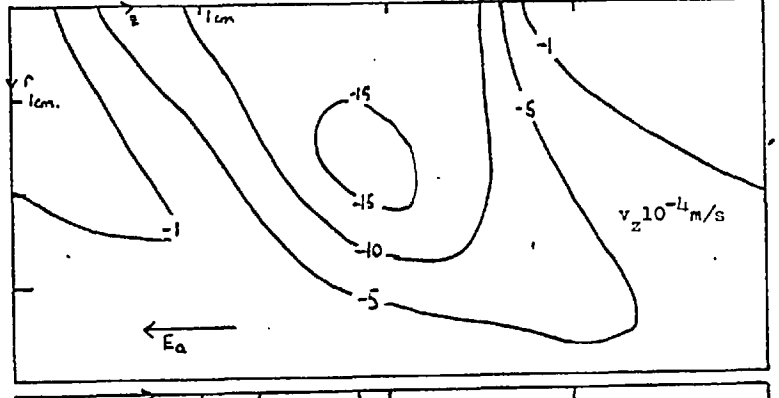

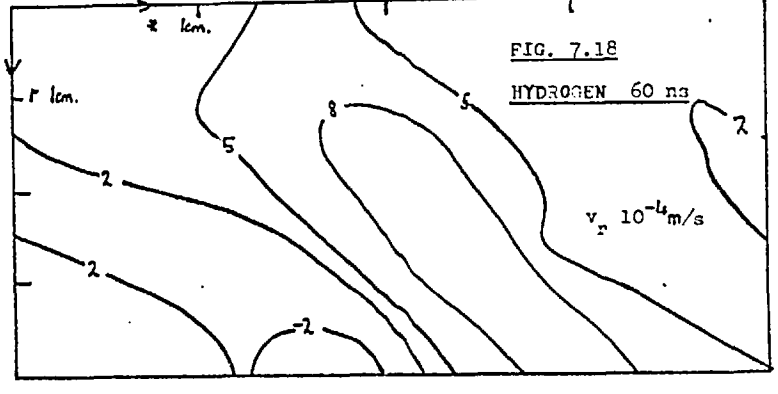

FIG. 7.18

HYDROGEN 60 ns

it has accumulated in a region downstream of the ring cusp. This compression has been enhanced by radial motion. The outward motion near the axis is due to the radial electrostatic field, whereas the inward motion near the wall, is due to the magnetic focussing. The z acceleration is greater upstream of the ring cusp as here the electrostatic field is greater. Under the coil and near to the axis, there is little net field but the effect of the applied field is greater near to the wall. The losses have only occurred upstream of the ring cusp and from the radial velocity will continue to occur here. Downstream of the cusp the magnetic focussing has caused the plasma to move away from the wall. Particles which have been accelerated through the ring cusp region have a Larmor radius of 3cm in a .1T field.

After 200 ns (fig. 7.19) the region upstream of the ring cusp has been cleared of plasma, although near to the axis, where v_z is larger, plasma has been convected from the next cusp. The high density region has been split, fast particles have moved downstream and the rest, which are those particles which have started in the region and not been accelerated, have moved outward, there only being focussing by virtue of v_z. Those which have moved downstream have not been accelerated as they have not reached the next cusp (moving at 30 cm/μs). Substantial loss has still only occurred

upstream of the ring cusp but is starting to occur downstream. Focussing onto the axis has started downstream of the ring cusp.

Later, after 500 ns, the particles have been split into two regions. Unfortunately most are in the region near to the wall, downstream of the ring cusp, moving towards the wall and upstream. The region near to the axis is still being accelerated. The plasma which is being lost, will appear at the wall downstream of the ring cusp.

This is seen at 815 ns. Losses are still occuring at the ring cusp. Some of the particles near to the axis have a velocity of at least 40 10^4 m/s. Their trajectories consist of low and high frequency oscillations. As shown in section 7.17 the frequency of oscillations is

$$\frac{eB_o}{2m_o} = 10^7 \text{ s}^{-1} \equiv > 2 \text{ cm.}$$

This periodic excursion to a large radius causes a scrape off of particles when they reach a maximum of their oscillation. The extremes of the oscillations could be further out than the initial radius as discussed in section 5.4.

Results of a run, simulating an argon plasma, are displayed in fig. 7.20. Here, with a low q/m ratio, the difference between the containment with and without an electrostatic field is marked. The radial loss of particles and the depth from the wall $m2E_r/(ZeB_o^2)$ from which loss

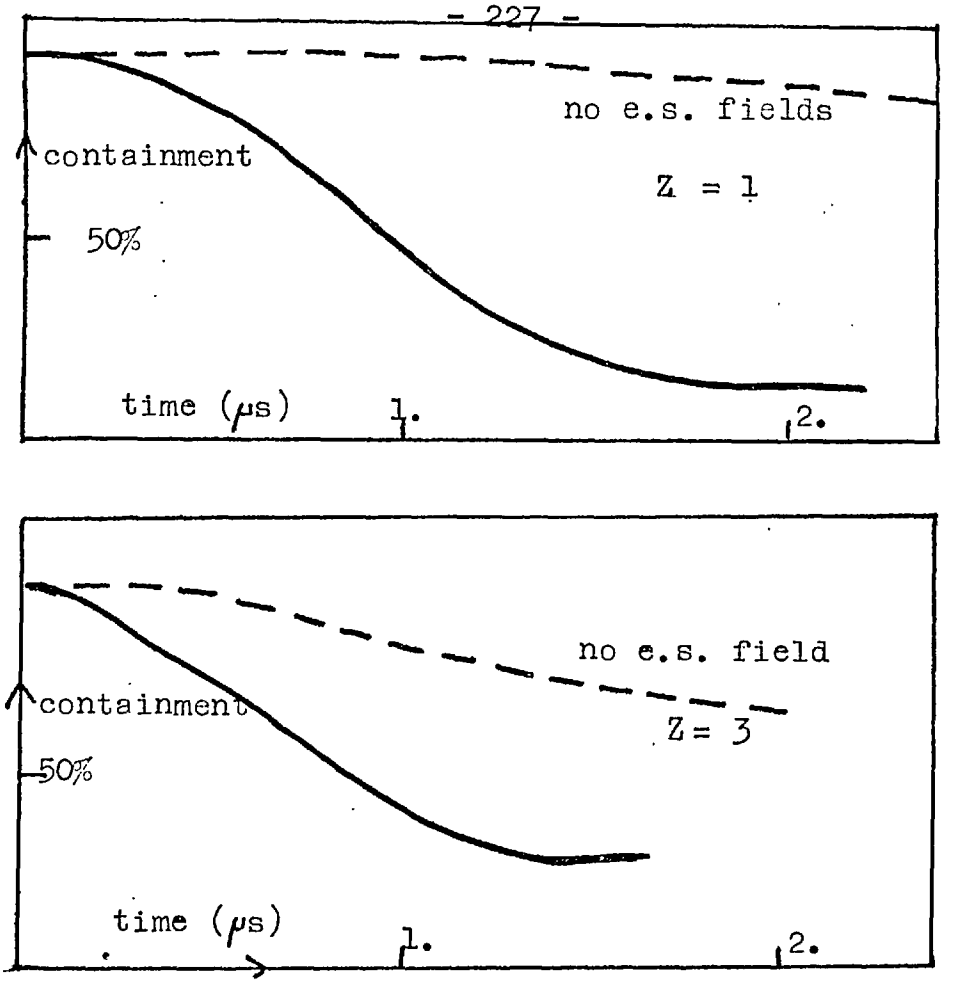

FIG. 7.20 PARTICLE CONTAINMENT FOR ARGON

$E = 10^4$ V/m , $B_o = .2$T.

can occur reduces the difference in loss for Z = 1 and 3.

7.14 The second stage of the simulation; application to higher density

The electric field which has been found in this low density plasma will also be present at higher number densities. The electric field is established on a timescale of $1/\omega_p$. In a plasma of $n = 10^{20} m^{-3}$, W = 10 eV, $\nu_c \sim 10^9 s^{-1}$

$\omega_p \sim 10^{12} s^{-1}$.

The electrostatic field will exist for times longer than $1/\nu_c$. It is caused by more electrons being able to move a distance λ_d into the ring cusp region than can move through it i.e. $\sigma E \gg \frac{\delta E}{1+\omega^2\tau^2}$,

so as long as $\omega\tau = \frac{\delta B_r}{ne} \gg 1$, the electrostatic field must exist. As shown in chapter 11 this is most of the tube.

7.15 A pathological self consistent solution

There is one steady state solution to eq. 7.37 suggested by M.G. Haines. This is

$$\frac{\partial U}{\partial z} = E_a, \quad \frac{\partial U}{\partial r} = 0.$$

This has to be violated at the boundary but if the potential is allowed to rise at the boundary $\frac{\partial U}{\partial r} = 0$ can be allowed throughout the region. The z translational symmetry implies a discontinuity in U across the ring cusp. This is allowable on this model as the electrons cannot cross the ring cusp.

The charge distribution necessary to create this potential is shown in fig. 7.21. It is a thin disc of + ve and - ve charge,

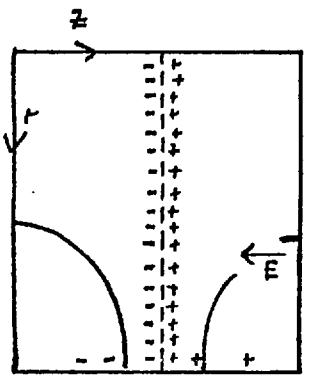

FIG. 7.21 SCHEMATIC DRAWING OF THE CHARGE DISTRIBUTION NECESSARY FOR THIS SOLUTION

together with a small amount of charge on the wall to prevent edge effects .

It can be seen that starting from neutrality this state will not develop easily, if at all. For the discs of charge arise from a bodily displacement of the electron fluid along only a few field lines. If however, initially there is neutrality, then much more charge than is necessary for the steady state solution is deposited on the walls. The result is radial and axial fields.

For the simulation this solution certainly does not develop within 10 plasma periods. The potential is similar to that suggested here, but is different in that there is a radial electric field. The effect of the radial electric fields is to broaden the region over which the axial discontinuity occurs. For field lines which are nearly normal to the axis the axial electric fields will have a much smaller effect than the radial field and so the axial field does not have to be annulled. As seen from the computation the 'discontinuity' in the potential occurs over L/4. If the steady state solution were set up then the thickness of the discontinuity would be

$$t = 2\sqrt{\frac{U_a m}{B_o^2 e}} \qquad (7.38)$$

twice the Larmor radius, U_a being the applied voltage

between the cusps. For $B_0 = .2T$ this is typically 2 mm.

The loss time on this model, is $\sqrt{2}$ smaller than for the case of the trajectories in chapter 6 . If the velocity of the ions in the ring cusp becomes $\sqrt{\frac{2U_e}{m}}$ and the loss time is the time taken to drift to the next ring cusp plane then

$$t_\ell = L\sqrt{\frac{m}{2U_e}} = 200\sqrt{\left(\frac{10,000}{V_m}\right)\frac{A}{Z}} \quad \text{ns.} \qquad (7.38a)$$

7.16 The field produced by the azimuthal electron current.

If the azimuthal electron current flows in a strip of thickness x, given by an electron Larmor radius then if

$B_r = B_o\, kr/2$

$$x^2 = \frac{8\, U_a m}{B_o^2 k^2 r^2 e} \qquad (7.39)$$

$$\therefore \quad j_e = ne\, v_e = \frac{2ne\, U_a}{xB_o kr}$$

$$\therefore \quad dI_e = j_e\, x\, dr$$

$$\therefore \quad b_z^1 = \frac{\mu_o ne\, U_a}{B_o k\, r_s} \quad \text{if} \quad x \ll r$$

where r_s is the radius where integration must stop because either the current flow stops or x becomes comparable with r, in which case

$$r_s = \left(\frac{8U_a m}{k^2 B_o^2 e}\right)^{\frac{1}{4}}$$

If the currents flows at smaller radii the solenoid approximation can be used for the field produced. r_s is typically 5 mm. (U_a = 200V , B_o = .4T). It is reasonable to take this as a value fixed by either an $\omega\tau < 1$ criterion or by the size of a magnetic probe. In this case

$$b_z = 120 \left(\frac{n}{10^{20}}\right)\left(\frac{V_m}{10kV}\right)\left(\frac{.4}{B_o}\right) \quad \text{gauss} \qquad (7.40)$$

7.17 The equilibrium of the polytron

The particle description of the polytron allows an estimate to be made of the equilibrium. The effect of pressure gradients and self pinching are included here although heuristically. The experiment is not achieving the necessary velocities, and so the question of equilibrium is academic. It is necessary though to have some idea of where an equilibrium may lie.

Initially the azimuthal field produced by the plasma can be neglected and so in cylindrical coordinates the azimuthal equation of motion is

$$\frac{dv_\theta}{dt} = v_z \omega \frac{kr}{2} \sin kz - v_r \omega \cos kz \qquad (7.41)$$

where $B_r = B_o \frac{kr}{2} \sin kz$, $B_z = B_o \cos kz$, $\omega = \frac{eB_o}{m}$

If $v_r \ll \frac{kr}{2} v_z$ then $v_\theta = -\frac{\omega r}{2} \cos kz + A$.

As shown in chapter 6, if $kz \rightarrow kz + \pi$ then $v_e \rightarrow -v_e$ and so A = 0. This can be substituted into the radial equation of motion giving

$$\frac{dv_r}{dt} = -\frac{\omega^2 r}{2} \cos^2 kz = -\frac{\omega^2 r}{2} \cos^2 kv_z t \qquad (7.42)$$

In the interval $kz = \pi$ this gives the Busch lens formula

$$\frac{\overline{dv_r}}{dt} = -\frac{\omega^2 r}{4} \qquad (7.43)$$

but otherwise it can be integrated if v_z is constant

$$\therefore v_r = -\frac{\omega^2 r}{2}\left(\frac{1}{4kv_z} \sin 2kv_z t + \frac{t}{2}\right) + A$$

and so the condition $\frac{krv_z}{2} \gg v_r$ becomes

$$\frac{v}{\omega^z} \gg \frac{1}{2k}$$

Integrating again for $t \ll 1/\omega$, $r = r_o + v_{ro}t - \frac{\omega^2 r t^2}{8} + \frac{\omega^2 r}{8k^2 v_z^2} \cos 2kz$ (7.44)

Examination of the high frequency part shows that the particles come in under the ring cusp and are at a maximum under the coil This is in contrast to the situation when they start from rest and reach a maximum excursion near to the ring cusp.

At a lower frequency the particles execute harmonic motion about the axis with a frequency $\omega/2$ from eq. 7.43.

Collective forces acting are the pinching and the radial pressure gradient. As this is only a heuristic treatment suppose there is a flat number density gradient up to $r = r_o$ and only ions are carrying axial current, then

$$j_z = ne\ v_z$$

and $$b_\theta(r<r_o) = \mu_o r\ ne\ v_z/2$$

The radial acceleration due to this pinch is

$$\frac{dv_r}{dt} = \frac{e}{m} v_z\ b_\theta = -\ r\ \mu_o\ \frac{ne^2 v_z^2}{2m}$$

Also there is an electrostatic field set up dragging the ions out , which is seen in section 7.12. This electrostatic field is $E_r = f\ \frac{kT}{er_o}$ where $f \sim 6$. The equilibrium condition is then approximately

$$f\ \frac{kT}{mr_o} = r_o\left(\frac{\omega}{4}^2 + \frac{\mu_o ne^2 v_z^2}{2m}\right)$$

The values of radius as a variable dependent on n, T_e and v_z are shown for hydrogen, with B = .1T.

r (cm)	T (eV)	$n(10^{20}m^{-3})$	v m/s
.6	10	1.	10^5
2	100	1.	10^5
.8	10	.1	10^5
2.6	100	.1	10^5
.3	10	10.	10^5
.06	10	1	10^6

The values of the radii are approximately 6 times larger for argon.

The axial particle density can also be described by this model. The axial equation of motion, in the absence of a net accelerating field is,

$$\frac{dv_z'}{dt} = -\omega \frac{kr}{2} v_\theta = \frac{kr}{8} \omega^2 r \sin 2kz$$

$$\therefore \quad v_z' = -\frac{r^2\omega^2}{4v_z} \cos 2kz + v_z \text{ if } v_z' - v_z \ll v_z$$

If N(z) is the axial line density then

$$N(z)\, v(z) = \text{constant}$$

$$\therefore \quad N(z) = N_o \left(1 + \frac{r^2 \omega^2}{8 v_z^2} \cos 2kz\right)$$

The line density is greatest in the region beneath the coil. As energy is conserved then the axial velocity is lowest here because the azimuthal velocity is largest.

$$n = \frac{N}{\pi r^2} \quad \text{and so from eq. 7.44}$$

$$n(z) = n_o \left(1 + \frac{\omega^2}{4v^2} \left(\frac{r_o^2}{2} - \frac{1}{k^2}\right) \cos 2kz\right)$$

The modulation of number density will depend on the larger of $r_o^2/2$ and $1/k^2$, but in any case will be much less than 1 as $\frac{2k\, v_z}{\omega} \gg 1$.

In conclusion an equilibrium is expected if for hydrogen $v_z \sim 5\ 10^5$ m/s, The necessary number density, temperature and radius requirements seem quite easy to meet. As far as extension to a toroidal geometry is concerned this is below the limiting velocity derived in chapter 5.

7.18 Summary of chapter 7.

The objective of the work of chapter 7 was to establish the amount of additional loss caused by the electrostatic field. This has been achieved as well as the unexpected (a priori) result that plasma acceleration is primarily from under the ring cusp. The single particle approach provides a straight forward cause and effect reason for this. The thickness of the plane is not clear. The simulation indicates that it is a quarter of the coil separation, but arguments are advanced that it could be either the electron Larmor radius, or the separation of lines of force for which $\omega\tau > 1$ along their whole length. Experimentally this sheath may be blurred by it moving because of the field produced by the plasma. Also the effect of b_θ could cause drift of electrons across the ring cusp.

A sheath formation is implied in the m.h.d. code, reported in the paper with Watkins(p.399). The fluid is seen tobe accelerated only in a region beneath the ring cusp, the width of the region being mesh limited. Hence the axial electric field necessary for ion acceleration must also appear across this sheath even in this m.h.d. approximation.

CHAPTER EIGHT

A FLUID APPROACH TO THE HEATING AND IONISATION OF THE POLYTRON

A spatially independent model (similar to Haines(1963), Dunnett (1968)) is used to study the heating and ionisation of the polytron. A motivation for this work was to use the ionisation rate as a temperature diagnostic for the experiment.

A more complete solution of the m.h.d. polytron equations has been attempted by Watkins(1971) but he has so far avoided the ionisation equation by considering fully ionised hydrogen.

8.1 The corona model

The details of the models applicable for equilibrium relations are described exhaustively by a number of authors such as Griem (1964) and McWhirter (1965).

A necessary condition for a plasma to be in l.t.e. is

$$n_e > 10^{14}\ W^{\frac{1}{2}}\ \chi(p,q)^3\ cm^{-3} \qquad (8.1)$$

where W is the electron temperature (eV) and $\chi(p,q)$ the largest energy level difference in eV. As χ is typically 10's of eV , l.t.e. is not applicable in the polytron.

Thus the rate equations for the number density of the ground level of an ion of charge Z, n(Z) have to be solved. These are of the form

$$\frac{dn(Z)}{dt} = n(Z-1)\, n_e\, S(W,Z-1) - n(Z)\, n_e\, S(W,Z) - n(Z)\, n_e\, \alpha(W,Z) + n(Z+1)\, n_e\, \alpha(W,Z+1) \quad (8.2)$$

where S is an ionisation coefficient and α a recombination coefficient.

$Z \geqslant 0$ and it is a sufficient experimental approximation to consider only $Z < 6$.

It is assumed that all the atoms are in their ground state. Kolb and McWhirter allowed for the metastable state of helium but found that the population of this state did not exceed 10% of the ground state population.

The ionisation rate is calculated from

$$S(W,Z) = \frac{1.64\ 10^{-6}}{\chi(Z,g) W^{\frac{1}{2}}} \exp(-\chi(Z,g)/W)\ \mathrm{cm}^3\ \mathrm{s}^{-1} \quad (8.3)$$

taken from Bates et al (1962). α is taken from Seaton (1959),

$$\alpha(W,Z) = 5.2\ 10^{-14}\ Z\ \lambda^{\frac{1}{2}}(.43 + \ln(\lambda^{\frac{1}{2}}) + .47\ \lambda^{-\frac{1}{2}})\ \mathrm{cm}^3\mathrm{s}^{-1} \quad (8.4)$$

where $\lambda = \chi(Z-1,g)/W$. Typically $S(W,Z) \gg \alpha(W,Z)$.

The coronal equations neglect the effect of collisions on transitions between levels. This is not valid for high principal quantum number levels, and for these l.t.e. with the continuum applies (see for example chapter 3). But if collisional transitions are important the rate coefficients should be modified. Kolb and McWhirter quote

$$n_e < 10^{12}\ \chi^3\ W^{\frac{1}{2}} \exp(\chi/5W)\ \mathrm{cm}^{-3} \quad (8.5)$$

for there to be fewer collisional than radiative transfers,

which for the netural argon resonance line gives

$$n_e < 6\ 10^{15}\ cm^{-3}$$

at 5 eV , the minimum of this function.

For higher stages of ionisation the critical value of n_e is much higher, being proportional to Z^7 (Griem, 1964, eq. 6.55). It is this ease of satisfying the coronal criterion that is the reason for not considering collisional radiative modifications here, yet doing so in the lower temperature cusp compression simulation.

8.2 Results taken with a constant temperature

To gain insight into the orders of magnitude involved, in the ionisation of argon, the rate equations were solved with a constant electron temperature. The solutions consist of a linear rise of $\bar{Z}$, the average ionic charge, followed by a plateau when $\chi(\bar{Z},g) \gg W$. For the linear rise an experimental value is

$$\frac{d\bar{Z}}{dt} = .5 \pm .3 \left(\frac{n}{10^{20}}\right) \exp\ (-15/W)\ \mu s^{-1} \qquad (8.6)$$

(where n is the total ion density) for $\bar{Z} < 4$,

$10^{20}\ m^{-3} < n < 10^{22}$, $5eV < W < 100$ eV.

8.3 The use of an energy equation to determine W

The temperature here is determined by integrating an

energy equation. If S is the source of energy then

$$S = \frac{3}{2}\frac{d}{dt}((n^o + n_e)kT) + \frac{d}{dt}\left(\sum_{i=1}^{\infty} I_i\, n_i\right) \qquad (8.7)$$

where n_i is the number density of ionisation stage i, I_i is the total energy to create stage i ion from neutrals and

$$n^o = \sum_{i=0}^{\infty} n_i$$

$$\therefore \quad S = \sum_{i=1}^{\infty}\left(\frac{3kT}{2} + I_i\right)\frac{dn_i}{dt} + \frac{3k}{2}\left(n^o + \sum_{i=1}^{\infty} n_i\right)\frac{dT}{dt}$$

Two different values of S were used. Firstly $\frac{j_z^2}{\sigma}$ the Ohmic heating due to the toroidal current. Secondly $j_z E_z$, the total energy input to the plasma from the applied electric field. The neglect of the energy input from the azimuthal currents was due to the experimentally observed insensitivity of the temperature to ϕ . The theoretical justification is

$$\frac{j_\theta E_\theta}{j_z E_z} \sim ne\frac{E_z}{B_r}\frac{r}{2}\frac{\partial B_z}{\partial t}\Big/(nev_z E_z) = \frac{r}{2}\frac{1}{B_r}\frac{\partial B_z}{\partial t}\frac{1}{v_z} \ll 1$$

as $\frac{B}{B_r^z} \ll 1$ in the cusp region and $\frac{r}{2}\frac{\partial}{\partial t} \lesssim v_z$.

The source $j_z E_z$ should represent too much heating as some of the energy should go into mass motion. The source was related to experimental values of V_m(main bank voltage); $j_z = 15.3\, V_m t\, 10^7$ A/m^2, assuming the initial linearly rising current is uniform .

The result of using j_z^2/σ as a source, was that the time for the density of AIII to peak was much later than

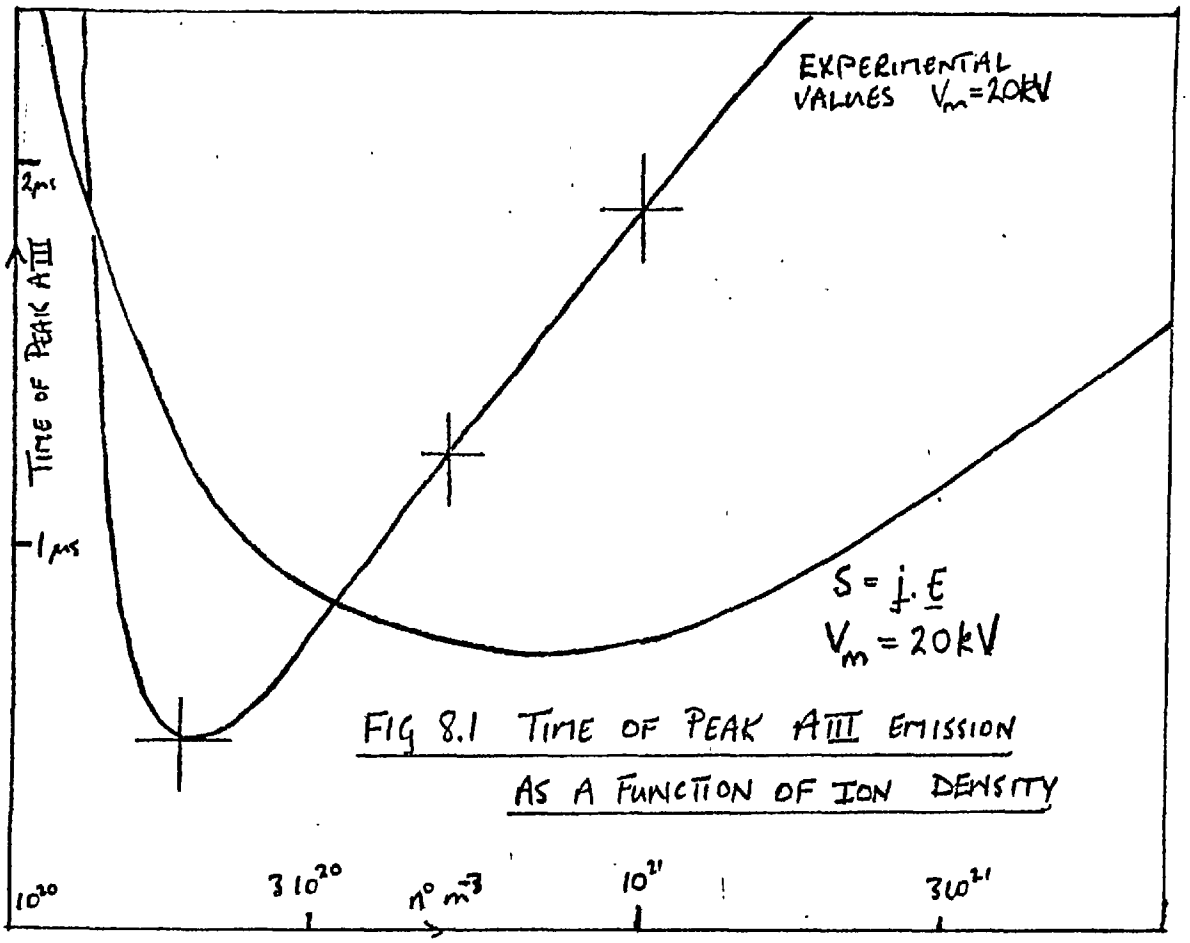

FIG 8.1 TIME OF PEAK AIII EMISSION AS A FUNCTION OF ION DENSITY

the experimentally observed times.

The results of using $j_z E_z$ are illustrated by fig. 8.1 together with some representative experimental results.

The calculation will agree with the experimental result, only if the charging voltage in the calculation is more than doubled. This would be equivalent to altering the area of current flow to fit the experimental data more accurately. As the initial density is decreased below $2.5\ 10^{20}\ m^{-3}$, there is a fall in the rate of ionisation, as seen experimentally.

8.4 The slab geometry polytron equations

To attempt to answer how much of the applied energy is used to heat the plasma the one dimensional polytron equations used by Haines(1963) are altered by including an energy equation.

An electric field E_o is applied in the z direction of a cartesian coordinate system, with $B_y = 0$, and $B_x = B_o \sin kz$, the volume being unbounded, and filled with a plasma mass density ρ, number density n and conductivity σ. The two components of Ohm's law are

$$j_{yo} = B_o \sigma (v_z - j_z/n_o eZ) \tag{8.8}$$

$$\frac{j_z}{\sigma} = E_o + \frac{j_{yo} B_o}{2 n_o eZ} - \frac{v_b B_o}{2} \tag{8.9}$$

as in chapter 1. Also

$$\frac{dv_z}{dt} = - \frac{j_{yo} B_o}{2\rho} \tag{8.10}$$

$$\frac{dv_a}{dt} = k v_b v_z \tag{8.11}$$

$$j_z = \frac{\rho}{B_o} \frac{dv_b}{dt} + \frac{\rho k v_a v_z}{B_o} \tag{8.12}$$

Additionally there is the thermal energy equation

$$S = j^2/\sigma = j_z E_z - j_z v_b B_o/2 + j_y v_z B_o/2 \tag{8.13}$$

assuming z independence of n_e and T, and then integrating with a sin kz weighting factor. Equations 8.8 and 8.9 can be used to eliminate the current from equations 8.10 to 8.13 thus

$$-\frac{2\rho}{\sigma B_0^2}\frac{dv_z}{dt} = v_z - \frac{\rho}{B_0 ne}\frac{dv_b}{dt} - \frac{\rho k}{neB_0} v_a v_z \qquad (8.14)$$

$$\frac{dv_b}{dt} = -kv_a v_z + \frac{E_0 B_0 \sigma}{\rho} - \frac{\sigma B_0}{ne}\frac{dv_z}{dt} - \frac{\sigma}{2\rho} B_0^2 v_b \qquad (8.15)$$

$$S = \left(E_0 - v_b \frac{B_0}{2}\right)\left(\frac{\rho}{B_0}\frac{dv_b}{dt} + \frac{\rho k v_a v_z}{B_0}\right) - \rho v_z \frac{dv_z}{dt} \qquad (8.16)$$

and from equation 8.14 and 8.15

$$\left(\frac{\delta\rho}{ne} + \frac{2\rho ne}{\sigma B_0^2}\right)\frac{dv_z}{dt} = \delta\left(E_0 - \frac{v_z ne}{\sigma} - \frac{v_b B_0}{2}\right) \qquad (8.17)$$

8.5 A numerical solution of the slab equations without heating

A solution of 1 dimensional equations including the effect of the induced current was presented by Dunnett (1968). A much simpler question, but more meaningful for the experiment is what value of $\omega\tau$ is required for full (i.e. $\frac{eE_0}{m}$) acceleration of the ions. Equations 8.11, 8.17, 8.15, were solved. As shown by Haines, the equations can be made dimensionless, the equations being parametised by $\alpha = \omega\tau = \frac{\sigma B_0}{ne}$, τ_a, and a limiting velocity $\sigma E_0/ne$. As expected for

$$\alpha \ll 1 \quad , \quad v_z \ll \frac{\sigma E_0}{ne}\frac{t}{\tau_a}$$

and for $\alpha \gg 1$, $v_z = \frac{\sigma E_0}{ne}\frac{t}{\tau_a}$, $j_z = nev_z$, $t \ll \tau_a$.

In the intermediate range of α there is nearly full acceleration (>90%) for $\alpha > 2.5$, and negligible (<10%) acceleration for $\alpha < .3$. At high α modulations of a frequency $k\,v_z$ are seen on v_a, v_b, and j_{yo}. These are due to the

azimuthal motion being convected with the plasma at the inter cusp frequency $k\ v_z$. From equations 8.11 and 8.15, taking the last 3 terms of 8.15 as F (i.e. $t < \tau_a$) they can be solved simultaneously as

$$\frac{d^2 v_b}{dt^2} = -(kv_z)^2 v_b \quad : \quad \frac{d^2 v_a}{dt^2} = -(kv_z)^2 v_a + F\ kv_z$$

assuming $v_b \frac{dv_z}{dt} \ll v_z \frac{dv_b}{dt}$ i.e. $kv_z \ll \tau_a$

The first term on the right hand sides account for the modulation, the second for a displacement of the mean value. From equations 8.8 and 8.9 the modulation on j_y comes from the $v_y\ B_x$ term in Ohm's law. It is due to the y current carried by the ions, modulating the mainly electron current.

8.6 An analytic solution for a limiting case of the equations

In the limit of:-

(1) a fully ionised plasma

(2) $k \to \infty$

(3) large or small $\omega\tau$

an analytic solution to the energy equation can be found. Despite these limitations the functional dependence on plasma parameters is instructive.

As $k \to \infty$ then from equations 8.11 and 8.15

$$v_a\ v_z = 0 = v_b\ v_z$$

but from eq. 8.17, $\frac{dv_z}{dt} \neq 0$ $\therefore\ v_a = v_b = 0.$

Physically the azimuthal motion of the ions is being neglected as the ion Larmor radius is much larger than the cusp separation. Solving equations 8.8 and 8.9 simultaneously gives

$$j_{Yo} = \sigma \frac{(V_z B_o - \omega\tau E_o)}{1 + \omega^2\tau^2/2} \qquad (8.18)$$

$$j_z = \sigma \frac{(E_o + \omega\tau/2\ B_o V_z)}{1 + \omega^2\tau^2/2} \qquad (8.19)$$

together with $$\frac{dv_z}{dt} = \frac{\sigma B_o}{2\rho} \frac{(\omega\tau E_o - B_o v_z)}{1 + \omega^2\tau^2/2} \qquad (8.20)$$

This is similar to chapter 1 except v_z is included. If

$$v_z B_o - \omega\tau E_o \simeq \omega\tau E_o \quad \text{i.e.} \quad \frac{\sigma E_o}{ne v_t} \gg 1 \quad \text{or} \quad \frac{t}{\tau_a} \ll 1$$

and $\omega\tau \gg 1$, then

$$j_{yo} = -\frac{2neE_o}{B_o}$$

$$j_z = \frac{2\sigma E_o}{\omega^2\tau^2} + n_e v_z \qquad (8.20a)$$

$\frac{2\sigma E_o}{\omega^2\tau^2} = j_{ze}$ is the electron current across the field lines, and $j_{zi} = n_e v_z$ is the ion current

$$\therefore \quad \frac{j_{zi}}{j_{ze}} = t \frac{eB_o}{m_i} \omega\tau$$

Also from eq. 8.20

$$\frac{dv_z}{dt} = \frac{eE_o}{m} - \frac{n_o^2 e^2 v_z}{\rho\sigma} = \frac{eE_o}{m} - \frac{v_z}{\tau_a}$$

neglecting the first part of τ_a in eq. 1.7.

$$\therefore \quad j_z = \frac{ne^2 E_o t}{m} \qquad \text{if } j_{zi} \gg j_{ze}$$

$$\therefore \quad \frac{3}{2} nk \frac{dT}{dt} = j_z^2 \frac{r}{\sigma} \frac{j_{yo}^2}{2} \qquad \text{where} \quad \sigma = \sigma_o T^{3/2}$$

$$\therefore \quad k \frac{dT}{dt} = \frac{2}{3} \frac{(neE)^2}{n\sigma_o T^{3/2}} \left(\frac{e^2 t^2}{m^2} + \frac{2}{B_o^2} \right)$$

$$\therefore \quad T^{5/2} = 1.66 \frac{ne^2 E_o^2}{k\sigma_o} \left(\frac{e^2 t^2}{3m^2} + \frac{2t}{B_o^2} \right) + T_o^{5/2}.$$

and if $T \gg T_o$ the temperature rise ΔT is given by

$$\Delta T = \left(\frac{10}{3} \frac{ne^2 E_o^2 t}{k\sigma_o B_o^2} \left(1 + \omega_{ci}^2 t^2/6 \right) \right)^{2/5} \qquad (8.21)$$

where $\omega_{ci} = \frac{eB_o}{m}$. When $\omega_{ci} t \gg 6$, heating is dominated by the z currents.

For $B = .1T$, $\omega_{ci} = 2\ 10^5 Hz$ for singly ionised argon, and so $\omega_{ci} t = 6$ when $t = 15\mu s$. The numerical values predicted by equation 8.21 are $\Delta T = 15eV$, for $B = .1^T$, $n = 10^{20}\ m^{-3}$, $E = .5\ 10^4\ V/m$, at $t = 1\mu s$.

When $\omega\tau \ll 1$, $j_{yo} = \sigma \omega\tau E_o$, $j_z = \sigma E_o$.

The expression for the temperature at a time t in this case is

$$\frac{1}{T^2} = \frac{1}{T_o^2} - \frac{1}{3} \frac{E_o^2 \sigma_o}{kn} t$$

where T_o is the original temperature.

A maximum in the Ohmic heating as a function of $\omega\tau$ exists when $\omega\tau \sim 1$. Either side of $\omega\tau = 1$, j_{yo} decreases.

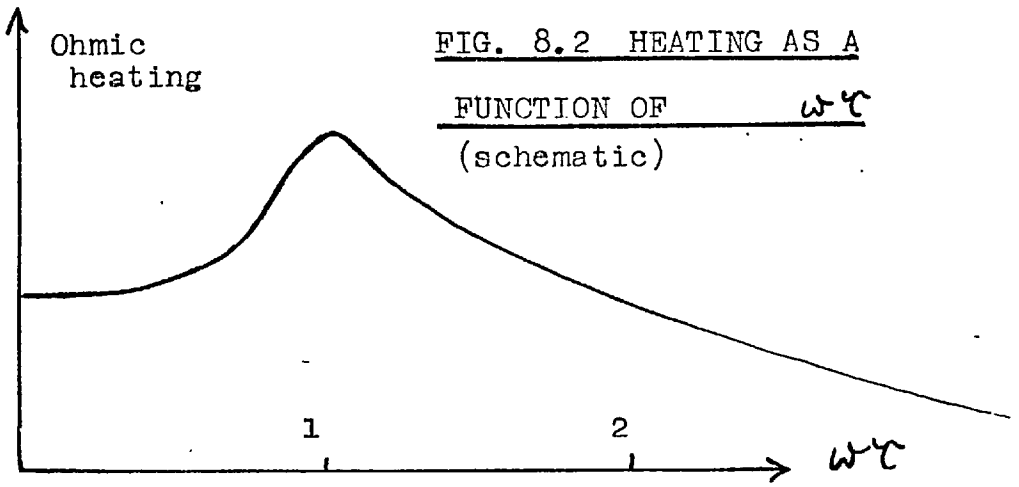

FIG. 8.2 HEATING AS A FUNCTION OF $\omega\tau$ (schematic)

8.7 A numerical solution of the energy and polytron equations.

The physical processes outlined so far are now amalgamated into 1 solution. The ionisation is calculated from the coronal equations, and the temperature from an energy equation with the currents determined by modified one dimensional polytron equations.

With the equations of section 8.6 $j_z \propto n$. To prevent this the geometric inductance must be included i.e.

$$E = E_o - \ell \, dI/dt \qquad (8.22)$$

where ℓ, the inductance/length is .45 μH/m. I, the plasma current is $5\ 10^{-3}\ j_z$ A . This prescription, in particular the value of ℓ, is somewhat arbitrary. However, an inductance is essential, and so the experimental value is no worse than any other. Numerically care must be taken with this

equation when $E \ll E_o$ i.e. $\ell \gg L_H$, the Hall inductance, otherwise a numerical instability develops.

An average of the values of γ_E (Spitzer, 1956, p.84) is taken and thus $\sigma = 2.3\ 10^3\ W^{3/2}\ Z$ mho/m $= \sigma_o W^{3/2}/Z$. Because of eq. 8.22, j_z must be determined by a differential equation. This makes 4 dependent variables, v_z, v_a, v_b and j_z determined by the equations.

$$\frac{dv_z}{dt} = W^{3/2} \frac{\sigma_o B_o^2}{2\rho Z} \left(\frac{j_z}{n_e Z} - v_z \right)$$

$$\frac{dv_a}{dt} = k\, v_b\, v_z$$

$$\frac{dv_b}{dt} = \frac{j_z B_o}{\rho} - k\, v_a\, v_z$$

$$\frac{dj_z}{dt} = \frac{1}{\rho A} \left(E_o - Z j_z \frac{}{\sigma_o W^{3/2}} - \frac{v_b B_o}{2} + \frac{\sigma_o W^{3/2} B_o^2 (v_z - j_z)}{2Z^2 n_e} \right)$$

The ion temperature is given by

$$\frac{dW_i}{dt} = \frac{(W - W_i)}{t_{eq}}$$

W_i being the ion temperature in eV, and t_{eq} taken from Spitzer p.80. There is a corresponding term in the electron energy equation.

There are few problems of numerical stability in the solution. The energy equipartition time will be of order μs. The oscillatory rise time $1/kv_z$, will be of order 100's ns. The acceleration time τ_a is long, many μs, and the ionisation time, $1/(\frac{dZ}{dt})$, again, is of order μs. By fixing the timestep for an accuracy of 10^{-4} there are no stability problems.

8.8 Solutions to the equations

The initial values used for each run were -

$W = W_i = 1eV$ (see chapter 3), 100% ionisation, (in the experiment $\sim 70\%$) $j_{yo} = j_z = v_z = v_a = v_b = 0$.

Fig. 8.2 shows the plasma parameters for a case where there is full acceleration, low j_{yo} and low Z. In the time 0 to 5μs, Z changes from 1 to 1.4 which is consistent with equation 8.6. Because Z does not vary much, the z velocity is almost linear, τ_a being 100's μs. The period of the azimuthal velocities can be seen to be $2\pi/(kv_z)$. This current carried by the ions is too small to modulate j_{yo}.

j_{yo} rises slowly (here) only because Z increases. The Hall inductance here is much greater than the assumed geometric inductance. The value of $\ell \frac{dI}{dt}$ is 300 V/m compared with the applied field of 5000 V/m. The Z current rises approximately linearly like v_z

The electron temperature rises steeply at first but then as the resistivity falls so does the heating and the temperature rises linearly. From equation 8.21 the temperature rise cannot exceed $At^{2/5}$. At all the times shown $\omega_{ci}\, t \ll 1$. At early times, when $W < 10$ eV equation 8.21 will be valid, but when $W > 10eV$, and Z starts to change, it will be an overestimate of the temperature rise. The electron temperature is decoupled from the ion temperature, as the equipartition time is $\sim 30\,\mu$s at this low number density. For the case shown the majority of the energy supplied is going into directed motion. A directed motion of $v_z = 10^4$ m/s corresponds to an energy

of 20 eV.

In contrast, fig. 8.3. shows a case where at the same value of n^o, initially $\omega\tau < 1$. j_z rises inductively and causes heating of the plasma. Once the temperature rises above 10 eV , the plasma switches over to a polytron case as $\omega\tau > 1$. The switching time is short, as shown in fig. 8.3. If this occurs at $t = t_s$, then for $t < t_s$.

$$j_z(t) = \frac{1}{\ell A}\int_o^t E_o \, dt = \frac{E_o t}{\ell A}$$

Suppose the switching occurs in a time Dt, then the particle motion obeys

$$\frac{dv}{dt}_z = \frac{e}{m}\ell A \frac{j_z(t_s-)}{Dt}$$

$$\therefore \quad Dv_z = eE_o t/m .$$

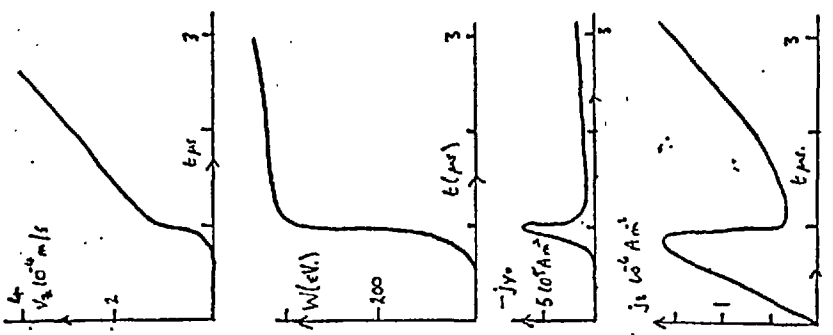

FIG. 8.3.
PLASMA PARAMETERS
E_o=.5 10^4V/m, B_o = 2 10^{-3}T,
n^o= 10^{20} m^{-3}, argon

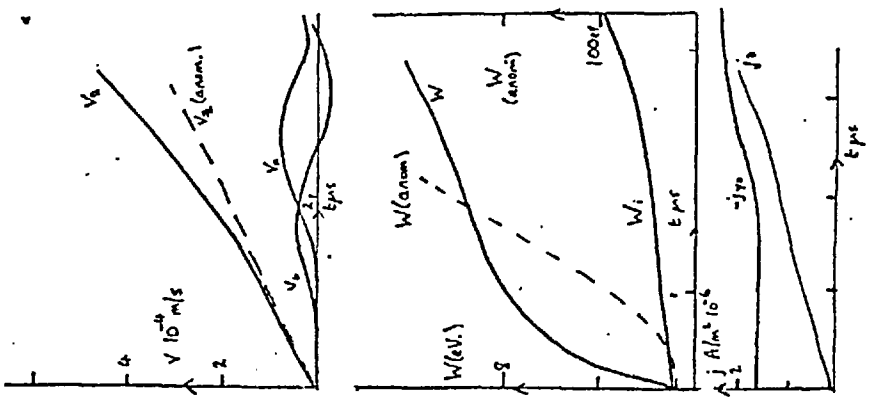

FIG. 8.2
PLASMA PARAMETER
E_o=.5 10^4V/m, B_o = .1T,
n^o = 10^{20} m^{-3}, argon

In fig. 8.3 the large $\frac{dv_z}{dt}$ is caused by the spike on j_y at 900 ns, which arises because of the large $\frac{dj_z}{dt}$. The spike in j_y also causes a large amount of heating. Again because of the low number density the value of Z does not change much, although it reaches 2 by 3.5 μs, earlier than in fig. 8.2. The ion temperature does not go above 3 eV , as the higher temperature increases t_{eq}.

Fig. 8.4 is at a higher value of n^o when ionisation is significant. Again there is the switch on phenomenon . The polytron mechanism switches on when the electron temperatures rises above 3 eV. The spike in j_{yo} causes a lot of electron heating. The number density of $8\ 10^{20}\ m^{-3}$ means that t_{eq} $8\mu s$. From eq. 8.6. $\frac{d\bar{Z}}{dt} \sim 1\mu s^{-1}$, and corresponding to this $\frac{dW}{dt} = .5\mu s^{-1}$, as the ionisation potential is $\sim$30 eV. Thus after the sharp rise in temperature there is a rapid fall, which stabilises at about 10 eV. This is seen by the point of inflexion in $\bar{Z}$. The ion temperature is able to approach that of the electrons as t_{eq} falls to 2 μs.

'Profiles' of $\bar{Z}$, and W are shown in fig. 8.5, as a function of B_o, at 1 μs. The abscissa also corresponds to a radius. The temperature is low at both small radii (B_o) and large radii. The former is because $\omega\tau \ll 1$ and the latter because $\omega\tau \gg 1$. The value of $\bar{Z}$ follows the general

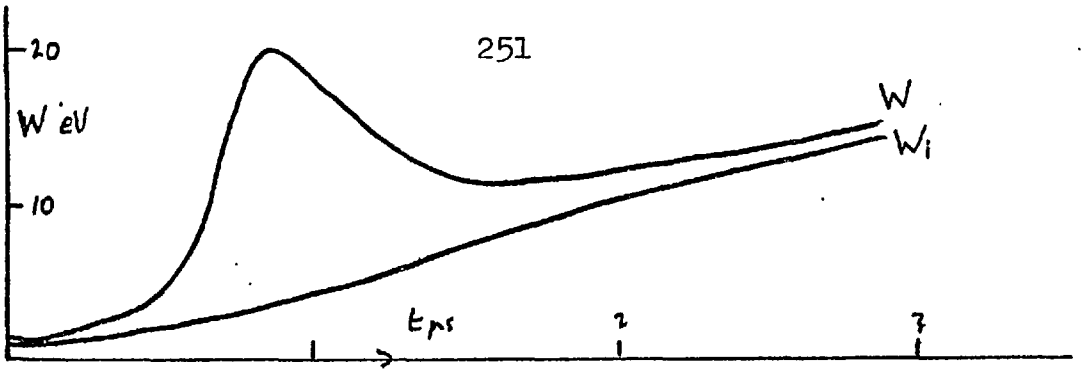

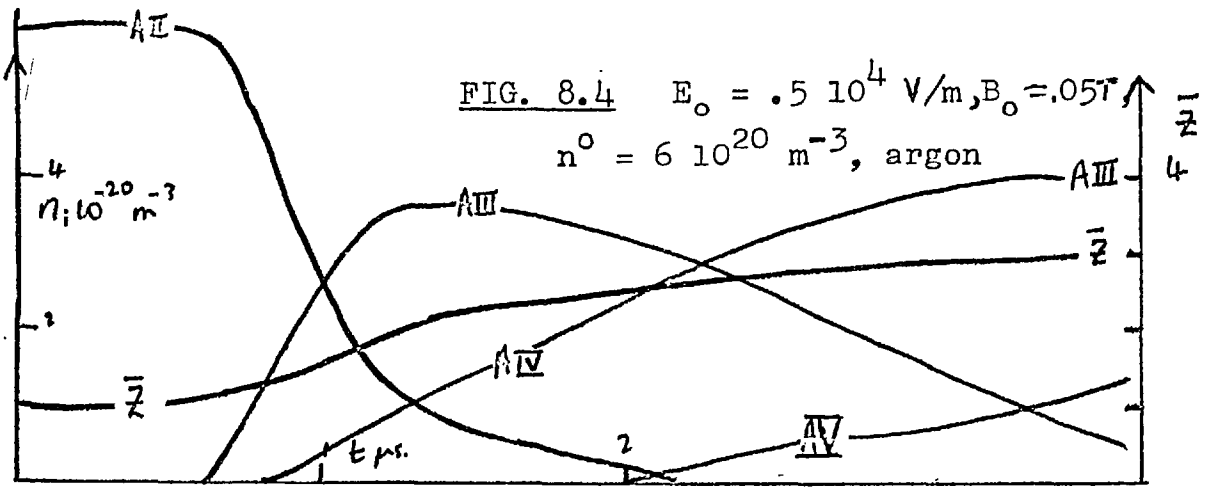

FIG. 8.4 $E_o = .5\ 10^4$ V/m, $B_o = .05$T, $n^o = 6\ 10^{20}$ m^{-3}, argon

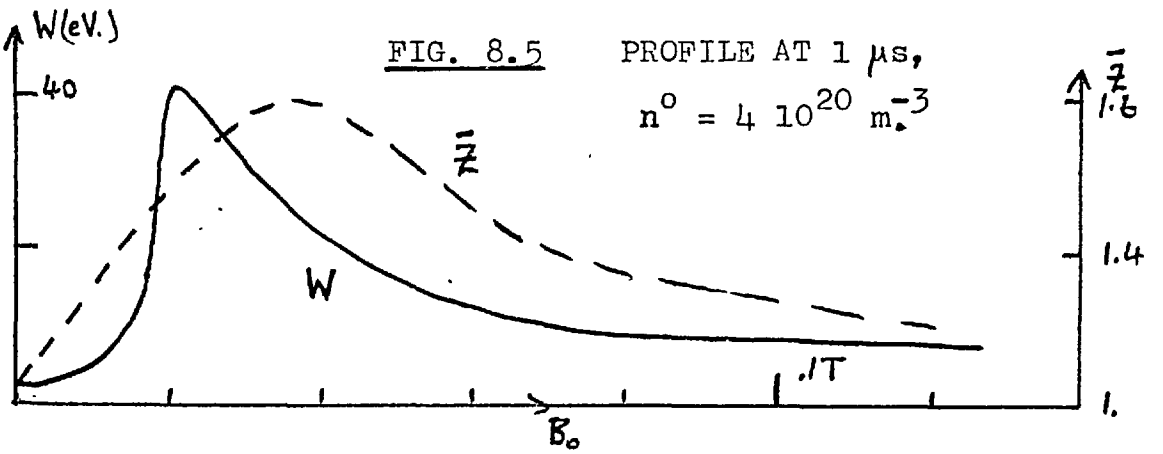

FIG. 8.5 PROFILE AT 1 μs, $n^o = 4\ 10^{20}$ m^{-3}

shape of W. The peak of $\bar{Z}$ is displaced outwards from that of the temperature because W can rise very fast, when the polytron switches on, but $\frac{dZ}{dt}$ cannot become large, and is only appreciable when W > 10 eV. Hence at small radii, where ionisation has only been occuring since the switch on, the degree of ionisation is lower than at larger radius where the temperature has been high for longer.

Temperature gradients as steep as shown in fig. 8.5, may not be real. The heat diffusion time, from eq. 3.8 is

$$\tau_o \sim \frac{a^2 (n_e + n_i)\ 2\omega^4}{10^{20}\ W^{3/2}} \ \mu s.$$

Even for $n^o = 8\ 10^{20}\ m^{-3}$, a=1 cm, W = 10 eV , $\tau_o = .1\ \mu s$. However the magnetic field isolates rings of different r, in the same axial position. For connection axially then a $\sim$ 2 cm and the diffusion time will be about .5μs. Hence in the region r < 1 cm the plasma temperature profile will be flat. At larger radii, r > 1.5cm, when in fig. 8.5 W < 5eV, a $\sim$ cm, $\tau_o > .7\mu s$ even for $n^o = 10^{20}\ m^{-3}$. For experimental comparison, at radii where $B_o(B_r) < .1T$, a high temperature (W > 10 eV) plasma can be expected. At larger radii, a lower temperature is expected and consequently little ionisation.

Fig. 8.6 shows the time at which the peak number density of AIII occurs as a function of B_o . This is important

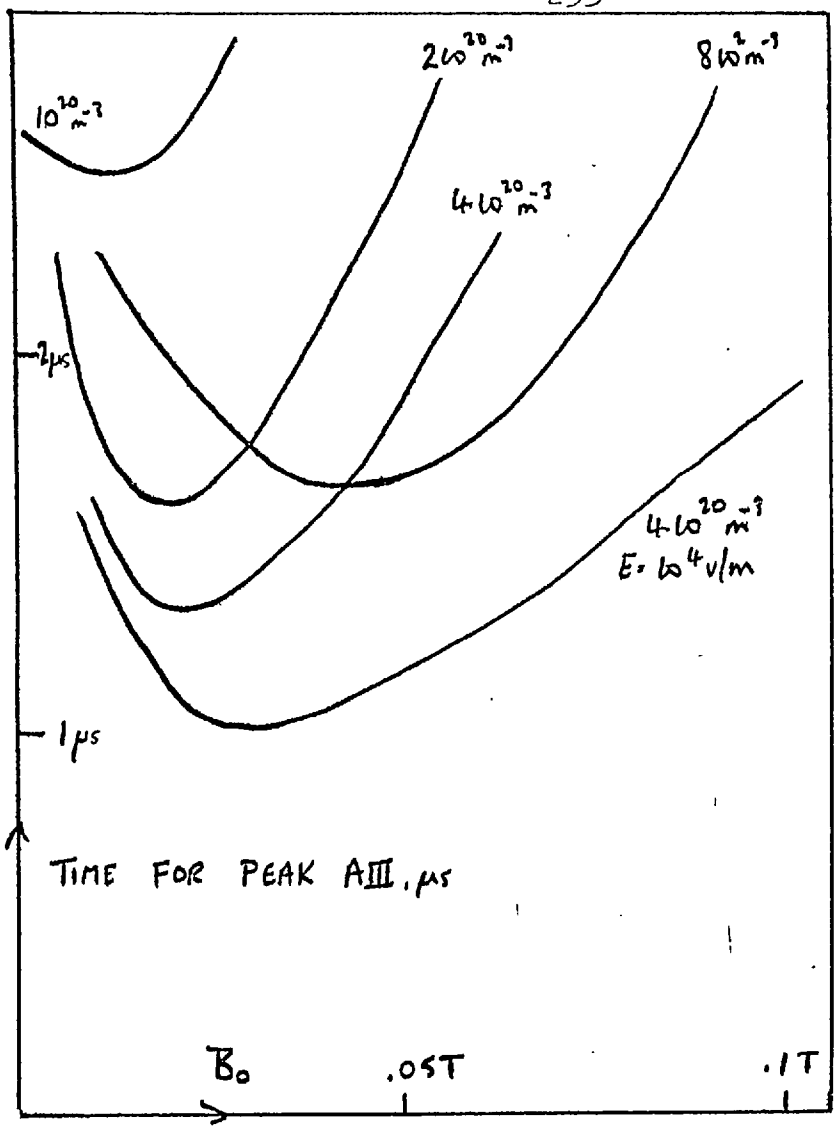

FIG. 8.6.

TIME FOR PEAK OF AIII

$E = .5\ 10^4$ v/m

Various B_o

experimentally as the peak intensity of an A III line is observed. With increasing n the rate of ionisation first increases but then starts to fall, as the inductance limits the energy input. Note that for an equivalent main bank voltage of 10 kV, the minimum time is 1.3μs.

8.9 The effect of an anomalous resistivity

The ionisation shown in fig. 8.6 seems too low to account for the experimental data. The effect of an ion

accoustic instability caused by azimuthally drifting electrons, drifting faster than the sound velocity (v_s) was investigated. An anomalous resistivity from Sagdeev (Bodin et al, 1969) was used in series with the Spitzer resistivity whenever $j_{yo} > Znev_s$. i.e.

$$\eta = \eta_s + \frac{m}{ne^2}\,\omega_{pi}\,\frac{W}{W_i}\,\frac{v_d}{v_s} \qquad \text{for } j_y > Znev_s$$

This anomalous resistivity can be much larger than the Spitzer values and some results are shown in fig. 8.2 illustrating that a much higher temperature can result. However, the smallest time for the peak value of AIII remained at 1.3μs.

A more likely cause of discrepancy with the experiment is incorrect rate coefficients.

8.10 Summary

The object of this work has partially been attained. Values for the heating, and ionisation, as a function of applied fields, and to some extent positions have been obtained. Variations of number density other than by ionisation have not been included. Nevertheless, a semi quantitative comparison with the experimental data is made in chapter 11.

CHAPTER NINE

THE LASER LIGHT SCATTERING DIAGNOSTIC ON THE POLYTRON

This chapter is an account of the light scattering experiment carried out on the polytron to measure the electron number density and temperatures. Light scattering is the only satisfactory way to make this measurement, and for an argon polytron plasma is probably the only way. HCN interferometry is too refraction sensitive; picking out high n spectroscopic lines in l.t.e. with the continuum might produce a satisfactory Boltzman plot but the higher lines will almost certainly be indistinguishable from the continuum; Stark broadening in argon is ~.1Å at polytron densities; in hydrogen n and T_e could be obtained simply by the broadening of the Balmer series, and line to continuum, but there would be the normal line of sight difficulties, even if hydrogen were a suitable plasma for the polytron configuration.

The low densities in the polytron make scattering inherently difficult. The difficulty is increased by the lack of access, high plasma emission and the need to work with an argon plasma. There follows a brief account of scattering theory, followed by a chronological and logical account of the experiment from design considerations to the n , T_e curves, and finally some novel findings on the shape of the scattered spectrum.

9.1 Scattering theory

Comprehensive accounts of scattering theory have been given by Bernstein et al,(1964)and Evans and Katzenstein (1969). Here their papers are summarised.

There are two parts to calculating the differential cross section of a plasma. Firstly the differential cross section of a microscopically inhomogenous plasma is calculated by simple electrodynamics, and then using plasma kinetic theory the microscopic fluctuations are related to macroscopic quantities.

Consider first the response of a single electron to an incident field $\underline{E} = \underline{E}_o \cos(\underline{k}_o.\underline{r} - \omega_o t)$. The acceleration in this field is substituted in the Lienard-Wiechert potentials. The curl of the magnetic vector potential gives the radiated magnetic field $\underline{B}(\underline{R},t)$. The power spectrum (Watt -sec/m.^{2}) is given by the Wiener-Khinchine theorem as

$$I(\underline{k},\omega) = \frac{c}{\mu_o \pi} \int_{-\infty}^{\infty} e^{i\omega\tau} \int_0^T \frac{\underline{B}(\underline{R},t).\underline{B}(\underline{R},t+\tau)\,dt\,d\tau}{T} \qquad (9.02)$$

The scattering vector is $\underline{k} = \underline{k}_o - \frac{\omega_o}{c}\frac{\underline{R}}{|R|}$. The values of $\underline{B}$ are those due to a sum over many scatterers, and so the time average is equivalent to an ensemble average.

$$I(\underline{k},\omega)dA = I_o N \left(\frac{e^2 \mu_o}{4\pi m}\right)^2 \sin^2\beta \frac{1}{\pi N} \int_{-\infty}^{\infty} e^{i\omega\tau} \sum_{ij} \overline{\cos(\underline{k}.\underline{r}_j(t) - \omega_o t)\cos(\underline{k}.\underline{r}_i(t+\tau) - \omega_o(t+\tau))}\, d\tau \qquad (9.04)$$

$$= I_o N \sigma S(\underline{k},\omega)\, d\Omega.$$

γ is the angle between $\underline{E}_0$ and $\underline{R}$ and dA the detector area.

For $\gamma = \frac{\pi}{2}$, $\sigma = 8\ 10^{-30} m.^2$

Note the difference between $\sigma = 8\ 10^{-30} m.^2$ and $\sigma_T = \int \sigma d\Omega$

$= \frac{8\pi}{3}\left(\frac{e^2\mu_0}{4\pi m}\right)^2 \qquad = 6.65\ 10^{-29} m.^2$

also that $I(\underline{k},w)$ is the power/area/sec.$^{-1}$ explaining $d\Omega$ in equation (9.04).

The parameter of importance for diagnostic work is the dynamic form factor

$$S(\underline{k},\omega) = \frac{1}{2\pi N}\int_{-\infty}^{\infty} e^{i\omega\tau} \sum_{i,j}^{N} \cos\left(\overline{\underline{k}.(\underline{r}_j(t) - \underline{r}_i(t+\tau)) - \omega_0\tau}\right) d\tau . \quad (9.05)$$

$$n(\underline{r},t) = \sum_{j=1}^{N} \delta(\underline{r} - \underline{r}_j(t))/\delta V$$

is the density of the point scatterers and so n $(\underline{k},t)$ the Fourier transform $= \sum_{j=1}^{N} e^{i\underline{k}.\underline{r}_j(t)}$

$$\therefore\ n(\underline{k},t)n^*(\underline{k},t+\tau)e^{-i\omega_0\tau} = \sum_{i,j}^{N} \cos\left(\underline{k}.(\underline{r}_j(t) - \underline{r}_i(t+\tau)) - \omega_0\tau\right)$$

+ terms odd in τ

$$\therefore\ S(\underline{k},\omega) = \frac{1}{2\pi N}\int_{-\infty}^{\infty} e^{i\tau(\omega-\omega_0)}\ \overline{n(\underline{k},t)n^*(\underline{k},t+\tau)}\ d\tau \qquad (9.06)$$

Thus the scattered spectrum is centred about ω_0, and picks out spatial density variations with $\underline{k}$ values the same as the scattering $\underline{k}$ vector. This result is important for section 9.18 but as here, interest is restricted to lowα scattering eq. 9.05 will be developed.

Suppose $\underline{r}_k(t) = \underline{r}_k(0) + \underline{V}_k(0)t$ then eq. 9.05 separates to

$$S(\underline{k},\omega) = \frac{1}{2\pi N}\int_{-\infty}^{\infty} e^{i\omega\tau} \sum_{j=1}^{N} \cos\left(\left(\underline{k}.\underline{V}_j(0) + \omega_0\right)\tau\right)$$

$$+ \sum^{N} \cos\left(\underline{k}.(\underline{r}_j(t) - \underline{r}_i(t+\tau))\cos\omega_0\tau\right) d\tau \qquad (9.07)$$

The double sum may be expressed in terms of the two particle correlation function $g(\underline{r}_j - \underline{r}_i, \tau)$, as

$$\frac{1}{2\pi N} \sum_{j \neq i} \cos\left(\underline{k}.(\underline{r}_j(t) - \underline{r}_i(t+\tau))\right) = \frac{1}{N} \int_0^\infty g(\rho, \tau) \cos(\underline{k}.\underline{\rho}) \rho^2 d\rho$$

where $\underline{\rho} = \underline{r}_j(t) - \underline{r}_i(t+\tau)$

Now $g(\rho,\tau) \propto e^{-\lambda_d \rho}/\rho$ (Boyd and Sanderson) so the effective upper limit to the integral is λ_d, the Debye length. If $k\lambda_d \gg 1$ then the cosine factor of the integrand will make the values of the integral approach zero. Thus if $\frac{1}{\alpha} = k\lambda_d \gg 1$ the scattering arises from the first term only.

Integrating eq. 9.07 over τ gives

$$S(\underline{k}, \omega) = \frac{1}{N} \sum_{j=1}^{N} \delta(\omega - \omega_0 + \underline{k}.\underline{v}_j(0))$$

The sum over j can be converted to an integral over velocity space, with the velocity distribution $f_{ce}(v_e)$ as a weighting normalised to N. v_e is the component of $\underline{v}_e$ in the direction of $\underline{k}$. Then $S(\underline{k},\omega) = f_{oe}\left(\frac{\omega - \omega_o}{|\underline{k}|}\right)$ the frequency shift being given solely by the Doppler shift from the moving electrons.

$$\therefore \quad I(\underline{k}, \omega) dA = I_o N \sigma f_{oe}\left(\frac{\omega_o - \omega}{|\underline{k}|}\right) d\Omega \qquad \int_{\infty}^{-\infty} f_e\left(\frac{\omega'}{k}\right) d\omega' = \frac{1}{\pi} \quad (9.07a)$$

From fig. 9.1. $|\underline{k}| = 2\, k_o \sin\frac{\theta}{2} = 2\frac{\omega_o}{c} \sin\frac{\theta}{2}$

and is fixed for a given geometry. Equation 9.07a can be rewritten as the power density reaching the detector as a

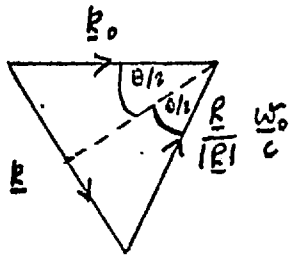

FIG.9.1 VECTOR DIAGRAM OF THE SCATTERING GEOMETRY

function of wavelength shift $\delta\lambda = -\frac{2\pi c}{\omega_0^2}\delta\omega$ for $\delta\omega = \omega - \omega_0 << \omega_0$

For a Maxwellian velocity distribution of electron temperature Te,

$$I(\delta\lambda)dA\,d\lambda = I_0 N\sigma \sqrt{\frac{m_e}{2kT_e\pi}}\,\frac{c}{\lambda_0 2\sin\frac{\theta}{2}}\exp\left(-\delta\lambda^2 c^2 m_e/(\lambda_0^2(2\sin\theta/2)^2 2kT)\right)d\lambda\,d\Omega$$

where $d\lambda$ is the wavelength interval centered about $\delta\lambda$

$$\therefore\ I(\delta\lambda)dA\,d\lambda \propto \frac{I_0 N}{\sqrt{W_e}}\exp(-2.63\times10^{-3}\delta\lambda^2/W_e)\,d\lambda\,d\Omega \qquad (9.08)$$

where $d\lambda$ is in Å and W_e, the electron temperature, is in electron volts. In this limit of large volume c.f. $\underline{k}^{-1}$ and low α the scattering is called incoherent and random, being incoherent and correlated for large α. It is worth noting from equation 9.08 that

$$\delta\lambda)_{1/e} = 19.6\sqrt{W_e}\ \text{Å}.$$

9.2. The values of α for which random scattering is observed

If $\alpha << 1$ scattering is random, however experimentally the requirement is not as stringent as this, it only being necessary that $\alpha < .5$. To make this statement plausible

brief consideration will be given to high α scattering.

Evans and Katzenstein show that for an equilibrium plasma

$$S(\underline{k},\delta\omega) = \tau_\alpha(x_e)\,|\underline{k}|\sqrt{\frac{kT_e}{m_e}} + Z\left(\frac{\alpha^2}{1+\alpha^2}\right)\tau_\beta(x_i)\,|\underline{k}|\sqrt{\frac{kT_i}{m_i}} \qquad (9.09)$$

where $$x_e = \frac{\delta\omega}{kV_e} = \delta\lambda\sqrt{\frac{2.6\,10^{-3}}{W_e}}$$

$$\beta^2 = Z\left(\frac{\alpha^2}{1+\alpha^2}\right)\frac{T_e}{T_i} \quad : \quad x_i = x_e\sqrt{\frac{T_e}{T_i}\,\frac{m_i}{m_e}}$$

The large disparity in scale makes $\tau_\beta(x_i)$ small when $x_e \sim 1$ as here $x_i \gg 1$. A plot of $\tau_\alpha(x)$ is shown in fig. 9.2. The peaks at high α are due to the electrostatic waves. For $.5 < \alpha < 2$ the position of the shoulder is given by $x = \alpha$, whereas for large α it is at $x^2 = \frac{1}{2}(\alpha^2+3)$

$\tau_0(x) \propto \exp(-x^2)$ is a reproduction of the electron velocity distribution. Considering the electron profile only, $\tau_{\frac{1}{2}}(x_e)$

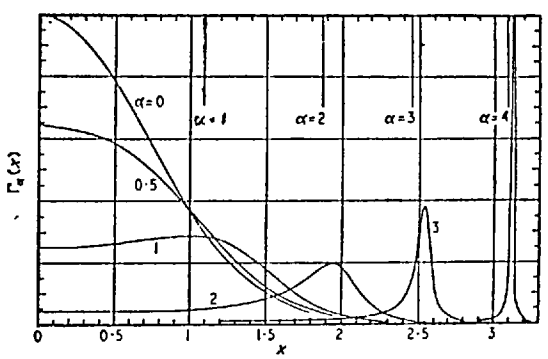

FIG.9.2 THE FUNCTION $\tau_\alpha(x)$

differs significantly from $\tau_0(x_e)$ only for $x_e < .5$, which is for $\delta\lambda < 10\sqrt{W_e}$ Å. High α is most likely for low W_e, say $W_e = 4.\text{eV}$, and so the scattered profile will

differ from a Maxwellian of the same shape and intensity scale only for $\delta\lambda < 20\text{Å}$, when $\alpha = .5$. In this case the error in n and W_e would be about 20%, but as $\delta\lambda < 20$ Å was not sampled experimentally, the error would be much less.

For these values of $\delta\lambda \sim 20$ Å, as $x_i = 300\ x_e$, (for an argon plasma)

$$\therefore \qquad \tau_\beta(x_i) \ll \tau_\alpha(x_e)$$

The analytic expressions for the total scattering cross section are, $S_e(\underline{k}) = \int_{-\infty}^{\infty} S_e(\underline{k},\omega)\, d\omega = \frac{1}{1+\alpha^2}$

$$S_i(\underline{k}) = \frac{Z\alpha^4}{(1+\alpha^2)(1+\alpha^2(1+Z\tau_e/\tau_i))}$$

For $\alpha = .5$, $S_e(\underline{k}) = .8$, but this difference from $\alpha = 0$ will not be evident experimentally.

The value of α for 90° scattering is,

$$\alpha = 1.05\ 10^{-11} \left(\frac{n}{W_e}\right)^{\frac{1}{2}} \qquad (n \text{ in } m^{-3},\ W_e \text{ in eV})$$

9.3 Experimental design

The major constraint on any scattering experiment is the smallness of the scattering cross section. In this experiment 10^{-11} of the incident photons reach the entrance slit. Allowing a realistic spectrometer throughput, sufficient channels for spectral resolution and p.m. quantum efficiency, 10^{-15} of the incident photons will produce photoelectrons. For reasonable shot noise 10^4 photoelectrons

are needed, ∴ 3J at 6943Å. High power for time resolution, and narrow line width mean a choice between a ruby and a Nd^{3+} system and the lack of good detectors at 1.06 μm eliminates Nd^{3+}.

The laser was obtained commercially from Laser Associates, being their 501 system. It is a 6" x $\frac{5}{8}$", Q spoiled ruby oscillator. The switching is by a K.D.P. P ockels cell and a Brewster stack. The output is horizontally polarised. The planar cavity is formed by a dielectric mirror and a temperature controlled sapphire etalon. The rod is pumped by a helical flash tube and is water cooled. The specifications are: maximum output energy 4J; power at 3J, 150 M watts; divergence 3 mrad ; line width .1Å. The wavelength can be tuned by the temperature control on the output etalon by .2Å, half the free spectral range. Care must be taken to prevent lasing at two wavelengths.

The delay of 1.6 ms. between starting pumping the laser and Q spoiling the cavity is provided by two variable tandem delay units. The input pulse to the second unit is used to trigger the polytron timing units and there is a jitter of 100ns between the main bank and the laser .

For some time it was impossible to get consistent high power from the laser, the pulse length being long, about 100ns and multipulsing being common. Fortunately this behaviour eventually was traced to the setting of the

temperature control of the etalon, proper lasing action occuring only when the laser lases at one wavelength. The correct setting is achieved by trial and error.

The limited access to the torus restricted the laser beam to going vertically through the plasma. The torus had to be modified by the addition of 3 ports, and a Rayleigh horn viewing dump.

It is more convenient to have the laser shining down than up. This allows the heavy beam dump to be supported from the floor. The laser is supported on the mezzanine floor on a welded R.S.J. table. Runners and height screws allow positional adjustments to the laser.

The beam is reflected down to the torus by a rigidly held spectrosil B prism. This arrangement is shown in fig.9.3. Adjustments are provided horizontally so that the prism can be in line with the centre of the input and output ports of the torus, vertically so that it can be at the same height as the laser and also for its orientation so that the ruby beam direction can be adjusted by fractions of a milliradian.

For system alignment a 5mW He-Ne laser was mounted onto the base of the ruby laser. Reflexion by a beam splitter into the ruby cavity made the alignment with the ruby cavity easy. This is also shown in fig. 9.3.

The laser beam is dumped by a plate of Pilkington

Chance OB10 glass at the Brewster angle of the polarised laser output. Any reflexion of any other polarisation impinges on another Brewster angle dump set to absorb the normal polarisation. The plates are mounted on 'Tombac' seals so that the He-Ne can pass through the dump onto a reference mark on the floor. Additionally the dump has a double Wilson seal in it through which an alignment mirror can be moved from a retracted position in the dumpport to the centre of the torus, to check the spectrometer alignment.

Originally the total laser output was monitored by a photodiode picking up secondary reflexions from the He-Ne beam splitter. A more satisfactory arrangement replaced this using a second beam splitter to take a fraction of the ruby beam onto a diffusing surface and placing a pin diode 1m away. This provides a monitor current of a few mA.

9.4 The detection system

The detection system was designed to match the expected plasma of 10^{21} m^{-3}, 10eV. Scattering had to be 90^{o} (because of access) and so it was low α scattering. From eq. 9.08 a spectral resolution of 10Å was required. A diffraction grating is the only suitable instrument.

The grating spectrometer used was built by Key (1965) and described by him. As built by him it used a Littrow

mount, a Hilger 70cm x. 7 cm collimating lens, and a Baush and Lomb 7.6. cm x 6.5 cm. grating with 2160 lines/mm. The fine scan across the exit slit was achieved by rotating a block of glass. The linear dispersion was 4Å/mm. As originally modified a mirror replaced the scanning block and the spectrum was focussed onto a 25 channel fibre bundle array, each channel being 1cm x 1mm. The transverse position of the spectrum relative to the array could still be adjusted finely by rotating the mirror.

The scattering region was focussed onto the entrance slit of the spectrometer by a f = 10cm biconvex lens, with a magnification of 1.

At the time the photomultiplier with the highest quantum efficiency at 6943Å was the R.C.A. 7265.

The photomultiplier bias circuit is shown in fig.9.4 For safety the photo cathode was run - 3kV from earth, i.e. the output pin was earthy, however because of this the metal ferrules on the light pipes had to be kept 5mm. from the p.m. envelope otherwise a stray capacitance effect caused an increase in the dark noise of the p.m. Six photomultipliers were eventually available and these were all tuned for maximum output by the controls on the biasing circuitry.

As up to 8 recording channels were to be needed a new screened room had to be constructed. This was built from

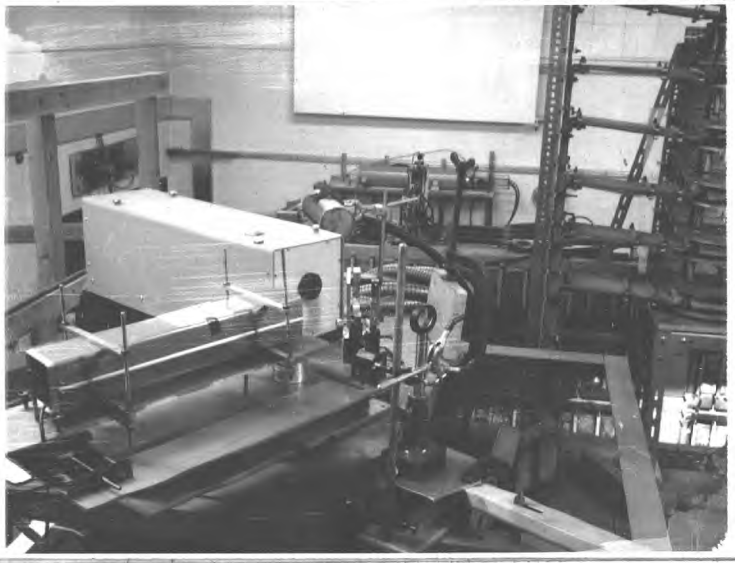

FIG.9.3

THE LASER MOUNTING

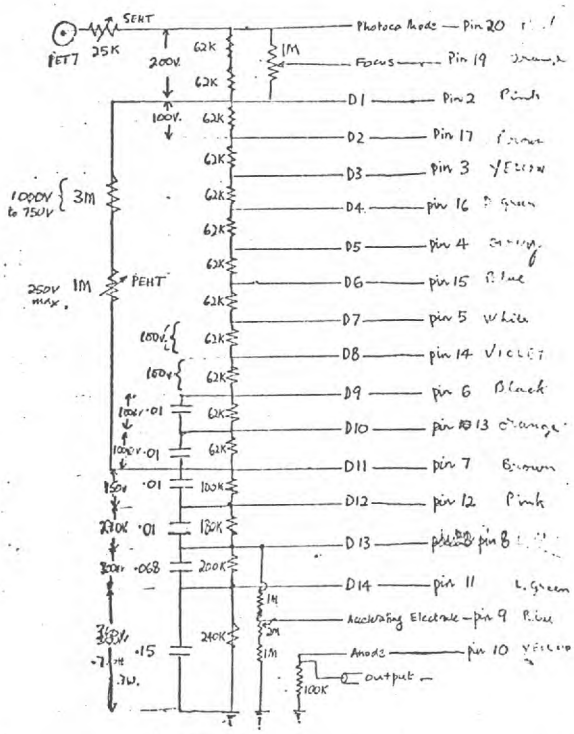

FIG.9.4

THE PHOTOMULTIPLIER BIAS CIRCUIT

$\frac{1}{8}$" aluminium sheeting screwed to an angle ion frame and was air conditioned. The essential high conductivity across the breaks in the sheeting was ensured by use of conducting tape. The mains voltage was brought in through isolation transformers in series with 4 Belling-Lee mains filters. The oscilloscopes were photon coupled to the triggering circuitry. All of the photomultiplier bias circuits were run off the same power pack located in the screened room. The photomultipliers were housed in a soldered brass box, connected to the screened room by a 1" bore copper tube. In effect the brass box was an extension of the screened room and so the earth loops formed by the connections of the photomultipliers to the oscilloscopes did not cause excessive pickup. The result of these common sense precautions is a pickup of less than 1 mV when the 20kV main bank fires.

Each photomultiplier was connected by 10m of UR43 50Ω cable to Tektronix 551 oscilloscope , the cables being terminated with the characteristic impedance. The rise time of the system was 15 - 20 ns depending on whether 'G' or 'A' preamplifiers were used. Allowance was made for differences in frequency response of the preamplifiers.

In scattering experiments it is important to have a high rejection ratio in the dispersing instrument, values of 10^3 to 10^4 being common. The rejection ratio of this

instrument, defined as the ratio of the signal on the central 15Å channel to the neighbouring 15Å channel was only 150. Furthermore this value did not increase much for channels further away from the centre. Cleaning the grating did not help, and ultimately it was concluded that the poor rejection ratio was an intrinsic fault of the grating.

The throughput of the polychromator was measured as 4%. The approximate figures for each element were:- lens 70% (8 surfaces), grating 30%, fibre optics 25%.

9.5 Focussing the laser beam

There are three distinct requirements of any beam focussing system:

1. A small spot
2. A low divergence beam to cut down parasitic scatter.
3. Small beam angles to the axis so that the input and output ports are not struck by the laser beam.

A single lens can satisfy 1 , and can in fact produce a diffraction limited spot by sufficient demagnification of the laser aperture, but cannot simultaneously satisfy 2 and 3. A suitable two lens system is shown in fig. 9.5.

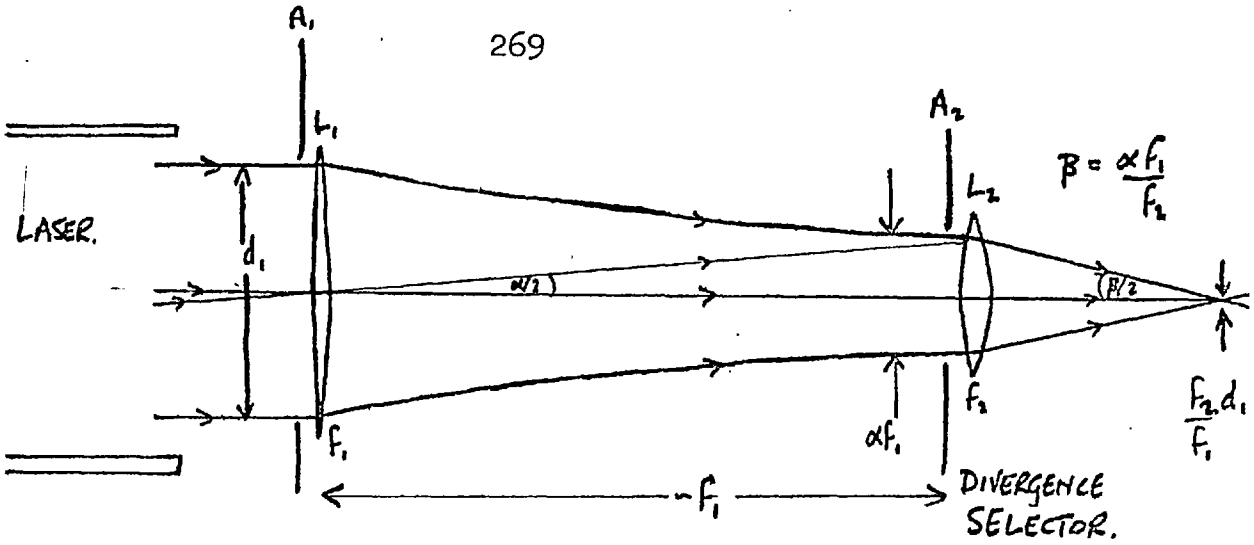

FIG. 9.5. FOCUSSING THE LASER BEAM

It is required that $f_2 << f_1$. Lens L_2 demagnifies aperture A_1, to a spot size of $2s = \frac{f_2}{f_1} d_1$. This would happen without L_1 but β, the angle of the converging cone would be large. (if all the light were collected.) Lens L_1, because it is near to the laser aperture, restricts the size of the beam at L_2 to αf_1, where α is the generic laser divergence, and so $\beta = \frac{\alpha f_1}{f_2}$.

Aperture A_2 is used so that light of divergence $> 2\alpha$ does not pass into the scattering region.

9.6. Parasitic scatter

Parasitic scatter is light entering the detector by multiple reflexions from surfaces. The spectrometer will discriminate against this light for wavelengths off 6943Å but will only reduce it by the rejection ratio. The poor rejection of the Baush and Lomb grating was only workable because trouble was taken to minimise parasitic scatter.

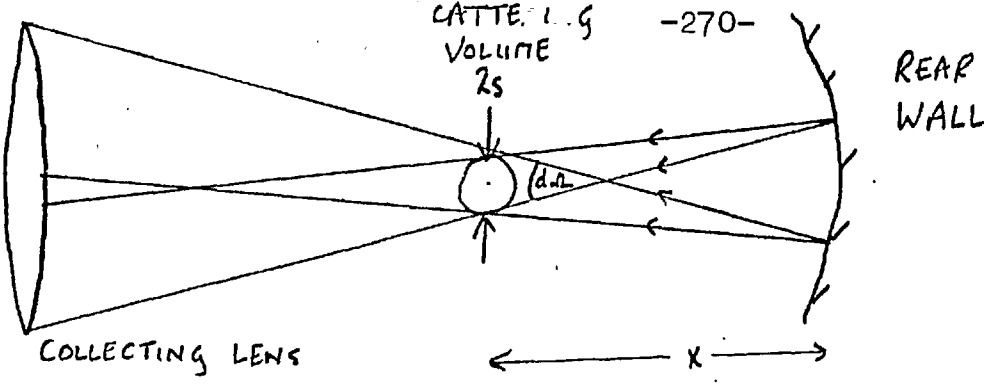

FIG. 9.6. THE COLLECTING OPTICS

The prime source, as the beam was well defined by the focussing system, was the input windows. Light from here reaches the wall behind the scattering region by multiple reflexions. In fig. 9.6., suppose the stray reflexions cause the back surface of the vessel to have an emissivity per solid angle S. It can be assumed $S = A/f_2^2$, proportional to the solid angle subtended by the window at the scattering region, where A is a constant. ℓ is the slit length.

$\therefore$ Parasitic scatter = area of wall x solid angle from wall x emissivity of wall.

$$= x\ell\,(d\Omega)^{1/2} \cdot \frac{2s\ell}{x^2} \cdot \frac{A}{f_2^2} = \frac{\ell^2 s (d\Omega)^{1/2} A}{x f_2^2}$$

$\therefore$ $\frac{\text{Thomson scatter}}{\text{Parasitic scatter}} \propto \frac{f_2^2 (d\Omega)^{1/2}}{s}$ (9.09)

Consequently in the early experiments f_2 was made large utilising the large linear dispersion of the spectrometer. A 3mm entrance slit still meets the resolution requirement of sec.9.4, but enables f_2 to be 75 cm The value of f_1, the first lens, is fixed by the laboratory geometry at 3m. The resultant spot size, 2s,

was 3.5mm. The scattering region was slightly inside the focus of lens L_2 as here the spot was slightly smaller. The input window, of spectrosil A, was near to lens L_2, at the end of a long glass tube. A set of irises of OB10 glass with chamfered edges encircled the beam to reduce the stray light. The geometry is shown in fig. 9.7. The parasitic scatter achieved was 1.8 torr CO_2 equivalent to Thomson scattering off an electron density of $4\ 10^{20}\ m^{-3}$. This was thought to be a very respectable level.

9.7 The alignment of the system

The procedure for alignment is enumerated.

1. The narrow bore of the short quartz input and output ports (20mm) necessitates the laser beam passing centrally down them. This line was defined by a He-Ne laser shone upwards, and centralised in the quartz input and output ports by apertures.

2. The t.i.r. (totally internally reflecting) spectrosil A prism, was positioned centrally on the upcoming He-Ne beam, and rotated so that the reflected beam was horizontal and entering the ruby laser aperture. The inclination of the ruby laser was adjusted to be approximately parallel to the He-Ne beam. The long glass input port was positioned with its axis and the beam, coincident, by

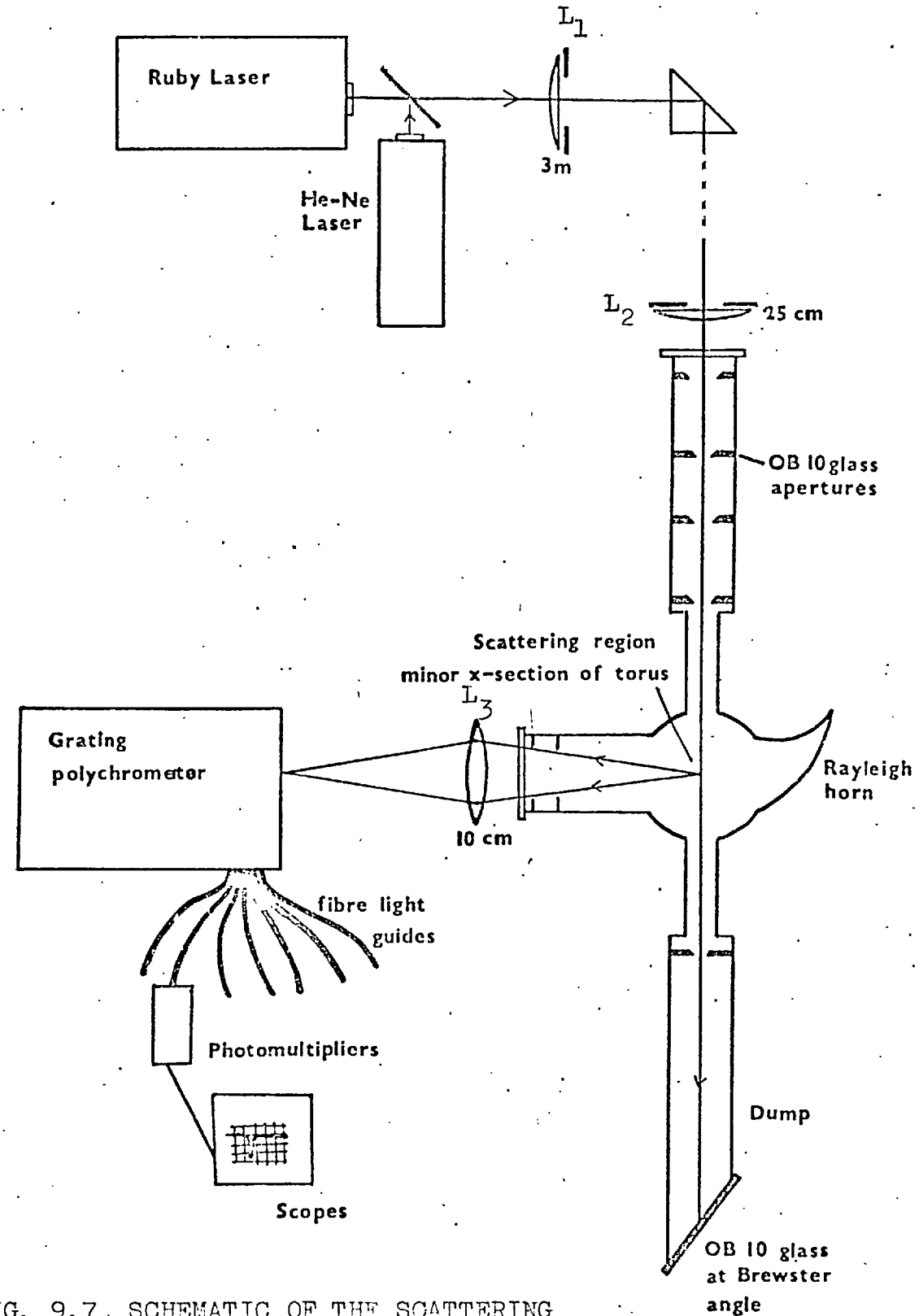

FIG. 9.7 SCHEMATIC OF THE SCATTERING APPARATUS.

centralising the beam at the top of the input port. This position did not change when evacuated. An aperture in the seal at the top of this port, and an aperture centralised on the upcoming beam near the ruby laser defined the upcoming beam.

3. The He-Ne laser was removed and placed at right angles to the ruby laser on the ruby laser table. A thick glass plate reflected the He-Ne beam into the ruby laser, so that the He-Ne beam was coincident with the ruby laser axis, verified by interference fringes from the etalon and the back mirror of the laser. The He-Ne beam reflected by the ruby laser was then passed through the apertures defining the upcoming beam, by adjustment of the ruby laser table.

4. At this point the He-Ne beam was shining through the torus and onto the floor. The position was marked. The lenses L1 and L2 were positioned so that the position of the spot on the floor did not change. The glass output port and the Brewster angle light dump were positioned.

5. The ruby laser produces a horizontally polarised beam; in its passive state it only reflects a vertical polarisation, and so the E vector of the He-Ne beam was vertical. The Brewster angle light dump was rotated (about a vertical axis) for minimum reflexion of the He-Ne beam, and then rotated through 90^{o} to give best absorption of the ruby laser.

6. The collecting optics had to be lined up at this stage. The retractable mirror was moved into the torus. The spectrometer was pointed in the right direction by shining a laser beam backwards through the spectrometer, so that it shone on the mirror. The collecting lens, L3, was inserted and the image of the mirror moved onto the slit by adjusting the position of L3. That the ruby beam would also go into the slit was checked by firing the ruby laser onto a piece of polaroid on the entrance slit, via the mirror.

7. Daily realignment of the system was then a relatively quick procedure. The aperture at the end of the input port and the mark on the floor were found not to move relative to the torus and the beam could be realigned with these points. The adjustment was made by rotation of the t.i.r. prism and simultaneous adjustment of the position of the beam on the prism. Usually the latter part of paragraph 6, checking the position of the ruby laser beam, was also repeated daily.

9.8 The initial experiments

The initial experiments showed that Thomson scattering was feasible on the polytron but that accurate measurements would require some improvements to the system.

Rayleigh scattering off neutral gases was performed with a milliwatt He-Ne laser. The drop of 10^{-11} in the

He-Ne power was compensated for by a factor of 10^3 in the p.m. voltage gain, and observing for a time 10^9 longer than the ruby pulse.

With the scattered signal going straight into a photomultiplier, scattering off 50 torr N_2 could be seen on an oscilloscope. The scattering was measured through the spectrometer using a phase sensitive detector. These experiments revealed the vital importance of filling the torus very slowly. Unless this was observed, fluctuations on the scattered signal were many times the scattered signal; this was due to dust on the bottom of the torus being raised. Letting the gas stand, even overnight, did not help. A suitable filling rate was 1 torr/ minute. It would have taken much longer to realise this using a pulsed laser.

Rayleigh scattering with the ruby was then performed. A false, high parasitic scatter ($n = 10^{23}$ m^{-3}) was evident, but this was greatly reduced by screening the spectrometer from the laser beam, some of the 4% light reflections being able to reach the photomultipliers. Carbon dioxide was used for the Rayleigh scattering. Very slow filling of the torus (1 torr/minute) gave reproducible results. An early result is shown in fig. 9.8. The parasitic scatter is $1.8 \pm .3$ torr CO_2 which is equivalent to an electron number density of $3.8 \pm .7\ 10^{20}$ m^{-3}, for Thomson scattering. From fig. 9.8

FIG. 9.8 RAYLEIGH SCATTERING OFF CO_2

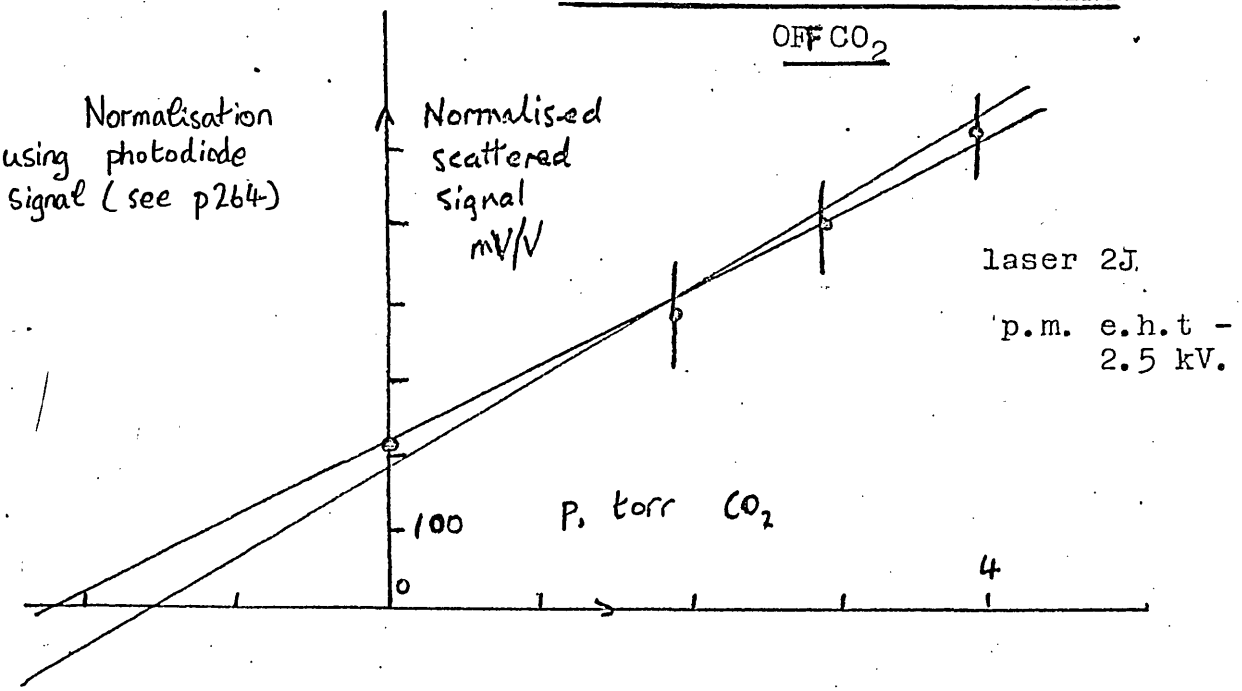

it can be seen that the total Thomson scattered signal across a 50Ω termination would be about 50mV for $n_e = 10^{20}$ m^{-3}. Detection of fractions of this voltage is required which is inconvenient because of the limited number of high gain oscilloscope preamplifiers. The voltage gain was doubled by operating the photomultipliers at -2.7kV. The laser energy was increased to 2.5J.

Thomson scattering was first seen in the preioniser plasma. Results are shown in fig. 9.9. As can be seen scattering

Fig. 9.9. Initial scattering results, 36 μs in the preioniser, initial filling pressure 25 mtorr argon, p.m. eht - 2.7 kV.

Channel A	Scattered signal(mV/V)	Vacuum signal(mV/V)	Plasma light	W (eV)	$n_e 10^{-20}$ (m^{-3})
A ± 10	400	450 ± 100	20 mV	4±1	4.1±2
B-10 to-25	43	−5 ± 5	8 mV		
C-25 to-40	26	1 ± 2	9 mV		

would be difficult if $n = 10^{20}$ m^{-3} as the scattered signal would be of similar size to the plasma light, and the overspill from channel A. Both of these are known quantities and can be accurately subtracted from the signal if the shot noise is sufficiently small. The plasma light should decrease at small number density but not the overspill.

Preliminary attempts were also made to observe scattering from the polytron. The size of the signal from the plasma light was about 3 times larger than the scattered signal, making measurement of the scattered signal inaccurate because of the shot noise of the plasma light.

The signal shot/noise ratio $\propto \sqrt{\text{number of photons in each channel}}$. Increasing the wavelength range of each channel increases this but with a loss of resolution.

The system was modified as described in section 9.9.

9.9 Modifications to the system

The principle modification of the system was an increase in the light gathering power, by altering the polychromator from f/13, to f/6, and simultaneously increasing the rejection ratio to in excess of 10^3.

A Jobin-Yvon diffraction grating, 1200 lines/mm , 10cm x 10cm, blazed at 7500 Å, and a 60cm, x 10 cm doublet collimating lense were used, giving the spectrometer an f/6

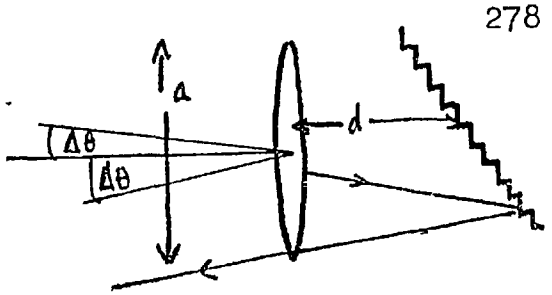

FIG. 9.10 VIGNETTING OF THE SPECTROMETER COLLIMATING LENS

$$f_{eff} = \frac{f_{lens}}{(1 - \frac{2d}{a} \sin \Delta\theta)}$$

aperture. Care was taken to keep the grating as close to the lens as possible to avoid cutting off part of the grating as shown in fig. 9.10. This improved the original design of Key. The dispersion was 13Å/mm, still low enough to satisfy the resolution requirement, if the entrance slit were shut to 800μm. Consequently the scattering region had to be made smaller. The increase in the rejection ratio allowed the restriction on the parasitic scatter to be relaxed. So lens L_2 (fig. 9.5) was changed to a 25 cm focal length, and the glass input port shortened. The spot size was 1mm.

The collecting lens was also replaced. The previous singlet lens had too much spherical aberration at high aperture and so two plano-convex lenses at f/7 replaced it.

The best parasitic scatter achieved was 6 torr CO_2, an increase of 3-4 over the previous system. Equation 9.9. predicts an increase of 4-5.

This figure for the best values was taken when the system was installed. Deterioration occurred due to markings of the input and observation window. For the

f/7 system the parasitic scatter rose to 20 torr CO_2 after 200 shots. Cleaning the components with nascent hydrogen was successful in reducing the parasitic level again.

A 400Å bandwidth interference filter was used between the two collecting lenses. The 70% transmission of 6943Å was acceptable as spectrometer overspill from higher quantum efficiency regions of plasma light was avoided.

A polariser at the input slit increased scattered signal to plasma light by 3 as the transmission of the vertically polarised (i.e. E to the grooves) radiation was twice that of horizontally polarised light. Unfortunately no $\lambda/4$ plate was available to take advantage of this.

The number of surfaces the laser light crosses to reach the photomultipliers is 22. To cut down reflexion losses the lenses and plasma windows were MgF1 coated. However, this was largely unsuccessful as the coatings were destroyed by the plasma and the laser.

9.10 The absolute power levels involved in the experiment

The scattered power P_s, from an incident power P_o, is given by

$$P_s = \frac{LP_o}{\pi s^2} \cdot n \cdot \ell \cdot \pi s^2 \sigma \, d\Omega = LP_o \, n \, \ell \sigma \, d\Omega$$

where ℓ is the length of the slit and L is the loss factor of

the polariser and filter. Under typical polytron conditions, with the system defined in section 9.9,

$$P_o = 80\text{MW}, \alpha << 1, \ell = 10^{-2}\text{m}, d\Omega = .02\text{st}, L = .5$$

$$\therefore \quad P_s = 60\ 10^{-6}\text{W} \equiv 2.\ 10^{14} \text{ photons/s giving } 4\ 10^{6} \text{ photons.}$$

If $\delta\lambda = 13\text{Å}$ and $d\lambda = 13\text{Å}$ then eq. 9.08 shows that 10% of P_s goes into the spectral range nearest the laser line. So with a 5% throughput and 2% quantum efficiency there are $2\ 10^{10}$ photo electrons/s, a total of 400 photoelectrons.

The photomultiplier gain is $\sim 10^6$ and so the current is $2\ 10^{10} \cdot 10^6 \cdot 1.6\ 10^{-19}$ A $= 3$ mA $\equiv$ 150.mV into the characteristic impedance. This is what is found. A check on the figure of 400 photoelectrons is provided by the $\sqrt{\frac{1}{400}} = 5\%$ plasma shot noise.

9.11 Plasma light

Any spectroscopic imaging system will collect light from a volume of plasma, larger than a cylinder of rotation of the entrance slit. A knowledge of this volume is required as the plasma light is a severe problem. The scattered signal must be distinguished from the noise on the plasma light. Evans and Katzenstein (1969 p.235) consider the problem of signal to noise and find that the incident power density $I_o > .1$ MW cm $^{-2}$. In the polytron, a power density 4 orders of magnitude larger is required. The criterion given by Evans

and Katzenstein is wrong, in that the scattering volume is much smaller than the volume from which emission arises, and inapplicable here, in that there are sources of light other than bremsstrahlung.

An analysis of the problem is given for the geometry used in the scattering experiment.

In any plane the plasma can be split into 8 regions shown in fig. 9.11, no light from other regions reaching the slit. It is assumed that the imaging lens does not quite fill the spectrometer, and is 1:1.

The problem can be simplified to 2 dimensions as the slit is long and narrow. With s = .9mm , $\frac{sf}{d}$ = 70 mm , which is much larger than the plasma dimensions, L_p. Thus in the plane of the length of the slit all of the plasma lies within region (1). In the plane of the width of the slit, $\frac{sf}{d}$ = 5.5 mm and so all of the regions must be treated. The product of acceptance <u>angle</u> (radians) and area will be evaluated, for all the regions.

(1) All emission from region (1) will reach the slit if it goes through the lens.

$$\text{Area x angle} = \frac{2s^2 f}{d} \cdot \frac{2d}{f} = 4s^2$$

(2) A fraction of emission from region (2) that goes through the lens reaches the slit. With reference to fig. 9.11 the angle between the extreme rays which pass

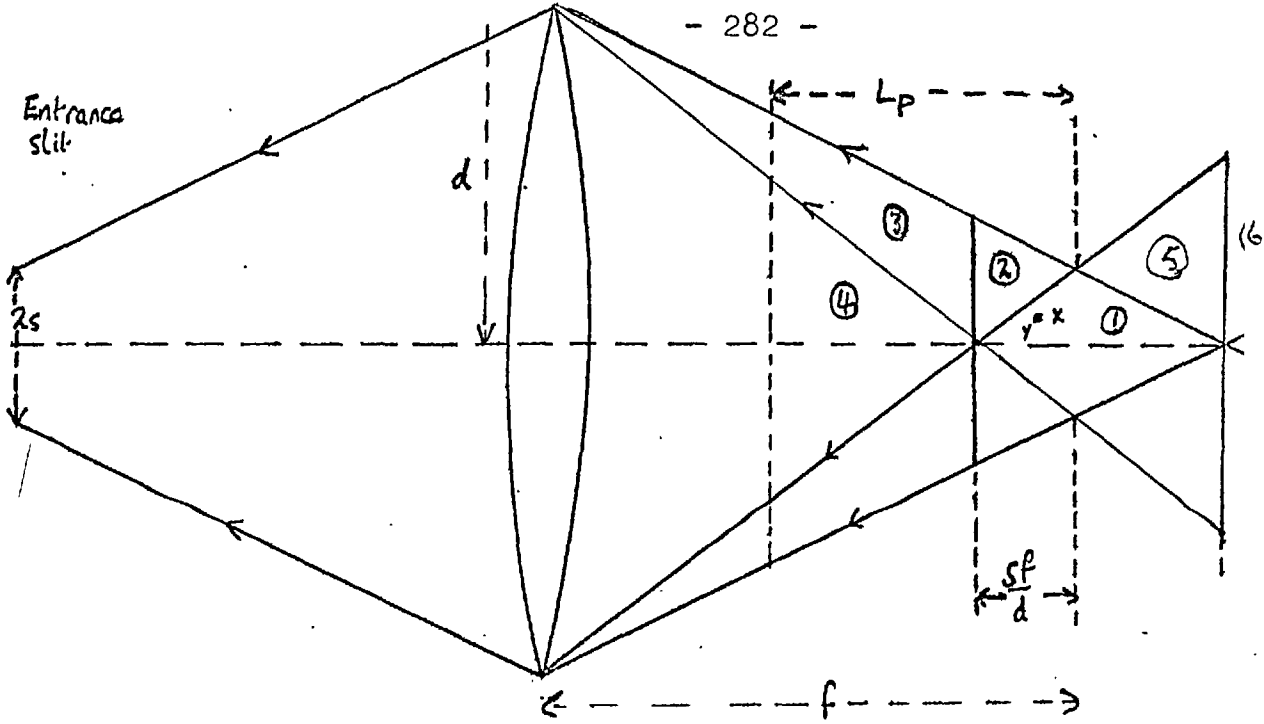

FIG. 9.11 THE REGIONS FROM WHICH PLASMA EMISSION REACHES THE SPECTROMETER.

f	=	170 mm
2d	=	25 mm
Slit width 2s	=	8 mm
Slit length f	=	9 mm
$\frac{1}{2}$ length of plasma	=	1 cm

through the slit is $\left(\frac{d-y}{f}\right) - \left(\frac{y-s}{x}\right)$, as all angles are small, and $s \ll f$

$$\therefore \text{ Area x angle } = 2\int_0^{sf/d} \int_{s-xd/f}^{s+xd/f} \left(\frac{(d-y)}{f} + \frac{(s-y)}{x}\right) dy\, dx$$

$$= 2s^2 \quad \text{as} \quad s \ll d.$$

(3) In region (3) the integrand is as before: the limits are altered. The integral is

$$2\int_{\frac{sf}{d}}^{L_p}\left(\left(\frac{d}{f}+\frac{s}{x}\right)y+\frac{y^2}{2}\left(-\frac{1}{x}-\frac{1}{f}\right)\right)_{-s+xd/f}^{s+xd/f}dx$$

$$=4s^2\ln\left(\frac{L_p d}{sf}\right)-\frac{2sd}{f^2}\left(L_p^2-\left(\frac{sf}{d}\right)^2\right)$$

(4) Region (4) is small c.f. (3) as $L_p \sim 1$cm.

(5) With reference to fig. 9.11 the angle between extreme rays is $\frac{y+d}{f}-\frac{(y-s)}{x}$. The limits are the same as in region (2); the term $\frac{y}{f}$ is discarded in (2) and so the integral here is the same as for region (2).

$\therefore$ Area x angle = $2s^2$

(6) Similarly region (6) is the same as (2) except for a change of sign

$\therefore$ Area angle = $4s^2 \log_e \frac{L_p d}{sf} + \frac{2sd}{f}\left(L_p^2-\left(\frac{sf}{d}\right)^2\right)$

(7) Region (7) can be neglected c.f. (6)

Totalling (1) to (7), the volume of emission x solid angle (steradians) is

$$2\ell.\frac{d}{f}\left(4s^2+4s^2+8s^2\log_e\frac{L_p d}{sf}\right)$$

where ℓ is the length of the slit. For the parameter of fig. 9.11, $\log_e \frac{L_p d}{sf} = .5$

$\therefore$ Volume x solid angle = $24\,\ell\, s^2\frac{d}{f}$ (steradians). Dividing by the collecting solid angle $\frac{4d^2}{f^2}$ gives an equivalent volume of

emission, $V_p = 6\ \ell . s^2 \frac{f}{d} = \frac{1}{8}\ cm^3$. By comparison the scattering volume $V_s = \pi s^2\ \ell = .5\ 10^{-2}\ cm^3$, is 30 times smaller.

9.12 Comparison of the plasma light with the expected level.

The classical expression for the rate of bremsstrahlung emission, per unit volume, per unit wavelength in hydrogen like plasmas, is

$$I_p = Z^2\ 2\ 10^{-36} \left(\frac{n^2}{\lambda^2 W^{\frac{1}{2}}}\right) \exp\ (-1.2 \times 10^{-4}/\lambda W)\ Wcm^{-1}\ cm^{-3} \quad (9.10)$$

(Glasstone and Lovberg). n and λ are in cm units, W is the electron temperature in eV.

An absolute calibration of the measured plasma light can be obtained from the Rayleigh scattering. This converts the experimentally measured plasma light to $P^E = 10^{-6} W$ from the 13Å band at 701 5 Å, when V_m=10kV, V_c=1.5kV, 3.5 mtorr argon at peak emission. At this time $n = 6\ 10^{20} m^{-3}$, W = 10eV , Z = 3, therefore the calculated bremsstrahlung, from eq. 9.10 is

$$P^B = 10^{-8}\ W\ (\pm\ 50\%)$$

It can be shown that this large difference is caused mainly by wall emission, by doing a similar calculation for the preioniser pinch. This yields $P^E = 2\ 10^{-5} W$, and $P^B = 6\ 10^{-6} W$. There is no wall emission at the pinch and so the plasma emission is about twice the calculated emission

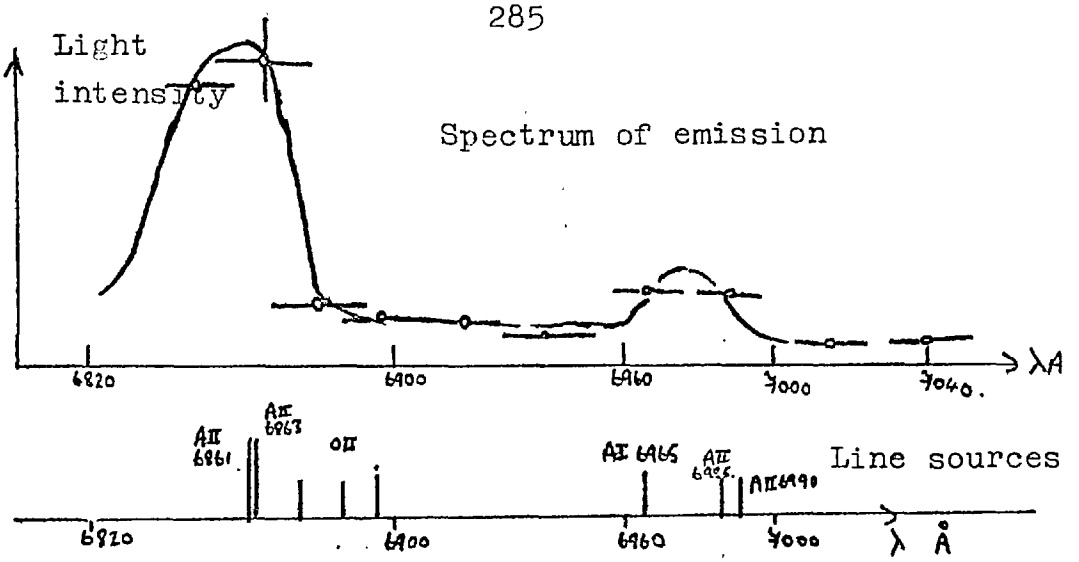

FIG. 9.12 PLASMA LIGHT EMISSION

(i.e. only considering bremsstrahlung). A similar ratio is expected for the polytron plasma, as it is a similar temperature and ionic charge, but as shown the measured emission is 100 times the bremsstrahlung. The conclusion is that most of the emission is due to wall light. This is confirmed by the photography in chapter 10.

The spectrum of plasma light emission is shown in fig. 9.12. Emission above a continuum level is evident at 6860Å, and 6980Å. This is due to listed AII and AI lines. The lines are not resolved in fig. 9.12 but were in a more detailed plot with higher resolution. Enhanced emission in the region of 6920Å is thought to be from listed oxygen lines in the region. It is evident from fig. 9.12 why most of the scattering experiments were on the red side of the ruby line.

9.13 Plasma perturbation by the laser

The simple case of heating of the plasma by inverse bremsstrahlung has been treated by Kunze. He considers the case of no heat diffusion during the pulse, and finds that

$$\frac{\Delta W}{W} = 5\,10^{-7}\left(\frac{nZ}{W^{3/2}}\right)\lambda^2\left(1-\exp(-h\nu/W)\right) I_0\,\Delta\tau$$

where n is in cm^{-3}, λ is in cm, I_0 the incident power in W cm^{-2} and $\Delta\tau$ is the pulse length in seconds. This is less than 10% for a 1eV, $5\ 10^{+21}$ m^{-3} plasma and so negligible in all the plasmas described in section 9.15.

There also exists the possibility of perturbing the number density of two atomic levels separated by the laser's photon energy. The only nearby line is the nitrogen 6942.9A. This possibility is considered by Measures, who shows that it is only likely for low temperatures, $W < .2eV$.

9.14 The calibration of the system

The scattered signals were normalised by the diode signal. The signal on fibre bundle I, in units of an electron number density for the total collected scattered signal is E_I. Bundle I, goes into photomultiplier J, producing a specific signal (i.e. mV signal per volt diode signal) S_J. S_J is related to E_I by $S_J = W_J E_I$ assuming E_I does not vary much over the range in the photomultiplier.

The value of W_c, where c is the channel monitoring 6943A, was found by Rayleigh scattering. The alternative of using a standard ribbon lamp was rejected as too inaccurate, requiring knowledge of the absolute beam intensity in the scattering volume, the collecting optics, and the frequency response of the system. A Rayleigh scattering calibration requires only the pressure of the gas.

A linear relationship between the scattered signal and gas pressure has been shown, for CO_2. Scattering in nitrogen showed that the ratio of the two cross sections was close to that quoted by Evans, 2.3. For an experimental run two points were established on such a graph, one under vacuum and one at typically 15 torr CO_2, CO_2 having a large scattering cross section. At least three shots were taken for each point.

The scatter on the points was 5%. The shot noise should be .5%. The 5% scatter was not due to dust, as it is seen on the parasitic scatter, and is probably due to variation in the mode of the laser output. The consequent error on W_c was 10%.

The filling pressure had to be 15 torr of CO_2 to be twice the parasitic level. An electron density of $10^{21} m^{-3}$ is equivalent to Rayleigh scattering from 4.79 torr of CO_2. Because the calibration signal was 10^0 times larger than the

Thomson scattering signal it was essential to check the linearity of the photomultipliers over this range. Rayleigh scattering was the ideal way of varying the light intensity. Any aperturing system will change the mean angle of incidence on the fibre optics. A filter was used to attenuate the parasitic scatter to the same level as the Thomson scattering. The result confirmed the p.m. linearity to 10% over the 1 decade tested.

To find the values of W_J for the other channels a cross channel calibration is necessary. A tungsten bulb was used for this; to avoid drawing too much d.c. current from the photomultipliers (> 1 mA) the signal from the bulb had to be measured across a large resistance (100 kΩ); the filament temperature was measured by an optical pyrometer being in the region of 1700°C. The spectral distribution is approximated by a straight line from Planck's law with

$$\frac{\delta E'(\lambda)}{E'(\lambda)} = \frac{\delta\lambda}{\lambda}\left(\frac{hc}{\lambda kT} - 5\right)$$

giving only a 10% correction. Variations in the pulse response of the oscilloscopes and the terminating resistances were measured by applying a fast rise step to the preamplifiers and measuring the signal after 20 ns. If L_J is the signal from the cross channel calibration then

$$L_J = AD_J\ W_J \qquad (9.13)$$

where A is a constant, and D_J is a factor allowing for the spectral emission from the lamp, and the frequency response of the channel

$$\therefore \quad W_J = \frac{L_J}{L_c} \frac{D_c}{D_J} W_c \qquad (9.14)$$

Calculation of n and W is then straightforward. The experimental data is measured to get S_J. Division by W_J gives the no. density/13Å. From equation 9.8

$$n_\lambda(\delta\lambda) = n_\lambda(0) \exp(-2.63\omega^{-3}\delta\lambda^2/W) \qquad (9.15)$$

$$\therefore \log_{10} n_\lambda = \log_{10} n_\lambda(0) - 2.63\omega^{-3}\delta\lambda^2/(W \log_e 10) \qquad (9.16)$$

A straigh line plot of eq. 9.16 gives the slope a

$$\therefore \quad W = \frac{-1.15\ 10^{-3}}{a} \qquad (9.17)$$

and $$n = \int_{-\infty}^{\infty} n_\lambda(0) \exp(-a\delta\lambda^2)\, d(\delta\lambda) = n_\lambda(0)\sqrt{\frac{\pi}{a}} \qquad (9.18)$$

9.15 The scattering results

Results were taken for 3 filling pressures (3.5, 12 and 25 mtorr argon, 2 main bank voltages (10 & 20kV) and 2 cusp bank voltages (1.5 and 3kV). For each discharge condition, scattering was done at least ten different times, from before 0 to after 2 μs from the initiation of the current.

A set of scattering results is shown in fig. 9.13. The current and the diode pulse are superimposed by using both inputs of a differential amplifier. The traces were recorded simultaneously, but the sensitivies of the photomultipliers differ. The vertical sensitivity was low to make the trace visible for the purpose of reproduction. Fig. 9.14 is a higher sensitivity recording of the $\pm$ 26A channels for the same discharge conditions, using the one high brilliance oscilloscope.

The data of fig. 9.13 is reduced to spectra in fig. 9.15. In fig. 9.15 the straight line fit means that the velocity distribution is Maxwellian to within the experimental error. The error bars are the shot noise, as gauged by the plasma light. From plots such as fig. 9.16 the errors on the number density and temperature are estimated, and are approximately $\pm$ 10% on both quantities. This error allows for shot noise on the scattered signal, shot noise on the plasma light, and errors in the cross channel calibration. The latter was repeated every run. Normal precautions were observed with the electronics i.e. allowing about 1 hour for the temperature of the photomultipliers, oscilloscopes and screened room to stabilise.

Additionally there is a 10% error in the absolute number density calibration. But the mode variations of the

+65A, 50mV/cm.

I_{ϕ} & diode

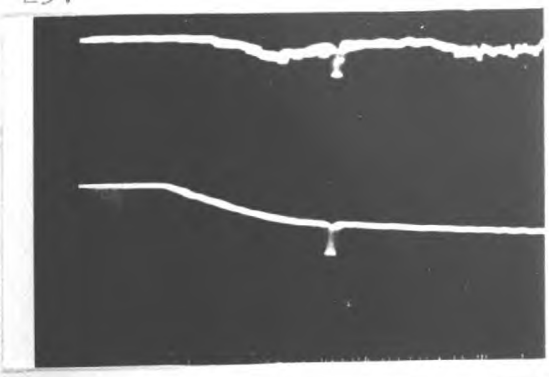

± 13A, 500mV/cm

± 52A, 100mV/cm

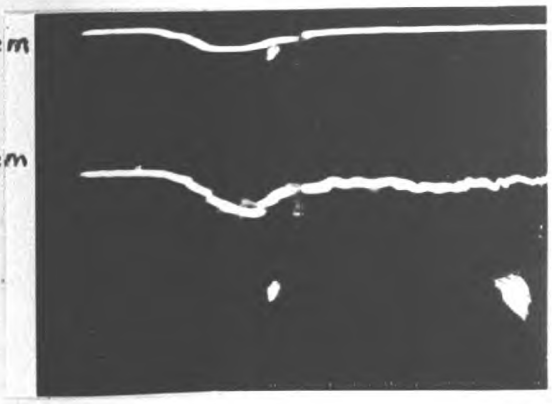

± 39A, 200mV/cm

± 26A, 500mV/cm

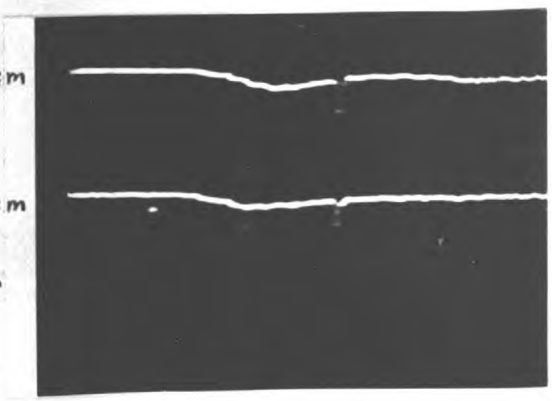

FIG. 9.13 Scattering off $n = 2.4\ 10^{21} m.^{-3}$, W = 6.4eV., 1 μs/cm., 13A/channel.

FIG. 9.14 Scattering signals with a higher gain, 1 μs/cm.

-26A, 20mV/cm.

+26A, 20mV/cm.

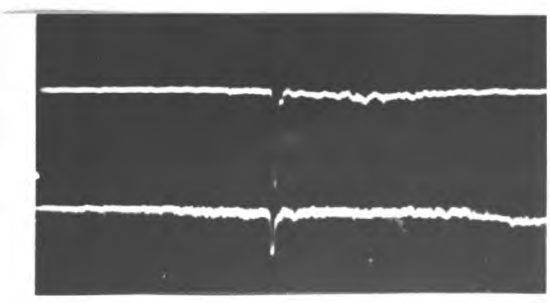

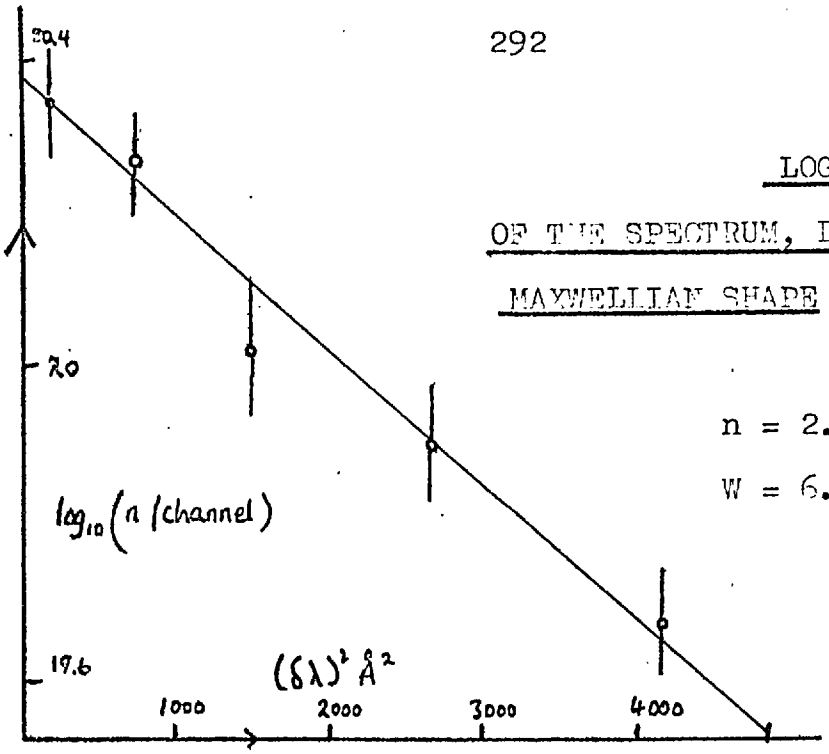

LOG - LINEAR PLOT OF THE SPECTRUM, DEMONSTRATING THE MAXWELLIAN SHAPE

$n = 2.4 \pm .3\ 10^{21}\ m^{-3}$.

$W = 6.4 \pm .5 eV$

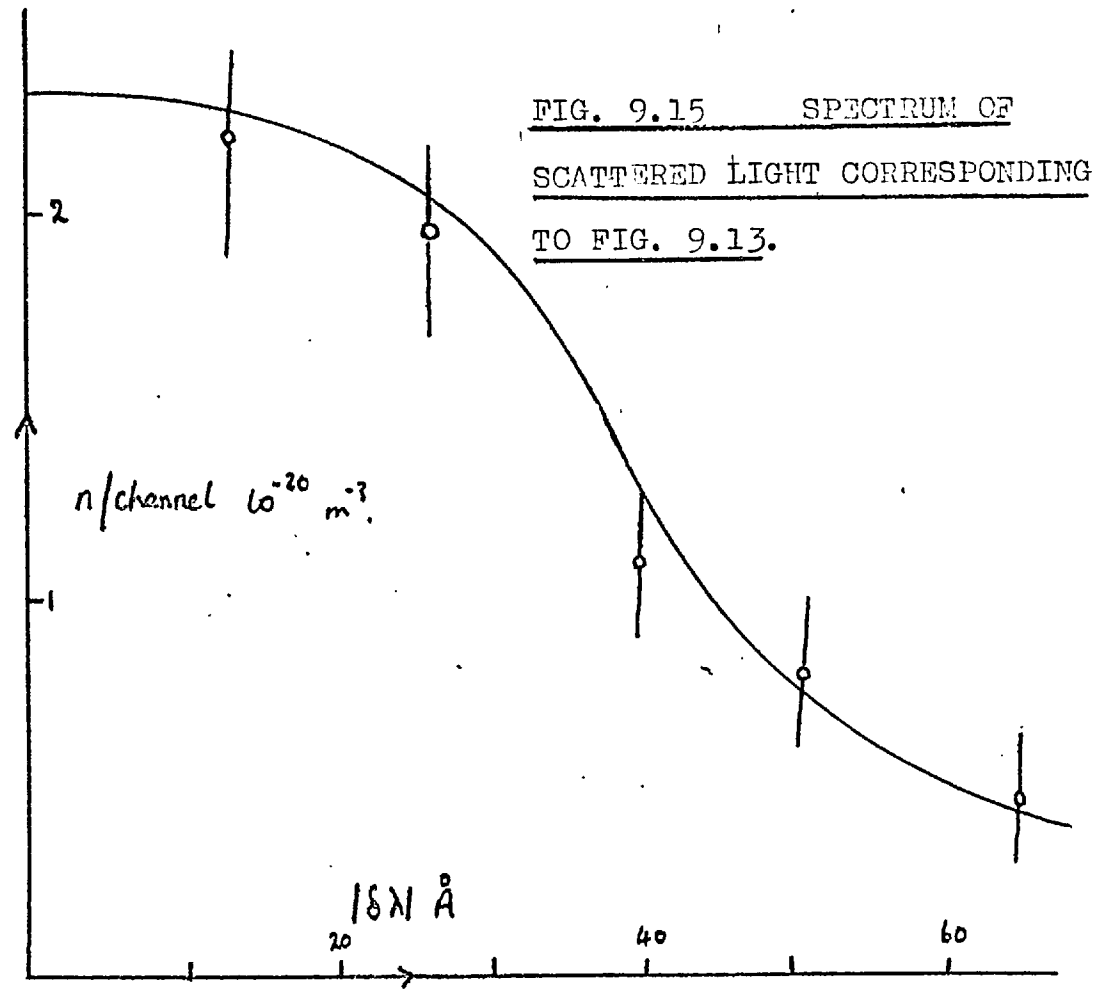

FIG. 9.15 SPECTRUM OF SCATTERED LIGHT CORRESPONDING TO FIG. 9.13.

laser which causes this error, by affecting the value of the parasitic scatter, will not cause random errors in the Thomson scattering. These 10% errors should be compounded for an error on the number density (say$(10^2 + 10^2)^{\frac{1}{2}}$ = 15%), but not on the temperature.

The number density calibration was repeated every run, the warm up time of the electronics coinciding with the filling time.

For some conditions the signal to noise ratio was less than in fig. 9.13 and for these conditions the errors could be as large as 30%.

Some results, as plots against time, are shown in fig. 9.16, 9.17 and 9.18. Where the points were taken during different runs this is indicated. The discrepancy between the points usually justifies the size of the error bars.

Errors in measuring the timing of the laser pulse relative to the start of the current were small, but there was an equivalent error because of non reproducibility in the evolution of the plasma. For example in fig. 9.17, the plasma which gave the point at 1.1 μs., n = 3.5 $10^{21} m^{-3}$, had probably evolved 100ns before an average plasma. This point is essential in accepting the lines drawn on fig. 9.18 (the low density case), e.g. the temperature of 13 eV at 450ns.

Ideally one would establish points on these plots at specific times by sufficient shots at these times. Unfortunately the timing difficulty makes this impossible. However the data presented was sufficient to establish n and W.

The general shape of the curves is the same for all conditions. The number density initially exhibits a slow rise, followed by a fast rise and an abrupt fall, to a very low value. The temperature rises during this time in a series of plateaux, reaching a peak just before the minimum number density, and then falling. After the minimum number density the plasma reforms.

These simplifying parameters are listed in fig. 9.19. Discussion of them is deferred to chapter 11.

9.16 The electron drift velocity

Suppose that in section 9.1 $f_{oe}(v_e) \propto \exp(-(v_e-v_d)^2 m_e/2kT)$ i.e. there is an electron drift velocity v_d, in the direction of $\underline{k}$. Then as

$$I(\delta\lambda) \propto S(\underline{k},\omega) \propto f_{oe}\left(\frac{\omega_o-\omega}{|\underline{k}|}\right)$$

$$\therefore I(\delta\lambda) \propto \exp\left(-\left(\delta\lambda/19\sqrt{W} - v_d (m_e/2kT)^{\frac{1}{2}}\right)^2\right)$$

$$R(+v_d) = I(\delta\lambda)/I(-\delta\lambda) = A \exp\left(\delta\lambda\, 2\sqrt{2}\, v_d\, m_e^{\frac{1}{2}}/(19\sqrt{W kT})\right)$$

where A is the ratio of the sensitivities of the two channels. If $\delta\lambda$ is chosen such that $\delta\lambda = 19\sqrt{W}$ Å and $v_d \ll \sqrt{\frac{m}{kT}}$ then

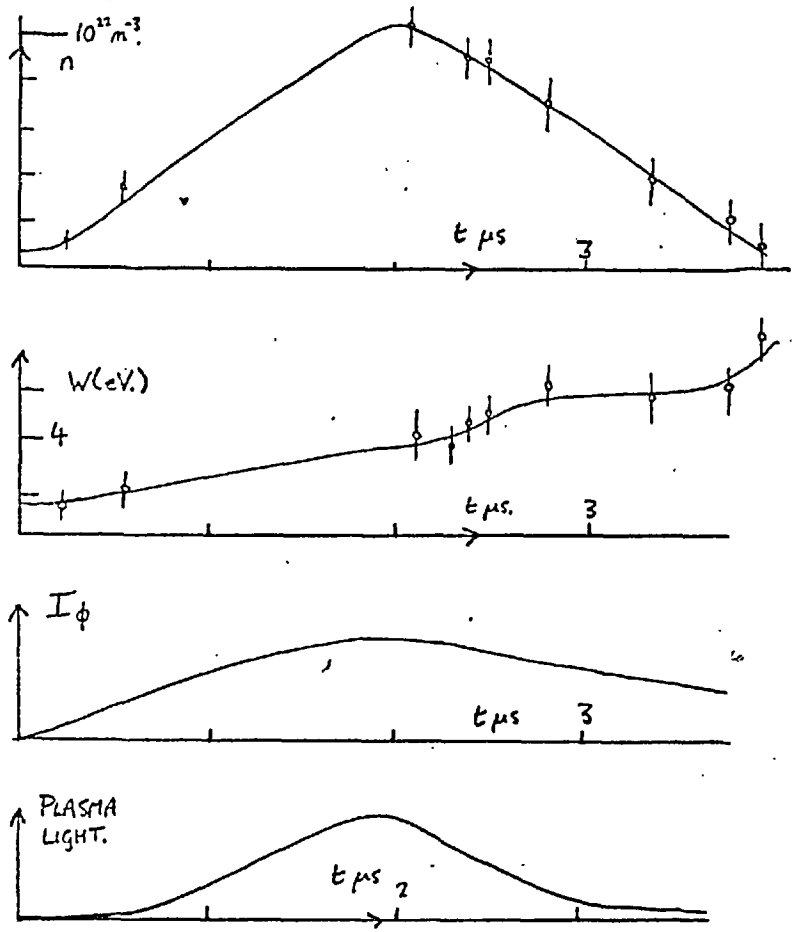

FIG. 9.16 : n and W for
V_m = 10 kV, V_c = 1.5 kV,
p = 25 mtorr, argon.

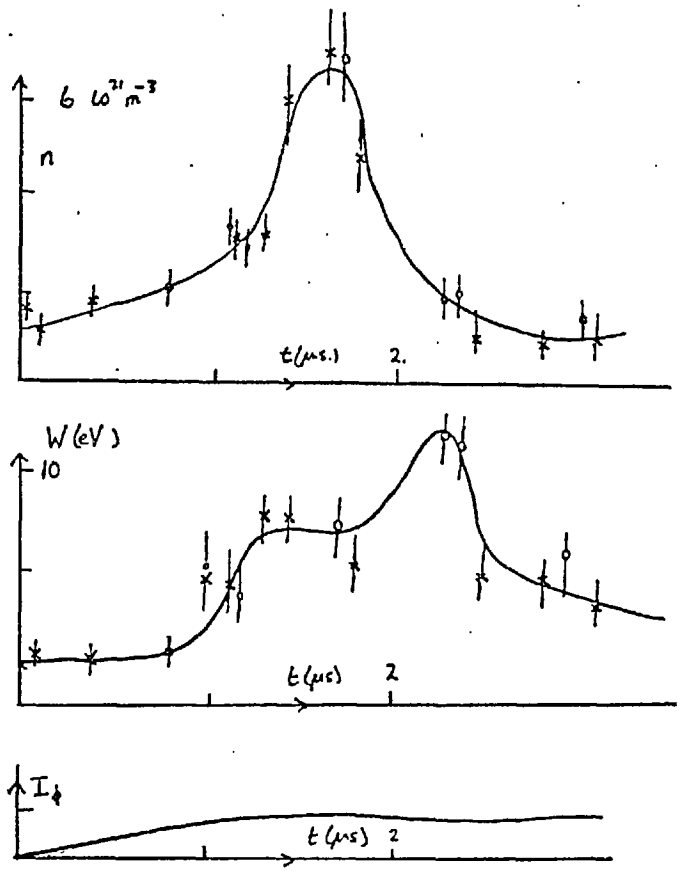

FIG. 9.17 n and W for
V_m = 10kV, V_c = 1.5kV,
p = 12 mtorr, argon

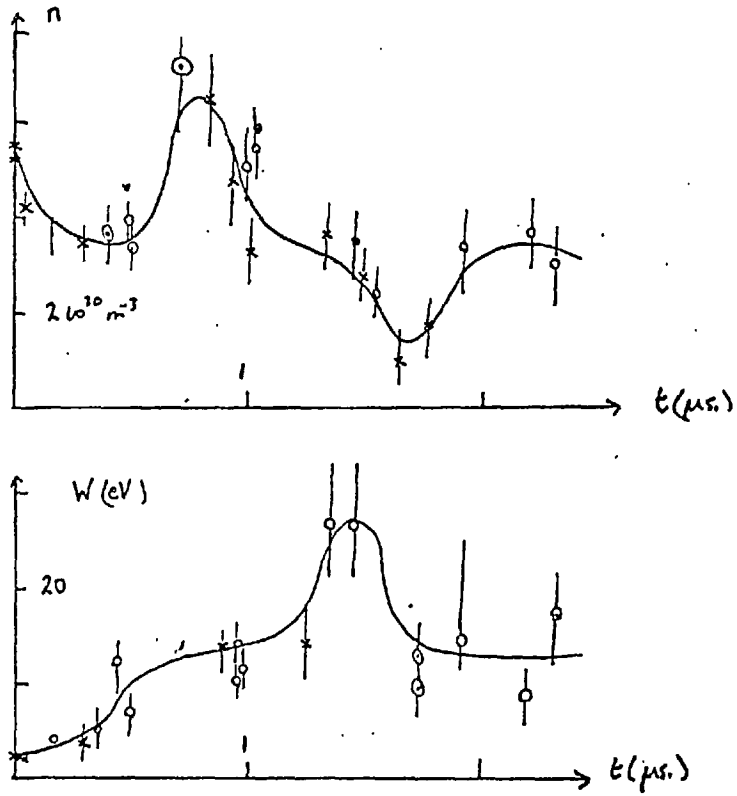

FIG. 9.18 n and W for
$V_m = 20\ kV$, $V_c = 1.5\ kV$
$p = 3.5$ mtorr, argon

FIG. 9.19 A SUMMARY OF THE SCATTERING RESULTS

V_m	V_c	n_n^o	n_e^o	n_e^x	τ_n^x	τ_n^n	W^o	W^x	τ_W^x
10	1.5	10	10	120	2.1	4.0	1.5	9.	4.0
10	1.5	4	8	60	1.7	2.5	2.0	12.	2.2
10	3.0	4	12	35	1.5	2.4	2.6	16.	2.0
20	1.5	4	8	41	1.3	1.8	2.0	6.	1.8
20	3.0	4	12	23	1.3	1.7	2.6	12.	1.7
20	1.5	1	5	6	.8	1.6	2.	30.	1.4

V_m main bank voltage, kV.

V_c cusp bank voltage, kV.

n_n^o neutral number density $10^{-20}\ m.^{-3}$

n_e^o initial electron number density $10^{-20}\ m.^{-3}$

n_e^x maximum electron number density $10^{-20}\ m.^{-3}$

τ_n^x time of maximum electron number density μs.

τ_n^n time of minimum electron number density μs.

W^o initial electron temperature eV.

W^x maximum electron temperature eV.

τ_W^x time of maximum electron temperature μs.

All quantities are local values, on axis, in the plane of the ring cusp, in argon.

$$R(+v_d)-R(-v_d) = 4\sqrt{2}\, A \frac{\delta\lambda}{19\sqrt{W}} \frac{v_d}{\sqrt{\frac{kT}{m_e}}} \qquad (9.19)$$

which is independent of n.

In the context of the polytron v_d is a poloidal velocity about the magnetic axis in the direction of $\underline{k}$: the poloidal drift can be reversed by reversing the magnetic field. The difference in equation 9.19 will be most obvious when $(R(+v_d)-R(-v_d))\exp(-\delta\lambda/19\sqrt{W})^2$ is maximised (i.e. $\delta\lambda/19\sqrt{W} = 1/\sqrt{2}$) and when v_d is maximised. As $j_e \propto \frac{E}{B^2}$ it is reasonable to expect $v_d = \frac{E \times B}{B^2}$ and this is why 20kV , 1kV , $\delta\lambda = \pm$ 26Å. were chosen as the most likely to give a positive result. (for V_m and V_c respectively)

Only the top half of the spectrometer slit was used. The cusp magnetic field along the laser beam was measured and it was found that the image of the centre of the top half of the slit was 4mm below the plane of symmetry, and (radially) outside the null point. $\frac{E \times B}{B^2}$ for the vacuum field will then be nearly parallel to $\underline{k}$, as illustrated in fig. 9.20. The main bank polarity was positive and so in fig. 9.20, $\frac{E \times B}{B^2}$ is clockwise around the null point. Therefore positive cusp bank should produce a blue shift, and a negative v_d. Fifteen shots were taken with alternating cusp polarity at t = 900 ns. Values of $R(v_d)$ with large errors were rejected, and the result was

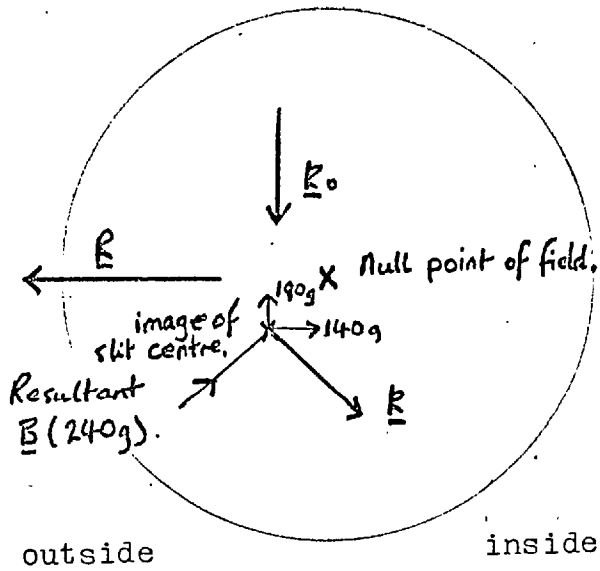

FIG. 9.20 X SECTION OF TORUS SHOWING THE SCATTERING GEOMETRY USING THE TOP HALF OF THE SLIT ONLY. LOOKING AWAY FROM THE LIVE COLLECTOR PLATE.

$$R(+\ v_d) \quad (V_c\text{-ve}) = 1.04 \pm .1 (5 \text{ shots})$$
$$R(-\ v_d) \quad (V_c \pm \text{ve}) = .88 \pm .1 (6 \text{shots})$$

Substitution into 9.19 will give a positive value of v_d which shows that the choice of v_d to correspond with V_c was correct, i.e. the shift is in the direction $\underline{E} \times \underline{B}/B^2$.

$$v_d = 2\ 10^4 \pm 1.5\ 10^4 \text{ m/s.}$$

This is smaller than $\frac{E}{B} = 3\ 10^5$ m/s. $\omega\tau = 1$ at this point and so $v_d \approx \frac{E}{2B}$. Even this cannot account for the low values of v_d observed. However, chapter 7 indicates that E_ϕ only appears across the ring cusp, which will be shifted by the induced field. Hence the negative result here is verification of chapter 7.

9.17 Radial profiles of the number density and temperature

The slit length was restricted to 4mm and the number density and temperature measured for 3 different positions of the image of the slit, 0, 10, and 20 mm upwards from the plane of symmetry. The absolute number density calibration had to be repeated at each point. For the last position half of the aperture was cut off by the output port. Here scattering was made additionally difficult by the low number density and the increase in plasma light, and so the number density and temperature at this poisition is not well established, except for an upper limit.

Albeit it is evident (from Fig 9.21) that:

1. the initial number density and temperature is not very peaked;
2. the number density drops on the outside first, and forms a sharp peak:
3. the temperature rises first on the outside evidencing a skin effect, and then drops with the number density:
4. the shape of the number density vs. time, 1 cm off axis compared with the axial number density is caused by an outward radial flow.

9.18 Non Maxwellian scattering

It has been possible to represent all of the profiles so far by Maxwellian distributions. This implies low α scattering and the values of n and W found are consistent with low α. Later in the discharge, after the time of minimum n , this was not true. The profiles found for these conditions are shown in fig. 9.22.

The profiles could not be established with only 6 channels and so many runs were used to establish them. The profile at 5 μs was established in greatest detail. The lack of detail at other times probably accounts for the non appearance of a double peak on the blue side . The red wing may appear double peaked, if a resolution greater than 13Å were available. It does seem though that the profile is not symmetric, the wing being nearer the centre on the blue side.

The wings develop slowly after 3 μs, are more pronounced at lower pressure than fig. 9.22, not so evident for a lower cusp field, but are at roughly the same $\delta\lambda$.

The question arises as to whether the wings are due to high α scattering. If this is the cause then from the shape α = 2. The position of the wing would give the number density as

$$n = 2.4\ 10^{19}\ (\Delta\lambda^{w})^{2}\ m^{-3} = 10^{23}\ m^{-3}$$

However this number density is far too large for 3 reasons. Firstly the filling pressure was only $5\ 10^{20}\ m^{-3}$

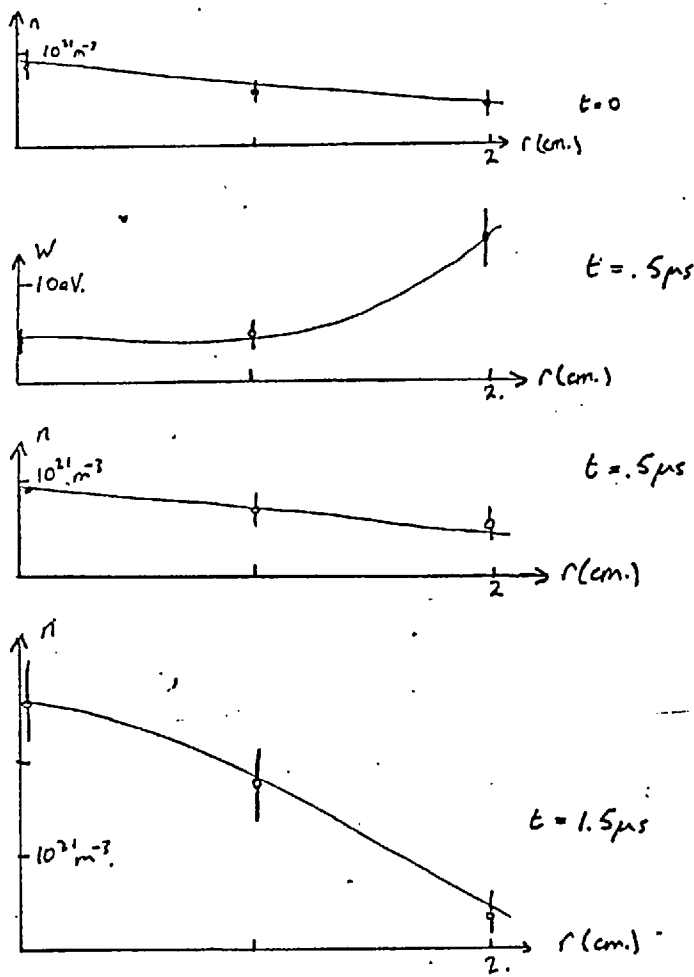

FIG. 9.21 RADIAL PROFILES

$V_m = 10kV, V_c = 1.5kV$, p = 12 mtorr, argon.

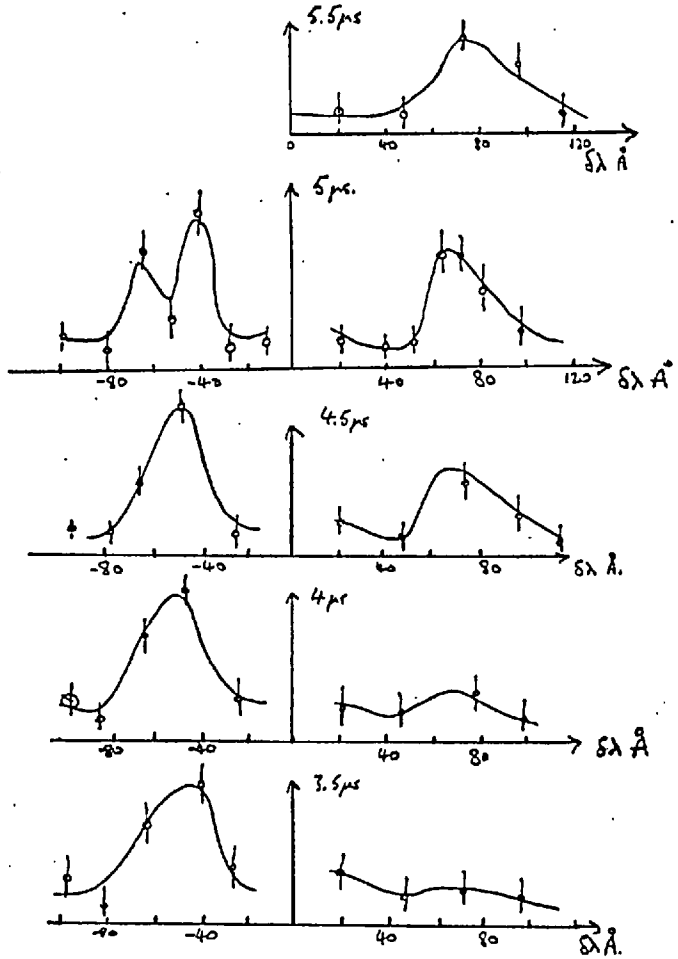

FIG 9.22 NON MAXWELLIAN SCATTERED PROFILES

$V_m = 20kV, V_c = 3.0kV$, p = 12 mtorr, argon.

and Z = 1. Secondly the plasma light is not large enough. By comparison with the preioniser when $n = 2\ 10^{22}\ m^{-3}$ at least one volt of bremsstrahlung emission, 3 channels away from the centre, instead of the observed 10 mV should be seen. Thirdly, from section 9.1, .2 of the total Thomson scattered light would be in the electron feature when $\alpha = 2$. The integral of the line profile should be $2\ 10^{22}\ m^{-3}$ instead of the actual value of $1.6\ 10^{20}\ m^{-3}$, from integrating fig. 9.22.

Anomalous scattering has also been reported by Ringler and Nodwell(1969). However, this takes the form of peaks at multiples of the plasma frequency.

The near symmetry, and distance from the centre rules out Raman scattering. The laser could be exciting atomic transitions. The argon line radiation in fig. 9.12 does not coincide with the wings. An impurity could be the scattering but this seems unlikely because of the symmetry, the width of the wings and the time history of the scattering which follows the laser emission.

A likely cause is scattering off a wave. The wave would only be excited at late time when the temperature is low and is assisted by a large cusp field. To amplify this consider $n = n_0 + n_1 \cos(\omega_1 t + \underline{k}_1 . \underline{x})$

then $n(\underline{k}, t) = n_1\, \delta(k, k_1) \cos \omega_1 t$

and from equation 9.6, $\delta(\underline{k},\omega) \propto \int_{-\infty}^{\infty} \delta(\underline{k},\underline{k}_1)\, e^{i\tau(\omega-\omega_0)} \cos\omega_1 t \cos(\omega_1 t + \omega\tau)\, d\tau$

$$= \tfrac{1}{2} \int_{-\infty}^{\infty} \delta(\underline{k},\underline{k}_1)\, \delta\, e^{i\tau(\omega-\omega_0)} \cos\omega_1\tau\, d\tau$$

$$= \frac{T}{2}\, \delta(\underline{k},\underline{k}_1)\, \delta(\omega_1, \pm\omega-\omega_0)$$

where the integration is terminated at T, half the pulse length. $\underline{k}$ is fixed and so fixes $\underline{k}_1$ of the wave to observe scattering. There are scattering wings at $(\omega-\omega_0) = \pm\omega_1$. If it is caused by a wave then for $k_1 = 13\ 10^6\ m^{-1}$, $\omega_1 = 2.5\ 10^{13}$ Hz.

Keilhacker and Steuer (1971) have seen enhanced scattering off turbulence but with their k_1 100 times smaller, and with a cut off to the scattering when $k_1 > 1/\lambda_d$, whereas here $k_1 > 1/\lambda_d$, is implied.

An alternative explanation is that there is electron drift along the direction of $\underline{k}$, of $3\ 10^6$ m/s, the velocity necessary to give the observed Doppler shift. Supposing that this is produced by an $\underline{E} \times \underline{B}/B^2$ drift, then the applied voltage has to appear across only 2 mm. This is consistent with the photography of section 10.1 and with chapter 7. Also the value of $E_\phi \times B/B^2$ can be independent of the value of V_c as observed in this experimental work.

Further work on this experiment will be needed to distinguish between these two possibilities.

CHAPTER TEN

EXPERIMENTAL WORK ON THE POLYTRON EXCLUDING SCATTERING

This chapter describes the measurements of the plasma parameters other than number density and temperature. It follows the laser scattering measurements because in many ways the number density and temperature are the basic parameters. Chronologically though much of this work preceeded chapter 9.

The objectives of the measurements are, in decreasing importance:-

(1) to quantify the acceleration process, measuring the electrical parameters, the force on the plasma, the velocity, the spatial variation of plasma and of the plasma currents.

(2) to measure, although less quantitatively, the loss of plasma.

(3) to observe the properties of the plasma after the loss.

This chapter is mainly descriptive. A few checks of the internal consistency of the measurements are made, but a detailed discussion of the results is postponed until chapter 11. Except where stated the results are taken in argon.

10.1 Plasma Photography

An image coverter camera was used to take both framing and streak photographs of the plasma. Only three frames per discharge could be taken from the camera used, so a sequence of photographs had to be obtained from several shots.

A sequence of such photographs is shown in fig. 10.1. This shows the importance of varying the aperture even at a given time in the discharge, because of the large spatial variation in emissivity. Initially an axial column of diameter 2 cm forms, together with a brighter region under the ring cusp extending across the whole tube diameter. A cusp shaped plasma is present initially. The cusp shaped plasma remains up to the loss time. Before the loss time, e.g. 200ns and 500 ns fig. 10.1, a dim region can be seen outside of the highly luminous region. This could come from ionisation of neutrals near the wall. The intensity increases with time, up to the loss time. After this the photographs become less reproducible. This is shown more clearly in fig. 10.2. where V_m is increased, and the pressure decreased, with respect to fig. 10.1.

At the loss time the diameter of the luminous region under the coil broadens, and the intensity drops. Simultaneously a sharp interface forms under the ring cusp with a

tail downstream (parallel to E_ϕ). The direction of the tail changes with the main bank polarity, c.f. fig. 10.1 to 10.4. Later e.g. 1.1μs in fig. 10.2, the rest of the plasma is still emitting slightly but there is a contrasting dark band next to the sharp ring. This is not a false effect due to a dirty wall.

The effect is also seen when viewing through the clean window of the laser scattering port. Also the band can be seen to move e.g. 1.1μs, 1.6μs, and 2.1μs, fig. 10.2. The band is stable for up to .5μs in fig. 10.2, but then a ragged, scalloped edge forms. For one discharge in fig. 10.2. the characteristic wavelength is 4mm. In another case shown(1.6 s, fig.10.2) it is 1cm. Measurement of a sequence of exposures from the same plasma in fig. 10.2, (1.1μs., 1.6μs., and 2.1μs) shows that the scallops form by the emitting region moving downstream, leaving dark spaces. This photograph shows that the velocity exceeds $.5\ 10^4$ m/s. (From the distance moved between 1.6μs and 2.1μs). The scallops look similar to Rayleigh-Taylor instabilities in z pinches (Curzon et al., 1960).

The different perspective of the next ring cusp(in fig. 10.2) shows that the light is emitted from a ring near to the wall. For the ratio of major to minor axes of the ring is $.2 \pm .05$, equal to sin 10^0 , the next ring cusp being 10^0 further around the torus.

Increasing the cusp field increases the growth time for this instability. At 3kV , it is not seen up to 3μs,

whereas at .75kV., it is seen after 1.2μs. Also when the cusp field is increased the width of the ring decreases.

It is seen that the width of the ring, as well as the stability of the light front, is related to the Larmor radius of the ions, for in hydrogen the ring is much thinner, about 1mm , as shown in fig. 10.3. There is no pronounced instability on the light front in hydrogen, but there is a curvature with the convex side facing upstream.

Fig. 10.2, after 1.5μs , shows that the plasma under the coil is shifted vertically up under the right hand coil, and down in the left. A photograph with the cusp polarity reversed, is also shown and the shift inverts, but it is independent of main bank polarity. The current flow is outside of the magnetic axis and so there is a vertical force on the plasma by virtue of the $\overline{j_\phi B_r}$ interaction. It is supposed that the shift is caused by this force and is advected to the coil region by the plasma motion. This explanation accounts for the observed direction of the shift and its dependence on the polarities of the fields.

Fig.10.4. shows a set of stereoscopic photographs obtained by placing a mirror beneath the torus. These show unequivocally that the plasma under the coil is not in contact with the wall, and forms about the minor rather that the magnetic axis. Also it can be seen that only a very narrow peninsular of plasma extends to the wall at this early time .

The ring cusp region presumably looks brighter because of the longer line of sight. At later times, 1.5μs, the luminous region in contact with the wall broadens, and after the instability has set in the plasma is only off the wall near to the coil.

Fig. 10.4. shows the cusp second from left making good contact with the wall at 1.5μs. The next frame shows that this cusp, .5μs later, is much dimmer than its neighbours, suggesting a cooling because of the larger area of wall contact.

The steroscopic view confirms the conclusion from viewing the next cusp in fig. 10.2. that most of the light after the loss time comes from the region near the wall. However, there is still emission from the volume of the plasma, except from the dark space upstream of the ring cusp. The implication is that a singular disk of low emissivity plasma, only a few mm. thick, but extending across the whole tube, exists.

Streak photographs of the plasma, viewed from below, through a slit parallel and adjacent to a cusp coil, are shown in fig. 10.5. These should be interpreted with the help of fig. 10.4.

From fig. 10.5. the cusp field keeps the plasma off the wall. From fig. 10.4, eg. 3μs, the light in fig. 10.5. does not come from debris which has been swept along the wall, but is representative of the position of the plasma.

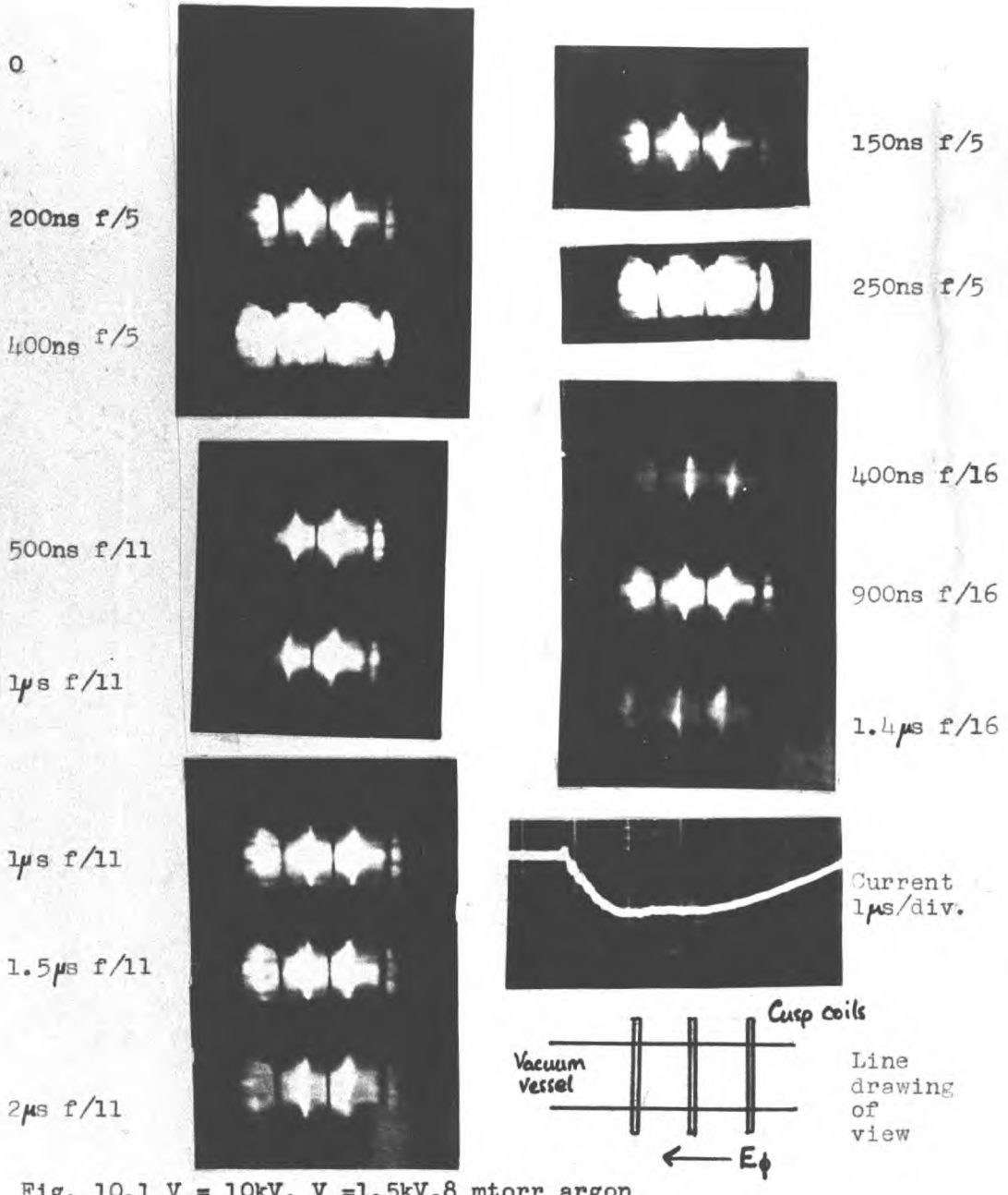

Fig. 10.1 V_m= 10kV, V_a=1.5kV,8 mtorr argon

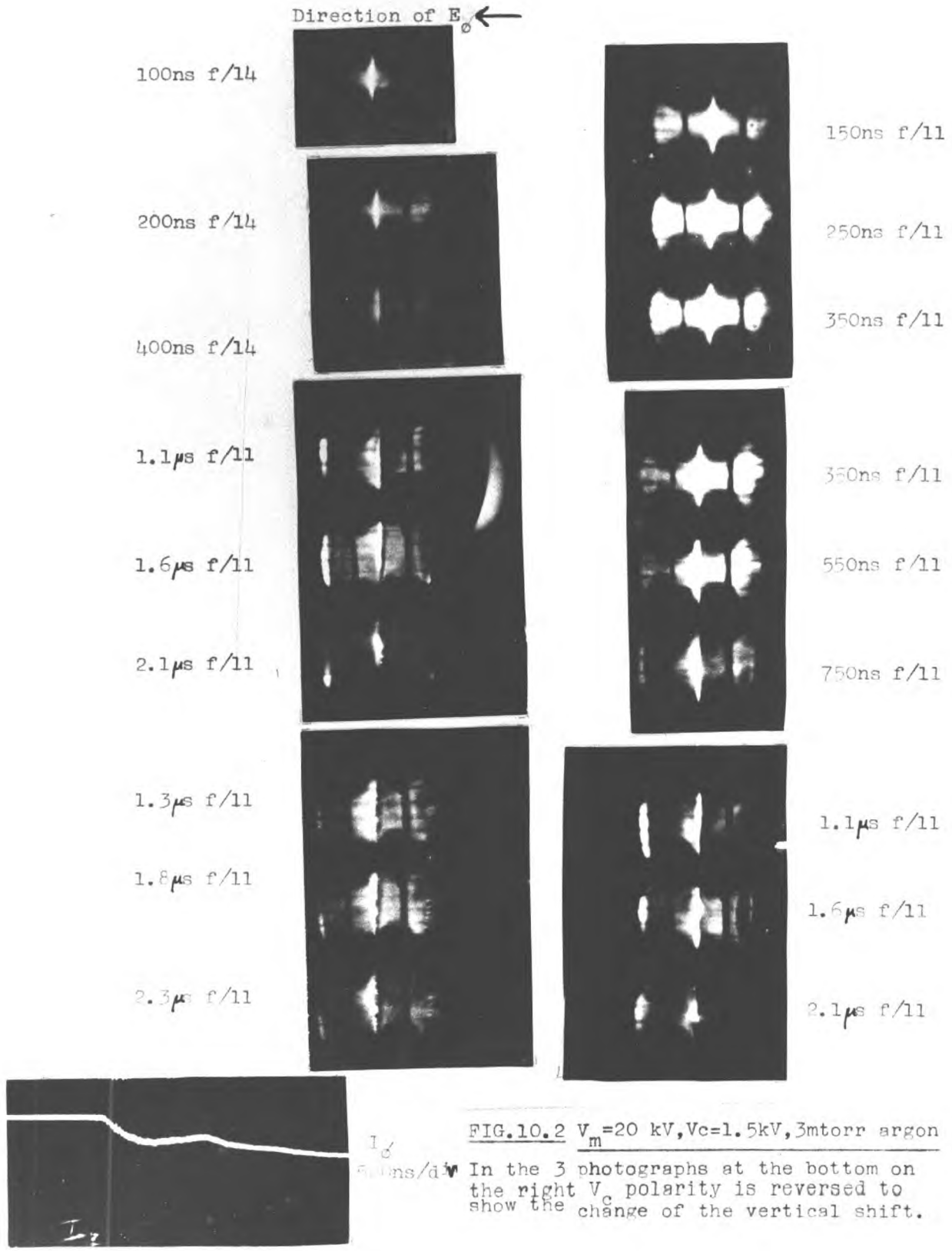

FIG.10.2 V_m=20 kV, Vc=1.5kV, 3mtorr argon

In the 3 photographs at the bottom on the right V_c polarity is reversed to show the change of the vertical shift.

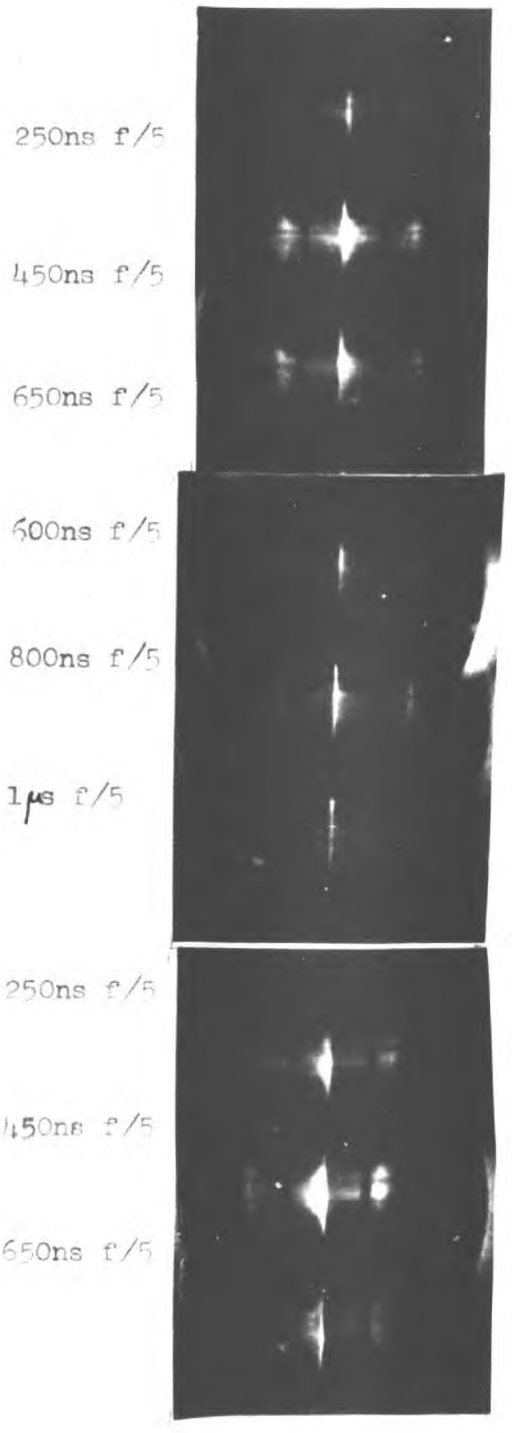

FIG 10.3

V_m=20kV, V_c= 1.5kV, 6 mtorr hydrogen

Direction of E_ϕ for 1st 6 →

Direction of E_ϕ for last 3 ←

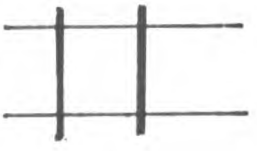

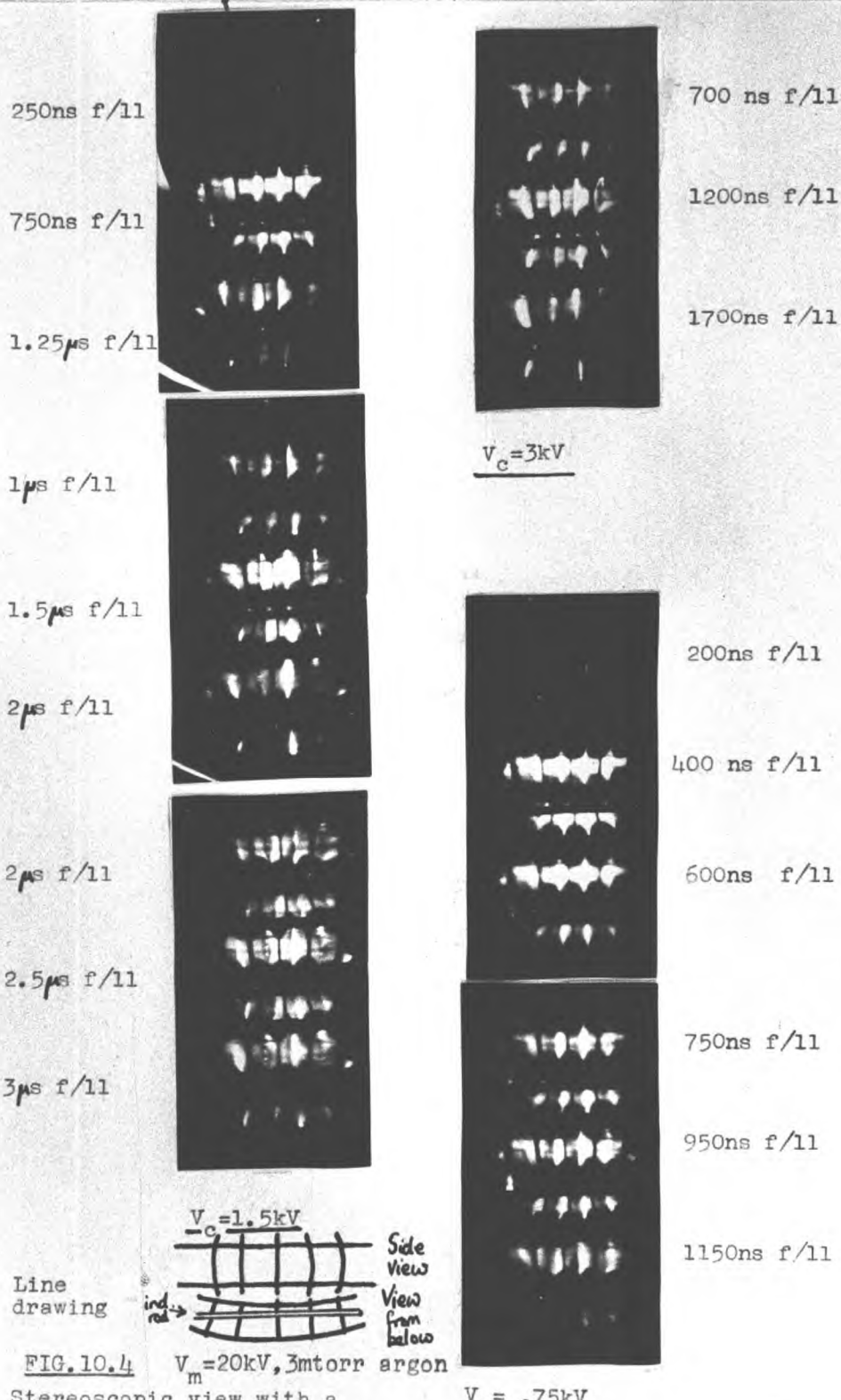

FIG.10.4 V_m=20kV, 3mtorr argon

Stereoscopic view with a mirror beneath the torus to view from below as well as straight on

FIG. 10.5 STREAK PHOTOGRAPHY

VIEWING FROM BELOW

V_m = 20 kV., 3.5 mtorr argon

V_c = .7 kV. f/16

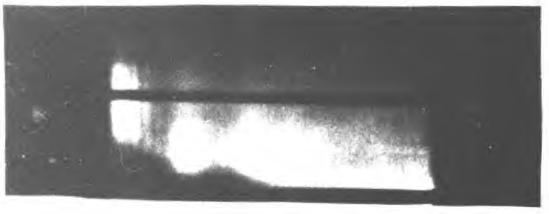

V_c = 1.5 kV. f/16

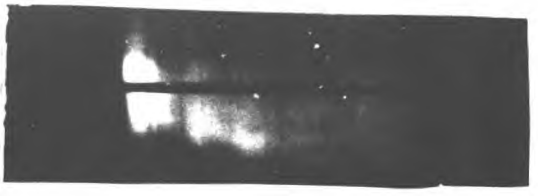

V_c = 3 kV. f/16

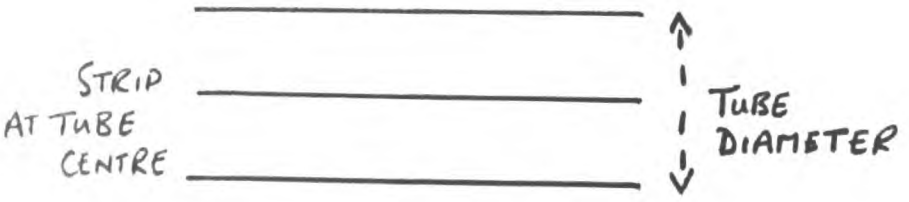

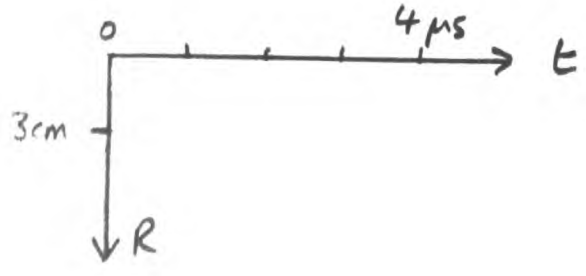

Outward drift of the plasma is evident in fig. 10.5. At lower values of main bank voltage than V_m = 20kV., the streak photographs show that the plasma does not hit the wall, but is displaced outwards. Similarly at p = 2mtorr, V_m = 20kV, V_c = 3kV, the inner boundary of the plasma curves back towards the centre of the torus. These observations indicate that the displacement is proportional to the toroidal current. Fig. 10.5. also shows that the displacement is decreased if the cusp field is increased.

10.2 Toroidal current measurements

The plasma current was measured by a Rogowski coil. A compensated coil was used. The frequency response of the system is discussed by Cooper(1963), who shows that it is limited by the transit time along the coil, considered as a delay line. An equivalent view is that there is a L/R rise time, but R is the characteristic impedance of the coil not the terminating resistance. For the coil used

$\frac{C}{\ell} = 10^{-10}$ F/m; $\frac{L}{\ell} = 10^{-5}$ H/m; giving a transit time of 10ns. By applying a step I it was shown experimentally that the rise time was less than 100ns. Calibration was by the measured coil parameters and against a known current.

Parkinson (1969), studied the plasma current. However, he was only interested in the peak current, which occurs after several μs , and never measured the initial stage. Only

by taking greater care with pick up have the results described here, taken at early times, been obtained. Some of these measurements have already been published (page 397).

The current waveform typically consists of a linear rise for .5μs to 1μs, a shoulder, whose position defines the loss time, a smaller or negative $\frac{dI_\phi}{dt}$, and then another rise depending on the values of V_m and V_c. Two such current waveforms for V_m = 10kV and 20 kV , V_c = 1.5kV, p = 3.5 mtorr , argon are shown in fig. 10.6.

A detailed study of the rate of rise of the current has been made. In fig. 10.6. there is a slight curvature of the 'straight' part; the value of $\frac{dI_\phi}{dt}$ at t = 0 was measured for this study. Some of these results are shown in fig. 10.7. Each point was established by at least 4 shots. A linear relationship between $\frac{dI_\phi}{dt}$ and V_m is seen. An independence of V_c, once V_c is above a critical value, and also an independence of p, once p is above a few mtorr , is evident.

The experimental value for large V_c, but p = 3.5mtorr argon is

$$\frac{dI_\phi}{dt} = 8.5. \left(\frac{V_m}{10kV}\right) \text{ kA}/\mu\text{s} \qquad (10.1)$$

A detailed numerical comparison with theory is made in chapter 11. In general terms these curves can be explained by the current being mainly an ion current, thus the linear

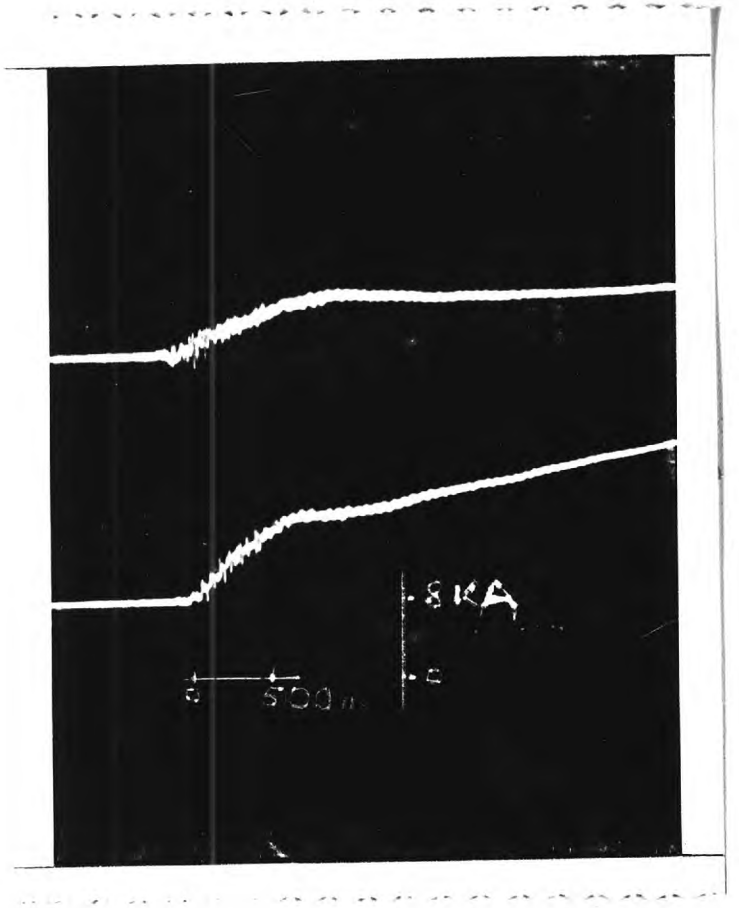

FIG. 10.6 I_ϕ IN ARGON

500 ns/cm, V_c = 1.5 kV.

3.5 mtorr, 1 cm = 8 kA.

V_m = 10 kV.

I_ϕ

V_m = 20 kV.

FIG. 10. 8 I_ϕ IN HYDROGEN

500 ms/cm, 1.6 kA/cm

V_m = 20 kV. V_c = 1.5 kV.

p = 0

p = 10 mtorr

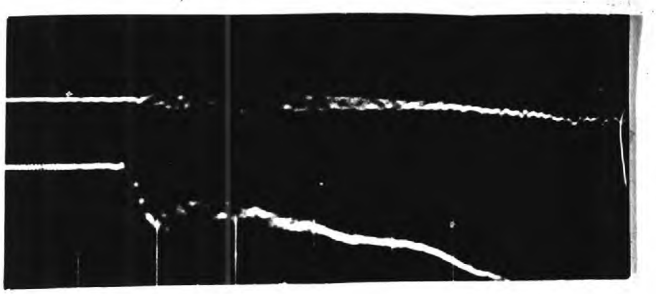

I_ϕ

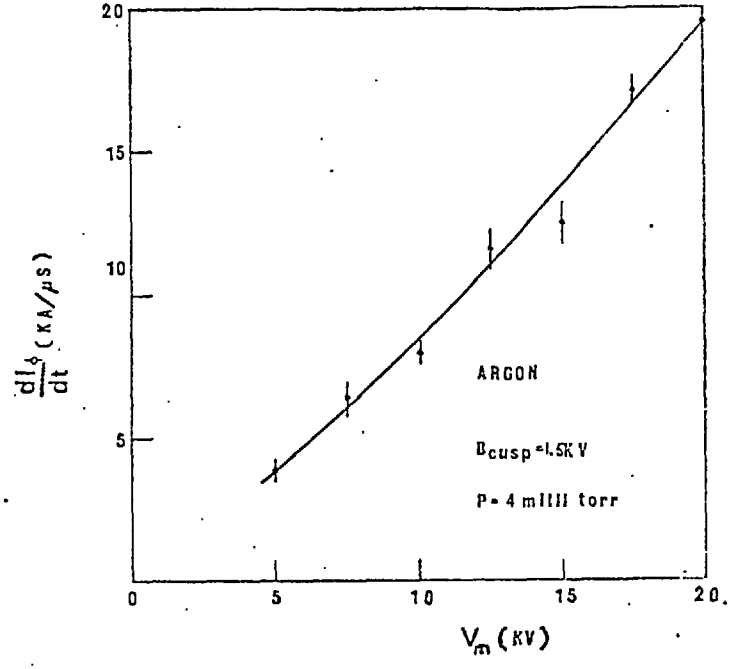

FIG. 10.7c $\frac{dI_\phi}{dt}$ vs. pressure

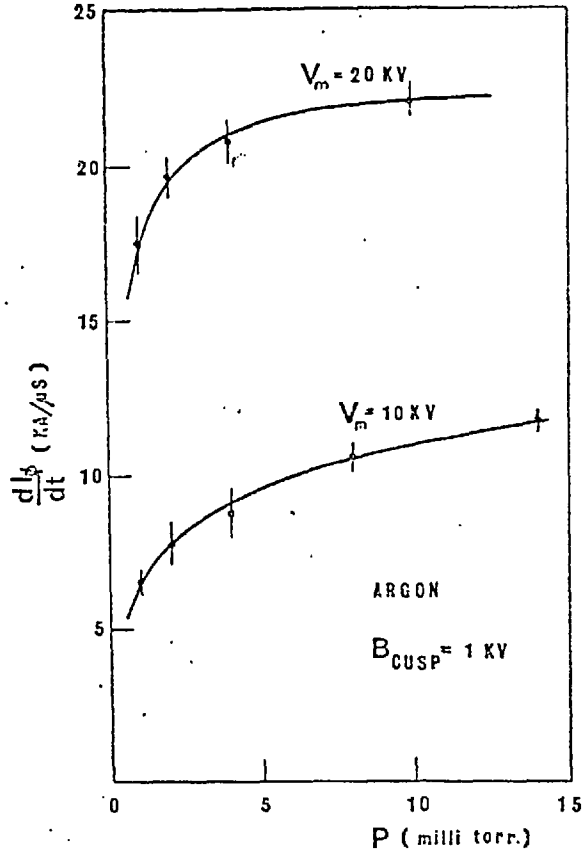

FIG. 10.7a $\frac{dI_\phi}{dt}$ vs. $V_m(E_\phi)$

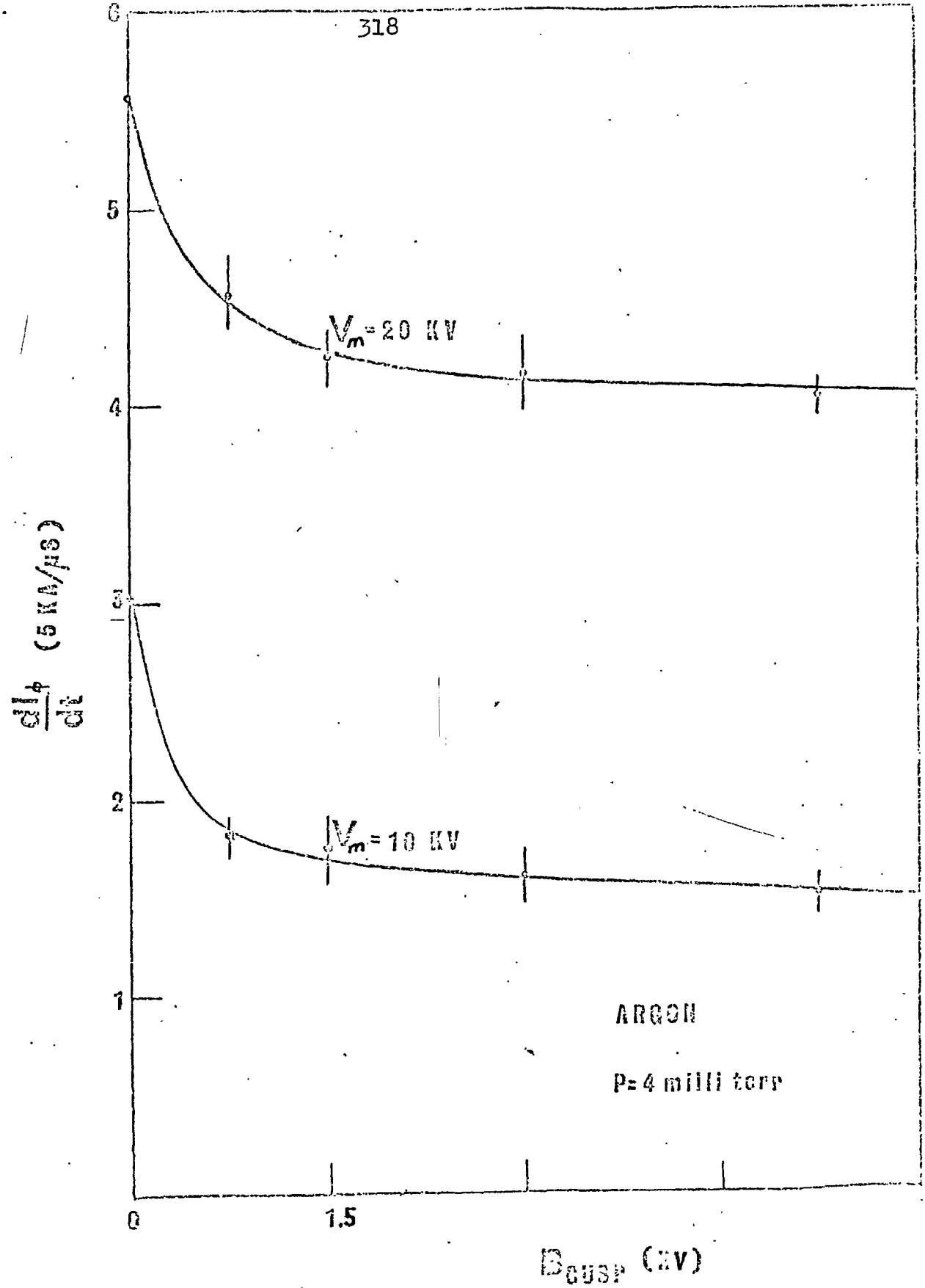

FIG. 10.7b $\frac{dI_\phi}{dt}$ AGAINST V_c

dependence on V_m. At high pressures the Hall inductance, associated with the energy of directed motion of the ions, falls, and so $\frac{dI_\phi}{dt}$ is limited by the geometrical inductance alone. At low V_c the electron current increases, and so $\frac{dI_\phi}{dt}$ increases.

Experiments were also done in hydrogen. The current is similar to argon, except that the time scale is shorter. A current waveform in hydrogen is shown in fig. 10.8. A similar dependence of $\frac{dI_\phi}{dt}$ on V_m, V_c and p as for as argon is observed. However, as the lower limit on breakdown in hydrogen is 6mtorr, and the Hall inductance of hydrogen is low, no dependence of $\frac{dI_\phi}{dt}$ on p was observed. The linearity between $\frac{dI_\phi}{dt}$ and V_m is also seen to be poor at large V_m. This is probably because the loss time is not sufficiently large compared with the time resolution. The time resolution is the time for the main bank voltage to appear around the torus. This can be seen in fig. 10.6. where V_m = 10kV, the current reverses first, because the trigger voltage appears around the torus before the main bank voltage.

The loss time increases with the pressure or number density. At low pressure it is constant as the Hall inductance dominates the geometric inductance, or equivalently the electric field is constant. In fig. 10.9, it is plotted as a function of initial n. The dependence of the loss time

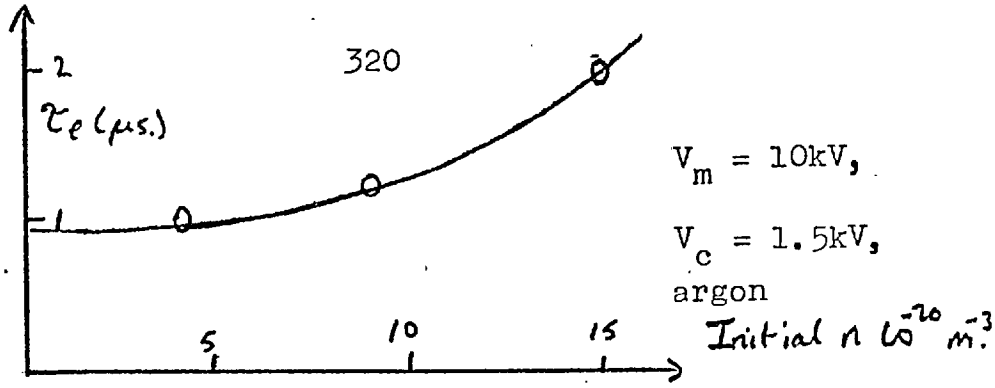

FIG. 10.9: VARIATION OF LOSS TIME WITH n

τ_ℓ on the bank parameters at low pressures is

$$\tau_\ell = \left(\frac{10kV}{V_m}\right)^{\frac{1}{2}} \left(\frac{1.5kV}{V_c}\right)^{\frac{1}{3}} \mu s \qquad (10.2)$$

accurate to about 20%. In hydrogen

$$\tau_\ell = .3 \left(\frac{10kV}{V_m}\right)^{\frac{1}{2}} \left(\frac{1.5kV}{V_c}\right)^{\frac{1}{3}} \mu s \qquad (10.3)$$

although this value is larger than the low pressure limit because of the inherently low value of the Hall inductance in hydrogen.

Although at high V_c $\frac{dI_\phi}{dt}$ $(t = 0)$ is independent of V_c, the current after the loss time is not. The effect of a large cusp field is to decrease this current. This is an effect of the ion Larmor radius. In hydrogen, at large values of V_c, the current is suppressed so much that it is only non zero in the linear rise up to the loss time and shortly afterwards.

10.3. The toroidal electric field

A loop of wire was threaded between the cusp coils and the vacuum vessel, vertically below the minor axis. Thus there are 3 coupled circuits. Suppose i_b is the total current

in the induction rods, i_p is the plasma curent, and i_m the current in the measuring loop. The mutual inductances are:- M_a rod—plasma, M_b plasma—measuring loop, M_c rod—measuring loop. The plasma and measuring loop circuit equations are

$$M_a \frac{di_b}{dt} + (L_p + L_H)\frac{di_p}{dt} + R i_p = 0$$

$$M_c \frac{di_b}{dt} + M_b \frac{di_p}{dt} + R_m i_m = 0$$

where R is the effective plasma resistance, and L_H the Hall inductance of the plasma. As i_m is kept small by making R_m large, the inductive terms due to i_m is neglected above. The loop is near to the plasma and so $M_a = M_c$, $L_p = M_b$, in which case the voltage around the loop V, which is measured across the resistance R_m in the loop circuit, is

$$V = i_m R_m = + L_H \frac{di_p}{dt} + R i_p$$

the driving voltage for the non magnetic impedance of the plasma.

V is many kV. To measure it a 1.5kΩ, high voltage potentiometer was used. It was connected by short leads to the voltage loop, the potentionmeter output being fed by a 50Ω terminated cable to an oscilloscope. The resistance of the potentionmeter restricted the loop current to a few amps, much less than the current in the rods. Nevertheless the loop made the preioniser ineffective for $p < 10$ mtorr. Presumably breakdown at low pressure depends on a high frequency field, which is damped out by the loop. For low pressure measurement

a small loop near the major axis was used, the large loop calibrating it.

A characteristic output is shown in fig. 10.10. The initial voltage, when $V_c = 0$, should be zero, the measured voltage was small but not zero for $V_c = 0$, because of imperfect coupling. This voltage, scaled by the ratios of $\frac{di_p}{dt}$ is subtracted from the values of voltage when $V_c \neq 0$, to correct for this error. The ratio $\frac{dI_\phi}{dt} / V$ is plotted in fig. 10.11 against pressure. The value of V used is that of the shoulder near to t = 0. The ordinate is the inverse Hall inductance, $\frac{1}{L_H} = \frac{e^2 Z^2 n A}{m_i \ell}$. The measured Hall inductance is <u>not</u> a function of the cusp voltage for $V_c > 1.5$kV. The importance of this is that $\frac{dI_\phi}{dt}$ vs. V_c is a simply interpreted graph, because V is independent of V_c, whereas $\frac{dI_\phi}{dt}$ vs. p is not, because V depends on p, as shown in fig. 10.12.

The field seen by the plasma peaks at the loss time. This is illustrated in fig. 10.10. This peak value of the resistance of the plasma is .7Ω at 15 mtorr, decreasing as the pressure increases. This resistance is not due to electron-ion collisions, (a temperature of .5eV would be necessary) but is due to the rate of change of the Hall inductance (section 11.4), accounting for the lower resistance at higher pressure, because the Hall inductance is lower (fig. 10.11).

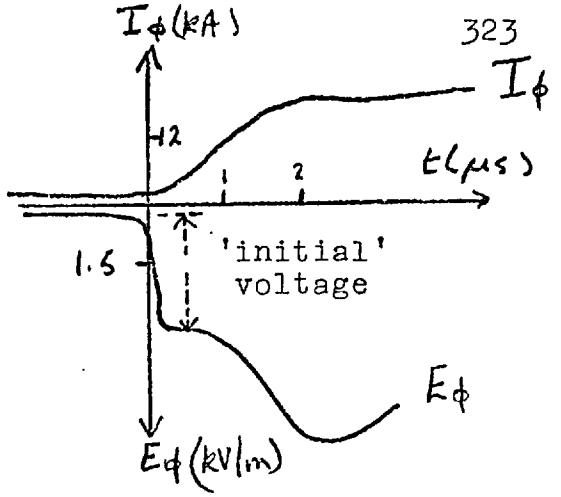

FIG. 10.10. I_ϕ and E_ϕ

V_m = 10kV

V_c = 1.5kV

p = 25 mtorr, argon

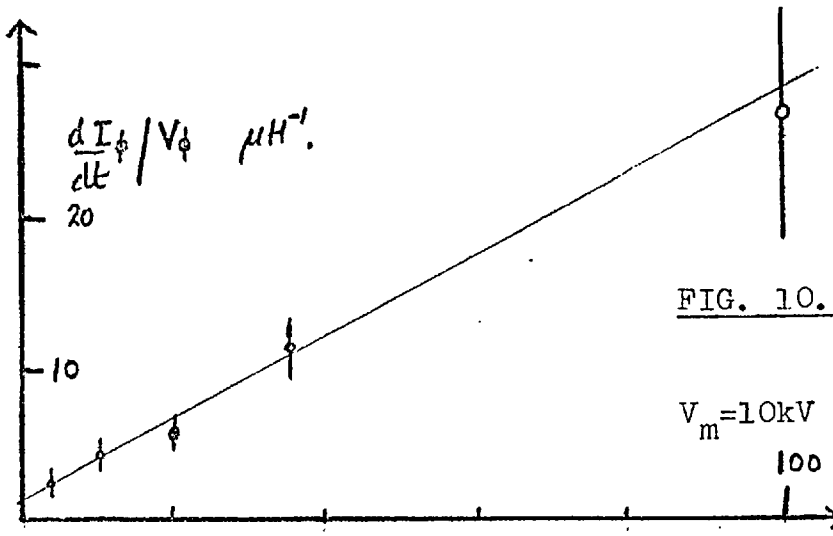

FIG. 10.11 THE INVERSE HALL INDUCTANCE

V_m=10kV , V_c=1.5kV argon

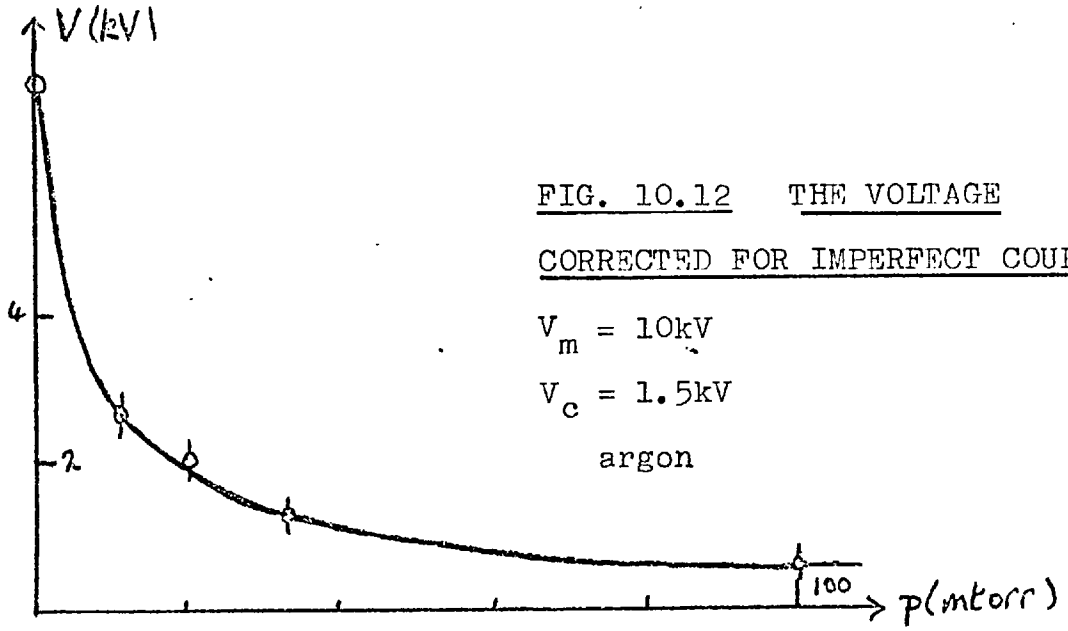

FIG. 10.12 THE VOLTAGE CORRECTED FOR IMPERFECT COUPLING

V_m = 10kV

V_c = 1.5kV

argon

10.4. The ionisation of an argon plasma

The time history of spectroscopic lines, identified as belonging to different stages of ionisation of the argon plasma, was recorded. Only medium quartz optics were available, which limited the study to A IV and lower. The entrance slit of the spectrometer was imaged into the centre of the plasma, along a horigontal line, thus light emitted from a radial line of sight was collected.

Fig. 10.13 is a tracing of the intensities of A II , A III , and A IV , lines, together with the current. The absence of overlap of lines indicates that the highly emitting regions are reasonably uniform in degree of ionisation.

The intensity of a spectroscopic line from a ion of charge Z = 1 can be dependent on the number density of either stage Z or Z - 1, of ionisation, depending on whether the upper state of the line is in l.t.e. with the continuum or not.

In the case of l.t.e. of the level then the number density of the level with quantum number n of stage z - 1, is given by the Saha equation

$$N_1^z \propto \frac{N_n^{z-1} W^{1/2}}{n_e} \exp(-E_n^{z-1}/W) \qquad (10.4)$$

where E_n^z is the binding energy of level n.

In the case where the level is not in l.t.e. then

$$I_n^{z-1} \propto N_n^{z-1} \qquad (10.5)$$

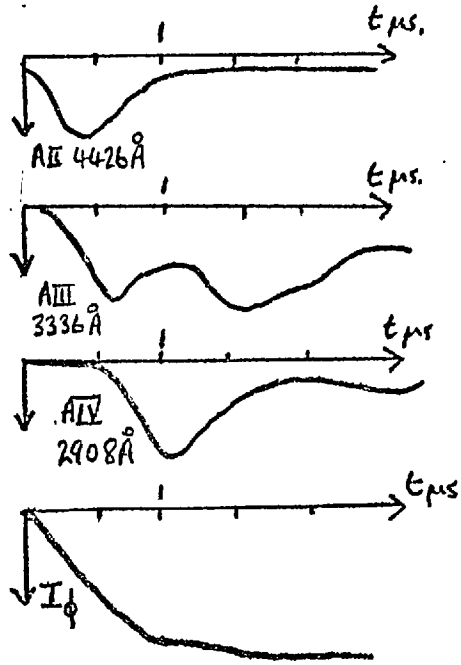

FIG. 10.13 $V_m = 10kV$, $V_c = 1.5kV$ 3.5 mtorr argon

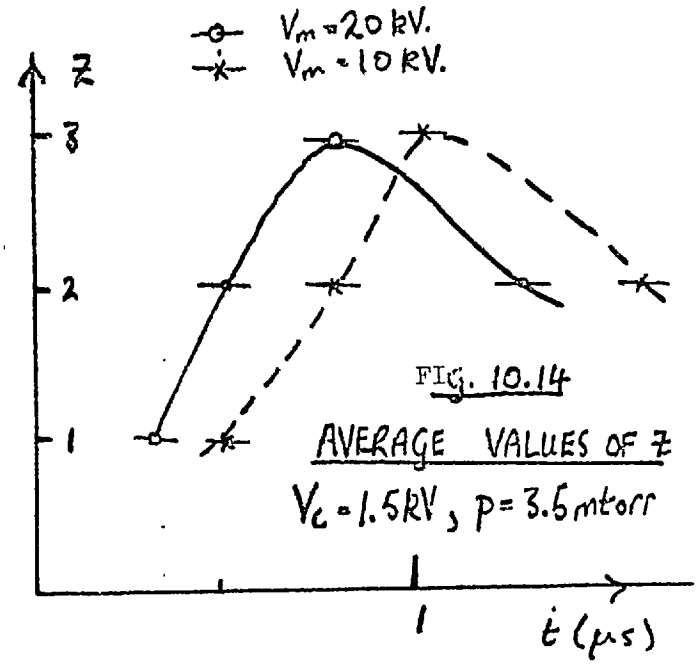

FIG. 10.14

AVERAGE VALUES OF Z

$V_c = 1.5kV$, $p = 3.5$ mtorr

FIG. 10.15 THE ION NUMBER DENSITY

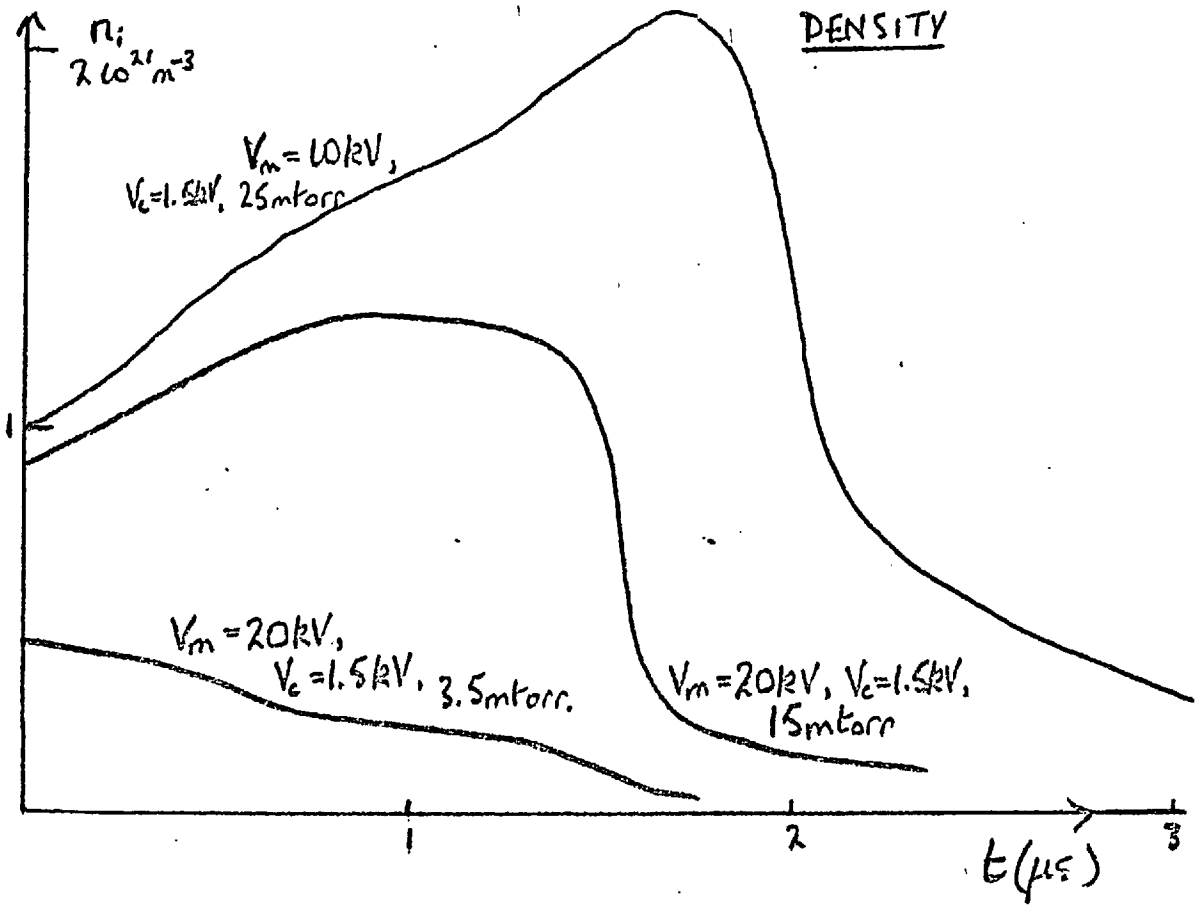

In chapter 3 it was shown that the upper states of AII are just in l.t.e. for p = 25 mtorr. At higher temperature and Z, l.t.e. is harder to satisfy (Griem, 1963, eq. 6.82), and so eq. 10.5 has been used to interpret the results here.

Thus from fig. 10.13, burn through from AII to AIV occurs. The subsequent reappearance of AIII indicates that AV is not formed, and that a cooling occurs after the peak of AIV. Cooling at this time, coincides with the shoulder of the current waveform, a sharp fall of the number density, directed velocity, and reaction force on the coil. The peak of AIV could be caused by the cooling with the density of AIV being smaller than AIII. Nevertheless Z could be larger than 2 as there is a peak of AIII . These oscillographs (fig. 10.13) have been used to evaluate values of Z (fig. 10.14) which in turn are used to evaluate the ion number density from the electron density curves in chapter 9. These are shown in fig. 10.15. The times for the peak intensity to appear decrease with increasing V_m, (shown in fig. 10.16) with increasing V_c, and with increasing pressure (fig. 10.17). For filling pressures below 3 mtorr, no AIV line is seen, and a smaller AIII emission.

Spatial scans of the lines

The spectrometer was scanned in a horizontal, and vertical direction to obtain spatial information about the hot regions of plasma. Some of the results are shown in fig.

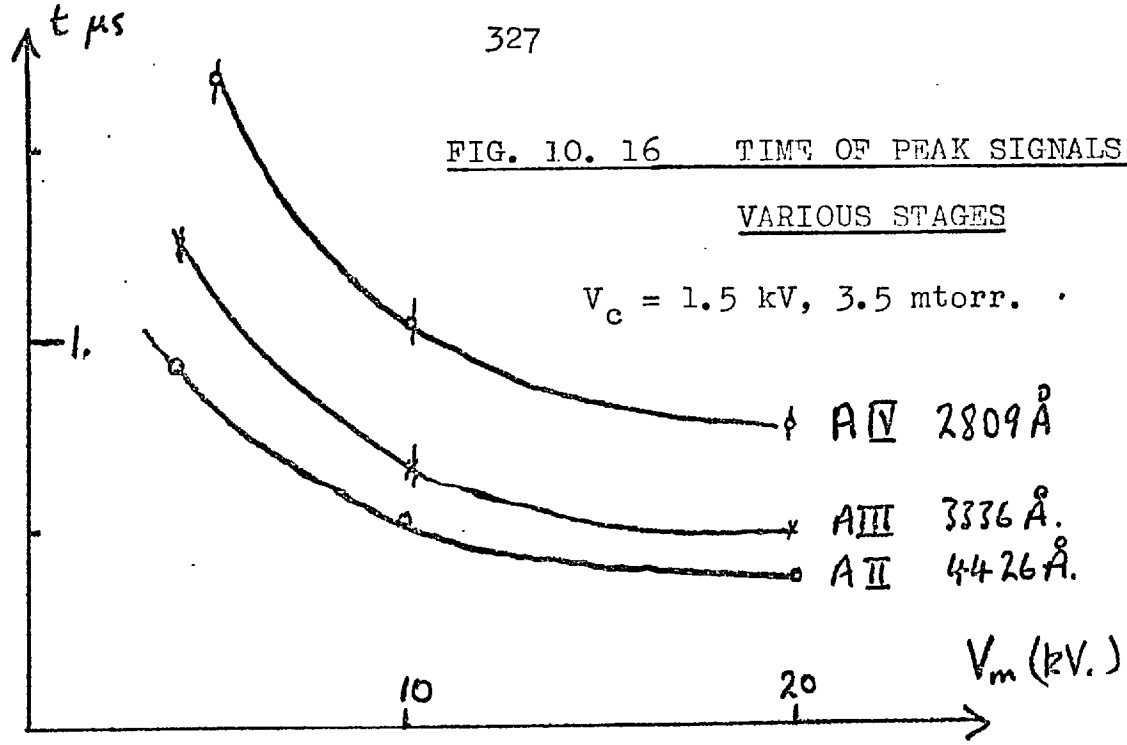

FIG. 10. 16 TIME OF PEAK SIGNALS FROM VARIOUS STAGES

V_c = 1.5 kV, 3.5 mtorr.

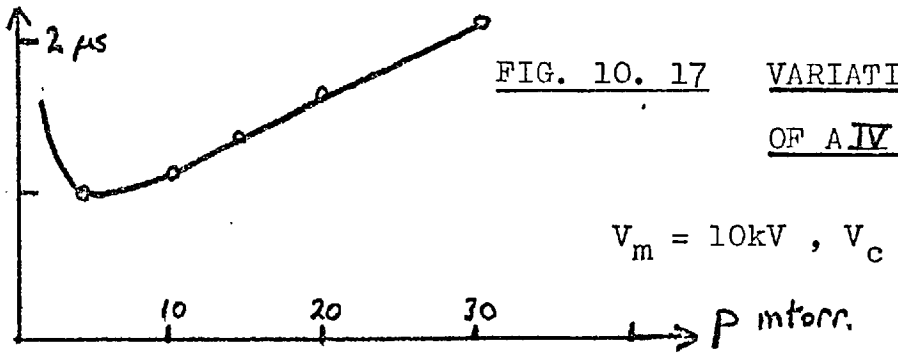

FIG. 10. 17 VARIATION OF THE PEAK OF A IV WITH PRESSURE

V_m = 10kV , V_c = 1.5kV

10.18. A vertical scan, through the observation port for laser scattering is shown for A III and A IV . Absorption by the tube wall was thus avoided. The profile of A III could be caused by vignetting by the port, but comparison of A IV with A III shows that the A IV profile is only 19mm wide. These profiles are at the time of peak intensity, which does not vary with the radius. The width of the hot plasma corroborates the scattering results, the current density and the photography.

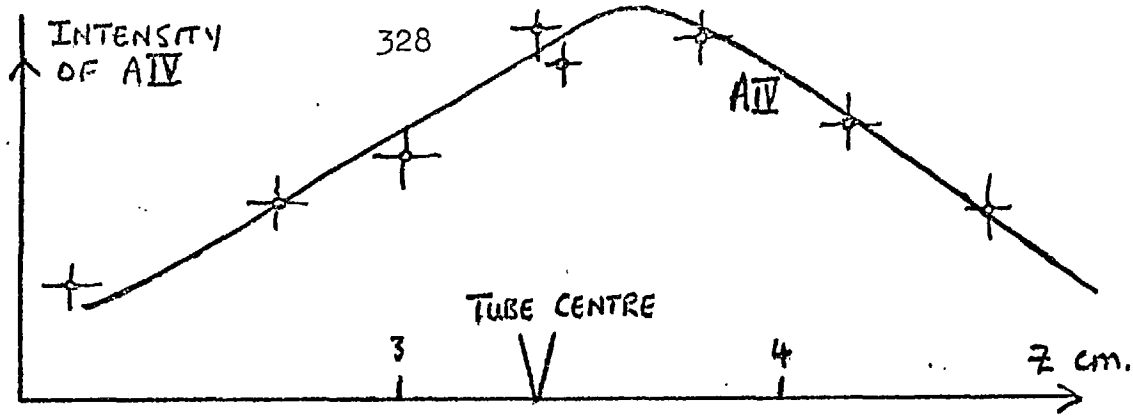

A VERTICAL SCAN OF PEAK INTENSITY

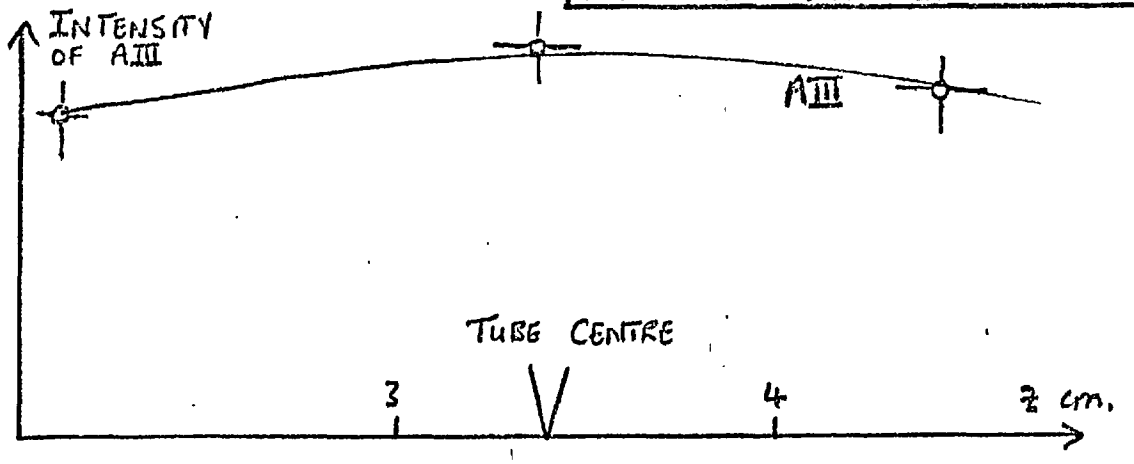

FIG. 10.18 SPATIAL VARIATION OF IONISATION

$V_m = 20kV$, $V_c = 1.5kV$, 3.5 mtorr

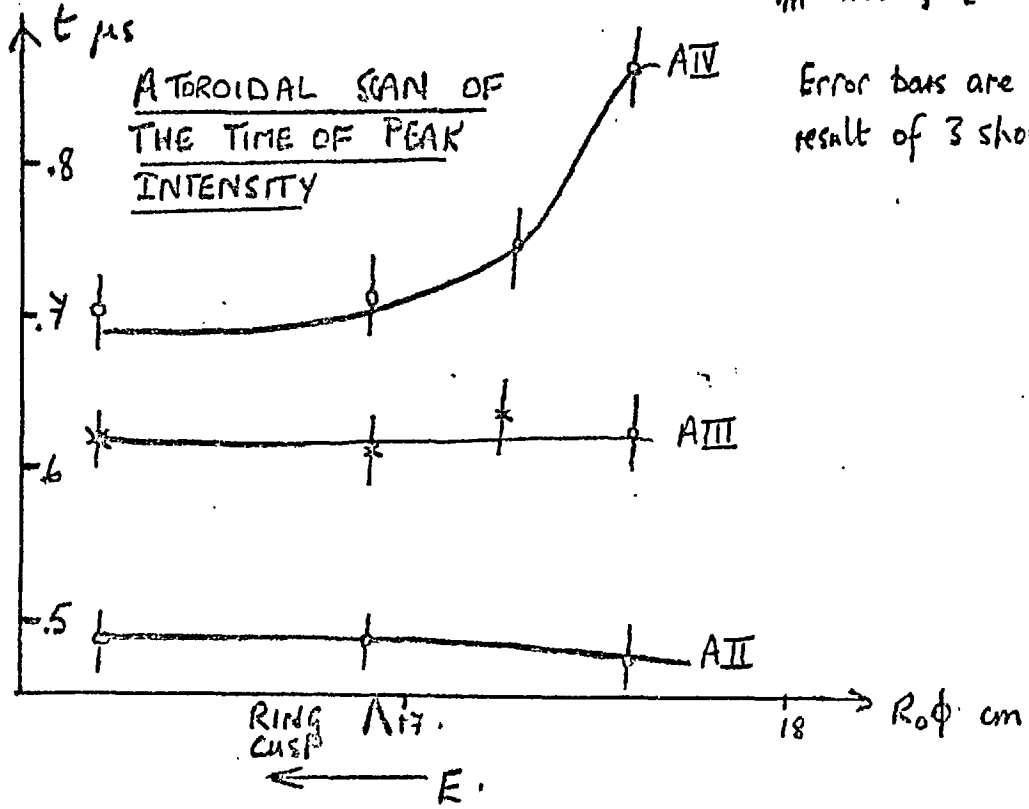

Error bars are the result of 3 shots.

Note that there is a vertical shift of the plasma, relative to the minor axis, which is in the same direction as $\overline{v_\phi B_r}$.

A vertical scan of the peak line intensity in the region next to a cusp coil shows a width similar to that in the ring cusp region, i.e. a full half width of the 20mm. The profile has however, a sharper fall off than evidenced in fig. 10.18. The vertical shift is 6 ± 2mm, in the 'correct' direction.

A horizontal scan of the time of peak line intensity through the scattering observation port is also shown. This is a horizontal scan about the region of the ring cusp. This graph indicates that it is delayed cooling rather than slower heating, which causes the AIV upstream of the ring cusp to peak later than the region downstream. Otherwise there would be a difference in the time of peak AIII and AII . A similar phenomenon is seen by the photography, which shows that debris is swept downstream.

10.5. The magnetic field of the Hall currents

The magnetic fields produced by the plasma currents were measured by internal magnetic probes. The probes made by Parkinson were available. These were loosely based on the design of Ashby (1963), but had a small turns area, .15cm^2, and a high frequency response(> 25MHz, measured). As is well known the desirable qualities of a magnetic probe, (1)large turns

area, (2) high frequency response, and (3) small physical size, are usually mutually exclusive. Initially a large turns area was needed because of lack of expertise in noise suppression. To satisfy conditions(1) to (3), a hollow, single turn coil, of 7mm radius, was constructed. The loop of wire was sheathed from the plasma by a looped capillary tube of quartz. The frequency response of the coil was higher than 20MHz.This coil was used to measure the field produced by the Hall current, in the toroidal direction, at the minor axis, under the ring cusp.

Fig. 10.19 shows some typical oscillograms . The correct signal polarity and dependence on the field polarities was observed. The field rises up to the loss time. This far it is reproducible, but not afterwards. There are non reproducible oscillations at a frequency of typically 1MHz. For large values of the cusp field the signal <u>after</u> the first peak, is suppressed (fig. 10.19) . The step in the first 100ns at V_m = 20kV is reproducible, and indicates that the inherent rise time of the signal, i.e. an L/R time, is faster than the loss time.

As can be seen, the field at the first peak is proportional to V_m (fig. 10.20). Also at zero cusp field there is no <u>Hall</u> signal.A signal is observed but does not rise as fast as the Hall signal, and is not reproducible. The Hall

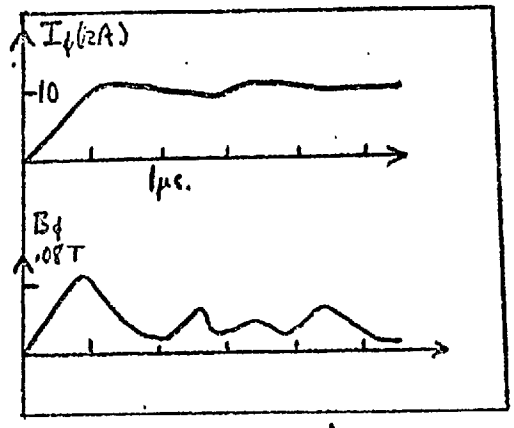

V_m=10kV, V_c=1.5kV, 3.5mtorr

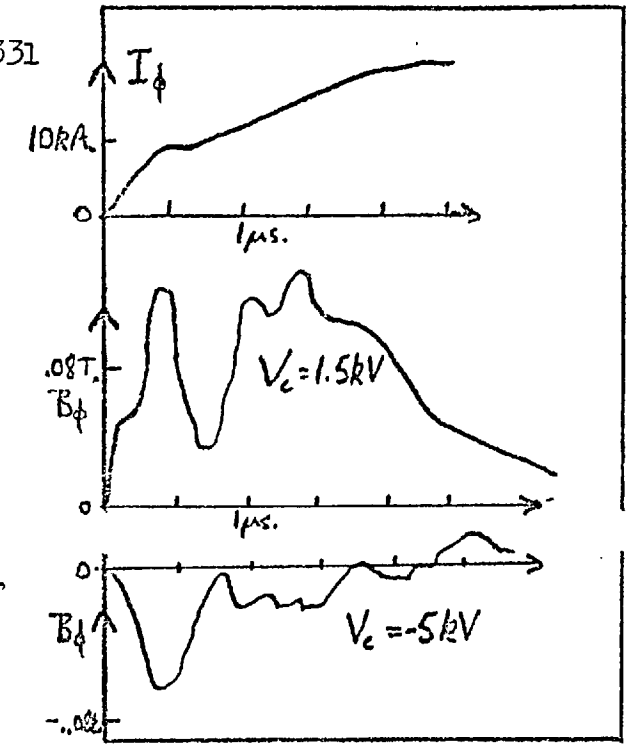

V_m=20kV, 3.5mtorr

FIG. 10.19 B_ϕ, ON AXIS, $\phi = 5°$

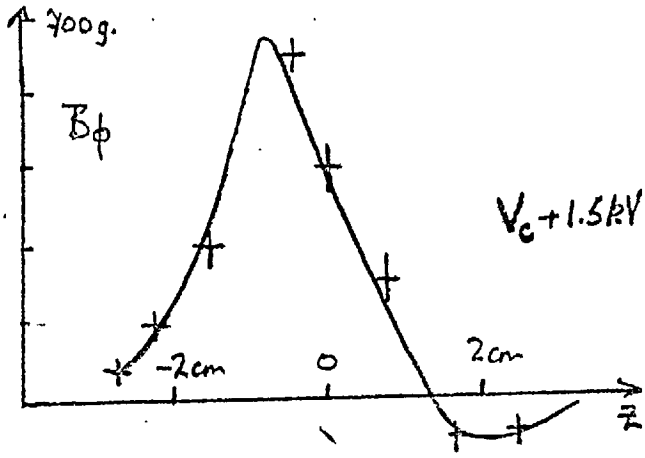

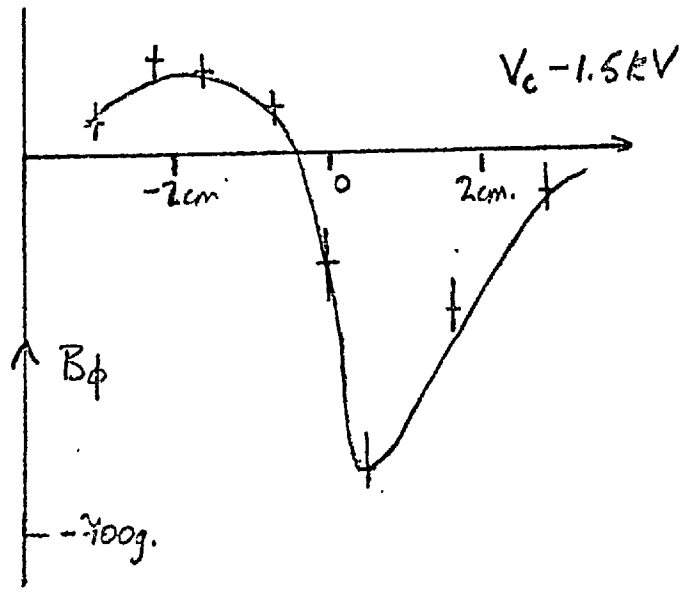

FIG. 10. 21 VERTICAL SCANS OF THE FIELD OF THE HALL CURRENT

V_m = 20kV, 3.5 mtorr, 1μs.

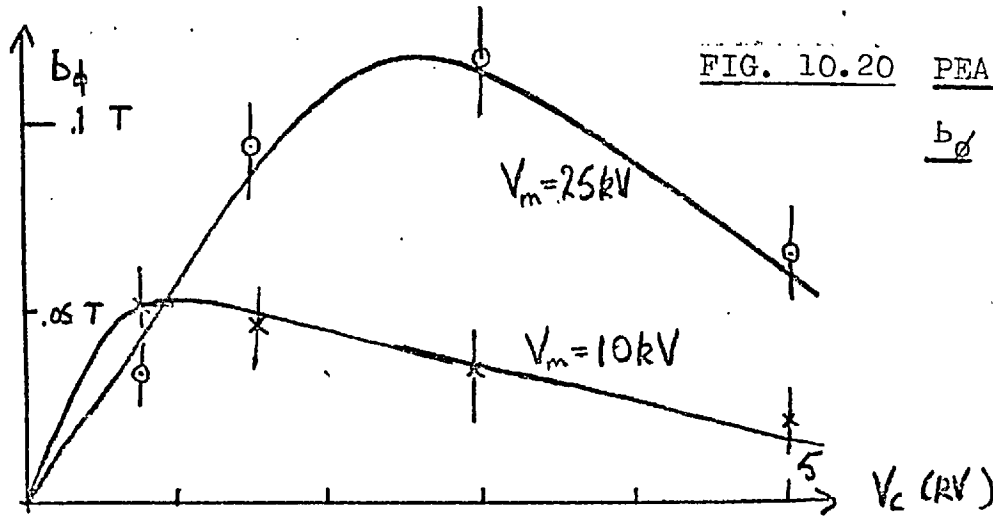

FIG. 10.20 PEAK VALUES OF b_ϕ 3.5 mtorr.

signal increases with V_c, until an average $\omega\tau_c > 1$, after which B_ϕ decreases approximately as V_c^{-1}. The observed peak field is

$$b_\phi = 500 \left(\frac{V_m}{10kV}\right) \text{ gauss} \qquad (10.6)$$

at 3.5 mtorr. In the pressure range 2 to 10 mtorr, there was only a 20% increase in b_ϕ, with pressure.

The profile of the Hall current field was measured by a conventional internal probe. The turns area was 6.25cm^2, and the rise time into 100-Ω was .7μs. The probe was scanned vertically, under the ring cusp, along a vertical line through the minor axis. The axis of the probe was aligned by turning through 90° from the orientation giving a null signal in a toroidal field. The careful alignment and comparable sizes of b_θ and b_ϕ, eliminates the possibility of pick up of b_θ on a supposedly b_ϕ signal. The profiles at 1μs for both cusp polarities are shown in fig. 10.21. It should be emphasised that this is only the field of the plasma Hall currents. A similar shape is seen at .5μs. A vertical shift between the two cusp polarities is evident. The direction of the shift is the same

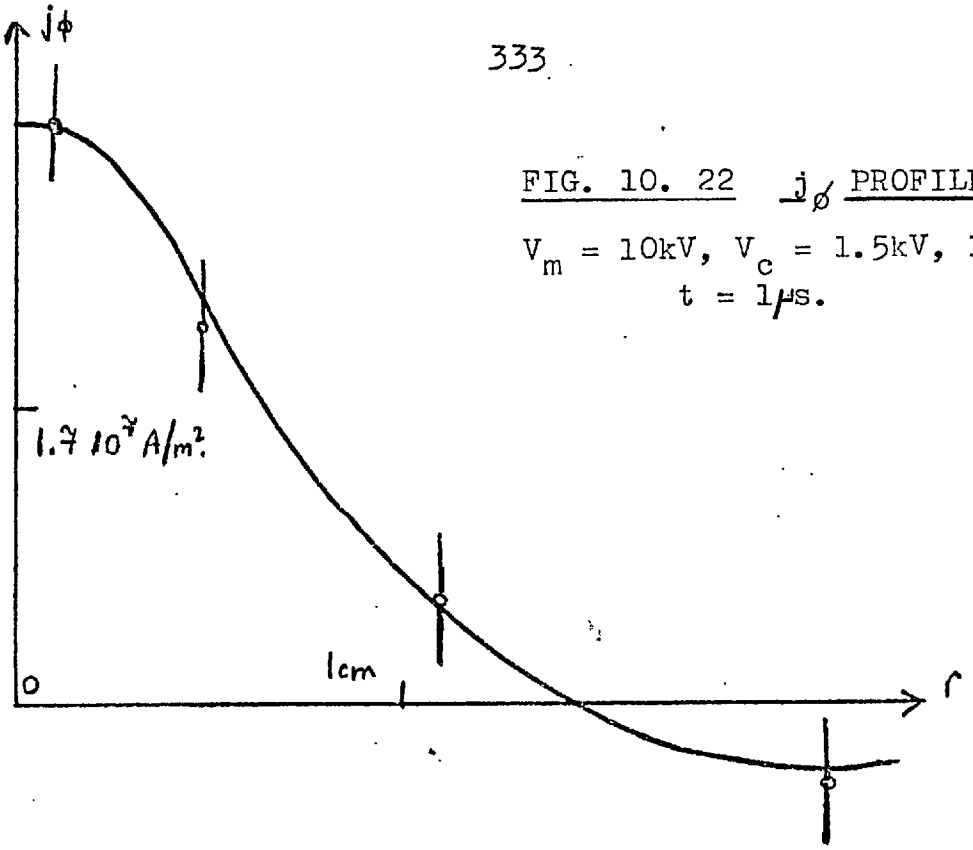

FIG. 10. 22 j_ϕ PROFILE VERTICALLY

V_m = 10kV, V_c = 1.5kV, 15 mtorr argon
t = 1μs.

as observed photographically i.e. $j_\phi \overline{B}_r$.

10.6 The poloidal magnetic field

The toroidal geometry makes the calculation of j_ϕ from measurements of b_θ difficult. Properly a full spatial plot of b_θ and b_r is necessary. However an analytic approximation is probably no worse than the experimental approximation that the probe does not perturb the plasma. Suppose that for a fixed value of ϕ

$$b_\theta (r,\theta) = b_\theta^0 (r) + b_\theta^1 (r, \cos\theta)$$

where θ is the poloidal coordinate.

$$\therefore \quad \mu_0 \int_0^r j_\phi 2\pi r\, dr = 2\pi r\, b_\theta^0(r) \qquad \text{(Ampere's Law)}$$

$$\therefore \quad \mu_0 j_\phi^0 = \frac{b_\theta^0(r)}{r} + \frac{\partial b_\theta^0(r)}{\partial r} \qquad (10.7)$$

b_θ was measured along a vertical line through the minor axis. The point where r = 0 was chosen so that $b_\theta(r,\pi/2) = b_\theta(r,3\pi/2)$. An average of the values of b_θ, with both cusp polarities, either side of r = 0, was used to evaluate j_ϕ from eq. 10.7. and is shown in fig. 10.22. The negative j_ϕ shown is not definite because of the large errors. The integral $I_\phi = \int_0^{3.5cm} j_\phi \, 2\pi r \, dr$, of fig. 10.22. is 7. kA, compared with 6.0kA from the Rogowski coil.

Later in the course of the project a profile of b_θ was measured with a fast, low sensitivity coil. The probe was inserted horizontally, so measuring $b_\theta^o + b_\theta^1$. The lack of poloidal symmetry is evident in the plots, and so no attempt was made to numerically evaluate j_ϕ, but qualitative features can be seen. A port was available to do a scan both in the region under the ring cusp, and 2mm away from the coil.

As a control experiment, a scan was made for identical conditions as the polytron, except that there was no cusp field, and so a toroidal z pinch formed. This scan, fig. 10.24. behaves as expected. A skin j_ϕ forms which slowly moves in, pinching the plasma to a point near the minor axis. The field is slightly larger inside because of toroidal effects.

Fig. 10.23 shows the profiles obtained for the polytron both under the coil and the ring cusp. No skin current is evident, at least for times greater than 100ns.

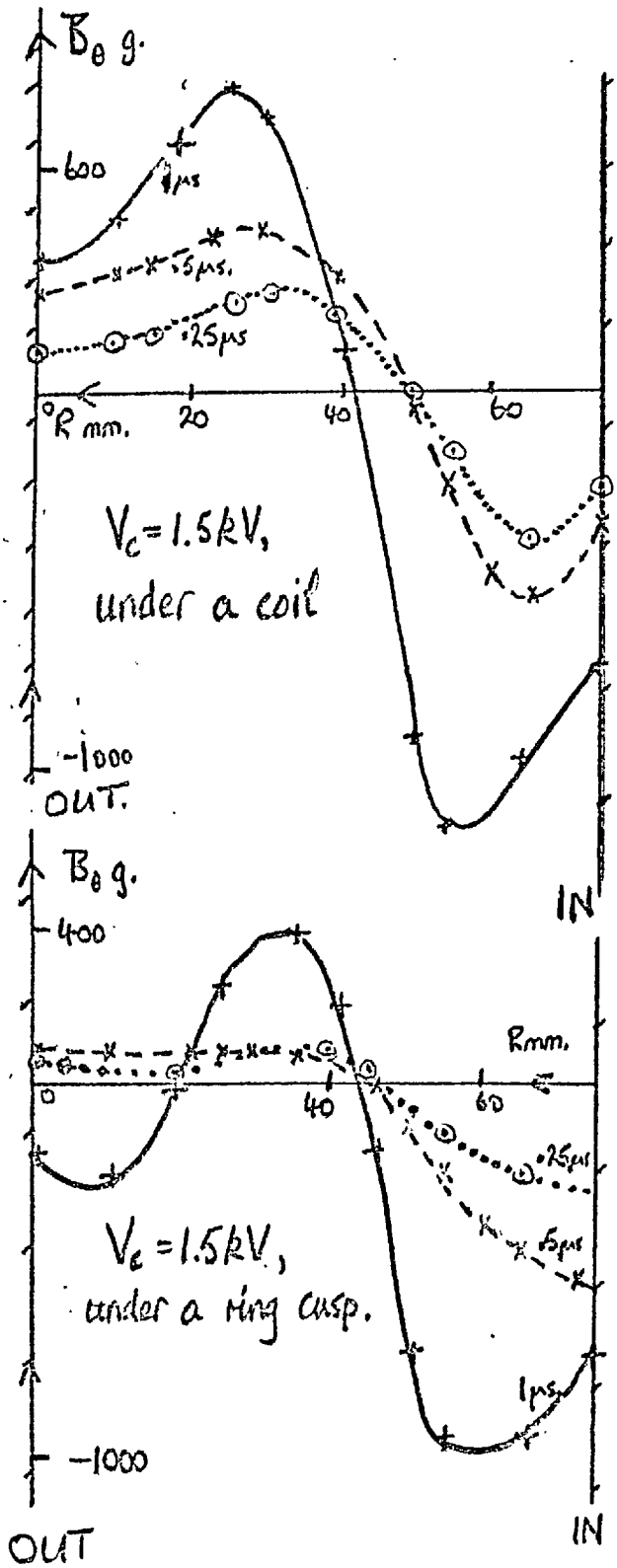

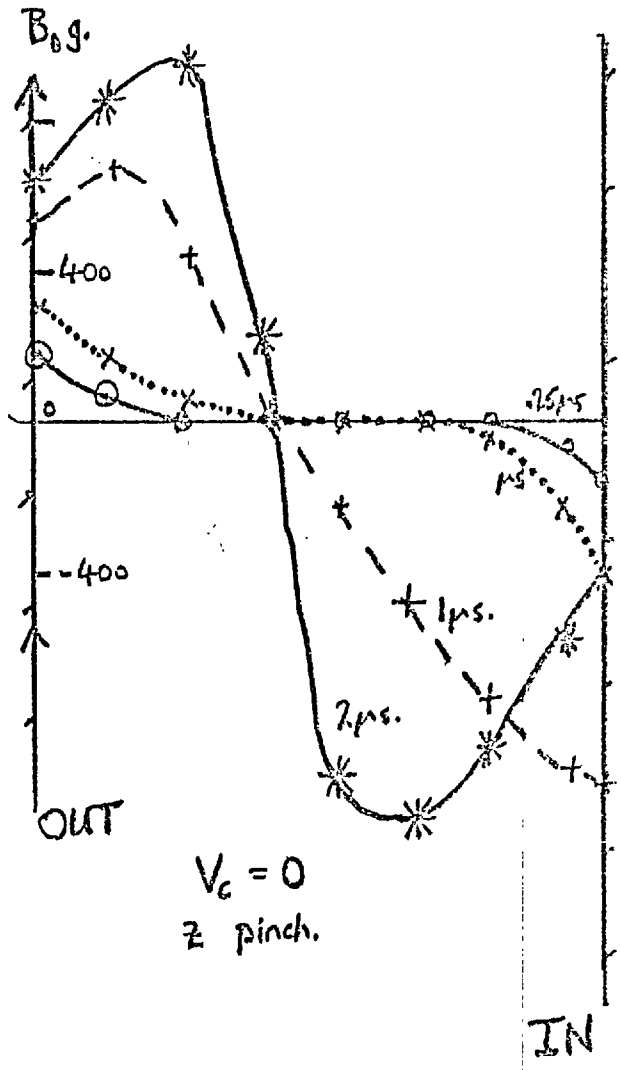

FIGS. 10.23 & 10.24.

RADIAL SCANS OF B_θ AT DIFFERENT TIMES

V_m = 20kV, 15 mtorr, argon.

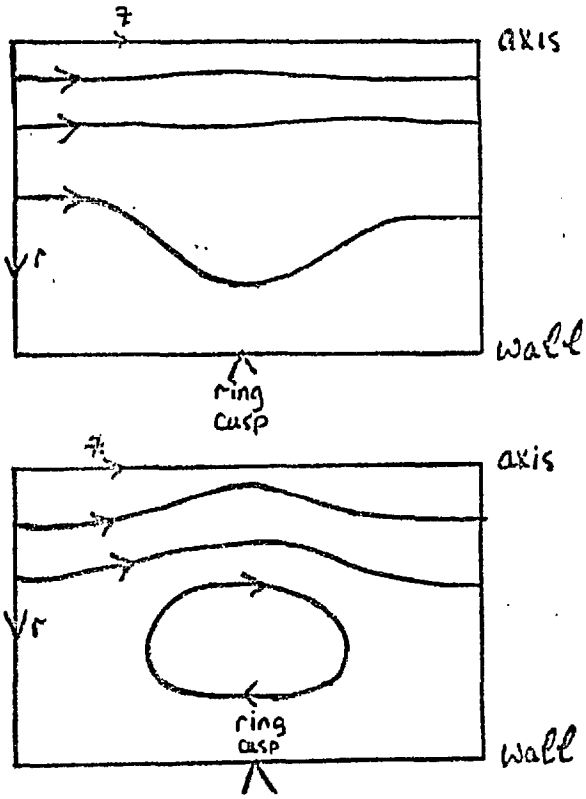

t = 250ns

t = 1μs.

FIG. 10.25 INFERRED CURRENT FLOW LINES

There is a region of positive current (parallel to E_ϕ) about the magnetic axis initially. (50mm on the abscissa). At early times under the ring cusp, on the outside (30mm) there is possibly a negative current accounting for the dip in b_θ. Further out, another 10 to 20 mm , there is a positive current as b_θ increases again.

Later, at the loss time, there is a negative current flow through the outer part of the ring cusp, in agreement with fig. 10.22. At this time the current flow under the coil is displaced outwards from the magnetic axis.

Under the cusp coil the profiles are similar to an ordinary pinch but again with no skin effect; there is current flow on the magnetic axis no later than 100ns. The current flow is restricted to a diamter of 3.2 cm outside of which b_θ falls off approximately a 1/r. A sketch of the inferred current flow lines is shown in fig. 10.25.

10.7 Measurement of the force on the plasma

By measuring the magnetic field outside of the plasma, the electromagnetic thrust on the plasma has been calculated. This measurement was originally made on a linear Hall accelerator by Etherington(1965). The electromagnetic force acting on material in a volume V bounded by a surface S is

$$\underline{F} = -\frac{\partial}{\partial t}\int_V \underline{D}\times\underline{B}\, dV + \oint_S (\underline{E}.\underline{D} + \underline{H}.\underline{B} - u\,\underline{\underline{I}}).\underline{n}\, dS$$

where $u = \frac{1}{2}(\underline{E}.\underline{D} + \underline{B}.\underline{H})$ and $\underline{\underline{I}} = \delta_{ij}$. Etherington and Haines evaluated the reaction force on the coil producing the radial magnetic field. In the case of the polytron the symmetry to toroidal displacements of a cusp separation, simplifies the integration, which need only be done along a path equivalent to Etherington's ab, as long as ab = cusp separation. A simpler way of analysing the situation is to directly evaluate the force on the plasma, which, because of symmetry, yields more simply minus the expression for the force on a coil, as

$$F_\phi = -r_1\int_0^{L\pi}\int_0^{L/R} H_\phi(r_1,\theta,\phi)\, B_r(r_1,\theta,\phi)\, R\, d\phi\, d\theta$$

where r_1 < radius of a cusp coil, and L is the cusp separation. The θ integration was reduced to the average of two points because of the large aspect ratio, thus

$$F_\phi = -\pi r_1\int_0^{L/R}\Big(H_\phi(r_1,\pi/2,\phi)\, B_r(r_1,\pi/2,\phi) + H_\phi(r_1,-\pi/2,\phi)\, B_r(r_1,-\pi/2,\phi)\Big) R\, d\phi \qquad (10.8)$$

The Rdø integration was done over a range .8L by a two coil probe vertically below the minor axis.

The integrand of eq. 10.8 consists mainly of the vacuum field which integrates to zero. The plasma field is at most 5% of the vacuum field. The measurement is easier in the small torus used by Parkinson. A measurement of the total field was not attempted, instead the vacuum and plasma fields $\underline{B}$ and $\underline{b}$ respectively, were measured separately.

$$\therefore \quad F_\phi = -\frac{2\pi r_1}{\mu_0} \int_0^{L/R} (B_\phi + b_\phi)(B_r + b_r)\, R\, d\phi$$

$$\doteq -\frac{2\pi r_1}{\mu_0} \int_0^{L/R} (B_\phi b_r + B_r b_\phi)\, R\, d\phi \qquad (10.9)$$

Here the analytic fact $\int_0^{L/R} B_\phi B_r \, R \, d\phi = 0$ has been used, and thus experimental errors which might be much larger than F_ϕ have been eliminated. Also $|b| << |B|$.

The plasma and vacuum fields were differentiated by their frequency spectrum using a passive high pass filter. The filter response was .5 at 2μs. Using the filter the shape of the plasma signal for a slowly varying high pressure case was identical to the signal without a filter.

Instead of taking measurements at $\theta = \pi/2$ and $-\pi/2$, but equivalent, shots were taken with both cusp polarities. This also eliminated any pick up of b_θ, as both b_r and b_ϕ change polarity with V_c.

b_r reaches its peak value under the coil where $B_r = 0$, and vice versa. The integral for the force had to be evaluated graphically. One such graph is shown in fig. 10.26. which shows that the terms in eq. 10.9 can be approximated by first Fourier components initially, i.e.

$$B_\phi b_r \propto \cos 36\phi \quad ; \quad B_r b_\phi \propto \sin 36\phi$$

It was very noticeable that the Hall field outside of the plasma rose very quickly. At 3.5 mtorr in 100ns, and at 25 mtorr in 200 ns. This is in contrast to the field near to the minor axis, which has a 1μs rise time, although a faster initial rise.

The main error in the experiment is the non reproducibility of the plasma fields. This is the cause of the error bars in fig. 10.27 which shows the force on the plasma. This force is in the correct direction i.e. parallel to E_ϕ.

The variation of the force with V_c is shown in fig. 10.28. This was taken from the first Fourier component, using the known shape, at early times. At later times this is not a good approximation. Only b_r under the coil and b_ϕ at the ring cusp were measured. The switch on nature of the polytron, as the cusp field increases, also seen in $\frac{dI_t}{dt}$ vs. V_c is evident.

A linear variation of F_ϕ with V_m up to 20 kV, was also seen from this measurement.

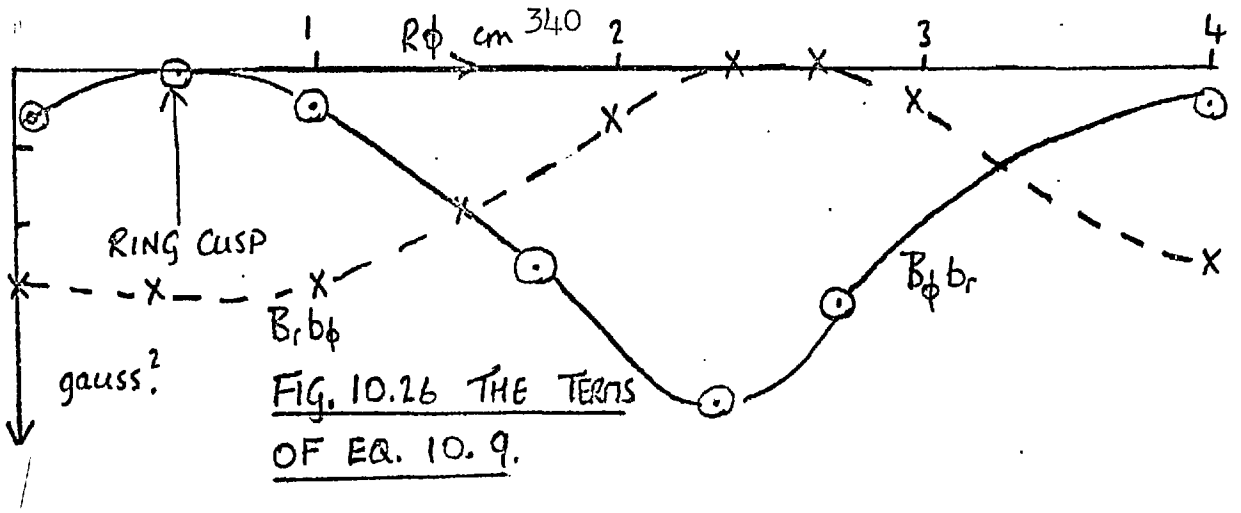

FIG. 10.26 THE TERMS OF EQ. 10.9.

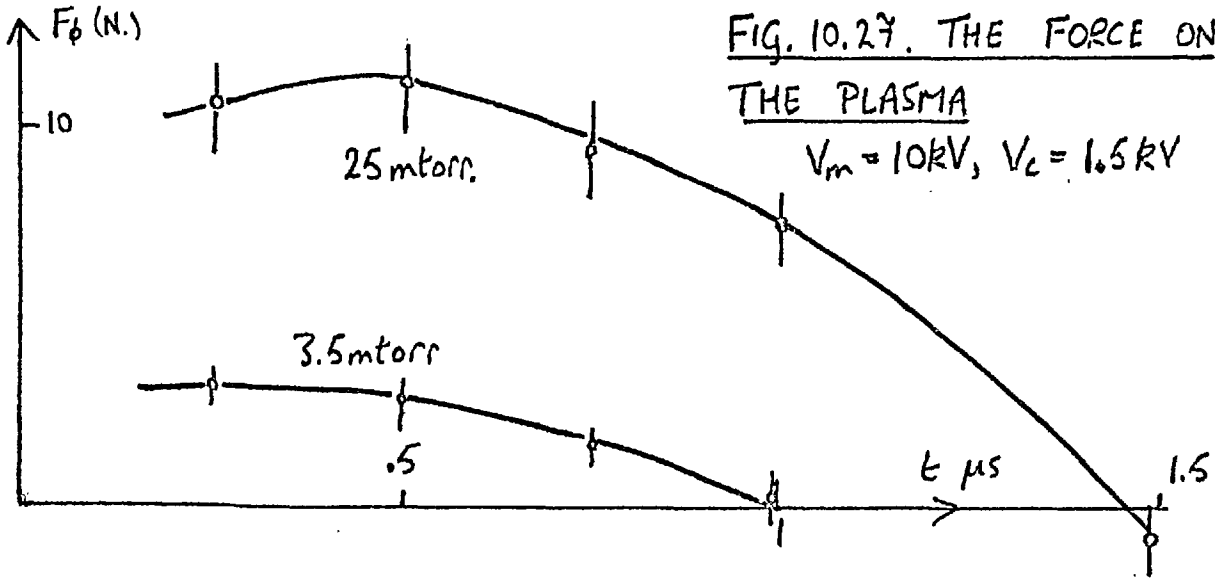

FIG. 10.27. THE FORCE ON THE PLASMA
V_m = 10kV, V_c = 1.5 kV

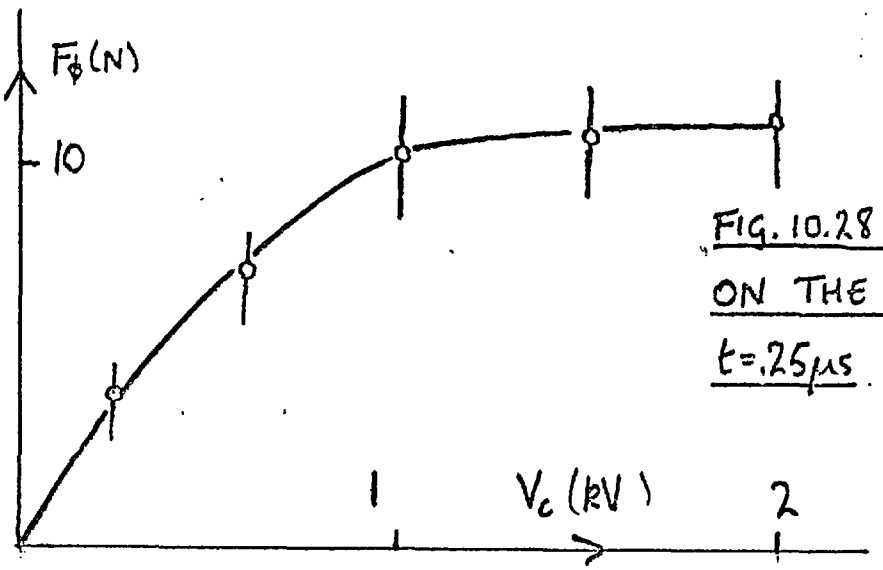

FIG. 10.28 THE FORCE ON THE PLASMA AT t=.25μs. V_m = 10kV, 25mtorr.

10.8 Measurement of plasma loss with an ion probe

The outward flux of particles was measured by an ion probe, described in chapter 3. The inner electrode was biased negative to repel electrons ($V_b = -50v$) and so the current is

$$I = nv_r Ze\ A$$

where A is the area of the hole and v_r >> the thermal velocity. The current was measured by the voltage across a resistance. Successful operation was achieved after conditioning shots with the bias reversed.

The interpretation of the results was hindered by a signal seen when $V_b = 0$. This was thought to be due to the high plasma potential (+ 200v). Moreover there is a high frequency oscillation to the plasma potential which causes a noisy signal. Frequencies higher than 2 MHz were eliminated by measuring the voltage across 47Ω and 10,000 pF in parallel. I, the true signal from the probe was taken as the difference between the signal with and without a bias voltage.

$A = (1.65)^2\ 10^{-8}\ m^2$ $\quad\therefore\quad n\ v_r = \frac{1.26}{Z}\ 10^{25}\ m^{-2}\ s^{-1}$

for a current of .2A, 1cm. on fig. 10.29.

The time history of the loss agrees well with the rest of the diagnostics. The increasing loss as V_c is increased is probably more obvious here, than in the photography. From the photography the loss occurs through rings of width w = 2mm and w = 4mm for fig. 10.29. If loss

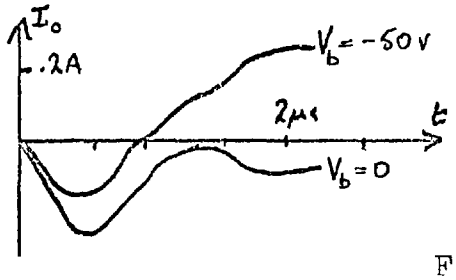

V_c = 1.5kV

FIG. 10.29 RADIAL LOSSES AT THE RING CUSP

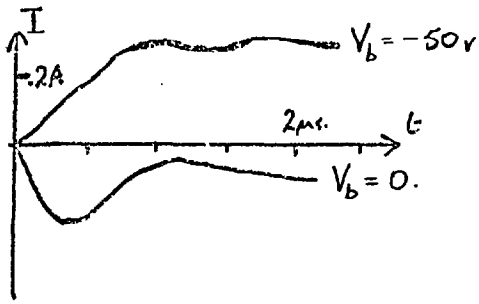

V_m = 20kV., p = 3.5mtorr

V_c = 3 kV

occurs only through this ring the decay equation for the total number N of particlesassociated with onc cusp is

$$\frac{1}{N}\frac{dN}{dt} = \frac{2\pi r\,\omega}{\pi r^2 L}\,\frac{n v_r}{n}$$

From fig. 10.29, n v_r = .5 10^{25} m^{-2} s^{-1}

and n = 10^{20} m^{-3} for V_m = 20kV, V_c=1.5kV, p=3.5mtorr

at t = 1 μs.

$$\therefore \quad \frac{1}{N}\frac{dN}{dt} = \frac{1}{3}\,10^{6}\ s^{-1}$$

This factor of 3 is remarkably good agreement for a probe . Systematic errors such as stagnation and poor alignment with the ring cusp could easily account for this difference.

The probe shows that an appreciable fraction of the plasma, 10's% is lost, quantifying the photography.

10.9 Measurement of the plasma velocity by Doppler shift

Parkinson first showed that there was a toroidal plasma velocity in the polytron. He made a shot by shot scan of the AIV 2809Å line, at the time of peak intensity at a particular wavelength setting. The line of sight was toroidal a shift being detected by changing the direction of E_ϕ. This process cannot give an accurate value of the Doppler shift, for the points on the profiles are not being plotted at the same time. The time of peak intensity will depend on both the line intensity and the time variation of the velocity. As the shift in the large tube had not been measured a shot by shot scan, measuring the profiles at a given time, was repeated.

A medium quartz f/13 spectrometer was used on the AIV 2809Å line. An ultraviolet line was used because of the high linear dispersion of the spectrometer at short wavelengths. Nevertheless the instrumental width, 1.3Å, is much larger than the shift, and so the shift is not easily detectable. Tangential viewing was by means of a mirror protruding from a port.

A shot by shot scan of the line was made, changing the main bank polarity each time. The profiles at 1μs show a shift, which is in the same direction as E_ϕ. To obtain more information about the magnitude of the shift, full use must be made of the line wings. A least squares fit of the data to a profile $F(\lambda) = 100b_3 \exp(-(\lambda-b_1)^2/b_2)$ was made. The resultant values were:-

$$V_m + : b_1 = 2.01\text{Å},\ b_2 = 1.14\text{Å},\ b_3 = 81.8$$
$$V_m - : b_1 = 2.19\text{Å},\ b_2 = 1.20\text{Å},\ b_3 = 94.2$$

Therefore the total shift of .18Å. corresponds to a plasma velocity of .95 10^4 m/s. with respect to the laboratory frame.

A single shot Doppler shift measurement

The major source of error in the Doppler shift measurement is the non reproducibility of the plasma. And as the velocity of the plasma is an important parameter a single shot technique was used. The simplest technique is that used by Berezin (1963). The line profile is simply split into two separate parts, each being monitored.

Consider a line profile p as a function of a reduced wavelength x, where $x = (d + \lambda - \lambda_0)/w$. Suppose the line is divided into two at $\lambda = \lambda_0$, the unperturbed centre when the shift d = 0, and these two signals are monitored. The intensities will be

$$I_1 = \int_{d/\omega}^{\infty} P(x)\,dx \quad \text{and} \quad I_2 = \int_{-\infty}^{d/\omega} P(x)\,dx$$

$$\therefore \quad I_1 + I_2 = \int_{-\infty}^{\infty} P(x)\,dx$$

$$\text{and } I_1 - I_2 = \int_{d/\omega}^{\infty} P(x)\,dx - \int_{-\infty}^{-d/\omega} P(x)\,dx - \int_{-d/\omega}^{d/\omega} P(x)\,dx$$

Hence if the profile is symmetric

$$R = \frac{I_1 - I_2}{I_1 + I_2} = \frac{-2\int_0^{d/\omega} P(x)\,dx}{\int_{-\infty}^{\infty} P(x)\,dx} = f(d/w)$$

So, properly, splitting the profile into two will measure the shift to width ratio of the line (Burgess, 1964). But if w is constant because the instrumental width dominates, R will be only a function of d. A criterion on the Doppler width so that w is mainly instrumental will be considered, but is not very restrictive. An elegant technique for splitting the line, so that R is not a function of w is described by Ahlborn (1966), but is unnecessary here.

The experimental technique

The highest linear dispersion readily available was 5Å/mm. from the Littrow mounted 2000 ℓ/mm grating, described in chapter 9. A spectrosil f/10 collimating lens was obtained, for u.v. work. The fine scanning block had to be replaced by a fixed mirror, so a set of reduction gears was connected to the grating drive, for fine scanning. The profile was split by the 30^{o} apex of a finely ground prism. The prism was aluminised for reflexion of u.v. Each side of the profile shone onto one of two 1P28 photomultipliers. The apex of the prism was in the plane of an exit slit to restrict the admissible wavelength range. The photomultipliers were housed in a screened box.

At the entrance slit a broad band filter, Wratten 18B for u.v., or a piece of glass for the visible, was used to reduce overspill and overlapping orders. It was necessary of course to

have the image of the entrance slit, focussed on, and parallel to the apex of the prism. In the u.v. this was facilitated by using a piece of phosphor to 'see' the image for a rough focus, and then improving it iteratively. As the collimating lens was very dispersive in the u.v. a Hg line at 2814Å, had to be used for focussing for the A IV 2809Å.

The plasma was viewed through the laser scattering port. A schematic of the optics is shown in fig. 10.30. Light was collected mainly from a region on the minor axis 3 cusps away from the port.

The outputs from the photomultipliers were taken to an A-B and an A+B differential preamplifier (Tektronix CA unit). The sensitivities of the two channels(which are wavelength dependent) were equalised by varying the preamplifer gain on channel B to obtain zero signal on A-B from a region of continuum adjacent to the line being studied.

To calibrate the change in $R = \frac{A-B}{A+B}$, as a function of wavelength the position of the line in the focal plane of the prism was varied, by the fine scan. This was done with the preioniser using the A IV 2809Å line, and with the Hg lamp using the 2814Å line, as a known narrow line. The calibration curve of R vs λ was linear for $.5 > R > -.5$ with the same slope for both lines, of 1.2 $Å^{-1}$. The criterion for maximum

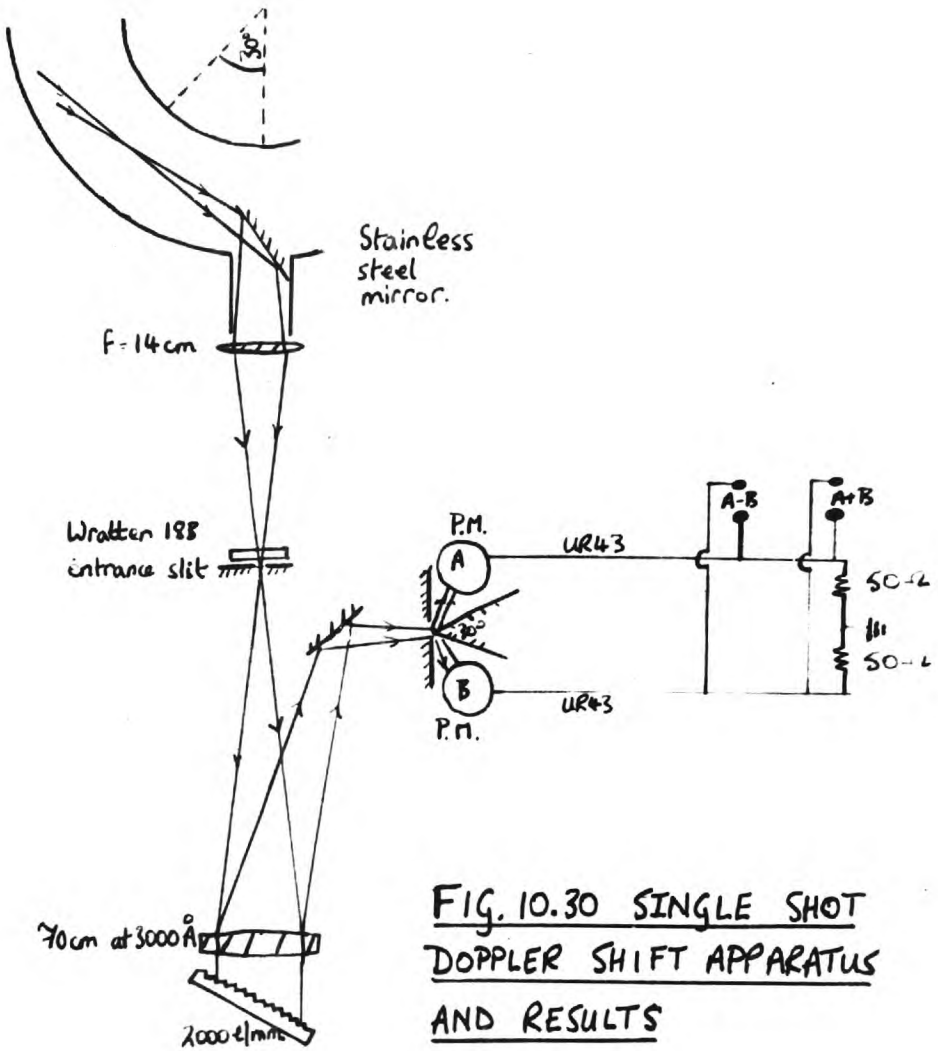

FIG. 10.30 SINGLE SHOT DOPPLER SHIFT APPARATUS AND RESULTS

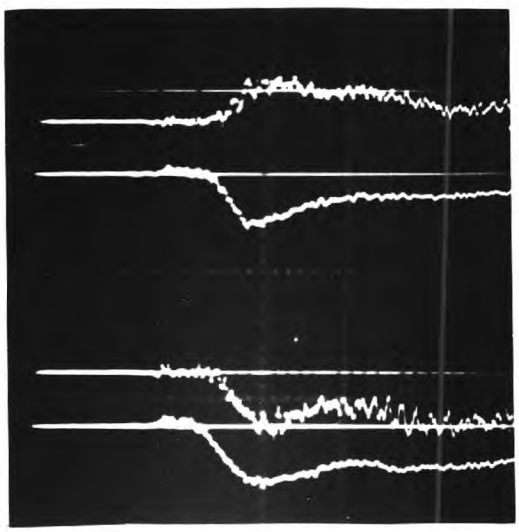

A III 3336Å
V_m = 20kV., V_c = 1.5kV., 2mtorr.
A-B 200mV/cm.
A+B 1 V./cm V_m+
500ns/cm.

V_m-
A-B 200mV/cm.
A+B 1 V./cm.

Doppler temperature can now be derived.

The instrument width was measured as .8Å. Supposing that this is a dispersive profile then using the Voigt profiles a full Doppler width of .4 x .8Å ≈ .3Å is necessary to change the instrument width by 10%. Therefore provided the ion temperature does not exceed 20^{0}eV , the line plus instrument width will not increase by more than 10%.

Shifts of the following lines were measured:- (a) A IV 2809Å line using the Hg 2814Å as reference, (b) the A III 3336Å using the Hg 3341Å as reference, (c) the A II 4806Å using A II 4806Å from a Geissler (and Cd 4799Å) as a reference.

There was a variation in A-B/A+B for a simple pinch. That this was not due to mass motion was seen by varying the polarity of V_m. It was probably due to impurity lines and/or poor common mode rejection. However, as R is linear with λ, a true measure of the Doppler shift for the polytron was obtained by the difference in R for positive and negative polarities of V_m. As a further check that this was due to a true toroidal motion, the ratio R + to R - (the sign referring to the polarity of V_m) did indeed reverse when the toroidal viewing was in the opposite direction.

An oscillograph of A-B and A+B for V_m + ve and V_m-ve, illustrating the difference in R, is also shown in fig. 10.30.

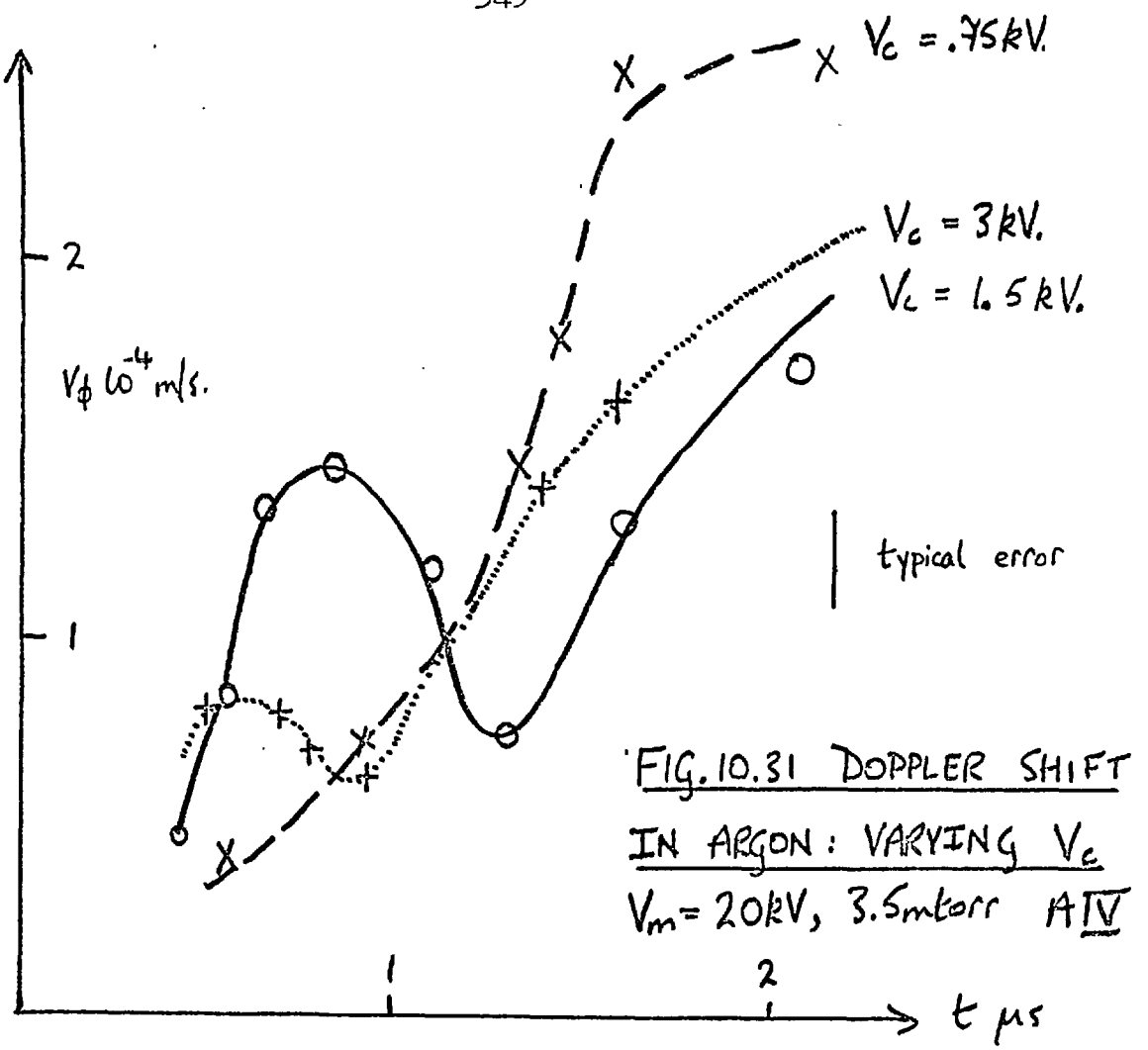

FIG. 10.31 DOPPLER SHIFT IN ARGON: VARYING V_c
V_m = 20kV, 3.5mtorr AIV

Results

Some of the results obtained are shown in figs. 10.31 and 10.32. The error bars shown are due to the non reproducibility. For the sake of clarity these are omitted from fig. 10.31. It is noticeable that the errors after the loss time are very large.

For p = 3.5 mtorr. it is only AIV which is moving very fast before the loss time. This early velocity is low for V_c = .75kV. As expected the velocity has a maximum at the loss time. But for V_m = 20kV , the velocity rises again

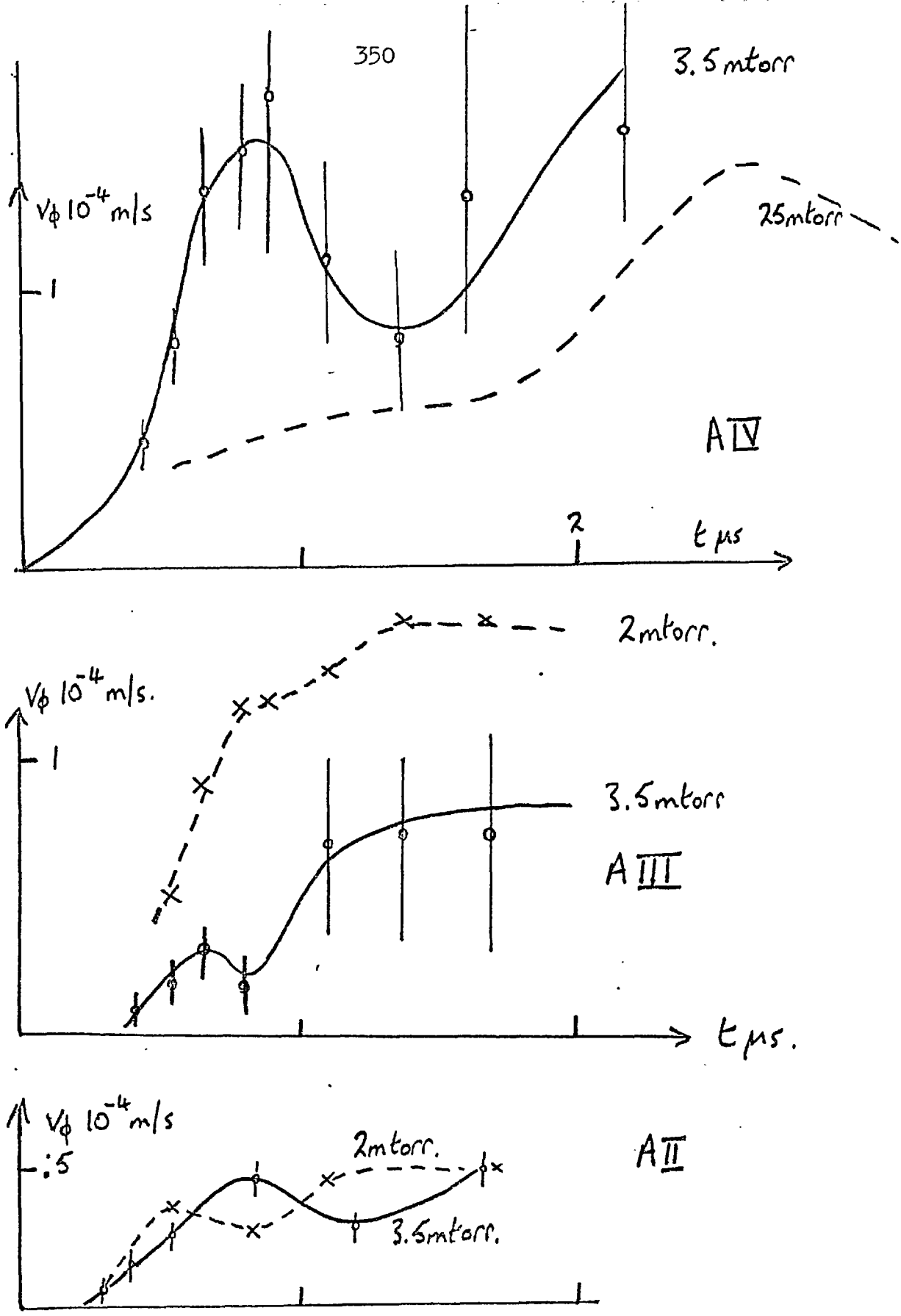

FIG. 10.32 DOPPLER SHIFT IN ARGON

= 20kV V_c = 1.5kV

after 1.5μs. This coincides with the current rising again. Large errors precluded measurements at later times, the errors arising principally from the low light intensity. At these late times, quite a high velocity of AIII and AII is also observed.

For lower values of V_m(10kV) the peak velocity is essentially the same as in fig. 10.31 but of course the peak occurs later. At these values of V_m, the velocity does not rise again after the loss time, but stays constant at about .5 10^4 m/s. Under these conditions $\frac{dI_\phi}{dt}$ remains small as well. Under extreme conditions of low electric field and high cusp field, V_m = 10kV , V_c = 3.5kV , the velocity reverses for .5μs after the loss time.

A velocity after the loss time is necessary for the explanation of the vertical shift of the plasma. That the shift is not very pronounced for V_m = 10kV (fig. 10.1) agrees with the measuremcnts here, that v_ϕ is small under these conditions.

For 2 mtorr, AIV is not formed. However, similar behaviour can be seen for the AIII velocity. At 25 mtorr, a peak velocity of 1.5 10^4 m/s is seen, again occuring at the loss time 2.5μs.

10.10 Measurements with a smaller torus

Measurements of $\frac{dI_\phi}{dt}$ and Z were made for a smaller vacuum vessel. This was the original polytron torus, bore

46mm, used by Parkinson. The purpose of the experiments was to examine the scaling with minor radius, however only the above diagnostics were used.

As expected the time of peak AIV occurs earlier than for the large torus. Again the peak coincides with the shoulder of the current waveform.

The $\frac{dI_\phi}{dt}$ vs. V_c plot is similar to the large torus. By comparison with the data for the large torus the following table has been compiled.

V_m(kV)	V_c(kV)	$\dot{I}_\phi$ large tube/$\dot{I}_\phi$ small tube (t = 0, 15% error)
10	0	1.3
10	1.5	2.1
10	3	2.0
10	5	1.7
20	0	1.3
20	1.5	2.3
20	3	2.0
20	5	1.8

The ratio for $V_c = 0$, can easily be accounted for. As shown earlier the toroidal current for $V_c = 0$ does flow in a

skin initially, and so for the case $V_c = 0$, the appropriate inductance is that of a hollow torus $L = \mu_o R(\ell n(8R/r) - 2)$

$$\therefore \quad \frac{L \text{ small}}{L \text{ large}} = 1.26$$

compared with $\frac{\dot{I}_\phi \text{ large}}{\dot{I}_\phi \text{ small}} \simeq 1.3 \pm .2$

The ratio for $V_c \neq 0$ provides valuable information about the Hall inductance. This will be discussed in the next chapter.

CHAPTER ELEVEN

A DISCUSSION OF THE EXPERIMENTAL RESULTS AND THEIR RELATION TO THE THEORY

Here the results of chapters 9 and 10 are discussed in relation to:-

(1) the particle models of chapters 5, 6 and 7.

(2) the ionisation model of chapter 8.

(3) the theoretical criteria of previous workers, listed in chapter 1.

The comparision is presented in the order in which the phenomena occur.

11.1. The value of $\omega\tau$

Polytron action will not occur if $\omega\tau$ is less than about 1. More specifically suppose that the results of chapter 7 are applicable, and acceleration occurs predominantly under the ring cusp. In cylindrical coordinates based on the minor axis $\underline{B} = (B_r(r),0,0)$

then $j_z = \sigma E_z + \omega\tau j_\theta \quad : j_\theta = -\omega\tau\, j_z$ initially,

where $\omega\tau = \dfrac{\sigma B_r(r)}{ne}$

and so $$\frac{dv_z}{dt} = \frac{(\omega\tau)^2}{1+(\omega\tau)^2}\ \frac{eE_z}{m} \qquad (11.1)$$

$$\therefore \quad \int_0^\infty \left(\frac{eE_z}{m} - \frac{dv_z}{dt} \right) d(\omega\tau) = \frac{eE_z}{m}\ \frac{\pi}{2}$$

Thus eq. 11.1 can be represented by zero acceleration for

$\omega\tau < \pi/2$ and full acceleration for $\omega\tau > \pi/2$. The radial weighting will not affect this much; a numerical integration giving 1.6. instead of $\pi/2$.

The radii corresponding to $\omega\tau = \frac{eB(r)}{ne} = \frac{\pi}{2}$ calculated from the measured values of W, n (p.295 & p.296) and Z (p.325) are shown in fig. 11.1 as a function of time., as a fun[illegible]

Fig. 11.1 CALCULATED RADII AT WHICH $\omega\tau = \pi/2$ (in the polytron)

V_m = 20kV , V_c = 1.5kV

time (μs)	0	.25	.5	.75	1	1.5
radius cm (3.5mtorr)	.5±.2	.1±.03	.06±.03	.06±.03	.04±.02	.001±.001
radius cm (25 mtorr)	1.3±.3	1.1±.3	1.7±.5	>2	>2	>2

Although initially efficient acceleration can be expected for both pressures, poor acceleration (fig. 10.32) and a large electron current (p.379) can be expected for the 25 mtorr. case at ~1μs.

11.2 The ion Larmor radius and field perturbation criteria

The ion Larmor radius criterion has been investigated in detail, in chapters 5 and 6. The simple criterion, eq. 1.9 gives similar results. For example in argon, Z = 1, E = 10^4 v/m, B = .8T, (i.e. near the wall for V_c = 1.5 kV,)

$$r_\ell = \frac{Em}{B^2 e} = 7\ 10^{-3}\text{m}, \text{c.f. } \frac{L}{2} = 2.\ 10^{-2}\ \text{m}.$$

Near the wall under these conditions argon ions are marginally

accelerated depending on their initial axial position. But for hydrogen ions $r_\ell = 1.7\ 10^{-4}$m, and so there can be no acceleration. Decreasing B will eventually satisfy eq. 1.9 for hydrogen, but will violate eq. 1.11 and $\omega\tau > 1$.

The field perturbation criterion, eq. 1.10 implies polytron action for

$$r > 1.5\ \frac{(1500)}{V_c}\text{cm.} \qquad (11.2)$$

for $n = 4\ 10^{20}\ m^{-3}$, $E = 4\ 10^{3}$ V/m. A straight forward application of eq. 1.10 may not be rigorous. However, near to the axis an electron current will flow because $\omega\tau < 1$. This corresponds to a radius similar to eq. 11.2.

Consider the ion and electron currents flowing in parallel. The inductance of the ion current consists of the magnetic and the Hall inductance, summing to $L_i = 1.9\,\mu$H. The minor radius used to calculate the magnetic inductance of the electron current, from $L = \mu_0 R(\ln(8R/r) - 1.75)$, is given by eq. 11.2. The results are shown in fig. 11.2 where

$$\frac{1}{L_T} = \frac{1}{L_i} + \frac{1}{L_e}$$

Fig. 11.2 THE CALCULATED TOTAL PLASMA INDUCTANCE

V_c (kV)	L_e (μH)	L_i (μH)	L_T (μH)
.75	.85	1.19	.48
1.5	1.05	1.19	.55
3.	1.28	1.19	.63

From fig. 10.7 a significant change in L_T is expected only when $V_c < 1.5$ kV, and also from eq. 10.1 the total inductance is~1.0μH. Accordingly it seems that eq. 11.2. should be modified so that there is a free electron current inside

$$r = .12 \pm .1 \ (\frac{1500}{V_c}) \quad \text{cm.}$$

This is not incompatible with eq. 1.10 as the electron current would generally follow the field lines, and flow through a smaller radius on average, than in the plane of the ring cusp. Even so the variation of L_T with V_c is not as rapid as expected.

In hydrogen it is necessary that $V_c < 1.5$ V (p.355, p.320) in which case a large electron current flows (p.319).

Eq.1.11 is a statement that the number density must be much less than 1.7 10^{20} m^{-3} for hydrogen and much less than 7 10^{21} m^{-3} for argon. Experimentally this cannot be satisfied for hydrogen, (p68) for the experimental preionisation.

11.3 An experimental verification of the validity of a particle equation for the acceleration

Here the measurements of sections 10.3, 10.7 and chapter 3 are used to show that the acceleration obeys $\frac{dv_\phi}{dt} = \frac{e}{m} E_\phi$: m is the ionic mass. Suppose that in the length L between coils only a length $\Delta L(r)$ is accelerated. The toroidal force F_ϕ on the plasma between 2 coils is

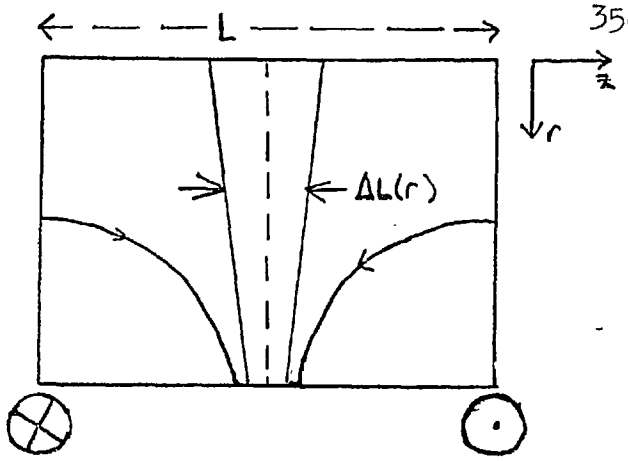

THE ACCELERATED REGION

$$F_\phi = \int_{r_{min}}^{r_{max}} \Delta L(r)\, n(r)\, m \frac{dv_\phi(r)}{dt}\, 2\pi r\, dr$$

If $eE\phi = m\frac{dv_\phi}{dt}$ and using $E_\phi(r)\,\Delta L(r) = V \neq f(r)$

where V is the voltage between the coils, then

$$F_\phi = eV \int_{r_{min}}^{r_{max}} n(r)\, 2\pi r\, dr$$

$$\therefore \frac{F_\phi}{eV} = N \qquad (11.3)$$

N is the line density, r_{max} and r_{min} are radii at which acceleration stops. All of the quantities in eq. 11.3. have been measured. The two sides of the equation are shown in fig. 11.4.

FIG. 11.4 EXPERIMENTAL VALUES ILLUSTRATING EQ. 11.3
$V_m = 10.V, V_c = 1.5kV$, argon, t=0

p, mtorr.	3.5	25.
F_ϕ, N	3.1 ± 1	10.5 ± 1
V, volts	110. ± 25	45.
F_ϕ/eV, $10^{17} m^{-1}$ (=N, eq. 11.3)	1.8 ± .8	14.5 ± 1
measured N, $10^{17} m^{-1}$	3.2 ± 1	16.4 ± 4

The measured values of the line density are taken from the peak and line of sight values of chapter 3. Profiles are constructed so that the shape is similar to that predicted in chapter 4, and the line density and peak values agree with the measured values. The line density is calculated from the profile taking r_{min} from section 11.1. and r_{max} as 3.1 cm, the smallest distance from the magnetic axis to the wall.

Fig. 11.4. shows that the single particle approximation is not in error by more than 1.5. The good agreement at higher pressure, where the fractional error is less, suggests that $m \frac{dv}{dt} = eE_{\phi}$ is exact to 10%.

The value of line density used is that under the ring cusp. The average line density is smaller, and would give a better agreement, as would the effect of the cool plasma near to the wall not being accelerated, either because of a low value of $\omega\tau$, or because of shorting of the voltage by the wall.

11.4 The polytron as a circuit with a Hall inductance

The initial stages of the polytron can be adequately described by a simple circuit equation. This is strictly only applicable for full electron trapping and ion acceleration, but can be modified to include momentum loss to the magnetic field, and electron current.

The toroidal current is split up into the ion and electron components, I_i and I_e. E is the applied electric field, L the geometric inductance, and R the resistance of the plasma to ion and electron current flow. The local electric field E′ is given by

$$\ell E' = \ell E - L\frac{dI_i}{dt} - \frac{dL}{dt}(I_i+I_e) - R(I_i+I_e) - L\frac{dI_e}{dt}$$

where ℓ is circumference of the torus.

The ion current is carried by a number density n, of charge Ze, across an area A, i.e. $I_i = neZAv$

The equation of motion of the ions is a small volume Adl is

$$\ell E' A n e Z\, dl = m_i \ell \frac{d}{dt}(nAv)\, dl - \ell S\, dl$$

where S is the rate of gain of momentum per unit length, from the walls and neutrals.

$$\therefore \quad \left(\ell E - L\left(\frac{dI_i}{dt}+\frac{dI_e}{dt}\right) - \frac{dL}{dt}(I_i+I_e) - R(I_i+I_e)\right) neZ$$

$$= \frac{\ell m_i}{eZA}\frac{dI_i}{dt} - \frac{\ell m_i n v}{Z}\frac{dZ}{dt} - \frac{\ell S}{A}$$

Suppose $S = m_i v \frac{d}{dt}(nA) = \frac{m_i I_i}{neZA}\frac{d}{dt}(nA)$

which represents the loss of momentum as a loss of line density.

The circuit equation becomes

$$\ell E = \left(L + \frac{\ell m_i}{e^2 Z^2 nA}\right)\frac{dI_i}{dt} + I_i\left(R - \frac{m_i \ell}{AnZ^3 e^2}\frac{dZ}{dt} + \frac{dL}{dt} - \frac{m_i \ell}{n^2 e^2 Z^2 A^2}\frac{d(nA)}{dt}\right)$$

$$+ L\frac{dI_e}{dt} + RI_e + I_e\frac{dL}{dt} \qquad -(11.4)$$

Thus in series with the geometric inductance is a

Hall inductance, $\frac{\ell m_i}{e^2 Z^2 n A}$ which represents the kinetic energy stored in the ions. The dependence on line density rather than volume density makes it amenable to experimental verification. The fourth and sixth terms on the r.h.s. of eq. 11.4. are <u>similar</u> to $I_i \frac{dL_H}{dt}$, and account for the high resistance of the plasma at the loss time.

In a similar vein there is a Hall capacitance associated with the plasma. The electrons must move on average an electron Larmor radius before the ions can be acclerated. Therefore a charge $Q = N e r_\ell$ passes, where r_ℓ is the electron Larmor radius $r_\ell = \frac{U}{36\ell'} \frac{m_e}{eB^2}$, $\frac{U}{36}$ is the potential between the two cusp coils and ℓ' the length of plasma being accelerated, across which the voltage is developed.

$$\therefore \quad C_H = \frac{Q}{U} = \frac{N m_e}{36 \ell' B^2}$$

The equivalent circuit is

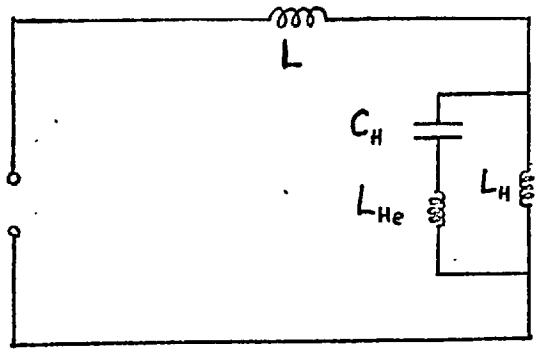

L geometric inductance

L_H ion Hall inductance

L_{He} electron Hall ind.

The rise time of the voltage across L_H is then

$$t_r \approx (L_H C_H)^{1/2} = \left(\frac{m_e m_i}{B^2 e^2 Z^2}\right)^{1/2} = \frac{240}{\omega_{ce}}$$

for argon, if $\ell = \ell'$. This is typically 10ns for B = .2T , and might be experimentally detectable in a future experiment.

11.5 Experimental evidence for the role of the Hall inductance

In fig. 10.7c, the variation of $\frac{dI_\phi}{dt}$ vs. p demonstrates the Hall inductance. For all the pressures shown $\omega\tau > 1$ over most of the tube, and so there should only be a small electron current. When the Hall inductance dominates the geometric inductance

$$\frac{dI_\phi}{dt} = \frac{\ell E}{L_H} = \frac{\ell E e^2 Z^2 n A}{\ell m_i}$$

At high pressure the geometric inductance dominates and

$$\frac{dI_\phi}{dt} = \frac{E\ell}{L}$$

Hence from fig. 10.7c, the Hall and geometric inductances are approximately equal at 3 mtorr in argon

The linear relationship between $\frac{dI_\phi}{dt}/V$ and p, fig. 10.1 is also evidence for the current being limited by a Hall inductance $\propto \frac{1}{n}$.

$\frac{dI_\phi}{dt}$ is independent of the cusp field (at high V_c) which again indicates that the total current is limited by an ion current. In contrast an electron current would be expected

to be reduced by increasing V_c, and thus $\omega\tau$.

Comparison of the values of $\frac{dI_\phi}{dt}$ (at high V_c) with the small tube shows a ratio of 2 ± .2, close to the ratio of areas of the two tubes 2.3. This would be expected if $\frac{dI_\phi}{dt}$ were limited by the Hall inductance. In contrast the ratio of the inductances of the two tubes is 1.3, the ratio of the two currents when $V_c = 0$, as shown in section 10.10.

The correlation between I_ϕ and v_ϕ was pointed out in section 10.9. In section 11.3. it was shown that all of the measured voltage is necessary to accelerate the ions. This would not preclude an electron current, but the electric field distribution needed to drive the electron current would have to be the same as the distribution which is accelerating the ions. The voltage measurement(section 10.3) is indicative of the plasma being mainly an inductance, rather than a resistance, as would be the case if the current were an electron current.

The accumulation of evidence is convincing of the role of a Hall inductance.

11.6 Quantitative values of the Hall inductance

From eq. 11.4.

$$V_e = \ell E - L\frac{dI_\phi}{dt} = L_H \frac{dI_i}{dt} + R_E I_i + R I_e + I_e \frac{dL}{dt} \qquad (11.5)$$

where R_E is the effective ion resistance,

$$R_E = R - \frac{\ell m_i}{AnZ^3e^2}\frac{dZ}{dt} + \frac{dL}{dt} - \frac{m_i}{n^2e^2Z^2A^2}\frac{d(nA)}{dt} \qquad (11.6)$$

and $I_\phi = I_i + I_e$. Algebraically the r.h.s of eq. 11.5 simplifies at t = 0 as $I_\phi = I_e = I_i = 0$. Experimentally $\frac{dI_\phi}{dt}$ was measured after 100ns and so I_ϕ could be as large as 1kA. Classical resistivity gives $RI_\phi = 100V$ for $I_\phi \simeq 1kA$. The other terms in R_E are of order $\frac{d}{dt}(L_H)$ and so the product with I_ϕ is negligible c.f. $L_H \frac{dI_\phi}{dt}$. Thus it is valid to simplify the equation for the experimental results, to

$$V_e = L_H \frac{dI_i}{dt} = \frac{\ell m_i}{e^2Z^2N}\frac{dI_i}{dt} \qquad (11.7)$$

A straightforward application of this theory is illustrated in fig. 11.5. where $f = I_e/I_i$ $\therefore I_\phi = I_i(1+f)$.

$\therefore \frac{dI_\phi}{dt}/V_e = (1+f)/L_H$

Fig. 11.5 V_m = 10kV, V_c = 1.5kV, argon, t = 0.

p(mtorr)	3.5	25.
$\frac{dI_\phi}{dt}/V_e$ μH^{-1} (fig.10.12)	2.1	7.
N x $10^{-17} m^{-1}$ (11.3)	1.8	14.5
$\therefore e^2Z^2N/(\ell m_i)$ μH^{-1}	.043	.36
$\therefore$ f	48.	18.

The value of the line density used is that calculated in section 11.3. As can be seen the value of f would indicate little polytron action, the amount decreasing as the pressure decreases. This dependence would not be expected nor would the very large values of f. Moreover, for the reasons of section 11.5. the concept of Hall inductance seems valid. It would be hard to interpret all of section 11.5 in terms of an electron current.

Fortunately the contradiction can be resolved using the results of chapter 7. The single particle approach of chapters 5 and 6 was inspired by the experimental evidence for Hall inductance. It is gratifying that chapter 7 evolved from 5 and 6, can then be used to explain the experimental results.

Only a length ΔL of plasma is accelerated. This is at the ring cusp which electrons cannot cross. $\nabla \cdot j = 0$ so in the rest of the plasma electrons must carry the toroidal currents. However, the amount of current is restricted by the ion current. The electron current just flows to maintain neutrality. This occurs in the model of chapter 7. The electric field accelerating the ions is enhanced by $L/\Delta L$ over the value expected for a uniform distribution of field, so increasing the ion current, which is the total current. The new value of the Hall inductance is

$$L_H = \frac{\ell m_i}{e^2 Z^2 n A} \frac{\Delta L}{L} \qquad (11.8)$$

Eq. 11.7, with this new value of L_H, is used to determine ΔL. V_e is the potential difference measured in section 10.3. Two values of N are used, the values inferred in section 11.3. and the measured value. These results are shown in fig. 11.6.

Fig.11.6. WIDTHS OF THE ACCELERATED REGIONS OF PLASMA (inferred from eqs. 11.7 and 11.8)

$t = 0$, $V_m = 10kV$, $V_c = 1.5kV$, argon

p mtorr.	3.5	25
minimum ΔL(mm)	.9	3.4
ΔL using measured N (mm)	1.6	4.

The self consistent particle calculation gives the width of the accelerated plasma as 4mm. That value could be limited by the Debye length. The values of fig. 11.6. do not contradict the theory in chapter 7 that the width is the separation of the flux surface outside of which electrons are attached to flux surfaces because their Larmor radius is much less than characteristic scale legnths, and $\omega\tau \gg 1$. The

case here is of a sheath limited by collisional effects. The flux surfaces can be equipotentials only if $\omega\tau \gg 1$, along the whole flux surface. This is illustrated experimentally in fig. 11.6. where the sheath is wider for higher pressures, lower $\omega\tau$ (fig. 11.1). It would be expected that $\Delta L \propto (r(\omega\tau = \pi/2))^2$. The ratio of ΔL for these two pressures is ~ 1 (fig. 11.6), whereas the ratio of $r(\omega\tau = \pi/2)$ the radii at which $\omega\tau = \pi/2$ is 2.6 : 1 for the two pressures.

This width is comparable with the experimentally observed width of the dark band (section 10.1). A similar sheath width is deduced from the non Maxwellian scattering of section 9.17.

A more definitive measurement of this width is necessary. Possible methods are to attempt spatial resolution of the Doppler shift (Davis et al, 1971), measurement of the electric field distribution with a double Langmuir probe (Hamberger et al. 1970) or measuring the distribution of the Hall current by laser scattering (chapter 9). The first two methods are unsatisfactory even a priori. The last method would only require a more thorough experiment, (with a toroidal scan) than that reported in section 9.15. Indeed the negative result of that experiment was probably because $E_\phi = 0$ at the scattering volume, the Hall current causing the ring cusp to move upstream from the $\phi = 5^\circ$ plane.

The scans of the poloidal magnetic field in section 10.6 do not contradict this model of current flow. At 250ns the current distribution under the ring cusp is uniform on the inside. In contrast under the coil at this time the current flows within a radius of 15mm. from the magnetic axis. The electron current, which flows in the region under the coil in response to the ion current, must follow the field lines, and so will flow at small radii under the cusp coil.

11.7 The diffusion of b_θ

For normal resistive diffusion (chapter 3) the poloidal magnetic field will take a time

$$\tau = a^2 \frac{\mu_0 \sigma}{\gamma_0^2}$$

to diffuse to the axis. For a 1eV. plasma this is 400ns, illustrated by the diffusion observed with no cusp field in section 10.6. By contrast, the diffusion time observed for b_θ in the polytron is less than 100ns (p344). This is strong evidence for polytron action. Now $\nabla^2 E_\phi = -\mu_0 \frac{\partial j_\phi}{\partial t}$ using eq. 8.20a, $\nabla^2 E_\phi = -\frac{\mu_0 n e^2}{m_i} E_\phi + \frac{\sigma \mu_0}{1+\omega^2\tau^2} \frac{\partial E_\phi}{\partial t} = \frac{E_\phi}{\delta^2} + \frac{\sigma \mu_0}{1+\omega^2\tau^2} \frac{\partial E_\phi}{\partial t}$ Therefore E_ϕ will diffuse in rapidly in a time $\tau/1+\omega^2\tau^2$, but only to a depth of δ the collisionless ion skin depth. But $\delta \gg L$, from eq. 1.11, and so experimentally b_θ will diffuse in in $\ll 100$ns. Borzunov et. al. (1964), in a plasma confined by a travelling cusp field, observed a large skin depth. This they attributed

to the Hall term in Ohm's law, causing a large effective resistance.

11.8 A momentum balance before the loss time

As long as no momentum is lost to the wall, all of the electromagnetic momentum must produce plasma momentum. The measured velocities are line of sight values, and so an axially averaged equation.

$$F_\phi = n\,AL\,m_i \frac{dv_\phi}{dt}$$ can be checked.

Consider the initial momentum balance of the plasma associated with one coil. For the conditions V_m = 20kV, V_c 15 kV, t = 0, p = 3.5 mtorr argon

$$F_\phi = 6 \pm 1\ N, \quad m_i\, n\, AL = 1 \pm .2\ 10^{-9}\ kg$$

$$\therefore \quad F_\phi/(m_i nAL) = 6 \pm 2\ 10^9\ m/s^2$$

where the value of n used is the toroidal average.
An estimate of the acceleration at this time can be obtained from fig. 10.32, the velocity measured of AII , as $6 \pm 2\ 10^9\ m/s^2$.

Now consider the momentum in the plasma at the loss time. Little momentum will have been lost to the wall as only particles with low v_ϕ are lost. For the condition of V_m = 20kV , V_c = 1.5kV , t = 800ns , 3.5 mtorr

$$\int_0^{800ns} F_\phi\, dt = 4 \pm 1\ 10^{-6}\ Ns$$

For the momentum in AIV $A = 3 \pm 1\ 10^{-4}\ m^2$.

$n = 2.5\ 10^{20}\ m^{-3}$ and $v_\phi = 1.4\ 10^4 m/s$

For the momentum in AIII $A = 12 \pm 10\ 10^{-4} m^2$,

$n = 1 \pm 1\ \ 10^{20} m^{-3}$ and $v_\phi = .2\ 10^4 m/s$.

A similar amount of momentum is carried by AII with a similar error. Fortunately the momentum of AI and AIII for which n and A have large errors, is small c.f. AIV

$$\therefore \text{ Total momentum } = \underset{\uparrow A_{IV}}{(2.8 \pm 1)} + \underset{\uparrow A_{III}}{(.8 \pm .8)} + \underset{\uparrow A_{II}}{(.8 \pm .8)} \text{Ns.}$$

$$= 4.4 \pm 1.4 \text{ Ns.}$$

Again the comparison is good. It would of course be surprising if the momentum input could not be accounted for. The fact that the balance can be demonstrated adds confidence to the measurements of chapter 10, and the deductions of section 11.3 and 11.6.

At the loss time the momentum input to the plasma drops. The increase in the velocity observed in section 10.9 can be accounted for by the drop of the ion number density due to the loss, the momentum staying constant.

11.9 The ionisation rate

In chapter 8 the ionisation rate equations were solved, the results being used as a temperature diagnostic before the laser scattering was available. The procedure can now be reversed, and the rate coefficients checked. The empirical

result obtained from section 8.2 was $\frac{dZ}{dt} = .5\left(\frac{n}{10^{20}}\right) \exp(-15/W)\ \mu s^{-1}$

The values of the r.h.s. of this expression are shown in fig. 11.7.

FIG. 11.7 CALCULATED VALUES OF dZ/dt FROM CHAPTER 8

V_m = 20kV , V_c = 1.5kV , 3.5 mtorr

time (μs)	.25	.5	.75
n x 10^{-20} m^{-3}	4.	3.	2.5
W(eV)	4.	8.	13.
$dZ/dt(\mu s^{-1})$	.04	.21	.3

The measured dZ/dt is $2.5\mu s^{-1}$. Thus the ionising rate coefficients used in chapter 8 are an order of magnitude too small. Presumably the effect of collisional radiative ionisation, and of many optically active electrons is not negligible. An experimentally appropriate coefficient c.f. eq. 8.3. is

$$S(W,Z) = \frac{2.10^{-5}}{\chi(Z,g)W^{\frac{1}{2}}} \exp\ (-\chi(Z,g)/W)\ cm^3 s^{-1}$$

The numerical agreement with the value used in chapter 4, when W = 10eV , is good.

11.10. The energy balance

Here the measured plasma parameters are used to account for the terms in the plasma energy equation,

$$\frac{\partial}{\partial t}\left(\tfrac{1}{2}\rho v^2 + \tfrac{3}{2}n(kT_e + kT_i) + \sum_{i=1}^{\infty} n_i I_i\right) + \nabla\cdot\left(\tfrac{1}{2}\rho v^2 \underline{v} + U\underline{v} + \underline{\underline{P}}\cdot\underline{v} + \underline{q} + \underline{S}\right) = \underline{j}\cdot\underline{E}\,.$$

when n_i and I_i are the number density and ionisation energy of stage i, $\underline{\underline{P}}$ the pressure tensor , $\underline{q}$ the heat flux, U the internal energy and $\underline{S}$ the radiation flux. As shown in section 8.3. $j_\theta\ E_\theta \ll j_\phi\ E_\phi$.

$$\therefore \int_0^t\int \underline{j}\cdot\underline{E}\, dV dt = \int_0^t V_e I_\phi\, dt = 70 \pm 10\ J$$

for V_m = 20kV , V_c = 1.5kV , 3.5 mtorr, argon at 800ns. A radial scan of the temperature under these conditions was not made, but at 8 mtorr , 2 cm off axis the electron number density and temperature were a $\frac{1}{4}$ of their peak value. The full half width of the A IV emission was 18 mm at 3.5 mtorr, and so the cross section for computing the thermal energy of the plasma is 4 cm^2, which is probably an over estimate. The cross section for the ionisation energy is more certain as A IV contributes most to the ionisation energy . The measured ion densities, and profiles of A IV and A III allow these energies to be calculated. The directed energy is predominantly in the motion of A IV , the proportion that is in other species is even less than for the momentum. All these energies are shown in fig.11.7.

An error is estimated for the thermal energy from the uncertainty in the cross section. The ion thermal energy is

estimated assuming equal ion and electron temperatures. In this sense the plasma is supersonic.

FIG. 11.7 THE ENERGY BALANCE FOR THE WHOLE TORUS

V_m = 20kV , V_c =1.5kV, 3.5 mtorr, t = 800ns

$\int_0^{800ns.} V_e I_\phi \, dt$	70 ± 10 J
Electron thermal energy	4.2(±4)J
Energy of ionisation	5.4(±2)J
Ion directed energy	4 ±1 J
Estimated ion thermal energy	1 J

Clearly even allowing generous experimental error, 85% of the energy is lost from the system. This is either by thermal conduction along the field lines, or by radiation loss. The energy advected to the wall is small and certainly not greater than the measured thermal energy. The thermal diffusivity is

$$D = \frac{2\delta K_\perp}{3nk} = .2\, W^{5/2} \left(\frac{10^{20}}{n}\right) \quad cm^2/\mu s$$

using the notation of Spitzer (1956) p.88. Radial geometry (chapter 3) effectively reduces the radial diffusion distance to the wall to $3.5/\gamma_0 \sim$ 1cm , and so a cooling time is $\tau_c = \frac{30}{W^{5/2}}$ μs. By 800ns the central temperature is 10eV , for which $\tau_c \sim$ 100ns., but more realistically τ_c could be larger, as W is smaller nearer the wall.

Classical bremsstrahlung causes an energy loss of $5\ 10^{-4}$J in 1μs. (Spitzer, eq. 5.49). As shown in chapter 9 the continuum emission is 100 times the bremsstrahlung level. If the spectral range studied in chapter 9 is typical, the line emission will not be more than 10 times the continuum. Thus the maximum radiation loss is .5J , 2 orders of magnitude too low. The defecit in the energy balance must be caused by conduction.

With reference to chapter 8, the heating rate predicted there is too low. For example a temperature rise of 15 eV in 1 μs is predicted in section 8.6 for conditions comparable with the experimental values at 3.5 mtorr. Experimental temperature rises of this value are observed even though there is ionisation and thermal conduction. However the values of chapter 8 must be enhanced by a factor $L/\Delta L$, to account for the large j_ϕ. There is no clear indication of the roles of toroidal and poloidal current in the heating. From fig. 10.18 the temperature is independent of the toroidal position. The toroidal diffusion length is 2 cm, and the temperature is about 10eV, and so $\tau_c \sim$ 300ns which is just short enough to make W independent of ϕ. The width of the A$\overline{\text{IV}}$ spatial profile is narrower under a coil. But this could be due to the flow pattern of the toroidal current, or due to Hall currents.

In contrast the toroidal difference in the time for A$\overline{\text{IV}}$ to peak, exhibited in fig. 10.18, is clear evidence for:-

(1) the AIV maximum being due to a cooling of the plasma.

(2) the cooling occuring sooner downstream of the ring cusp, and thus cooling being due to reentrant plasma. This is corroborated by photography.

11.11 Comparison with the single particle models

The validity of a single particle model has been demonstrated in section 11.6. for the first part of the discharge, where a simple analytic model is suitable. An experimental comparison is now made with the single particle calculations of chapters 6 and 7, in order to discuss the plasma behaviour at the loss time and later.

(a) Loss regions

The area of contact with the wall agrees. That is, at the ring cusp shifting downstream at later times (section 10.1 and fig. 7.19). The time at which this loss occurs is the same experimentally, as seen in chapters 6 and7. Experimentally the loss time is measured by the photography and the time of peak AIV emmision.

(b) Current profiles

The shapes of the experimental current waveforms are very similar to those in chapter 6. As already shown, the magnitude of the single particle current is arbitrary and depends on the small length of the plasma being accelerated.

However a meaningful comparison at the loss time, with chapters 5 and 6 can be made, whereas the drop in the toroidal current at the loss time for the simulation of chapter 7, is too large to compare well with the experiment. Qualitatively this can be seen to be due to the ring cusp moving. The field produced by the Hall current moves the ring cusp antiparallel to E_ϕ. The fluctuating Hall current causes the ring cusp to move through a large volume of plasma, the plasma being accelerated when the ring cusp passes through it. Because much of the plasma is accelerated, chapters 5 and 6 are not bad models for the loss, although radial electrostatic fields are neglected.

The experimental loss times are

$$\tau_e = 1. \left(\frac{10kV.}{V_m}\right)^{1/2} \left(\frac{1.5kV.}{V_c}\right)^{1/3} \mu s. \qquad \text{for argon}$$

and

$$\tau_e = .3 \left(\frac{10kV.}{V_m}\right)^{1/2} \left(\frac{1.5kV}{V_c}\right)^{1/3} \mu s. \qquad \text{for hydrogen.}$$

The computational value for hydrogen is

$$\tau_e = .28 \left(\frac{10kV.}{V_m}\right)^{1/2} \mu s.$$

and argon $\tau_e = 1.3 \left(\frac{10kV.}{V_m}\right)^{1/2}$ μs where Z = 2 has been assumed. As can be seen agreement is good. There was a slight computational dependence of τ_e on the cusp field but it was omitted from the loss time formula, whereas the stronger dependence observed experimentally was included.

(c) <u>The magnetic field of the Hall currents</u>

Experimental values were only obtained in argon, and as usual the degree of ionisation causes difficulty in a

comparison with single particle calculations. The peak experimental magnetic field is

$$b_\phi = 1000g. \text{ for } V_m = 20kV \text{ , } V_c = 1.5 \text{ kV ,}$$

$n = 7\ 10^{20}\ m^{-3}$. The field expected from chapter 6 is

$$b_\phi = 61 \frac{n}{10^{20}} \frac{V_m}{10kV} \frac{.4}{B} \text{ g.} \quad = 2000g.$$

This is not bad agreement, as in the simulation there are azimuthal currents flowing at radii of 4mm.

(d) The voltage

The shape and magnitude of the voltage waveforms are in reasonable agreement (e.g. fig. 6.9 and 10.11). The exact magnitude depends on the Hall inductance, whose value is given by collisional effects. (sect 11.6)

(e) The plasma loss

The experimental measurements of the loss from the ion probe, are not very precise. However the experimental variation with V_c and V_m are as expected from chapter 6. That is the loss increases as V_c is increased and as V_m is decreased. The laser scattering shows that the maximum n on axis decreases as V_c increases, but decreases as V_m is increased. However, the streak photography of section 10.1. shows that this dependonce on V_m arises because the plasma moves away from the axis at V_m = 20kV. The larger maximum temperature for large V_c (fig. 9.19) is because of the lower number density.

(f) The accelerated plasma

The velocity measurements of section 10.9 show that despite the loss of plasma there is still some contained plasma

which for high values of V_m (20kV.), continues to be accelerated. This must be a narrow core of plasma, 2cm. diameter as there is only a significant Doppler shift for AIV radiation. Again this is in agreement with chapters 6 and 7, where v_ϕ is large near the axis and reverses at larger radii (fig. 7.19). However, for low values of V_m, where a radial drift is not catastrophic, the plasma is slowed down, whereas according to the collisionless particle models the plasma which is not lost should be accelerated.

(g) The current reversal at large radius

Experimentally this was only measured under the ring cusp. There is a reversal of the ion motion in the simulations, e.g. fig. 7.19 or fig. 6.9, under the ring cusp, where the particles are spiralling about the radial field. When these ions cross the ring cusp they constitute a reversed current. Conversely the positive j_ϕ is restricted to $r < 2$ cm.

(h) The profiles of the Hall current

The experimental profiles of b_ϕ due to the Hall current at the loss time, fig. 10.21, show that j_θ is localised to a diameter of 2.5cm., reversing further from the axis. This is seen in the simulation e.g. fig. 6.6. In fig. 6.6. at $t = 0$ there is only a small reversal of b_ϕ at large radius. The larger reversal in fig. 10.21 implies a current being carried by the azimuthal motion of the ions.

(i) The axial number density

The particle models predict that up to and beyond the loss time the axial ion density decreases, e.g. figs. 6.6 and 6.7. or fig. 7.19. After the loss time there is an increase in the ion density in fig. 6.7. but because of radial drift this will not be seen in the scattering experiments.

Experimentally similar behaviour is observed at 3.5 mtorr (fig. 10.15), but at higher filling pressures the ion density increases because of pinching. However, as shown in section 11.1 at these higher pressures $\omega\tau<1$ over all of the scattering volume, and so a pinch would be expected. Conversely $\omega\tau<1$ because a pinch forms! Clearly the initial conditions will determine whether or not a pinch forms. For example as a criterion, the condition that plasma at a radius where $\omega\tau=1$ can be pinched into half that radius before appreciable heating from the current causes $\omega\tau$ to rise, is $\frac{(kT)^2}{m}\frac{\mu_0 n b^2}{j^2}>1$. If some such condition is not satisfied then the non polytron region will quickly become small, as illustrated in fig. 11.1. Otherwise it will become large, again illustrated in fig. 11.1.

At high pressures the fall in the ion density at the loss time is due to the number density at large radii decreasing because of the normal polytron loss, and setting up a pressure gradient sufficiently large to cause the axial plasma (which has been heated) to expand. Photographically at very high pressures a stable cusp formation is seen until

the number density drops, when the polytron acceleration switches on, breaking up the cusp formation.

11.12 The plasma behaviour after the loss time

The equivocal scattering measurements inhibit the understanding of the plasma behaviour after the loss time. However, it is clear that at V_m = 20kV and V_c = 1.5 kV , there is further acceleration correlated with an increase in the currents, whereas at V_m = 10kV , there is no further acceleration. But for V_m = 20kV , V_c = 1.5kV , the plasma drifts out to the wall at~2 μs. This interpretation explains the shapes of the Hall signals, b_ϕ, in fig. 10.21.

For low V_m, or high V_c, there is no sizeable b_ϕ after the loss time. But for V_m = 20kV , V_c = 1.5kV , there is a b_ϕ signal after the loss time. Fluctuations on it correspond to the poloidal ion current, and the non reproducibility can be attributed to the photographically observed instability. The b_ϕ signal drops at 2.5 μs, the time at which the plasma hits the wall.

At lower pressure, 2mtorr, the plasma does not hit the wall. But, from fig. 10.30, v_ϕ seems to be limited to 2 10^6cm/s. This can be explained by the slowing down mechanism of section 11.14. Another possible reason is that the Hall acceleration is inhibited when the plasma moves off the magnetic axis . Certainly when the plasma is clear of the

axis the Hall current will be reduced. Cole(1970) has shown that in a linear Hall accelerator when the flow of the Hall current is prevented by baffles the Hall acceleration stops.

To decide which of these mechanisms is responsible requires more accurate measurements of n_n and α_x (section 11.14) or a theoretical understanding of the acceleration in the absence of poloidal symmetry, or an experimental measurement of the force on the plasma after the loss time.

11.13 The vertical shift of the plasma

This was observed by 3 separate diagnostics in chapter 10, where an explanation for the direction and dependence on V_m and V_c was proposed. The measured value of j_ϕ is $2\ 10^7\ A/m^2$, which if the plasma drifts outwards by a few mm. will interact with an average radial field of .05 T, causing a vertical acceleration of $5\ 10^{10} m/s^2$. This is more than adequate to displace the plasma 1cm during the transit of the ring cusp; the actual value of the displacement will depend on the amount of refocussing of the ions by the lens effect. The shift is large when the velocity is large.

11.14 Deceleration of the moving ions, and their terminal velocity

The proposed model of the polytron is ions being accelerated in a sheath, and then drifting through the rest

of the plasma until the next accelerating sheath is reached. In this drift there will be collisions with stationary electrons, ions, and neutrals, with collision times τ_s^e, τ_s^i, τ_s^n respectively.

From Chandrasekhar, (1942) the slowing down rate of particles interacting by Coulomb collisions with field particles of species i is given by

$$\frac{dv}{dt}_{\parallel} = -\frac{\ell_i^2 e^4 n_i Z^2 Z_i^2 \ln\Lambda (1 + m/m_i) G(\ell_i v_{\parallel})}{2\pi \epsilon_0^2 m^2}$$

where $\ell^2 = m/2kT$ and $G(x) = \left(\int_0^x e^{-\gamma^2} d\gamma - x \frac{\partial}{\partial x} \int_0^x e^{-\gamma^2} d\gamma \right) / (\pi^{\frac{1}{2}} x^3)$.

For polytron ions colliding with electrons $\ell_i v_{\parallel} \ll 1$

$$\therefore G(\ell_i v_{\parallel}) = \frac{2\ell_i v_{\parallel}}{3\pi^{\frac{1}{2}}} \qquad \therefore \tau_s^e = .58\, W^{3/2} A \left(\frac{10^{20}}{n}\right) \mu s$$

where A is the atomic weight of the ions.

For moving ions colliding with stationary ions $\ell_i v_{\parallel} \gg 1$

$$\therefore G(\ell_i v_{\parallel}) = .5/(\ell_i v_{\parallel})^2 \qquad \therefore \tau_s^i = \frac{3.5 A^2}{Z_i^4} \frac{10^{20}}{n_i} \left(\frac{v_{\parallel}}{10^5}\right)^3 \mu s.$$

The dominant momentum transfer interaction with the neutrals is charge exchange. Hasted gives the cross section of the AII - AI interaction as $50\ 10^{-20} m^2$. There seems to be no available data on charge exchange with higher stages of ionisation. Using $\sigma_x = 50\ 10^{-20} m^2$ gives

$$\tau_s^n = \frac{2 \cdot 10^4}{v_i} \frac{10^{20}}{n_n}$$

where n_n is the number density of neutrals.

After the loss $n \sim 10^{20} m^{-3}$, $W \sim 5\text{-}10eV$ (Chapter 9) hence τ_s^e is 10's μs, v_{11} is about $2\ 10^4 m/s$ and so τ_s^i is as long as τ_s^e. However the value of $\tau_s^\wedge$ is about $1\mu s$. The mean free path for neutral collision is

$$\lambda^\wedge = 2\ \frac{10^{20}}{n_n}\ cm.$$

Hence the difference between the measured ion velocity at V_m = 10kV and V_m = 20kV, can be explained by the higher loss at 10kV. (Chapter 6). This could cause a neutral number density after the loss, larger than $.5\ 10^{20} m^{-3}$, which would prevent plasma drift to the next ring cusp, whereas for V_m = 20kV the lower loss would keep n_n below $.5\ 10^{20} m^{-3}$.

11.15 The radial equilibrium of the polytron

From the single particle work of chapter 5 singly ionised argon ions with Z = 1; V_c = 1.5kV will be contained provided

$$1.4\ 10^5 m/s > v_\phi > 1.6\ 10^3 m/s$$

Experimentally this is satisfied. Nevertheless the streak photography of fig. 10.5. shows that there is a centrifugal drift. This is reduced if the current is reduced (either by decreasing the pressure or V_m) or if the cusp field is increased. A radial balance, or imbalance between the focussing effect of the cusps and the pressure difference of the poloidal magnetic field is suggested.

For the poloidal field the magnetic pressure difference between inside and outside the minor axis is $\frac{b_\theta^2}{2\mu_0}\frac{4r}{R_0}$ where R_0 is the major radius. This will cause a radial acceleration $\frac{b_\theta^2}{\mu_0 R_0 n m_i}$. With the measured values of chapter 10 this is an acceleration of $\sim 10^{10} m/s^2$ (for 3.5 mtorr), the right order of magnitude to cause the observed radial drift.

The single particle containment criterion should prevent loss if the acceleration is less than $\sim 5\ 10^{10} m/s^2$. However, this limit pertains when the acceleration is applied slowly, and the ions cross many cusps. This is not the case in the experiment, where the ions cross only one cusp. Moreover a single particle approximation is only valid when toroidal motion of the electrons is prevented by the cusp field. When there is a radial drift this will not necessarily be so, because of the poloidal electrostatic fields set up.

The pragmatic way of controlling this drift would be to externally apply a vertical field such as in some tokamaks, causing a inwards radial force $j_\phi B_z$.

The radial drift also explains an anomaly between the results of chapters 9 and 10. In chapter 10 it is shown that the peak of AIV occurs because of cooling. Yet in chapter 9 the laser scattering shows that the temperature is still high when according to AIV, cooling occurs. The reason is

that the AIV cooling pertains to the volume of the plasma which is radially displaced. The laser scattering measurement is near to the minor axis, away from the centre of the plasma, and the effect of the cooling is seen later here. A similar explanation, in terms of radial displacement, accounts for the higher density at lower values of V_m seen in fig. 9.19.

CHAPTER TWELVE

SUMMARY AND CONCLUSIONS

The contents of this thesis are summarised. The conclusions with regard the polytron project are stated, and future lines of research are suggested.

12.1 The contents of the thesis

The thesis can be categorised in 4 parts. The contents are stated emphasising particularly that which is new and contributes to the understanding of the polytron.

(1) Chapter 2 is a numerical study of the electromagnetic fields of the polytron. The results are useful for the polytron work. But the method for evaluating the fields is new and must be comparable in speed to other methods of evaluating the field of circular conductors.

(2) Chapters 3 and 4 are a study of a cusp compressio experiment. The main reasons for the work is to define the initial conditions of the polytron. Other workers have experimented with cusp compression devices as containment machines. The polytron apparatus is only a low energy cusp compression device, but the diagnostics described in chapter 3 are probably as comprehensive as used on most other cusp compression devices. They show that the low β compression

provides very poor plasma containment.

(3) Particle models of the polytron are described in chapters 5,6 and 7. Numerically it is shown that conditionally a single particle can be contained against centrifugal loss in the polytron fields. In the linear single particle model of chapter 6 the phenomenon which causes the experimental loss of plasma is described numerically and analytically. The scaling of the magnetic field produced by the plasma and the loss time are investigated.

In chapter 7 by making a guiding centre approximation for the electrons it is shown that a self consistent particle simulation of the polytron is possible, and furthermore , produces physically plausible results. In contrast if the motion of the electrons had been integrated exactly the simulation would have been much more difficult. The electrostatic field shows why there is no plasma acceleration under the cusp coil but large acceleration under the ring cusp. This adds greatly to the intuitive understanding of the accelerating mechanism. In contrast,in a m.h.d. model,the role of the electrostatic field is hidden.

These particle models have added enormously to the understanding of the experimental loss and the experimental acceleration. This is not surprising as they were the first theoretical work with a plasma in a realistic geometry.

(4) Experimental work on the polytron is described in chapters 9 and 10 and discussed in chapter 11. Chapter 8 shows the new feature of the switch on nature of the polytron but this will not necessarily occur in a realistic geometry. The work described in chapter 9 was experimentally difficult. The high level of plasma light probably makes this experiment as difficult as scattering off an electron number density on order of magnitude lower with normal plasma light. The non Maxwellian scattered spectrum of section 9.17 is certainly novel but can be explained in terms of the polytron mechanism. Most of the measurements of chapter 10 use standard techniques and thus many different diagnostics have been used. The Doppler shift measurement is not standard and might be applied to measure the poloidal velocities. Also the measurement of the force is not standard and this work seems to be the first serious use of the force measurement. Most of the results of the 9 different diagnostics of chapter 9 and 10 are accounted for in chapter 11 in terms of the models of chapters 5, 6, and 7.

The acceleration mechanism is examined in far greater detail than in any other work on Hall accelerators. The force measurement and the understanding obtained from chapter 7 are principal reasons for the detailed comparison.

The experimental plasma loss shows agreement with the

particle models. The behaviour after the loss is not in agreement with the particle models, probably because of one of the two mechanisms suggested.

12.2. Conclusions of the thesis

The Hall acceleration described by Haines has been modified to take into account the toroidal variation of the acceleration. The experimental results are then in good agreement with a simple particle model. There is a loss of plasma which again is predicted by the particle models. Not all of the plasma is lost and the plasma which is not lost continues to be accelerated. However the acceleration stops because of effects which can probably be overcome. If so there seems to be no reason why the original idea of the polytron, with $v_d \gg v_{th}$ cannot be achieved. The accelerating mechanism works and the initial plasma loss is not catastrophic.

12.3 Possible further work

Many new phenomena have been discovered in this thesis. The sheath formation, the voltage rise time, the vertical shift of the plasma, the photographically observed instability and the anomalous scattering are all worth further study. Likewise the self consistent particle model could fruitfully be extended to include the effect of the self magnetic field (especially b_θ) and the non-adiabatic electrons

near to the axis. However the central line of research should be to accept the acceleration and loss of the plasma as understood, and to concentrate on preventing the radial drift, and then seeing if the plasma continues to be accelerated. This will require the following modifications to the aparatus:-

(1) Improving the insulation at the collector plate so that full use can be made of the 40kV of the main bank. The point here is that the initial loss should be less at 40kV.

(2) A variable vertical field must be provided, by an extra induction rod, with a variable inductance.

(3) The torus needs to be modified so that scattering can be done along the major radius. The best way to do this would be to introduce the laser beam horizontally and to scatter vertically.

(4) The power output of the laser should be improved by using it as an amplifier of a smaller laser.

The effect of the vertical field on the radial drift of the plasma can then be investigated. The way to measure the momentum lost to the wall or neutrals would be to measure the velocity and the force on the plasma. This would determine which of the mechanisms of section 11.12 was responsible for the loss of momentum when there is a radial drift. To measure the force would require simultaneous measurements of the magnetic field distribution outside of the torus, because of

the non reproducibility of the plasma.

If the radial dirft can be prevented and acceleration continues, the future of the polytron seems promising in view of the success of other toroidal machines.

Acknowledgements

The author is grateful to the following:-

Dr. R. Latham his supervisor.

Mr. A.E. Dangor for encouragement and practical help.

Dr. M.G. Haines the originator of the polytron idea.

Mr. A. Chapman and Mr. J. Westlake for valuable technical help.

The Science Research Council for a maintenance grant.

Culham Laboratory for the loan of the framing camera.

The National Physical Laboratory for the loan of the Putley detector.

References

Ahlborn B., Johannes Barnard A., A.I.A.A. Journal 1966 .

Allen T.K., Bickerton R.J., Nature 191, 794 (1961) .

Allen T.K., Cox A.J., Spalding I.J. 'Plasma Physics and Controlled Nuclear Fusion Research' (I.A.E.A., Vienna, 1966), p.427

Ashby D.E.T.F., Paton A ., Plasma Phys., 9, 359, (1967).

Ashby D.E.T.E., Holmes L.S., Kash M.A., J.Sci.Inst. 40, 364(1963).

Bates D.R., Kingston R.E. McWhirter R.W.P. Proc.Roy.Soc.(London) A 267, 297(1962).

Bates D.R., Kingston R.E. Plan.Space.Sci., 11, 1, (1963).

Ben Daniel D.J. Plasma Physic 3, (1961), 235.

Berezin, Sov. Phys. Tech.Phys., 1963, 8 no.3,213.

Bernstein I.B. , Trehan S.K, Weenink M.P. 1964, Nucl.Fusion 4, 61-104.

Bodin H.A.B., McCartan J., Wolf G .H., 'III European Conf. on Cont. Fusion and Plasma Phys.', p.74, 1969.

Boris J.P., Robert K.V., 'III European Conf. on Cont. Fusion and Plasma Physics', p.38, 1969.

Borzunov et al., Sov. Phys. Doklady, 8, 9 (1964),914.

Boyd T.J.M., Sanderson J.J., Nelson, 1969.

Burgess D.D., Ph.D. Thesis, 1965 London University.

Burgess D.D. Phys. Rev. Lett., 10, 3, (1964).

Burkhardt L.C., Birkrew J.N., Kan H.J., Phys. Fluids, 12(1968), 1894.

Cann C.L., Marlotts G.L., AIAA Journal, 2, 7, 1234

Chandrasekhar S., Astrophysics J., 97, 255 (1943).

Chapman S., Cowling T.G., 'The Mathematical Theory of Non Uniform Gases', C.U.P. (1939).

Cole H.C., CLM-P216, (1969)

Cole H.C., University of London Ph.D., 1970.

Cooper J., Plasma Physics, 5, 285, (1963)

Costley A., Ph.D. Thesis (to be published)

Curzon F.L., Folkierski A., Latham R., Nation J.. Proc. Roy. Soc. (London), A 257, 386, (1960).

D'Angelo N., Phys. Rev., 140, A 1488, (1965).

Dangor A.E., Parkinson G.J., Dunnett R.M., Haines M.G., Latham R., 'Plasma Phys. and Controlled Nuclear Fusion'. (I.A.E.A, Vienna, 1969) Vol.I, p.255.
Davies and Vaughan., Astrophysics J., 137, (1302), 1963.

Davis W.D., et al. 'Pl. Phys. and Cont. Nucl. Fus. Res.' (I.A.E.A., Vienna, 1972), Vol III, p. 289.

Dawson J., Phys. Fl., 5, 445 (1962).

Dunnett R.M., Nucl . Fus., 8, (1968), 287.

Dunnett R.M., 1968b, Ph.D. Thesis, London University.

Dunnett R.M. Nucl . Fus., 9, 85, (1969).

Etherington R.J., Haines M.G., Phys. Rev. Lett., 14, 25, 1019(1965)

Evans D.E., Katzenstein J., Rep. Prog. Phys., 1969, 32, 207-271

Firsov O.B. In Loenovich, M.A. ed. 'Plasma physics and the problem of controlled thermonuclear reactors', 3, 386, London Permagon Press, 1959.

Gibson A. et al., 'Plasma Physics and Controlled Nuclear Fusion Research', (I.A.E.A., Vienna, 1969), Vol.I, p.465.

Glasstone S., Lovberg R.H., 1960, 'Controlled Thermonuclear Reactiors', (London, Van Nostrand).

Grad H., 1961. 'Plasma Physics and Controlled Nuclear Fusion Research', (I.A.E.A., Vienna, 1962) p.61.

Green T.S., Newton A.A., Segre S.E., Fusion Nucleaire 6, 223, (1966).

Griem H.R., 'Plasma Spectroscopy', McGraw Hill, 1964.

Griem H.R., Chin-Fatt C., Phys. Rev. Lett., 25, 24, 1640 (1970)

Grover F.W., (1962), 'Inductance Calculations Working Formulas and Tables', Dover Publ. Inc., 1962.

Haines M.G., 1961 'Plasma Physics and Controlled Nuclear Fusion Research' (I.A.E.A. Vienna, 1962) CN310/75.

Haines M.G., '6th Int. Conf. on Ionis. Ph. in Gases', Paris 1963, 4 477

Haines M.G., 1963 Imperial College internal report.

Hamberger S.M., Jancarik J., Phys. Rev. Lett., 25, 15,999(1970)

Hasted J.B., in 'At. and Mol. Processes', ed. Bates D.R., Ac. Press, 1962.

Hockney R.W., Phys. Fluids, 9,(1966), 1826.

Hockney R.W., (b) J. Comput. Phys. 8(1971), 19.

Hockney R.W. (c) M.C.P., Vol.9, Ac. Press, (1970).

Kagan Y.M., Perel V.I., Usp. Fiz. Nank. 81, (409), 1963.

Keilhacker M., Steuer K.H., Phys. Rev. Lett., 26, 12,694,(1971).

Key M., 1965, Ph.D. Thesis, London University.

Kileen J., Rompell S.L., J. Comput. Phys. 1, 29,(1966).

Kilkenny J.D., Imperial College internal report.

Kolb A.C., McWhirter R.W.P., Phys. Fluids, 7,(1964), 519.

Kunze H.J., 1965, Z. Naturf. A. 20, 801-13

Lance G.N., Numerical Methods for High Speed Computers, Iliffe, 1960.

Lax P.D., Wendroff B., Comm. Pure & Appl. Math., 13,217,(1960).

Malesani G., Ellis W.R., Newton A.A. 'IV European Conf. on Cont. Fusion and Plasma Physics', p.42, 1970.

Marquardt D.W. Share Distribution No. 1428.

McWhirter R.W.P., 'Plasma Diagnostic Techniques' ed. Huddleston R.H., Leonard, S.L., Ac. Press, 1965.

Measures R.M., University of Toronto, AFOSR., 62-1422.

Miyake S., Inst. of Plasma Physics, Nagoya University, research report IPPJ-111, (1971).

Morozov A.I., Kislov A.Y., Zubkov I.P., CTO/516 (1969).

Northrop, Annals of Phys, 15, 79-100 (1961).

Olsen H.N., J.Q.S.R.T., 3, (305), 1963

Parkinson G.J., Dangor A.E., Chamberlain J., Applied Physics Letters, 13, 7, 233 (1968).

Parkinson G.J., 1969, Ph.D. Thesis, University of London.

Patrick R.M., Schneiderman A.M., VI Symp. on Eng. Aspects of M.H.D. 1965 (Pittsburgh, Pa.)

Ringler, Nodwell, Phys. Lett., 29, A151, (1969).

Roberts D.E., Phys. Fl., 15 (192), 1972.

Roberts K.V., Potter D.E., in 'Methods of Computational Physics,' Vol. 9., Ac. Press, 1970.

Seaton, Monthly Notices Roy. Astron. Soc, 119, 81 (1959).

Smith C.G., Bishop A.S., 'Plasma Phys. and Controlled Nuclear Fusion Res.' (I.A.E.A., Vienna, 1969), Vol.I, p.591.

Spitzer L., 'Physics of Fully Ionised Gases,' Interscience, 1956.

Stratton J.A., 'Electromagnetic Theory', (McGraw-Hill, 1941) p.263.

Taylor R.J., (1960) AERE-M563

Ware A.A., Faulkner J.E., Nuclear Fusion, 9 (1969)353.

Watkins et. al., 1971 'Plasma Physics and Controlled Nuclear Fusion Research' (I.A.E.A., Vienna, 1972), Vol.I, p.255.

Wiese W.L. in 'Plasma Diagnostic Techniques' ed. Huddlestone R.H., Leonard S.L., Ac. Press 1965

Experimental and Theoretical Progress on the Polytron

by

A.E. Dangor, M.G. Haines, J. Kilberry, G.J. Parkinson,

D.F. Potter, M.J. Watkins.

Physics Dept., Imperial College, London, England.

Introduction

Since our report in the third IAEA Conference on Plasma Physics and Controlled Fusion Research (1968) (1) the torus bore was increased from 46 mms to 71 mms. With this modification a twofold increase in the cusp radial magnetic field at the quartz wall is obtained using the same magnetic field coils. It was hoped that this increase together with the larger bore would increase the time before the leakage through the ring cusps became important. Measurements of the containment time show that the expected improvement was not obtained for reasons to be given. However, much progress in studying the Hall acceleration process has been made.

The computational work referred to in the abstract will be included in the oral presentation.

Containment time measurements

Fig. 1 shows typical oscillograms of the total current in the z-direction (cylindrical coordinates are used, in which the z-axis is taken to be in the toroidal direction) for the two different discharge regimes: the left trace is the regime in which the ions are the dominant current carriers and the right trace is the regime in which an electron current begins to grow at the time of the change in slope. At this time for both conditions the AIV 12309 Å radiation, shows an intensity peak and also it coincides approximately with the time at which the signal from a Faraday probe, at the wall, biased to collect ions, reaches half its maximum value. This time is therefore taken to be a measure of the containment time, i.e. the time at which cusp losses become evident. The value obtained is found to decrease with increasing applied electric field. This is probably due to a larger increase in the thermal speed of the particles through Ohmic heating outweighing any increase in axial directed motion. The containment time is also found to decrease weakly with increasing cusp magnetic field. Langmuir probe and microwave investigations of the interaction of the rising cusp magnetic fields with the decaying preionizer plasma show that the plasma is compressed into the region between cusp coils. The electron density in this region is found to be approximately four times larger than in absence of the cusp field. Ion probe measurements indicate that the size of each plasma leakage ring is approximately 3 mms in length, it decreases with increasing radial cusp field B_r and is of the order of the ion Larmor radius. Thus at the time when the main accelerating electric field is applied a very non-homogeneous plasma distribution obtains. The measured containment times is determined partly by this unfavourable distribution and this explains the similarity in the containment times found in the large and small bore vessels.

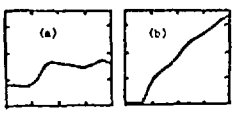

Fig. 1: I_z oscillograms for (a) E = 6.3 kv/m (b) E = 12.6 kv/m: B cusp = 4 kgauss, pressure 4 microns argon, 5 ka/div, time base. 1 μsec/div.

Acceleration Process

Some further measurements concerning the acceleration process are obtained at times earlier than the containment time. In particular the magnetic field generated by the azimuthal Hall currents (due to $j_z \times B_r$) is found using diamagnetic loops placed internally in the region where B_r is a maximum. These show a maximum in their variation with cusp magnetic field showing the expected linear dependence for small B_r and inverse variation for large B_r. Figs. 2-4 show the variation of the initial dI_z/dt with applied electric field E_z, applied cusp magnetic field, and initial gas pressure in argon. These graphs are consistent with a model in which the electrons are trapped by the cusp field and the ions along are accelerated by the applied electric field. Then the ion inertia enters the plasma toroidal circuit equations as an inductance in addition to geometrical inductance per unit length L. We write

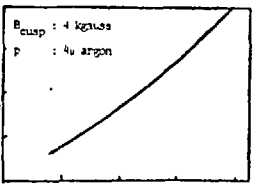

Fig. 2 3.15 kv/m/div. E_z →

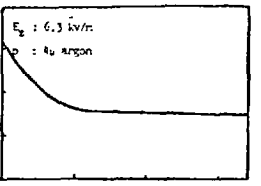

Fig. 3 4 kg/div B_{cusp} →

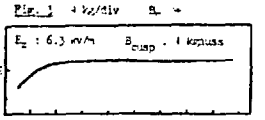

Fig. 4 1 micron/div p →

Fig. 2 - 4 : 1 vertical division : 5 ka/μs.

$$\left[L + \frac{m_i}{N_i e^2 z^2}\right]\frac{dI_z}{dt} + \left[R - \frac{m_i}{z^2 e^2 n_i^2}\frac{dn_i}{dt}\right] I_z = E_z$$

where N_i is the ion line density, R is the resistance per unit length, and ze is the mean ionic charge. For n_i small, the ion inertia dominates the equation when $I_z = 0$. This is in agreement with Fig. 4 where dI_z/dt is proportional to p at small pressure and is independent at large p. The variation of initial dI_z/dt with E_z (Fig. 2), is approximately linear for large E_z. Thus numerically

$$\left.\frac{dI_z}{dt}\right|_{t=0} = \frac{E_z \cdot 10^6}{[0.5 + 4.5/z^2]}$$

in MKS units. Experimentally $\frac{dI_z}{dt} = 1.2 \cdot 10^6 E_z$ A sec^{-1}, which indicates a value of z for argon between 3 and 4 in agreement with measurements of line intensities from various ionization states.

The variation of dI_z/dt with B_{cusp} is in agreement with the PIED calculations made by Dunnett (2) in which the magnetic field of the Hall current is included. In these calculations a critical applied electric field is derived, above which the electrons do not remain trapped. Approximately the condition for no axial current is

$$\frac{\omega_0 n_e e}{k \bar{B}_r^2} E_z = 1$$

where $\bar{B}_r$ is an averaged value of the cusp radial field and π/k is the cusp seperation. At low values of the cusp magnetic field this condition will be violated, and the electron trapping model with ion inertia in the circuit equation no longer holds. The initial dI_z/dt will be larger and determined by only the geometric inductance as found in Fig. 3.

References

1. Dangor, A.E. et. al. 1969. "Plasma Physics and Controlled Nuclear Fusion Research" Vol.1, pp.255-262 (I.A.E.A.: Vienna).

2. Dunnett, R.W., Nuclear Fusion 8, 4 (1968).

From: III European Conference on Controlled Fusion and Plasma Physics, Utrecht, 1969.

Particle loss from the Polytron

J.D. Kilkenny and A.E. Dangor
Physics Dept., Imperial College,
London, England.

Abstract Single particle calculations of the ion motion in the polytron configuration show that particles situated inside a volume close to the minor axis are contained indefinitely. Particles situated outside this volume are lost. Experimental confirmation of this loss region is presented.

The polytron experiment attempts to contain a high temperature plasma in a series of magnetic cusps arranged in the form of a torus. Leakage from the ring cusp should be prevented by accelerating the plasma in the toroidal direction by the application of a toroidal electric field E_ϕ. In previous experiments (1,2) it was found that a rapid leakage occurred about 1 μsec after the application of the electric field. Doppler shift measurements and spectroscopic temperature estimates indicate that the condition $V_d < V_H$ where V_d is the ion drift velocity in the toroidal direction and V_H is the thermal velocity of the ion is only marginally satisfied. This condition is thought to be necessary to avoid the normal thermal losses through the ring cusp. However a single particle calculation shows that $\underline{v} \times \underline{B}$ forces on the particle can give rise to additional leakage, which is found to dominate experimentally.

The equation of motion of a particle is solved numerically, taking the actual vacuum magnetic field produced by the 36 toroidally placed cusp coils, and starting the particles at rest. The motion of ions fall into three categories. Firstly there are those particles located near the magnetic axis which are accelerated in the toroidal direction straight through the magnetic

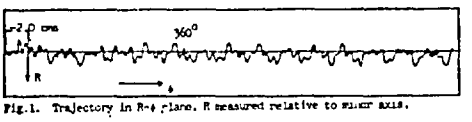

Fig.1. Trajectory in R-φ plane. R measured relative to minor axis.

cusps. Secondly, further away from the axis, the particles are reflected by the magnetic field towards the minor axis, whereupon reaching a region of smaller radial magnetic field they are accelerated and behave as particles in the first category. The third category of particles are still further off the magnetic axis. These particles are lost straight through the ring cusp. In all cases the instantaneous Larmor radius of the ions is comparable with or larger than the dimensions of the cusp field, and each coil acts as a focussing magnetic lens to the ions which are accelerated through.

In the toroidal configuration all of the ions which are accelerated initially are eventually lost, because of the curvature at high velocities of the centrifugal force. However when collisions are included we would expect a limiting ion velocity $v_\phi \approx E_\phi/\nu_i$. This is simulated in the model by making the toroidal electric field $E_\phi = E_\phi(1-v_\phi/v_d)$. With this modification the ions can be contained indefinitely as long as $6.0\ 10^3 V_c/A > v_d > 2.1\ 10^5 V_c/A$ m/s for this geometry. Fig. 1 shows such an ion trajectory in the R-φ plane. The field strength is specified by V_c, the charging voltage of the cusp coils in kV (1 kV is equivalent to an average radial field of .3tesla. V and A are the ionic charge and atomic weight respectively. This can be compared with a Busch formula, fig. 2, for a magnetic lens

$$\Delta\phi = \frac{\delta}{r} = \frac{1}{4v_d^2}\left(\frac{eA}{m}\right)^2 \quad (1)$$

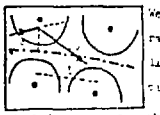

Fig.2. Focussing of particle by cusp field.

We require $\overline{\Delta\phi} = \frac{\bar{\delta}}{r_0} < \frac{2\pi}{j_0}$ where r_0 is the major radius. So a particle with a large δ undergoes a large deflexion. There is also a rotation of the particle about the minor axis of $\omega = \frac{1}{2}\left(\frac{eA}{m}\right)\frac{1}{r_d}$ which alternates in sign through successive cusps.

In order that particles do not accumulate a large angle between their trajectories and the minor axis we require $\frac{\omega}{\phi} < 1$ and as $\bar{\delta} < a$ (the tube radius) both conditions can be satisfied if $\frac{1}{2}\frac{eA}{m} < v_d < \frac{eA}{m}\frac{a}{r_0}$.

Numerical agreement is reasonable.

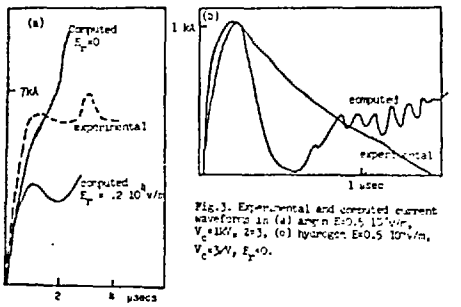

Fig.3. Experimental and computed current waveforms in (a) argon E_ϕ=0.5 10^8v/m, V_c=1kV, 2=3, (b) hydrogen E_ϕ=0.5 10^8v/m, V_c=3kV, E_ϕ=0.

The number of electrons which belong to the first and second category is very small and originate very close to the magnetic axis. The radial loss of these electrons will be prevented by electrostatic fields and to allow for this a radial field is included in the calculation. To compare the particle motion and losses in this computational analysis with experimental results a reasonable number of particles (256), distributed uniformly throughout the region of the discharge vessel are taken. As particles reach the wall in the calculation they are removed. It is found that losses are limited to the ring cusp region, and shift in the direction of the applied electric field. Experimental evidence for this exists in framing camera photographs of the discharge which show that at the time losses are predicted the wall at the ring cusp becomes luminous. A shift in the E_ϕ direction is also observed. Ion probes measuring the flux of particles also give an appreciable signal at this time. Fig. 3 shows the calculated and experimental toroidal currents. The fall off in the current is caused by particle loss. Good experimental agreement is obtained by including a radial electrostatic field equivalent to a temperature of 70 eV.

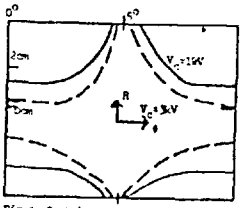

Fig.4. Contained volumes for hydrogen, E_ϕ=.5 10^8v/m. The ring cusp is at 60°.

The volumes from which lost and accelerated plasma originates are shown in fig. 4. The dependence of the contained volume on B, E_ϕ and e/m can be obtained as follows. Assuming cylindrical symmetry and using the constancy of canonical angular momentum and energy $|r^2\dot{\phi}\cos\alpha - r_0^2\dot{\phi}_0\cos\alpha_0| < \left(\frac{r_0 r_c}{r_0 - r_c}\frac{2eV_c}{m}\right)^{\frac{1}{2}}$ where (r_0,α_0) specify the initial position of the particle. The field is taken as $B_z = B_0\cos\omega t$, approximately. Since $r=a$, the tube radius, particles are lost if

$$r_0 > \left(\frac{a}{\left[\frac{2eV_c}{m}\right]^{\frac{1}{2}} - \left(\frac{eE_\phi}{m}\right)}\right)^{\frac{1}{2}}.$$

This dependence is in agreement with the calculations and the experiment.

Ref.: (1) Farrar et al., 1967, Proceedings, Vol.I, p.105 (IAEA).
(2) Dangor et al., 1969, Preprint, p.14 (Culham Laboratory).

From: IV European Conference on Controlled Fusion and Plasma Physics, Rome 1970.

IAEA-CN-28/D-9

NUMERICAL AND LABORATORY EXPERIMENTS IN THE POLYTRON CONFIGURATION

M.L. WATKINS, D.E. POTTER, J.D. KILKENNY,
M.G. HAINES, A.E. DANGOR
Physics Department, Imperial College, London,
United Kingdom

Abstract

NUMERICAL AND LABORATORY EXPERIMENTS IN THE POLYTRON CONFIGURATION.

A two-dimensional MHD two-fluid numerical model has been constructed to simulate the plasma behaviour in the r-z plane of a linear Polytron - a multi-cusped pinch device in which the plasma flows through the cusps. Of importance in this code compared to the earlier "Focus" code (a two-dimensional MHD code developed by Potter) is the inclusion of the other two components of magnetic field B_r, B_z and azimuthal velocity. With the dominance of the Hall effect, it is found that the characteristic velocity determining the mesh time-step is the whistler-wave velocity rather than the Alfvén speed. Present results show that the collapse of an axial current sheet to the axis is modified by the cusp field to give several interesting phenomena: firstly, Hall acceleration of the ions in the axial and azimuthal direction; secondly, asymmetric ion compressional heating and electron Ohmic heating; thirdly, due to the existence of a radial component of the current density locally, there can be reversal of Hall acceleration in certain regions leading to the circulation of plasma; fourthly, there is qualitative agreement with a single-particle model so that a central core of plasma appears well defined and detached from the walls.

Laser scattering diagnostics are being employed on the laboratory toroidal experiment in order to measure the electron temperature and density enabling direct comparison with the numerical model. Magnetic-probe measurements in the ring-cusp plane show that the axial current-density component is confined to the magnetic axis. From the line intensity of argon-IV radiation an axial asymmetry about the ring cusp has been found and confirmed by the numerical model. Toroidal effects have also been observed, namely the preferential outward drift of the plasma in the later stages of the discharge and the associated vertical shift of the plasma which is periodic with the radial magnetic field.

1. GENERAL INTRODUCTION

1.1. Basic Polytron Concept

The Polytron experiment is designed to study the containment and stability properties of a plasma that is moving rapidly through a series of cusp-shaped magnetic fields around the minor axis of a torus. The cusp fields have very favourable stabilising properties for plasma containment, and it is proposed that the convective motion of the plasma through the cusp fields should considerably reduce losses of plasma through the ring cusps. The axial motion of the plasma is achieved by inducing an electric field in this direction, and employing the Hall acceleration mechanism to attain an axial ion current (1).

1.2. Analytical Theory

1.2.1. Conditions for Hall Acceleration

A one dimensional MHD model of Hall acceleration of ions of mass m_i in the direction of an applied electric field E_z in the presence of a spatially periodic transverse magnetic field $B_{r0}\sin kz$ yields the condition for Hall acceleration of the ions (1)

$$\frac{m_i c}{eB_{ro}/\sqrt{2}} \cdot k \cdot \frac{cE_z}{B_{ro}/\sqrt{2}} > 0.8 \qquad (1)$$

valid for a wide range of the Hall parameter, $\alpha = \frac{\sigma B_{ro}}{\sqrt{2}\, nec}$. The characteristic time τ_a for acceleration of the ions to a terminal velocity cE_z/ne is given by

$$\tau_a = \frac{1 + \alpha^2}{\alpha \Omega_i} \qquad (2)$$

where $\Omega_i = \frac{e B_{ro}}{m_i c\sqrt{2}}$ is the mean ion gyro frequency. When the perturbation of the applied magnetic fields by the induced Hall currents is included in the model, a second condition is found, which essentially states that the azimuthal Hall currents should not be large enough to destroy the applied cusp fields (2). That is,

$$\frac{4\pi ne\, c\, E_z}{c\, B_{ro}/\sqrt{2}} \cdot \frac{1}{k\, B_{ro}/\sqrt{2}} < 1 \qquad (3)$$

If this condition is violated, an axial electron current flows and the ion acceleration time becomes much longer. Conditions (1) and (3) can be simultaneously satisfied only if

$$\frac{m_i c^2 k^2}{4\pi ne^2} = \frac{c^2 k^2}{\omega_{pi}^2} \gg 1 \qquad (4)$$

This condition places great problems in the numerical simulation discussed in this paper.

1.2.2. Conditions for containment

When the acceleration process is complete, containment will be possible if the ion centre of mass velocity is much greater than the ion thermal velocity, i.e. there are negligible ions at rest in the laboratory,

$$v_z \gg \sqrt{\left(\frac{2kT}{m_i}\right)} \qquad (5)$$

In order that electrostatic instablities do not arise, the ion centre of mass velocity however should be much less than the electron velocity, i.e.

$$v_z \ll \sqrt{\left(\frac{2kT}{m_e}\right)} \qquad (6)$$

These last two conditions can easily be satisfied since $m_e \ll m_i$. If we choose $v_z^2 = \frac{2kT}{\sqrt{(m_e m_i)}}$, the ions, constituting a current $I = Nev_z$ where N is the line density, can satisfy the self-focussing relations of Bennett

$$I^2 = 4NkTc^2 \qquad (7)$$

if the operating line density is

$$N = \frac{2\sqrt{(m_e m_i)}c^2}{e^2} = 4.3\times10^{14}\,\mathrm{cm}^{-1} \qquad (8)$$

Further theoretical work has been carried out on particle trajectories and on the stability of the configuration, but will not concern us in this paper.

1.3. Earlier Experimental Work

The Hall acceleration mechanism was investigated experimentally first in a straight configuration (3) and the magnetic stress tensor was measured, demonstrating an axial force of about 13 kgm.wt. Similar forces have been measured in the toroidal experiment in which 36 cusp coils have been energised. At Novosibirsk (4) measurements of the radial distribution of azimuthal Hall currents were presented, and an ion axial motion of 10^9 cm/sec was deduced from the Doppler shift of an argon IV line. About 2 kA of ion current was achieved, but not satisfying condition (5) above - the centre of mass velocity was only about sonic. In part this might be due to the fact that preionisation was limited to rather higher densities so that the line density was about 20 times that indicated by eq. (8). At Utrecht (5) it was shown that as the plasma density was increased the axial current switched over from being an ion current to a much larger electron current, in keeping, quantitatively, with condition (3). In all cases plasma losses through the ring cusp occurred after about 1 usec. Calculated single particle trajectories showed that these losses could be due to that plasma which originated near the walls, and that the remainder of the plasma could be accelerated and contained indefinitely (6). In the experiment the losses are probably also caused by an insufficiently large axial ion velocity, thus violating condition (5). The experimental time was also limited to times less than τ_a.

1.4. Present Research

1.4.1. Computational Model

The analytic work is limited either to a linear approximation or to a quasi-one-dimensional approach that precludes the theoretical study simultaneously of radial plasma compression with axial Hall acceleration, magnetic field distortion, radial losses, instabilities, etc. A single particle computational model gives an insight into the possible trajectories that can occur in the complex field configuration, but the most powerful theoretical model with which all these phenomena can be studied is a numerical simulation using magnetohydrodynamic equations for a two-fluid plasma. A computer code (GEMINI) has been set up to obtain axisymmetric solutions in the r-z plane of a straight cylinder (7). Several production runs have been made. GEMINI is a generalisation of the Plasma FOCUS CODE (8) which has been most successful in describing experimental phenomena. All three magnetic field components are present in GEMINI and this introduces new computational problems associated with the whistler wave. This will be discussed below.

1.4.2. Experiment

The present experimental work is devoted to more detailed measurements of electron density and temperature using laser scattering techniques. Also the problem of preionisation at lower densities is being studied in order that conditions (4) and (8) can be satisfied.

2. THE TWO-DIMENSIONAL MHD CODE, GEMINI

2.1. The MHD Equations

The numerical model employs a rectangular Eulerian mesh mapped on the r-z plane of a cylindrical infinitely long polytron configuration.

Periodic boundary conditions are applied in the axial direction, there being one complete cusp length in the domain. On the mesh points the following plasma and magnetic field parameters, ρ, B_θ, A_θ, v_z, v_r, v_θ, T_e and T_i, are found and followed in time using the equations below.

$$\frac{\partial \rho}{\partial t} + \nabla.(\rho\vec{v}) = 0$$

$$\frac{\partial(\rho\vec{v})}{\partial t} + \nabla.(\rho\vec{v}\,\vec{v}) = \vec{J} \times \vec{B} - \nabla(p_i + p_e) + \rho\,\vec{g}$$

$$\frac{\partial p_e}{\partial t} + \nabla.(p_e\vec{v}_e) = (\gamma-1)\,(\eta J^2 - p_e \nabla.\vec{v}_e - \text{EQUIP}\,(T_e - T_i) - \text{RAD})$$

$$\frac{\partial p_i}{\partial t} + \nabla.(p_i\vec{v}) = -(\gamma-1)\,(p_i \nabla.\vec{v} + \text{EQUIP}\,(T_i - T_e)) \qquad (9)$$

$$\frac{\partial A_\theta}{\partial t} - \eta\nabla^2 A - (\vec{v}_e \times \vec{B})_\theta = 0$$

$$\frac{\partial \xi_\theta}{\partial t} + (\nabla \times (\vec{\xi} \times \vec{v}))_\theta = -(\nabla \times (\eta \nabla \times \vec{\Omega}_\theta))_\theta - (\nabla \frac{1}{\rho} \times \nabla p_i)_\theta$$

where $p_e = \rho T_e$, $p_i = \rho T_i$, $\vec{v} = (v_r, v_\theta, v_z)$, $\vec{B} = (B_\perp, B_0)$, $B_\perp = \nabla \times \vec{A}_\theta$, $J_\perp = \nabla \times \vec{B}_\theta$ $J_\theta = -\nabla^2 A_\theta$, $\xi_\theta = \Omega_\theta + (\nabla \times \vec{v})_\theta$, $\Omega_\theta = eB_0/m_i$, $\vec{\xi} = \vec{\Omega} + \nabla \times r_\theta$, $\vec{\Omega} = e\vec{B}/m_i$, $\vec{v}_e = \vec{v} - m_i\vec{J}/\rho e$, $\vec{g} = \vec{r} v_\theta^2 / r^2$

EQUIP equipartition term (included implicitly), RAD bremsstrahlung radiation term (included explicitly to second order).

At present thermal conduction and viscous terms have not been included. These present additional difficulties because of the strong anisotropy of the transport coefficients in a large magnetic field, the direction and magnitude of which vary in time and space.

2.2. The Time-step for the Calculation

The equations (9) above may be studied analytically, allowing perturbations from an initial steady state in order to obtain the linearised dispersion relation for all possible mode frequencies w, the highest of which will determine the maximum time-step for proceeding with an explicit calculation.

It is found that the highest frequency present in the parameter range of interest is that of the whistler mode. Because this restricts the calculations to very small time steps, the possibility of damping or removing this wave by resistivity, viscosity and finite Larmor radius effects was investigated. For a uniform plasma immersed in a straight uniform magnetic field, the fastest mode is transverse with wave number $\underline{k}$ parallel to the magnetic field. The dispersion relation is a quartic which factorises into two quadratics.

$$0 = (w - iw_R)^2 \pm (1 + \beta)s(w - iw_R) - i(w_\nu - w_R)(w - iw_R)$$

$$-1 \mp i(w_\nu - w_R)s + \beta s^2. \qquad (10)$$

where the mode frequency w is normalised to the Alfven frequency kv_A, and the other parameters, in c.g.s. units, are

$$s^2 = \frac{m_i k^2 c^2}{4\pi n e^2} = \frac{k^2 c^2}{w_{pi}^2} \qquad (11)$$

and $$w_R = \frac{\eta k c^2}{4\pi v_A}, \quad w_\nu = \frac{\mu k}{\rho_0 v_A}, \quad \beta = \frac{4\pi p_i}{B_0^2} \qquad (12)$$

η and μ being the resistivity and viscosity respectively.
We note that the finite Larmor radius effects enter through the β of the plasma.

In absence of resistivity, viscosity and finite Larmor radius effects, w has the 4 values $\pm\{\sqrt{(\frac{1}{4}s^2 + 1)} \mp \frac{1}{2}s\}$.

From a comparison of equations (4) and (11) it is clear that for the polytron conditions where k is the wavenumber of the cusp fields we require $s \gg 1$. The highest frequency is then approximately $\text{sk}v_A = \frac{k^2 v_A c}{w_{pi}}$ sec^{-1}.

Because of the dispersive nature of this whistler mode, in its application to a finite difference scheme with mesh points separated by k_m^{-1}, the required timestep Δt_m of the mesh is given by

$$\Delta t_m = \frac{w_{pi}}{k_m^2 v_A c} \qquad (13)$$

In contrast, when the magnetic field is normal to the plane of the calculation (as in the plasma focus code), the time step is $(k_m v_A)^{-1}$ for $v_A \gg$ sound speed, corresponding to the fast magnetosonic wave. Thus, like the diffusion problem, doubling the number of mesh points quadruples the number of required time steps. We can estimate the number of time steps necessary to reach the characteristic acceleration time τ_a given by eq. (2) by taking the ratio of eqns (2) and (13), and using $v_A w_{pi} = \Omega_i c$, viz.,

$$\text{Number of time steps} = \frac{\tau_a}{\Delta t_m} = \frac{1+\alpha^2}{\alpha} \cdot \left(\frac{kc}{w_{pi}}\right)^2 \cdot \left(\frac{k_m}{k}\right)^2 \qquad (14)$$

Each of the factors in equation (14) is much larger than one, the factor k_m/k being the number of linear mesh points in the cusp period. In order to satisfy condition (4) and also have a fine mesh, the number of time steps is very large. It is well known that when the Lundquist number is smaller than one viscosity or resistivity removes the Alfven modes. Therefore methods of removing the short wavelength whistler modes, were investigated: eq. (10) describes the effect of viscous and resistive damping on these modes.

2.2.1. Resistive damping of the whistler mode

In figure 1(a) the real and imaginary parts of the normalised frequency w are plotted for different values of the parameter s. In each constant s curve, increasing w_R results in evolution along the curve in the direction of decreasing $|w_r|$ where $w = w_r + iw_i$ and k is real. The curves for s=0 indicate that for sufficiently small Lundquist number the Alfven wave is completely damped. However for finite s, whilst resistivity increases the damping and reduces w_r in all cases, for large s the reduction is small for two of the four modes. (Two modes are illustrated in figure 1, the other two modes simply correspond to $w = -w_r + iw_i$).

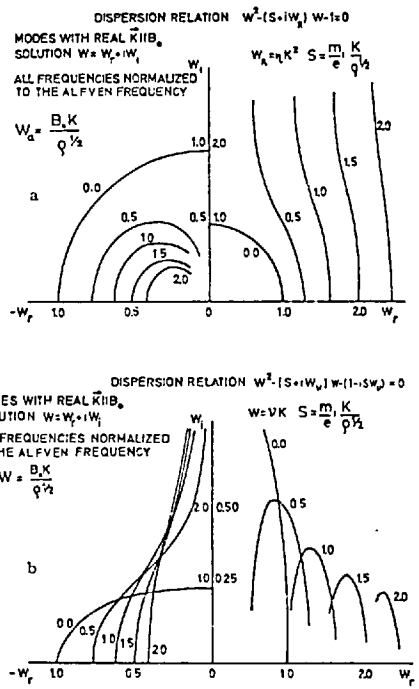

FIG.1. Dispersion curves showing resistive (a) and viscous damping (b) of whistler modes.

2.2.2. Viscous Damping of the Whistler Mode

With w_v non-zero but w_R and β zero in eq. (10) we can examine the effect of viscous damping which, for non-zero s, is different to resistive damping. In figure 1(b) the real and imaginary parts of the normalised frequency are similarly plotted for the indicated values of s. For large s, increasing values of w_v do not result in much reduction of w_r.

2.2.3. Finite Larmor radius effects

In absence of visecsity and resistivity, we retain the parameter β in eq. (10) which arose in the analysis through the inclusion of collisionless viscosity. w is real and has the values $\pm\{\sqrt{(\frac{1}{4}s^2(1-\beta)^2+1)} \mp \frac{1}{2}s(1+\beta)\}$. For large s, instead of two of the roots cutting off at the ion gyrofrequency, they now have a group velocity β times that of the other two modes.

2.3. Numerical Scheme for GEMINI

To simulate the differential equations (9) on a finite-difference-mesh, the set of equations are solved either implicitly - a most difficult, if not impossible, task due to the mixture of hyperbolic (essentially time-evolution) equations and elliptic (essentially boundary-value) equations - or explicitly. The latter was chosen, but is severely limited in the problem at hand due to the necessity of restricting the timestep of the calculation to such a value that the mode with the shortest timescale or fastest group velocity may be followed. If this timestep criterion is not satisfied, numerical instabilities will develop immediately. Although the equations solved are non-linear, the numerical stability criterion deduced from linear stability theory applies very well to assess the stability of small timesteps. The non-linearity will result in isolated regions of parameter space having much higher frequencies than those associated with the rest of the parameter space. The stability criterion reduces the error in most regions of parameter space due to taking a finite difference solution. (This error is of order $(w\Delta t)^n$ where n is the order of the scheme used and w is the fastest mode frequency.)

Clearly, from eq. (14), it is difficult to simulate for reasonable times the behaviour of the plasma in a polytron regime, i.e. with Hall acceleration and conditions (1), (3) and (4) holding. Alternatively, borderline cases can be followed for reasonable times or strongly satisfied cases for very short times. Whilst viscosity and resistivity dampen the fast whistler mode a little, no obvious solution to the problem of removing the whistler wave whilst retaining the Hall terms in the equations has been found.

The code GEMINI (7) has been developed for the numerical simulation of an axisymmetric plasma in a general magnetic field configuration. Equations (9) are written in a differenced form to apply to an Eulerian mesh, and solved using the second-order accurate explicit Lax-Wendroff method (9). All equations, with the exception of that for A_θ are solved this way, only initial values being strictly necessary for their solution; but due to the discrete mesh pseudo-boundary values have also to be applied. The equation for A_θ (determining B_r and B_z) is treated as a boundary value problem, using the method of Successive over relaxation (10) to solve implicitly at the end of each half- and full-timestep of the explicit calculation.

2.3.1. Boundary Conditions

In the polytron simulation, periodic boundary conditions are applied at z=0 and z=λ=10cm. For A_θ are imposed additionally the boundary conditions that at the axis (r=0) it is zero, whilst at the insulating boundary ($r=r_\theta$ =4cm) it has a sinusoidal form, representing the cusp-shaped magnetic field lines. In the laboratory experiment A_θ is generated by energising coils external to the region of the calculation. To minimise the computing to only that which is important A_θ is not calculated outside the region bounded at $r=r_\theta$. This is equivalent to having a perfectly conducting region immediately outside the insulating boundary.

In the toroidal laboratory experiment the axial current is induced by changing the magnetic flux threading through the torus. In the straight cylindrical simulation it is not possible to employ the same physical method because $\frac{\partial A_z}{\partial t}$ is a measure of the change of B_θ flux within a radius r rather than the change of flux in some external region. In the numerical code an electrostatic electric field is applied and a simple

external circuit for the total axial current I is considered. I is governed by the equations

$$I = -\frac{dQ}{dt} \quad \text{and} \quad \frac{Q}{C} = \frac{d}{dt} \iint B_\theta dr dz + L\frac{dI}{dt} \qquad (15)$$

The resulting value of the current is used to set B_θ on the insulator boundary for the next timestep.

3. COMPUTATIONAL RESULTS

The results of two numerical experiments are presented in this paper. Experiment 1 explores the polytron regime whilst in experiment 2 the Hall terms are virtually suppressed for comparison. This latter case illustrates the pinch dynamics in a cusp configuration including at later times the radial loss of plasma through the ring cusp region.

The initial conditions for each of the numerical experiments are as follows:

Initial velocity = 0
Initial filling density of deuterium = 4.5×10^{14} cm^{-3}
Initial electron and ion temperatures = 2 eV
Capacitance C = 20 μF
Charge on capacitance Q = 20 mC
Current I = 1 kA
Maximum B_z = 8 kG

A vacuum A_θ is set in the region by solving $\nabla^2 A_\theta = 0$, subject to the given boundary conditions.

3.1. Numerical Experiment 1

This experiment illustrates the asymmetry introduced into the problem by the inclusion of the Hall term $j_\theta B_z$, with the resultant Hall acceleration of the ions competing with the other dynamic effects of pinching and cusp-loss. In figure 2(a) the density, (b) B_θ, (c) the electron temperature are shown at the early time of 0.3 μsec, and then figure 2(d) (e) and (f) are the corresponding parameters at the later time of 0.7 μsec. In figure 3(a) contours of rA_θ illustrate the shape of the magnetic field lines at 0.3 μsec and 0.7 μsec; in 3(b) and (c) contours of rB_θ show the current flow pattern in the r–z plane at 0.3 μsec and 0.7 μsec respectively. The ion temperature and the velocity vectors in the r–z plane are shown in figure 3(d) and (e) respectively at 0.7 μsec.

Several phenomena are of interest, in particular, the growing asymmetric distortion of the cusp fields, and the tendency for the r–z current to follow the cusp shape field except at the ring cusp itself. In this region we note the axial plasma velocity ($\sim 3\times10^6$ cm sec^{-1}) resulting from the azimuthal Hall current. The axial component of the magnetic field also interacts with the azimuthal Hall current to set up a radial velocity component. In fact we expect $v_z/v_r \sim B_r/B_z$ i.e. motion normal to the cusp fields, which in the polytron act as a magnetic lens. In addition the $j_r B_\theta$ pinch forces are acting on the plasma and give a large compression of the plasma on the axis under the coils where the axial current is more concentrated. Nearer the walls the plasma density builds up in the ring cusp region, consistent with the single particle trajectory calculations (6), due to the flow of the plasma along the field lines. The ion temperature has maxima ($\sim$ 8eV) on the axis downstream of each coil due to compressional heating, whilst the electron temperature ($\sim$ 70eV) is also affected considerably by Ohmic heating. The ion temperature also rises downstream of the plane of the ring cusps due to axially accelerated ions compressing the downstream stationary plasma.

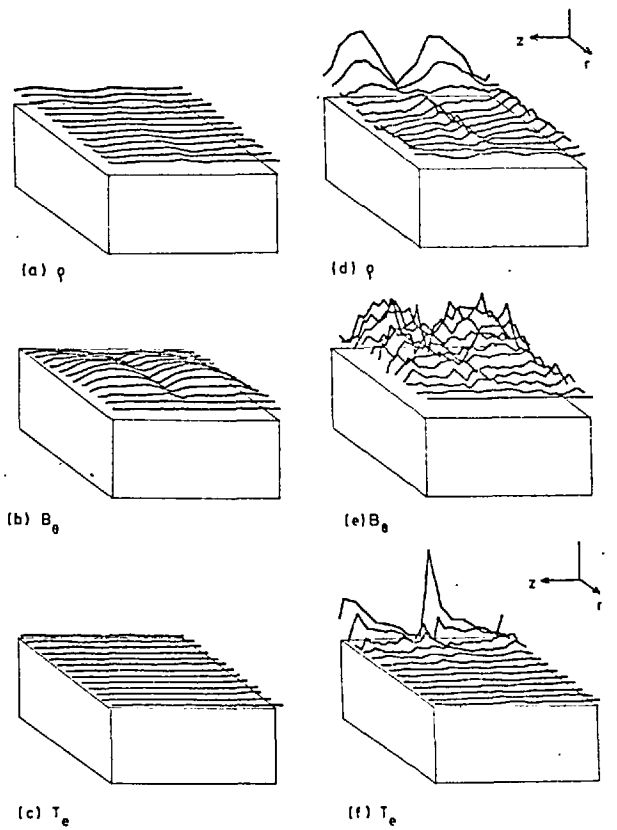

FIG. 2. Experiment 1 (Hall terms included).

Unfortunately this plasma at later times begins to be lost through the ring cusps, as indicated by the velocity diagram (fig. 3(e)). A set of parameters more in keeping with the conditions outlined in section 1 are required so that larger axial velocities occur before too many particles are lost.

As the plasma is compressed to the axis it leaves behind a plasma of low density. Within this region spurious closed loops of current develop in the r–z plane, which in turn induce azimuthal Hall currents of alternate sign. In figure 3(a) the 50% contour is thus distorted outwards at the later 0.7 μsec time. If the density of the plasma becomes less than

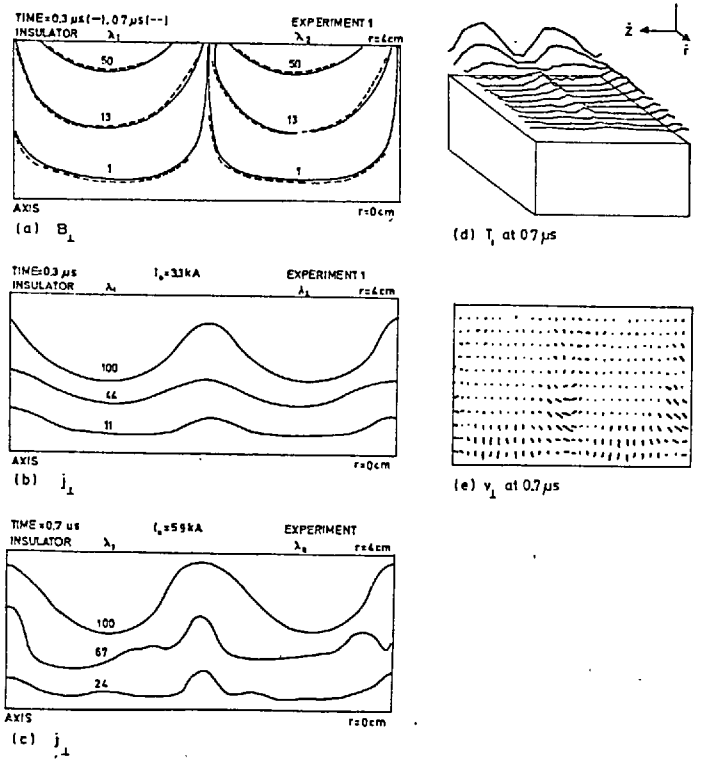

FIG. 3. Experiment 1. The magnetic field coils are positioned at λ_1 and λ_2 in (a), (b) and (c) and the contours are in terms of flux of $B_\perp$ or $j_\perp$ enclosed between the given contour and the axis.

a given (arbitrary) value, vacuum conditions of infinite resistivity, zero currents are imposed.

In figure 2(e) the growth of short wavelength modes on B_θ by 0.7 μsec shows the numerical problems that arise through the physical presence of such modes.

3.2. Numerical Experiment 2

In this experiment the Hall terms have been virtually removed, and symmetric behaviour each side of the ring cusp plane is expected.

Figure 4(a) shows rA_θ contour plots at 0.5 μsec and 1.0 μsec and figures 4(b) and (c) show the current flow patterns at these times. The effect of the inward diffusing B_θ on the vacuum cusp fields is to compress the field lines, thus generating an azimuthal current which causes a $j_\theta B_z$ force to oppose the $j_z B_\theta$ compression force. Figure 4(d) shows the azimuthal magnetic field at 1.0 μsec which has short wavelength Alfven wave structure superimposed on its profile.

A core of compressed plasma, compressed by a factor of 6, is formed on the axis (fig. 4(f)) but at 1.5 μsec it is being squeezed along the field lines into the ring cusps. Figure 4(e) shows the velocity vectors at each mesh point at 1.50 μsec, and the radial flow to the walls is dominant.

In comparison with experiment 1 we note that the current flow patterns follow more closely the cusp shaped vacuum fields, that there is no unidirectional axial motion, and that there is a much greater radial loss. All this is due to the suppression of the Hall effect.

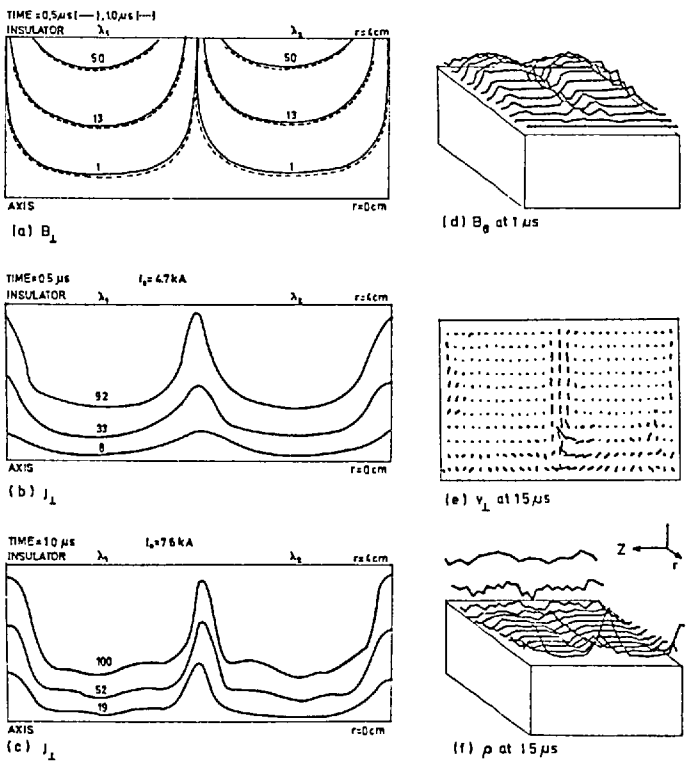

FIG. 4. Experiment 2. Hall term suppressed. a, b, c are as in Fig. 3.

4. RECENT EXPERIMENTAL RESULTS

At early times (~ 1 μsec in argon) image convertor photographs show a bright plasma well confined on the tube axis with a radius of about 1.5 cm expanding to 2 cm. The axial current profile in the plane of the ring cusp at this time is bell-shaped with a half width of 1.5 cm. From the time history of the appearance and disappearance of argon II, III and IV line radiation the temperature of this hot plasma is estimated to be 20 to 30 eV. Axial velocities of 1.1×10^9 cm/sec have previously been reported (4).

At about 1.5 μsec, the temperature falls rapidly to a few eV. Axial scans of argon IV and III line intensities in the neighbourhood of the ring cusp show that the cooling is more rapid downstream of the ring cusp plane. A narrow bright ring located at the wall in the ring cusp plane is obtained in photographs at this time. This ring shifts axially downstream.

These results are in qualitative agreement with the computational model.

5. SUMMARY

A two-dimensional MHD code for a general magnetic field configuration has been constructed and successfully run. An important problem, namely the limitation of the timestep for the calculation by the fast whistler mode, has been identified. The solution of this problem by resistive, viscous and finite Larmor radius damping is being studied.

The computational model shows qualitative agreement with experiment, and virdicates the predictions of Hall acceleration and ion focussing from earlier analytic theory. Further optimisation of parameters is required to reduce the radial plasma loss to an acceptable amount.

REFERENCES

(1) HAINES, M.G., Nuclear Fusion 1962 Supp. Pt 3 1122 (Abstract only). See also 6th Int. Conf. Ionization Phenomena in Gases, Paris (1963) 4, 477.
(2) DUNNETT, R.M., Nuclear Fusion 8 (1968) 4.
(3) ETHERINGTON, R.J. and HAINES, M.G., Phys. Rev. Lett., 14 (1965) 1019.
(4) DANGOR, A.E. et.al., Plasma Physics and Controlled Nuclear Fusion Research (1968) vol.1 (1969) 255.
(5) DANGOR, A.E. et.al., Third European Conf. on Plasma Physics and Controlled Fusion Research, Utrecht (1969) 83 (Wolters-Noordhoff).
(6) KILKENNY, J.D. and DANGOR, A.E., Fourth European Conf. on Plasma Physics and Controlled Fusion Research, Rome (1970).
(7) WATKINS, M.L., Second Conf. on Computational Physics, London (1970), 92 (I.P.P.S.).
(8) POTTER, D.E., Ph.D. Thesis, University of London (1970).
(9) LAX, P.D., WENDROFF, B., Comm. Pure and Appl. Math., 13 (1960) 217.
(10) ROBERTS, K.V., POTTER, D.E., "Magnetohydrodynamic Calculations", Vol.9, Methods of Computational Physics (ALDER, FERNBACH, ROTENBERG, Eds.), Academic Press, New York (1969).